Single-cell arrays for dynamic analysis of cell processes

Elisavet Chatzopoulou

München 2018

Single-cell arrays for dynamic analysis of cell processes

Elisavet Chatzopoulou

Dissertation
an der Fakultät für Physik
der Ludwig–Maximilians–Universität
München

vorgelegt von
Elisavet Chatzopoulou
aus Athen, Griechenland

München, den 27.06.2018

Erstgutachter: Prof. Dr. Joachim O. Rädler
Zweitgutachter: Prof. Dr. Angelika M. Vollmar
Tag der mündlichen Prüfung: 22.10.2018

List of associated papers

P1 **Chip-based platform for dynamic analysis of NK cell cytolysis mediated by a triplebody**
Elisavet I. Chatzopoulou, Claudia C. Roskopf, Farzad Sekhavati, Todd A. Braciak, Nadja C. Fenn, Karl-Peter Hopfner, Fuat S. Oduncu, Georg H. Fey and Joachim O. Rädler
Analyst, 2016, 141, 2284.

P2 **Rapid Analysis of Cell-Nanoparticle Interactions using Single-Cell Raman Trapping Microscopy**
Maria Steinke, Florian Zunhammer, Elisavet I. Chatzopoulou, Henrik Teller, Karin Schütze, Heike Walles, Joachim O. Rädler, Cordula Grüttner
Angewandte Chemie, 2018, 57, 4946-4950

M1 **A single-cell micro trench platform for automatic monitoring of cell division and apoptosis after chemotherapeutic drug administration**
E.I. Chatzopoulou, P. Raharja-Liu, A. Murschhauser, F. Sekhavati, F. Buggenthin, A. M. Vollmar, C. Marr and J.O. Rädler
submitted to Scientific Reports

Zusammenfassung

Auch in einer monoklonalen und scheinbar einheitlichen Zellpopulation sind Zellreaktionen im Allgemeinen heterogen. Daher gehen in Populationsmessungen, in denen das Signal über alle Zellen gemittelt wird, essentielle Informationen verloren. Aus diesem Grunde sind Zeitraffermessungen auf Einzelzell-Ebene nötig, welche durch Einzelzell-Arrays realisiert werden können und so die Dynamik von Zellprozessen erfassen. Die Analyse auf Einzelzellebene macht deutlich, dass die beobachtete Heterogenität biologisch relevant ist.

Im ersten Teil dieser Doktorarbeit werden Methoden zur Herstellung von Einzelzell-Arrays beschrieben. Bei den verwendeten Arrays kann zwischen 2D und 3D Arrays unterschieden werden. Im Grunde sind 2D Strukturen chemisch modifizierte Oberflächen mit einerseits zellfreundlichen Flächen, die mit Proteinen beschichtet sind, und andererseits zellabweisenden Flächen aus Polymeren. Die stereochemischen Eigenschaften von IgM Antikörpern machten die Entwicklung eines neuen 2D Arrays für nicht-adhärente Zellen möglich. Nicht-adhärente Zellen können auch mit topographischen 3D Arrays untersucht werden, bei denen die Form eines biokompatiblem Polymers durch einen mikrostrukturierten Stempel aus weichem Polymermaterial vorgegeben wird. In dieser Arbeit wurden hauptsächlich zylindrische und rechteckige Formen verwendet. Die beschriebenen Einzelzell-Arrays wurden zur Untersuchung von Zellheterogenität und dynamischen Zellreaktionen in folgenden Fällen verwendet: (i) Zytokin Sekretion, (ii), NK Zellzytotoxizität, (iii) Zellzyklusdauer und chemotherapeutisch induzierte Apoptose.

Im zweiten Teil, in dem 3D Arrays verwendet werden, wird die Entwicklung eines Einzelzell-Sekretions-Assay beschrieben. Die Kommunikation zwischen Immunzellen findet durch die Sekretion von sogenannten Zytokinen statt. Jedoch ist die Detektion der Zytokinsekretion einzelner Zellen schwierig, da die Anzahl sekretierter Proteine sehr gering ist. Daher wurden mit Hilfe enzymgekoppelter Immunadsorptionstests (ELISA) verschiedene Ansätze zur Analyse von Proteinsekretion einzelner Zellen im Micro-Wells entwickelt. Hierbei wurde festgestellt, dass der ELISA-on-cell, bei dem die sekretierten Proteine direkt auf der Oberfläche der Zelle nachgewiesen werden, sensitiver ist als die Detektion des Proteins am Boden des Micro-Wells. Um die Detektionseffizienz des offenen gegen über dem geschlossenen Micro-Well Ansatzes zu vergleichen, wurden numerische Simulationen unter Verwendung der Finite-Elemente-Methode (FEM) durchgeführt.

Im dritten Teil wird die Immunantwort gegen Zielzellen durch sogenannten natürliche Killerzellen (NK) in Anwesenheit von zell-spezifischen Triplebodies zeitaufgelöst verfolgt. SPM-2 Triplebodies aktivieren NK Zellen durch die Bindungs des Fc-Rezeptors CD16. Mit Hilfe von 2D Arrays, besetzt mit Zielzellen und Zeitraffer-Mikroskopie, konnten die individuellen Lyseereignisse zeitaufgelöst über einen Zeitraum von 16 Stunden gemessen werden. Der neue zytometrische chip-basierte Einzelzell-Assay ermöglicht nicht nur die längere Beobachtung, im Vergleich zu den vier Stunden des Standard Calcein Assays, sondern benötigt auch eine geringere Anzahl an Primärzellen. Darüber hinaus zeigten die Daten ein dosisabhängiges Maximum der Tötungsrate innerhalb des Reaktionszeitraumes eine dynamische Größe, die mit konventionellen Methoden nicht messbar ist.

Im letzten Kapitel wird die Effizienz von Chemostatika als Funktion des Zellzyklus quantifiziert, ohne molekulare Indikatoren der Zellzyklusphasen zu verwenden. Zu diesem Zweck wurde die Generationszeit von klonalen Zellfamilien, jede entstanden aus einer einzelnen Zelle, in länglichen 3D Micro-Well Arrays untersucht. Durch die Kombination dieser Arrays mit Zeitraffermikroskopie und automatisierter Zellerkennung und verfolgung konnten die Zellzykluslängen der einzelnen Zellen sowie Korrelationen bei Schwesterzellen festgestellt werden. Zudem wurde der Todeszeitpunkt, nach der Induktion von Apoptose durch die Zugabe von Chemotherapeutika, ermittelt. Die Ergebnisse zeigen, dass bei Vincristin, einem anti-mitotischen Reagenz, der Todeszeitpunkt davon abhängt wie viel Zeit seit der Zellteilung vergangen ist. Die Verteilung der Todeszeitpunkte wurde mit einer chemisch synchronisierten Population reproduziert und mit der nicht-synchronisierten Population verglichen.

Abstract

Cell responses are commonly heterogeneous over a monoclonal and seemingly uniform population, thus bulk measurements that extract average values are missing essential information. For this reason, single-cell time-lapse studies are required and can be realized with single-cell arrays that facilitate dynamic readout of cell processes. Analysis at the single-cell level elucidates the biological significance of the observed heterogeneity.

In the first part of this thesis, fabrication methods for single-cell arrays are developed. Two types are studied, namely 2D and 3D arrays. 2D arrays are chemically modified surfaces baring cell-adhesive areas, which are coated with proteins, and cell-repellent areas coated with polymers. A novel 2D array for non-adherent cells is introduced, that utilizes the favourable stereochemical properties of IgM antibodies. For non-adherent cells as well, 3D topographical arrays are made by moulding biocompatible polymers using microstructured masters of soft polymeric materials. Herein, we mainly used cylindrical and rectangular cavities. The single-cell arrays described are used to investigate cell heterogeneity and dynamic response in the following cases: (i) cytokine secretion, (ii) NK cell cytotoxicity, (iii) cell-cycle duration and chemotherapeutic drug induced apoptosis.

In the second chapter employing 3D arrays, the development of a single-cell secretion assay is investigated. Immune cell-to-cell communication is mediated via the secretion of proteins called cytokines. Studying cytokine secretion with single-cell resolution is challenging due to the small number of secreted cytokines. Herein, we developed various approaches to measure single-cell secretion events in micro-wells using locally embedded enzyme-linked immunosorbent assays (ELISA). We found that the ELISA-on-cell, i.e. capturing the secreted protein on the surface of the secreting cell was more sensitive than capturing it on the bottom of the micro-well. To compare the capture efficiency in the open versus closed micro-well configuration, we performed numerical simulations using the Finite Element Method (FEM).

Next, we studied the kinetics of the innate immune response against targeted cells mediated by natural killer (NK) cells in the presence of cell specific triplebodies. The SPM-2 triplebody recruits NK cells via a binding site for the Fc-receptor CD16. Employing 2D arrays of target cells in combination with live cell time-lapse microscopy, we directly measured individual lysis events in a dynamic fashion over 16 hours. The novel chip-based single-cell cytometric assay not only provides longer observation times compared to 4 hours of the standard calcein release assay, but also requires far smaller numbers of primary cells. Moreover, the data exhibited a dose-dependent maximum of the killing rate during the reaction interval, a dynamic property, unreachable with conventional methods.

Finally, we study the efficiency of chemotherapeutic drugs as a function of the cell cycle, without the use of molecular indicators specific to the cell cycle phase. To this end, we monitored the generation of clonal families of cells each derived from a single mother cell, using 3D elongated micro-trenches arrays. Combining these arrays with live cell time-lapse microscopy and automated cell tracking, we determined the cell-cycle duration of single-cells, sister cell correlations as well as the time-to-death after inducing apoptosis with chemotherapeutic drugs. We

found that for vincristine, an anti-mitotic agent, the time-to-death depends on the time passed after cell division. The time-to-death distribution is reproduced using chemically synchronised populations and the time-to-death between sister cells is correlated in non-synchronised cells.

Contents

Abbreviations

μCP	microcontact printing
2D	two dimensional
3D	three dimensional
ABTS	2,2'-azino-di [3-ethyl-benzthiazoline] sulfonate
ADCC	antibody dependent cellular cytotoxicity
ADC	antibody-drug conjugate
ALL	acute lymphoblastic leukemia
AML	acute myeloid leukemia
APL	promyelocytic leukemia
BSA	bovine serum albumin
CDC	complement dependent cytotoxicity
CTL	cytotoxic T-lymphocytes
DMSZ	Deutsche Sammlung von Mikroorganismen und Zellkulturen GmbH
DNA	deoxyribonucleic acid
DNR	daunorubicin
DOF	degrees of freedom
E : T	effector-to-target cell ratio
EC50	half maximal effective concentration
ECM	extracellular matrix
ELISA	enzyme-linked immunosorbent assay
ELISpot	enzyme-linked immunospot
FACS	fluorescence-activated cell sorting
FDA	Food and Drug Administration office
FEM	finite element method
FITC	fluorescein isothiocyanate
FN	fibronectin
FUCCI	fluorescent ubiquitination-based cell cycle indicator
HRP	horseradish peroxidase
HSC	haematopoietic stem cell
ICS	intracellular cytokine staining
IFNg	interferon gamma
IgG	immunoglobulin G
IgM	immunoglobulin M
IL-2	interleukin-2
IL-2Ra	interleukin-2 receptor a
IL-6	interleukin-6
IL1β	interleukin-1 beta

LAK	lymphokine activated killer cells
LDI	laser direct imaging
LIC	leukemia initiating cell
LLoD	lower limit of detection
LSC	leukemia stem cell
MACS	magnetic-activated cell sorting
MHC	major histocompatibility complex
MIMIC	micromolding in capillaries
MRD	relapse initiating cells
MW	molecular weight
NK	natural killer
NKT	natural killer T cell
NP	nanoparticle
PB	peripheral blood
PBMC	peripheral blood mononuclear cell
PBS	phosphate-buffered saline
PDE	partial differential equation
PDMS	polydimethylsiloxane
PEG	poly(ethylene glycol)
PEG-DA	poly(ethylene glycol)-diacrylate
PEG-DMA	poly(ethylene glycol)-dimethacrylate
PEG(2)	poly(ethylene glycol) with molecular weight 2000
PEG(5)	poly(ethylene glycol) with molecular weight 5000
PEO	poly(ethylene oxide)
PHA	phytohaemaglutinin
PI	propidium iodide
PKC	protein kinase C
PLL	poly(L-lysine)
PMA	phorbol 12-myristate 13-acetate
PMT	photomultiplier tube
PPMC	Pearson product moment correlation
PSA	prostate specific antigen
PU	polyurethane
PVDF	polyvinylidene difluoride
RDL	redirected lysis
RICs	radio-immunoconjugates
RNA	ribonucleic acid
ROI	region of interest
SCC	single-cell cytometry
scFv	single-chain Fragment variable
SEM	standard error of the mean
TCR	T-cell receptor
TIRFM	total internal reflection fluorescence microscopy
TMB	tetramethylbenzidine
TMSPMA	3-(trimethoxysilyl)propyl methacrylate
TNFa	tumour necrosis factor alpha
TRAIL	tumour necrosis factor-related apoptosis-inducing ligand
UV	ultraviolet
VCR	vincristine

Chapter 1

Introduction

Phenotypic heterogeneity is ubiquitous in every cell population, even in isogenic ones [1]. It has been a long-standing endeavour to better understand and explain the observed heterogeneity among cells of the same population. In the last decade, numerous studies have been carried out in an attempt to distinguish heterogeneity from insignificant noise and to extract biologically and clinically significant information [2–4]. Single-cell studies essentially contribute towards this ongoing effort providing data that are unreachable with standard bulk assays. The main purpose of this thesis was the development of single-cell dynamic assays that can shed light on the underlying heterogeneity of various fundamental cell processes such as intercellular communication including cell secretion (chapter 2), cell-mediated cytotoxicity (chapter 3), cell cycle duration and chemotherapeutic drug induced apoptosis (chapter 4).

Heterogeneity among cells of the same type is prevalent for both gene expression and protein levels [5–8]. A scheme describing the various levels of heterogeneity was proposed in [2] and is illustrated in figure 1.1. Even in isogenic cell populations, the stochastic nature of gene expression [9] and fluctuations in regulatory molecules lead to a significant deviation of single cells from the population average. Sequencing DNA of single cells revealed important insight in various cases. For instance, in breast cancer samples distinct cell populations together with spatial information were identified inside the tumour [10]; in single germ cells recombination sites were mapped [11]; in neurons the copy number variation was found to be significantly higher than other cell types [12] and also that chromosome structures vary among single T-helper cells at large scales [13]. Not only genetic but also phenotypic and developmental states contribute to the observed cell population heterogeneity. For example, non-genetic heterogeneity plays a key role in stem cell fate decision [14–17].

Bulk or population-average assays refer to standard techniques used extensively that provide important insight into cell external and internal signalling pathways, in essence for every cell process. They can also be multi-plex and/or high-throughput if they produce more than one signals simultaneously in one sample, such as bead-based assays (Luminex technology for detection of intracellular and secreted proteins) and gene microarrays. Even though they capture the state of a population under multiple perturbations, they are based on the assumption that ensemble averages reflect the dominant biological process of the individual cells in the tested sample. In many cases, this assumption is problematic as useful information is contained in heterogeneity and thus cannot be uncovered. For instance, subpopulations of clonally derived hematopoietic progenitor cells were found to have considerable different transcriptional states and to give rise to different blood cell lineages [15]. Furthermore, the detection of small or rare, yet highly significant, subpopulations of cells is not possible with bulk assays. Such an example is a very small number of dormant stem cells within larger hematopoietic stem cell populations that is crucial for re-establishing homeostasis [18]. An even more profound situation

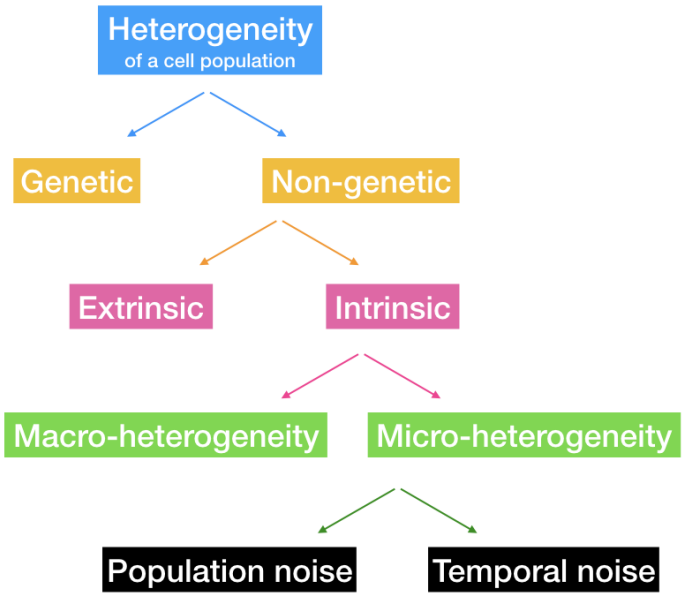

Figure 1.1: Schematic representation of the terminologies used for cell heterogeneity as described in [2].

is when a population consists of several dominant but phenotypically discrete subpopulations i.e. is described with a bimodal distribution [19, 20] and the bulk measurement will result in an imprecise average of these subpopulations.

To measure genetic heterogeneity and its biological significance, researchers initially used low-throughput techniques that measure limited parameters in each cell, such as fluorescent reporters and fluorescence in situ hybridization (FISH). On the contrary, high-throughput genomic approaches typically measure a pool of a large number of cells and an ensemble average is derived, which is not ideal as discussed above. Nevertheless, nowadays a genome-wide quantitative analysis of single cells is possible. The challenge in single-cell sequencing is whether the DNA yield will be sufficient, thus amplification methods are crucial [21, 22] and must ensure optimal genome coverage. For transcriptome analysis, a significant number of single-cell methods have been developed, such as microarrays, high-throughput real-time PCR and single-cell RNA sequencing [23–25]. With large-scale real time PCR a substantial number of genes in thousands of cells can be analysed, however since it is not possible to probe the entire genome all at once, only pre-selected genes can be analysed. On the other hand, single-cell RNA sequencing can provide genome-wide information [26, 27]. As far as single-cell proteomics is concerned, parallel detection of large numbers of proteins is possible using antibodies labelled with heavy metals [28]. Moreover, multiple protein detection in situ sheds light on protein interaction events at the single-cell level in heterogenous population, such cells in tissue section [29].

Single-cell assays are a valuable tool to investigate the heterogeneity and the interactions among immune cells which translates into the general capability of the immune system. An in-depth understanding of the capabilities of the immune system, not only provides knowledge on the evolution of diseases such as autoimmune disorders and cancer, but also on the development of diagnostic and therapeutic strategies. Phenotypic variability among cells even of the same type is a prevalent phenomenon, for instance for natural killer (NK) cells [30] and for T-cells [31].

An illustrative analogy of the importance of single-cell analyses and dynamic monitoring for the immune system is given in [32], where monitoring the immune system is compared with a game of soccer. The immune response resembles a soccer game, in the sense that it is a complex, dynamic network that evolves based on the specific responses and interactions between individual cells (or players). For instance, an average measurement of the position of the ball for example at the middle of the field cannot reveal the importance of the goals at the edges of the field. Likewise, a snapshot of the field at the time point of the goal gives little information for the previous individual events and interactions between the players that led to scoring. The roles of players and goals describe the interaction between cells of different type and their functional response respectively.

The most common types of single-cell platforms used for monitoring processes of immune cells are valved microfluidic systems [33, 34] and micro-well arrays [35, 36]. The advantage of valved microfluidic systems is the ability to precisely position cells and control their fluidic environment, nevertheless usually they require a large number of control elements that leads to a smaller number of cells analysed simultaneously and it is also more difficult to be scaled up for larger numbers of cells. On the other hand, simple micro-well arrays usually comprise a dense grid of micro-wells that enables the simultaneous analysis of larger number of cells (several thousands), at a scale that the identification of rare cells, such as for instance antigen-presenting T-cells, in a highly heterogeneous population. Nonetheless, usually they do not offer precise control over the fluidic environment at the single-cell level. Both technologies offer the capability of analysing very small clinical samples and therefore can be a valuable tool for patient stratification and personalized medicine. Moreover, they enable spatiotemporal analyses of the immune cells that is not possible with standard bulk measurements and flow cytometry. As a result, multiple complex functional and phenotypic processes including protein secretion [37,38], cytotoxicity [39], differentiation [35] can be analysed with such arrays depending on the question at hand. In addition, cell-to-cell communication studies with increased precision are enabled by such single-cell platforms due to the straight forward spatial confinement of different cell types [40, 41]. The distribution of the cells settled in micro-well arrays follows the Poisson distribution, which results in quantised arrangements of different types of cells, for instance different ratios of NK to target cells. This characteristic led to the discovery that NK cells do not cooperate in a paracrine manner to kill adjacent target cells [39]. In a similar manner, valved microfluidics were used to study the effect of cell-to-cell distance on intracellular signalling and secretion of tumour cell lines [42]. However, it should always be kept in mind that the results of such single-cell approaches may not reflect precisely the in vivo processes but they definitely give information on the potential range of states that cells may take.

A high degree of heterogeneity is evident among cancer cells as far as their phenotype and drug resistance is concerned [43–47]. Generally, tumour heterogeneity refers to cellular differences within a single neoplasm and not to the obvious differences due to organ site, cell origin, patient age and hormonal status [43]. Sources of cancer heterogeneity are the introduction of genetic and epigenetic alterations and their evolutionary selection. These alterations are influenced by the signalling environment, both stromal and immune but also by therapeutic interventions [48–50]. Tumours are constantly evolving and one tumour can be pictured as a tree of which the trunks represent earlier mutations (clonal) and the branches later ones (subclonal) [51–53]. In theory, mutations of the branches will only be present only in a subset of tumour cells while mutations of the trunk will be present in every cell, nevertheless there is evidence that not every clonal mutation will be present in every cell in a tumour [54]. Even though heterogeneity is regarded to assist tumours overcome evolutionary pressures, it can also be exploited for therapeutic interventions. In theory, a targeted therapy will be more potent if the target is a trunk mutation, i.e. a driver mutation [55].

Resistance to cancer drugs of usually a small fraction of the tumour population is an exemplification of the effect a drug can have on tumour heterogeneity but also on how heterogeneity within cancer cells impacts the outcome of a therapeutic strategy. In untreated cancer cell populations, patterns of basal signalling heterogeneity were identified and were shown to define subpopulations with different drug sensitivities [3]. Insight in tumour heterogeneity will pave the way for novel therapeutic approaches. For instance, accumulating evidence suggest that subclones within tumours both compete and synergize for growth [55, 56], thus targeting small populations that support growth of adjacent cell will be beneficial [57]. Moreover, according to adaptive therapy [58] instead of focusing on eradicating every single cancer cell, which results in resistant untreatable subclones, it may be better to control tumour growth via focusing on the selection mechanisms within a tumour. It is still unclear which aspects of tumour heterogeneity matter in clinical practice, but it is essential that the current effort will be translated to diagnostic and treatment strategies.

Since tumour diversity affect clinical outcomes, the establishment of sensitive methods that quantify tumour heterogeneity and are able to detect and monitor subclones dynamically is necessary [56, 59, 60]. Single-cell sequencing can shed light on cell lineages and phylogenies, but also on the heterogeneity of rare cell populations such as circulating cells [61]. For the latter, the coupling of single-cell sequencing with micro-fluidic devices is essential [62–65]. For single-cell RNA sequence protocols, sensitivity for lower expressed genes has to increase as well as methods to control amplification biases and technical noise. Furthermore, the number of cells analysed simultaneously is still limited and should be increased to at least tens of thousands of cells. Measuring protein heterogeneity at the single-cell level falls behind that of nucleic acids. Measuring the protein content of a single-cell is challenging with mass spectrometry due to the small sample size. Antibody-based assays are usually the followed way, but throughput is limited as well as high-quality antibodies. The most common methods so far are fluorescence-activated cell sorting (FACS) or mass cytometry (CyTOF), which however can detect a limited number of proteins per sample [66, 67]. Even though protein content is not as dynamic as the transcriptome, the phosphoproteome, which is essential to investigate cancer signalling, is even more sensitive and dynamic than the transcriptome. In addition, significant information about the tumour can be found in cell-free DNA and circulating tumour cells found in the blood. Nonetheless, such non-invasive sensitive methods to isolate these circulating cells and DNA from peripheral blood are yet to be developed. Thus, developing methods taking into consideration all the above challenges is critical to assess, quantify and model tumour heterogeneity.

Chapter 2

Development of single-cell arrays

2.1 Soft lithography

Soft lithography, a term introduced by George Whitesides [68], is an ensemble of microfabrication techniques independent from photolithography processes, which require sophisticated facilities (like clean rooms) and specialized reagents thus resulting in a significantly high fabrication cost. The mutual characteristic of all soft lithography techniques is the use of an elastomeric, soft material at any stage of the microfabrication process. The most commonly used elastomer for these processes is polydimethylsiloxane (PDMS), which is formed using a mould, called master. The master is usually fabricated by conventional photo- or laser-lithography, where a silicon substrate is spin coated with a thin layer of a photoresist, which is then illuminated with UV light through a chrome mask or a patterned transparent polymeric sheet baring the desirable shapes. Alternatively, a UV laser direct imaging (LDI) device can be used to create the master. The advantage of the LDI is that no mask is required for the process, however the exposure takes longer. In the end after developing, the silicon wafer is silanized to facilitate removal of the moulded PDMS, and it can be routinely used to cast PDMS. Several micro-patterning techniques, including microcontact printing (μCP), plasma-induced micropatterning and micromolding in capillaries (MIMIC), have been further developed and applied due to their practicability and reduced cost [69–74].

2.2 Two dimensional (2D) protein arrays

Micro-patterning techniques that were originally developed for microelectronics, found application also in cell biology and biophysics since they bridge the gap between standardised 2D culture on a petri dish and 3D assays and tissues. With these techniques the surface chemistry and geometry can be manipulated at the micron or submicron scale resulting in quantitatively controlling the cell micro-environment *in vitro*. They constitute a useful tool to analyse the environmental parameters contributing in cell physiology, which is difficult, if not impossible, to be done on a petri dish. Such substrates facilitated several studies that proved the importance of cell shape, cell spreading area, and geometrical parameters of cell adhesion on cell survival, proliferation, differentiation and polarity [74–76]. Even though initially sophisticated devices were needed for micro-patterned substrates, lately many simple methods, available to almost every biology lab, have been developed.

Herein, as 2D (two dimensional) protein array we define a chemically modified surface baring areas coated with proteins and areas coated with polymers. Protein-coated areas are more cell friendly, leading to the formation of a cell array. Organising the cells into cell arrays constitutes a practical strategy for real-time dynamic monitoring of cell processes using light and fluorescence

microscopy. Without immobilising the cells on exact positions, long duration measurements (for more than a few hours up to days) are not possible as cells will migrate out of the microscope field of view. This effect is more prominent with non-adherent cells. Moreover, cell arrays not only enable long duration measurements but also facilitate a great deal subsequent image analysis, which can be easily rendered semi-automated or even automated in some cases [77,78] (see chapters 4 and 5).

Herein, *plasma-induced patterning* was utilised to develop the 2D protein arrays suitable for the cell lines used. This method was first introduced by Bryan Langowski in 2005 [79] and by utilising a PDMS stamp and plasma treatment initially hydrophobic surfaces, such as polystyrene or PDMS, can be rendered hydrophilic in selected areas, namely those not protected by the PDMS stamp. Later, the patterned surface can be further functionalized with either proteins or other macro-molecules that adsorb either on hydrophobic or hydrophilic areas.

2.2.1 Adherent cells

The adherent cells used as a model cell line, were a transfected to express the surface antigen CD123, human embryonic kidney 293 cell line (HEK 293.123). This is a semi-adherent cell line, hence to immobilize the cells onto the desired areas, we coated the hydrophobic areas, the ones protected by the PDMS stamp during the *plasma-induced patterning* process, with various extracellular matrix (ECM) proteins. The proteins tested were the following:

- Human fibronectin
- Collagen type VI (purified from human placenta)
- Laminin
- Collagen A (type I, from calfskin)

The optimal cell array was acquired when fibronectin was used at a concentration of 50 μg/mL. Fibronectin is a high-molecular weight (approximately 440 kDa) glycoprotein of the extracellular matrix that bind to membrane-spanning receptor proteins called integrins.

The hydrophilic areas, resulted from the plasma-induced patterning process, were coated with poly(L-lysine)-grafted-poly(ethylene glycol) (PLL(20k)-g(3.5)-PEG). A schematic graph of the patterned surface is shown in figure 2.1. Two lengths of the PEG chain were tested namely 2 and 5 kDa. The 2 kDa size of the PEG chain was chosen since it resulted in better filling factor of the cell array (Figure 2.2). *Filling factor* is the percentage of the square patterns occupied with a single cell out the total number of squares on the tested surface. As far as the size of the protein squares is concerned, three different sizes were tested 20, 25 and 30 μm of side length. The optimal results were obtained with the 30 μm side length. In figure 2.3 a fibronectin array pattern is presented.

2.2.2 Non-adherent cells

To create a cell array of non-adherent cells we first tested whether the above described approach would work (2.2.1). As a model cell line for non-adherent cells we used the acute myeloid leukemia (AML) MOLM-13 cell line [80]. In theory, MOLM-13 cells can bind fibronectin through the VLA-5 integrin (alpha-5 beta-1) [81] or through VLA-4 [82,83]. Furthermore, most leukemia cells carrying mixed lineage leukemia (MLL) gene arrangements in both acute lymphoblastic leukemia (ALL) and AML cases, express the NG2 homologue, a chondroitin sulfate molecule [84]. NG2 homologue binds to matrix molecules including type VI collagen. Hence, the proteins tested for the MOLM-13 cell line were the following:

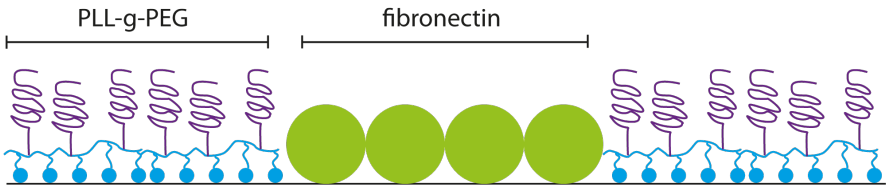

Figure 2.1: Schematic description of the 2D fibronectin array. The hydrophilic area between the square patterns is coated with PLL-g-PEG.

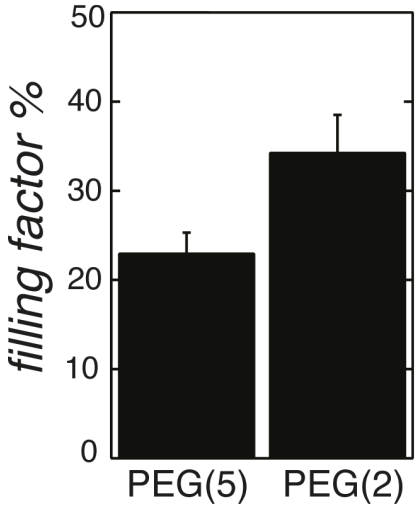

Figure 2.2: The *filling factor %* indicates the percentage of the fibronectin squares occupied by a single-cell. PLL(20k)-g(3.5)-PEG(5kDa) (PEG(5)) and PLL(20k)-g(3.5)-PEG(2kDa) (PEG(2)) were tested. With PEG(2) a higher filling factor is achieved as cells can migrate more easily on it. This seeding procedure requires no washing steps.

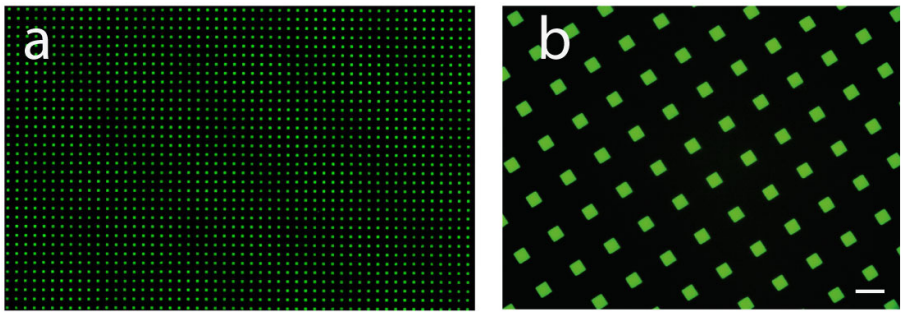

Figure 2.3: Fibronectin array generated with plasma-induced patterning. Squares with a side length of 30 μm are coated with fibronectin (here fibronectin is labeled with AlexaFluor488®) and the backfilling (black) area with PLL-g-PEG(2kDa). (a) Part of an overview scan acquired with a 4x objective. (b) Fluorescence image acquired with a 10x objective. The scale bar corresponds to 60 μm.

- Human fibronectin
- Collagen type VI (purified from human placenta)
- Combination of human fibronectin and collagen type VI
- HUVECS lysate

Unfortunately, non of the above resulted in the formation of a cell array, so the next step was to coat the hydrophobic square islands with antibodies targeting an antigen on the surface of the MOLM-13 cells. CD15 and CD13 (see chapter 4) were the best candidates and their expression levels on the surface of the cells was tested with flow cytometry (FACS). CD15 was the selected antigen to target, since 99.8% of the cells expressed it on their surface (see figure 2.4).

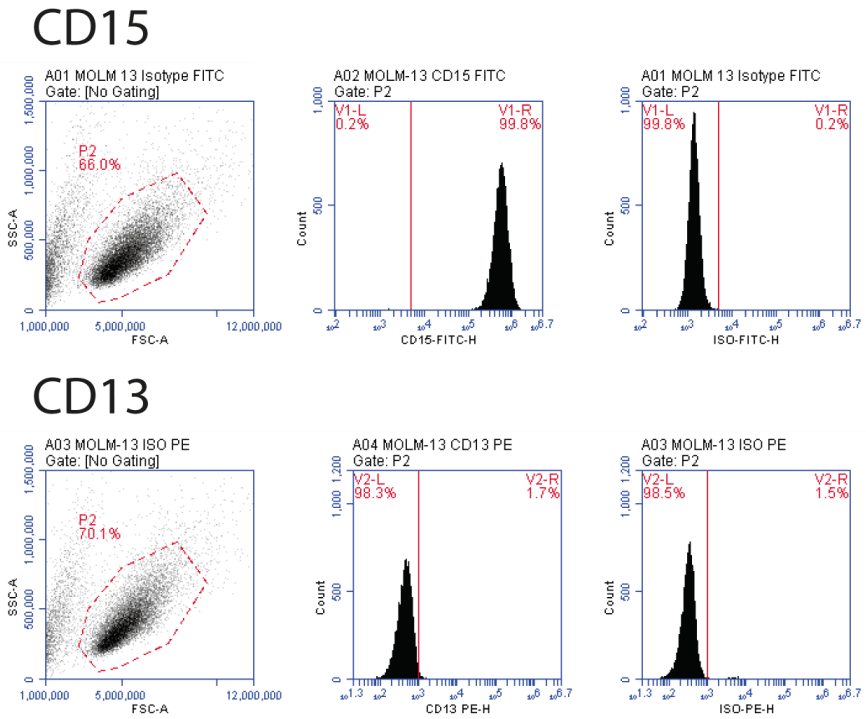

Figure 2.4: Expression profiles of the CD15 and CD13 antigens on the surface of MOLM-13 cells.

The first approach was to simply adsorb on the square hydrophobic islands a IgG anti-CD15 antibody, following the same plasma-induced patterning process described in 2.2. However, this approach was not successful, hence the immobilisation strategy described in [85] (see figure 2.5) was adapted and tested. Briefly, the hydrophobic square islands were coated with biotinylated bovine serum albumin (BSA), then with NeutrAvidin and lastly with a biotinylated anti-CD15 antibody (*bio-affinity immobilisation*, see section 3.3.1). Using the biotin-neutrAvidin complex a uniform orientation of the antibody is expected and hence immobilisation of the cells onto the coated patches should be possible. Unfortunately, even if the coating of all levels, i.e. BSA, neutrAvidin and antibody, was successful, formation of a MOLM-13 cell array on this patterned surface could not be achieved.

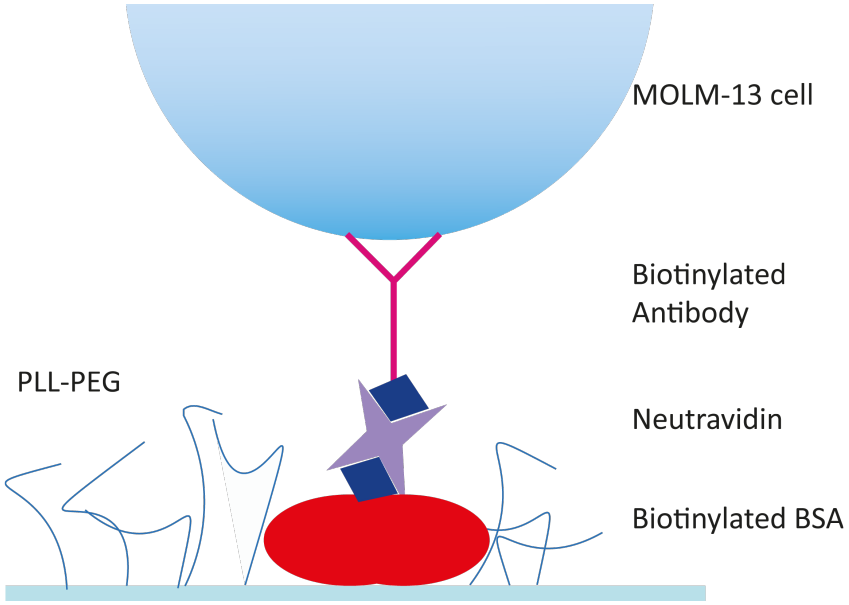

Figure 2.5: Surface patterning utilising the biotin-neutrAvidin complex to orient the antibody and hence potentially result in immobilisation of the non-adherent cell line MOLM-13.

The next idea was to coat the hydrophobic square patterns with an IgM antibody via adsorption. The IgM isotype is a pentamer, its structure is shown in figure 2.6. The shape of an IgM pentamer is symmetric, so one can hypothesise that this isotype does not need to be oriented as an IgG, due to its favourable stereochemical properties. In the end, IgM coated surface will present more available binding sites than a surface coated with an IgG (Figure 2.7). Indeed, the formation of a MOLM-13 cell array on the IgM coated squares was possible. The optimal side length of the antibody coated squares was 25μm for the MOLM-13 cell line. A IgM coated array is shown in figure 2.8.

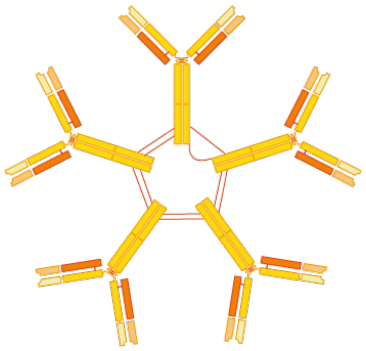

Figure 2.6: Structure of an IgM antibody

2.3 Three dimensional (3D) polymer arrays

Three dimensional (3D) polymer arrays have been a versatile and the most commonly used tool enabling straight forward single-cell assays [86, 87]. Different materials, manufacturing proce-

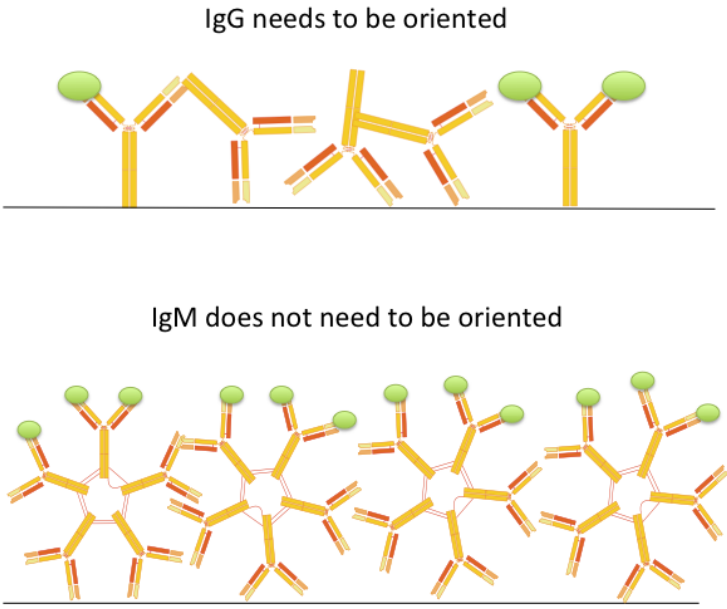

Figure 2.7: An IgG antibody needs to be oriented in order to present binding sites (noted with green ellipses) that are adequate to immobilize a non-adherent cell on the pattern, while that is not necessary for an IgM antibody, due to is stereochemical properties.

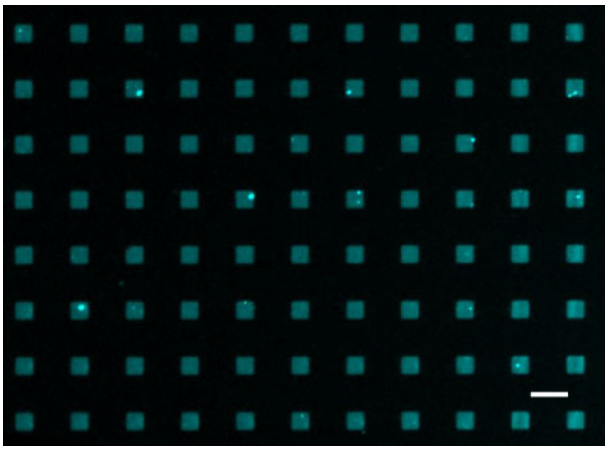

Figure 2.8: IgM antibody array generated with plasma-induced patterning. Squares with a side length of 25 μm are coated with an IgM anti-CD15 antibody and the backfilling (black) area with PLL-g-PEG(2kDa). For visualising the IgM coated squares a goat anti-mouse secondary antibody conjugated with AlexaFluor488®was used, the surface was blocked with 5% w/v nonfat dry milk. The image was acquired with a 10x objective, and the scale bar corresponds to 60 μm.

dures but also shapes have been applied in combination with microfluidic devices, elucidating numerous cell processes, such as embryonic stem cell differentiation, immune-cell activation, the role of cell shape on cell function and so on. These high-density arrays of micron-sized

cavities, most usually called *micro-wells*, are ideal for capturing and culturing large numbers of single-cells derived from rare and heterogeneous populations such as stem cells. Moreover, by engineering their bottom and side surfaces with lipids or ECM proteins, controlled single-cell micro-environments mimicking key features of the native 3D milieu can be developed. When only the bottom of the micro-well is modified the cell experiences a 2D environment [88–90], while when the side walls of the micro-well are modified too, the cell will experience a 3D micro-enviroment [91–93]. Since micro-well arrays are relatively simple and compatible with existing laboratory techniques and instrumentation, they are an attractive option when single-cell studies are needed. In essence, all cell types, both adherent and non-adherent cells, can be cultured in 3D polymer arrays. Evidently, non-adherent cells are usually easier to culture in such arrays without the need of additional surface modification steps. On the other hand, adherent cells tend to adhere and stretch along surfaces, as a result the properties of the material itself and of its surface can influence the behaviour of the cell in the array. For that reason further surface modification steps are usually necessary in this case. In the next section, the most commonly used materials to fabricate micro-wells will be shortly reviewed along with their most significant characteristics, which are their autofluorescence and their cytotoxicity.

2.3.1 Materials for micro-well arrays

The most commonly used materials for micro-well platforms are the following:

- poly(dimethylsiloxane) (PDMS) [36, 90, 94, 95]
- crosslinked polyurethane (PU) prepolymer (in combination with Matrigel) [96]
- poly(ethylene glycol) (PEG) and PEG-derivatives [70, 97–99]
  - poly(ethylene glycol)-dimethacrylate (PEG-DMA)
  - poly(ethylene glycol)-diacrylate (PEG-DA)
- SU-8 (glycidyl ether of bisphenol A) photoresist [100]
- fiber [101]
- glass [102]
- silicon [103]

The selection of the material is subjective and depends a lot on the type of the application, whether it is for single cells, small groups of cells, embryonic bodies, in vivo studies etc., but also on which equipment is accessible to each research group. PDMS, due to each simplicity is an attractive approach often used directly for cell culture. However, PDMS is hydrophobic and strongly adsorbs proteins such as growth factors from the cell culture medium, which is problematic especially for long duration measurements. Surface modification can help in this respect.

The material used to form micro-well arrays in the course of this work was mainly PEG-DA (MW 258) (three ethylene glycol repeats) [104] (Figure 2.9), along with PDMS in a much less extent. The main reason for selecting PEG-DA over PDMS was that the bottom of the PEG-DA could be either glass or ibidi®polymer coverslips, of which the background autofluorescence was the lowest possible. As an alternative, SU-8 photoresist was also tested as it would facilitate scaling up the fabrication process, however because of its high autofluorescence it was rejected. An alternative material for micro-well arrays can be *liquid glass* [105], yet a fabrication protocol

for high quality micro-well arrays is still under development. Below follows a short description of these materials and a comparison among them relatively to the two most important features for micro-well arrays, namely *autofluorescence* and *cytotoxicity*.

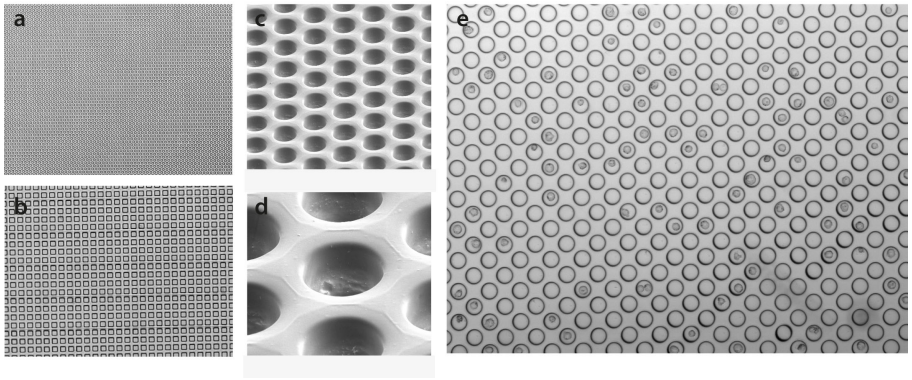

Figure 2.9: Arrays of PEG-DA (MW 258) micro-wells. A: Any different shape and space arrangement can be prepared. (a) Circular micro-wells of 25 μm diameter (b) quadratic micro-wells of side 50. The depth of the presented micro-wells is 30 and 38 um respectively. (c), (d) Scanning electron microscopy pictures of PEG-DA micro-wells (diameter: 35 um, depth: 30 um). (d) Micro-wells (diameter: 35 um, depth: 30 um) loaded with the non-adherent MOLM-13 cell line.

Poly(ethylene glycol) (PEG) derivatives

Poly(ethylene glycol) (PEG) or poly(ethylene oxide) (PEO), despite its structural simplicity $HO-(CH_2CH_2O)_n-CH_2CH_2OH$, is one of the most widely used materials in biomedical applications. It is a linear or branched, neutral polyether available in a variety of molecular weights (MW), soluble in water and most organic solvents. When the molecular weight of the PEG chain is less than 1000 g/mol, the polymer forms a viscous, colorless liquid, while at higher molecular weights PEG is a waxy, white solid.

Traditionally, PEG has been utilized for a variety of applications such as a precipitating agent for proteins, other biological macromolecules and viruses [106], and for preparing two-phase aqueous systems [107]. PEG also facilitates cell fusion, a technique widely used in cell hybridization technology [108, 109]. Currently, the most popular PEG applications are the following [110, 111]:

- PEG-protein conjugates for pharmaceutical applications
- PEG-enzyme conjugates for industrial processing
- surface modification with PEG to provide protein- and cell-repelling properties
- surface modification with PEG to provide control of electroosmosis
- aqueous two-phase partitioning for protein and cell purification
- PEG hydrogels for cell encapsulation, drug delivery and wound covering
- PEG-modification of small molecule pharmaceuticals
- PEG tethers for synthesis of biomolecules

- PEG tethering of molecules for biological targeting and signaling
- PEG-liposomes and micelles for drug delivery

PEG can also be used to modify the properties of a surface (see section 2.2). Surfaces modified by attachment of PEG chains (either covalent or not) are resistant to protein and cell adsorption i.e. are non-fouling. Attachment of PEG to a surface acts to alter the electrical nature of a surface exposed to an aqueous environment. The general mechanism behind the effective repulsion of the macromolecule from the coated surface is that if the macromolecule comes close to the surface, then the conformational degrees of freedom for the polymer are drastically reduced, and this causes an entropic repulsion between the surface and the macromolecule. The theoretical description of polymer molecules outside a surface has been developed by Scheeutjens and Fleer (SF) within the Flory - Huggins concept [112, 113]. In the SF model space is divided into layers parallel and that the Flory - Huggins model is applied to each layer. The SF model is easily merged with the conformational model [114]. Interesting explanations are derived from of this type of modeling. Firstly, the most important property of the PEG chain is that it is flexible and that the entropic repulsion consequently will be large. The PEG chain have some additional features, which are important for hydrophobic surfaces. The ability of the chain to change polarity, suggests that close to a hydrophobic surface, the polymer will have more non polar conformations, and this leads to an increased coverage of the surface, while far from the surface, in the bulk, the polymer will be more polar. As a result, the PEG chains penetrate far out into the water resulting in a stronger repulsion of macromolecules. The longer the PEG chain is the more protein and cell repellent the PEG, this positive effect of surface non-fouling effects reach a plateau around 5 kDa [115, 116].

Moreover, PEG hydrogels can be formed, if the PEG chain is functionalized with a polymerizable resin such as acrylate or methacrylate. The polymerization can be initiated thermally by azobisisobutyronitrile or peroxides or photochemically using photo-initiators such as benzophenones, hydroxipropiophenones or thioxanthones [117]. When a crosslinked network is formed with diacrylated PEG (PEG-DA), the final polymer backbone will have a mixed hydrophilic-hydrophobic character, because of the presence of a hydrophobic crosslinking agent. In the applications presented in this thesis, PEG-DA with average molecular weight 258 g/mol is used to form the 3D micro-well arrays. To crosslink the PEG-DA molecules the 2-hydroxy-2-methylpropiophenone photoinitiator is used, which is photocleaved under a specific UV wavelength resulting in the formation of highly reactive radicals. The polymerization reaction is initiated by these radicals, which attack the monomer and form new radicals. The polymerization of the polymer chain propagates until the monomer is depleted. The process terminates when radicals combine, either of two growing chains or a polymer chain with an initiator radical. The most important feature of the resulted PEG-DA solid matrix for the applications in this thesis, was that the longer the PEG chain was the more protein- and cell-repellent the resulted micro-wells were, while at the same time the shorter the PEG chain was the better the adherence of the micro-well array on the substrate. For that, for the current applications the molecular weight of 258 g/mol was the optimal solution. Furthermore, PEG-DA (258 g/mol) was resistant to swelling, which is common for longer PEG chains.

Poly(dimethylsiloxane) (PDMS)

Poly(dimethylsiloxane) (PDMS) is a widely used polymer for fabrication and prototyping of microfluidic devices. It is also used as a food additive and an anti-foaming agent in beverages or in lubricating oils. It is characterised as a mineral-organic polymer since it contains carbon and silicon. Its formula is $CH3[Si(CH3)2O]nSi(CH3)3$, with n being the number of monomer

repetitions. If the size of the monomer chain is small (low n) the non-cross-linked PDMS is almost liquid but for longer monomer chains (high n), PDMS gets semi-solid. The siloxane bonds result in a flexible polymer chain with a high level of viscoelasticity. For fabricating microfluidic devices, PDMS in liquid form is mixed with a cross-linking agent and then poured into a micro-structured mould. Using heat, PDMS is cross-linked and an elastomeric replica of the mould is obtained. The resulted elastomer is hydrophobic and polar solvents, such as water, struggle to wet the PDMS which leads to the adsorption of hydrophobic contaminants from water on PDMS surface. PDMS surface can be rendered hydrophilic for a short time (about 30 seconds) using oxygen plasma, by creating SiOH groups on its surface. After this process, PDMS surface becomes resistant to the adsorption of hydrophobic and negatively charged molecules. Moreover, PDMS can also be covalently bond with oxidised glass when treated with oxygen plasma via Si-O-Si bonds.

PDMS is by far the most widely used material in microfluidics and single-cell applications because of its following characteristics:

- It is transparent in the optical range of wavelengths (240 - 1100 nm).
- It has low autofluorescence [118].
- It is generally considered bio-compatible (although with some restrictions [119]).
- During cross-linking, it can be coated with controlled thickness with a spin coating process, thus multi-layer devices and valves can be created.
- It is deformable, thus allowing integration of microfluidic valves, easy connection of leak-proof fluidic connections and detection of very low forces (for example from cells).
- It is inexpensive in comparison to other materials such as silicon.
- It is easy to mold, even for very small structures of a few nanometers [120].
- It is gas permeable, thus enabling cell culture.

However, PDMS has certain characteristics that may impede its use especially for long-term cell culture applications. Firstly, it adsorbs hydrophobic molecules from the cell medium and also releases certain molecules due to poor cross-linking that can harm cell viability. Moreover, it is permeable to water vapour and as a result evaporation in a PDMS device is hard to be controlled.

SU-8 (glycidyl ether of bisphenol A) photoresist

SU-8 is an EPON™based epoxy resin used to fabricate microfluidic devices [121–123], since it is chemically stable and it is easy to use in lithography processes. Scaling up lithography protocols for high-throughput production of 3D micro-well arrays appears to be simpler. It has a very hydrophobic surface, thus surface activation is essential for its use in passive microfluidics [124, 125]. It is questionable whether it is biocompatible [126–128], hence its use in biomedical applications is still limited.

Liquid glass

PIREX®glass flasks and Petri dishes where the substrates used in the first cell culture applications at the beginning of the 20th century. Still, many cells especially primary cells, have a difficulty to attach on glass, thus glass surfaces usually need to be coated with collagen or PLL

to enhance cell adherence. Moreover, detergents used during cleaning should be meticulously removed to ensure cell viability. For these reasons, disposable plastic flasks or dishes prevailed cell culture practices and still remain the standard approach. Nevertheless, due to its optimal optical properties and both thermal and chemical resistance, glass slides are routinely used for observing cells under the microscope and when cells need to be fixed, for instance for immunostaining. *Liquid glass* [105] is an photocurable amorphous silica nanocomposite which can be cured in room temperature using soft lithography processes i.e. a soft mould made of PDMS. This fairly simplified procedure offers an advantage for microfluidic devices in comparison to the more complicated approaches used for high quality glasses [129, 130]. When liquid glass is cured a dense high-quality glass is formed by thermal debinding and sintering. Although, liquid glass has not been widely tested for cell culture applications and yet size precision for structures is round a few hundreds of micrometers, its low autofluorescence and low cytotoxicity renders it a promising candidate for 3D single-cell arrays.

2.3.2 Cytotoxicity

A single-cell platform must be made of a cell friendly material to substitute the well-established and widely accepted polysterene substrates. Cells constantly receive cues from their environment and respond to them in order to maintain homeostasis, a narrow variation window for physiological parameters of the intracellular environment. If they sense for example chemical or mechanical stress, they will adjust their structure and function to accommodate these changes in their milieu. Adaptive cellular responses of a cell under stress are the following:

- hypertrophy (increase in size)
- hyperplasia (increase in number)
- atrophy (decrease in size without cell number change)
- metaplasia (transformation from one mature cell type to another)
- neoplasia (genetic abnormalities)

If the adaptive cell capacity is surpassed then cell injury follows, which will lead to cell death. The goal of any cell culture substrate is to maintain a stressless environment for the cultured cells, so they will keep their physiological processes. Evaluation of cell growth, morphology and viability of every cell line used in a micro-well array of any material should be undertaken to ensure the suitability of the platform.

Although PEG is generally considered a non toxic material, there have been reports of acute, subchronic and other toxicities when PEG was administered in patients and animal models. It has been reported that PEGs of molecular weights less than 400 may be oxidised *in vivo* into toxic diacid and hydroxy acid metabolites via sequential oxidations by alcohol dehydrogenase and aldehyde dehydrogenase [131]. The reaction rate of the oxidation decreased significantly with increasing molecular weight of the PEG. More studies of PEG toxicity on various animal models and of various PEG sizes can be found in references [132–134]. Nevertheless, for many years PEG has been used in many pharmaceutical applications, such as an additive for creams, as solubilising agent and as a component of injectable formulations. As a result, PEG's toxicity is considered adequate for many uses on or in the body (Food and Drug Administration office (FDA) approved for internal consumption [135]).

PDMS is in general regarded non-toxic, inert and biocompatible based on experience of its use in medical device implants [136,137] and in numerous micro-fluidic devices, however this does

not guarantee that every cell type will grow as it usually does in the case of polysterene. The most common PDMS types are RTV-615 from Momentive materials™and Sylgard 184 from Dow-Corning®. Both types contain small amounts of irritants, ethylbensene (<1 %) and xylene, but it is unknown whether this affects cells when PDMS is cured [119]. In previous studies the biocompatibility of PDMS has been tested and surface treatment is usually recommended to ensure normal cell growth. PDMS can be treated with serum or with a concentrated protein solution such as fibronectin [138,139]. The amount of curing agent used also has an effect on cell proliferation [140]. Uncross-linked PDMS oligomers due to incomplete curing can contaminate the cell medium and may have an effect on cell growth and normal cell function, since they were detectable in the membranes of mouse fibroblasts after 24 hours [141]. Moreover, small (<500 Da) hydrophobic molecules absorb into PDMS [142], therefore care should be taken during studies that rely on such molecules such as stem cell differentiation, for instance retinoid acid (300 Da) is widely used to induce differentiation in many different cell types. All in all, PDMS can be suitable for many cell lines as long as the formulation and the surface modification is optimised for each cell line.

As mentioned above the biocompatibility of SU-8 is open to question. As far as the surface properties are concerned, the surface of SU-8 is very hydrophobic. Using oxygen plasma to hydrophilise it had a positive impact on cell proliferation on SU-8 surfaces [128], however whether the cells were metabolically active or stressed was not tested. The antimony salts present in SU-8 have been shown not to affect the proliferation of mouse embryonic stem cells [143]. However, the primary component of SU-8, bisphenol A, is known to be cytotoxic and to induce apoptosis [144]. Leachates from SU-8 were cultured with 9L glioma cells and was shown that cell growth was significantly inhibited for the 10% extract [145]. Furthermore, the in-vivo biocompatibility of SU-8 has been test in mice, where implantation of SU-8 led to a mild inflammatory reaction but in general it was concluded that SU-8 is a promising material for a biocompatible matrix for bio-molecular encapsulation [145]. All in all, SU-8 biocompatibility can be improved with surface modification steps, such as oxygen plasma [124], chemical treatment [146], or covalently linking a low molecular weight PEG on its surface at a low concentration [147].

2.3.3 Autofluorescence

Autofluorescence, the natural emission of light, is common in biological structures, due to molecules such as flavin groups, the reduced form of nicotinamide adenine dinucleotide phosphate enzyme (NAD(P)H) and amino acids such as tryptophan, tyrosine and phenylalanine. It was first reported by Stübel, a physiologist at Jena University, in 1911. In many cases, autofluorescence of biological structures has been utilised to monitor processes such as bacteria growth [148].

Nevertheless, autofluorescence occurs in many other materials too, such as artificial polymers and plastics, especially when excited with UV (< 400 nm), blue (400 - 500 nm) and green (500 - 550 nm) light [149]. This autofluorescence can be either intrinsic to the bulk polymer or due to additives, impurities or degradation products [150]. Moreover, it is undesirable in polymer-based devices made for single-cell assays, since the most common readout in such assays is fluorescence. A desirable material should have low autofluorescence i.e. low background noise, as in many micro-well array applications the detection of small fluorescence signals due to the small volumes and low concentrations of fluorophores, is required. So, in these cases the background autofluorescence of the material used can be significant compared to the signal of interest. If not, a simple difference algorithm may be sufficient for background correction [151]. Other approaches to overcome this issue include the use of confocal optics [152], two-photon excitation [153], long wavelength fluorophores [154] or simply using high fluorophore concentration until an acceptable signal-to-noise ratio is achieved. Yet, in some applications

the above mentioned strategies are not feasible.

A rough quantification of the autofluorescence of PDMS, SU-8, PEG-DA (MW 258) and liquid glass is shown in figure 2.10. PDMS and liquid glass showed the lower levels of autofluorescence. PDMS is generally regarded to have low autofluorescence, comparable to BoroFloat glass [118].

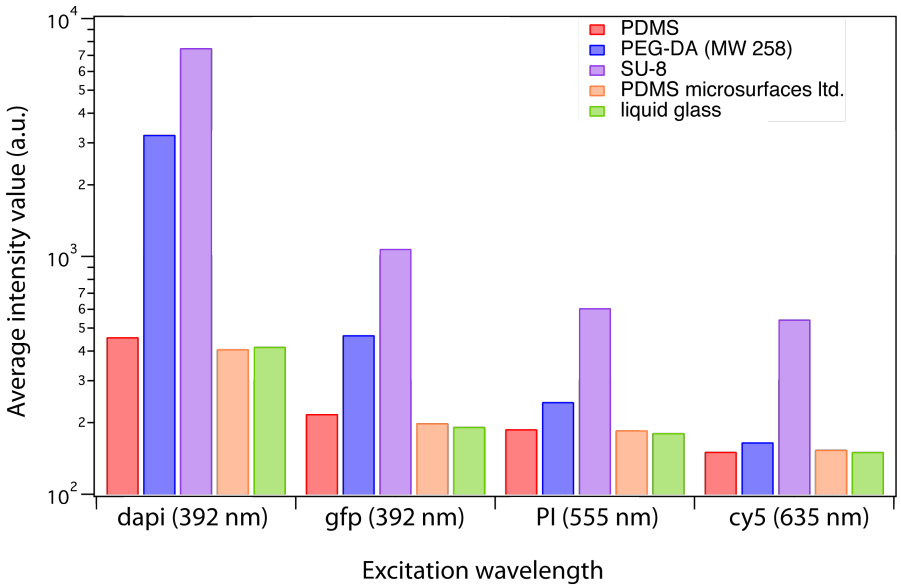

Figure 2.10: Autofluorescence of PDMS, PEG-DA (MW 258), SU-8 and liquid glass [105]. The images analyzed were acquired with an epi-fluorescence microscope and glass was used as a reference.

In conclusion the main characteristics of the materials presented above are summarised in table 2.2. These characteristics are based on literature search and experimental tests executed during the course of this thesis. The wavelengths regions that correspond to the filter names mentioned in this matrix are give in table 2.1.

	Excitation (nm)	Bandwidth	Emission (nm)	Bandwidth
dapi	377	50	447	60
cfp	436	20	460	50
gfp	470	40	525	50
pi	540	25	535	30
cy5	628	40	692	60

Table 2.1: Wavelengths regions that correspond to the filter names mentioned in figure 2.10

	PEG-DMA (550)	PEG-DA (258)	PEG-DA (575)	PDMS	SU-8
autofluorescence	medium	medium	medium	low	high
protein adsorption	less	medium	less	a lot	a lot
quality with MIMIC	perfect	perfect	perfect	perfect	-
quality photolithography	under optimisation	under optimisation	under optimisation	-	perfect
cytotoxicity	good	good	good	good	bad
adherence on substrate	bad	good	bad	-	good
polymer swelling	susceptible	resistant	susceptible	resistant	resistant
adherent cells	good	adhere on it	good	adhere on it	adhere on it
substrate	silanized glass/plastic	silanized glass/plastict	silanized glass/plastic	plasma activated glass	glass

Table 2.2: Summarised features of materials used for micro-well arrays

Chapter 3

Development of a single-cell secretion assay

3.1 Significance of cell-to-cell communication studies

Cells, either from a unicellular or multicellular organism, in order to survive need to sense their environment and communicate with each other. Using their plasma membrane receptors they sense external signals, which are then converted to responses within the cell. In practice, a signalling molecule binds to a receptor protein and causes its change of shape. Cascades of molecular interactions relay signals from receptors to target molecules in the cell. This signalling leads to regulation of transcription or other cytoplasmic activities. The process by which a signal on a cell's surface is converted to a specific cellular response is a series of steps called a *signal transduction pathway* [155].

For multicellular organisms, such as human, cell-to-cell communication is essential. The trillions of cells must communicate with each other in order to coordinate their activities to survive and develop. Cells in a multicellular organism not only can communicate with their adjacent cells but also with others far away from them via chemical messengers. Animal cells have cell junctions that, where present, directly connect the cytoplasms of adjacent cells. In this case, signalling substances dissolved in the cytosol can pass freely between adjacent cells. In addition to, animal cells can communicate via direct contact between membrane-bound cell-surface molecules, which occurs during a process called cell-cell recognition. This type of signalling is important in processes like the immune response.

In many other instances, messenger molecules are secreted by the signalling cell. These molecules may only travel for short distances; such as local regulators that influence cells in their vicinity. One typical example of such regulators are growth factors, which stimulate cells to grow and divide. Growth factors, which can also be cytokines, play a crucial role during the immune response as well, when haematopoietic stem cells need to differentiate into macrophages for example or other related cell types. Numerous cells can at the same time receive and respond to the molecules of a growth factor produced by a single cell in their vicinity. This type of local signalling is called *paracrine signaling*. Moreover in the nervous system, another more specialised type of local signalling occurs, which is called *synaptic signaling*. An electrical signal along a nerve cell triggers the secretion of a chemical signal carried by neurotransmitter molecules. These molecules, diffuse across the synapse, the narrow space between the nerve cell and its target cell. In this way, the neurotransmitter stimulates the nerve cell.

For long-distance signalling, multicellular organisms use chemicals called hormones. In animals, hormonal signalling is also known as *endocrine signalling*, in this case specialised cells release hormone molecules, which travel via the circulatory system to target cells in other parts

of the body. The transmission of a signal through the nervous system can also be considered an example of long-distance signalling. An electrical signal travels the length of a nerve cell and is then converted back to a chemical signal when a signalling molecule is released and crosses the synapse to another nerve cell. Here, it is converted back to an electrical signal. In this way, a nerve signal can travel along a series of nerve cells. Because some nerve cells are quite long, the nerve signal can quickly travel great distances, for instance from the brain to a toe.

From the above, it is apparent that signalling, either local or long-distance, is the way cells communicate with each and regulate their function. Cell populations are heterogeneous both in constitution and in timing. One of the most, if not the most, heterogeneous population in our body are the immune cells. The immune system is divided into two components the *innate* and the *adaptive immune system*. Each component is consisted of many other subtypes such as for example the Natural Killer cells (NK cells), T-cells, neutrophils etc.. Apart from this apparent diversity of cell types in a population, it is well-known that individual cells, even those that appear to be identical, differ in numerous characteristics such as the response to a given stimulus, the variability in the expression of a specific gene etc. [156]. This heterogeneity leads to a different phenotypic behaviour and as a result each of this subtypes can be divided into further subgroups [30].

3.2 Detecting proteins secreted from a single-cell

In order to study at the single-cell level the local signalling between cells, the first step is to be able to detect proteins secreted from a single-cell. These proteins will be the cue for the adjacent cell, which will react to this cue through the above described mechanism cue-signal-response. The reaction of the receiver cell can be anything, from committing to apoptosis, differentiate to another cell type, secrete another protein etc. To this end, the rest of the current chapter will focus on the development of a single-cell detection of secretion assay, with the long-term goal of studying local signalling between cells. In addition to cell-to-cell communication, quantification of secreted proteins can also reveal differences in other cellular processes such as activity against tumours [157]. To detect the secreted protein the sandwich Enzyme-linked immunosorbent assay (ELISA) will be used (see figure (3.1)).

ELISA is a biochemical technique used to detect the presence of an antibody or an antigen in a sample. For years, ELISA has been used as a diagnostic tool in medicine as well as a quality-control check in various industries. The immunoassay that Engvall and Perlmann first described has take many different forms. Briefly, in ELISA an unknown amount of antigen is fixed on a surface and then a specific to this antigen antibody is added and binds to the antigen. This antibody is linked to an enzyme and at the last step a matching substrate for this enzyme is added. The enzyme-substrate reaction will give a detectable and quantifiable signal that is proportional to the amount of the analyte being measured. The sandwich format of the assay is better choice if the protein to be detected has multiple epitopes. In this case, two antibodies are required that usually target different epitopes (3.2). For the sandwich ELISA format, combinations of monoclonal and polyclonal antibodies can be used. The most common combination is to use the monoclonal antibody as the *capture antibody* and the polyclonal as the *detection antibody*. Sandwich ELISAs usually require more optimisation than traditional ELISAs but the resulted signal-to-noise (S/N) ratio is usually higher.

To detect proteins secreted from a single-cell has been a longstanding endeavour, especially for cytokines. Detection of cytokines at the single-cell level will facilitate a deeper understanding in many inflammatory processes, since it will enable monitoring of immunological responses and measuring the frequency of cells within a population that produces a specific secreted factor. While amplification techniques (e.g. PCR) have boosted the development of single-cell genomic

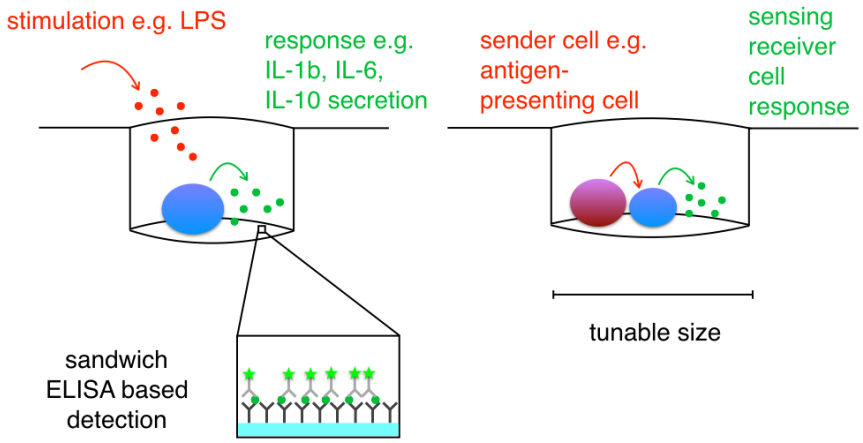

Figure 3.1: Detection of secreted proteins from a single-cell using the sandwich ELISA assay. The long-term goal is to study the local signalling between two single-cells.

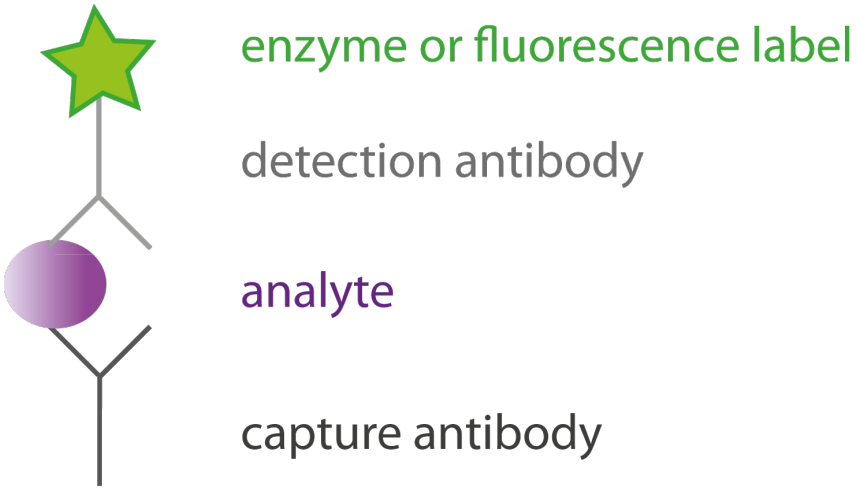

Figure 3.2: Sandwich ELISA illustration. *Capture antibody* is the immobilised antibody on the substrate, while *detection antibody* is the antibody baring the enzyme or the fluorescence label, which are essential for the quantification of the detected analyte.

analysis, detecting proteins secreted from a single-cell appears to be more challenging [158]. Measuring deoxyribonucleic acid (DNA) or ribonucleic acid (RNA) can provide a qualitative information about gene products (proteins) but cannot elucidate the activity of the protein, its location or its post translational modifications. In other words, an mRNA may be transcribed, however we cannot be sure about how much or whether the protein was translated at all. On the other hand, intracellular cytokine staining (ICS) for analysis with flow cytometry enables

the measurement of multiple proteins over a short period of time (4-6 h) [159], however this type of assay even though it can detect 19 parameters for each single cell, it focuses on either intracellular proteins or proteins on the cell membrane, without direct insight on whether the secretion pathway is completed. Another method for applications typically run by flow cytometry, mass cytometry [160], enables a multi-parametric analysis, since more than 30 parameters can be quantified at the single-cell level. Its detection technology is based on atomic mass spectroscopy, where stable isotope tags attached to antibodies using metal-chelating labelling reagents are measured. Another widely used method to study the release of protein (especially cytokines) from single cells is the enzyme-linked immunospot (ELISpot) [161]. In this assay, cells are incubated on a PVDF membrane, which is functionalized with specific antibodies for target analytes. During the incubation time, the proteins secreted from the cells are captured from the antibodies around the cell. Cells are then removed and the membrane is incubated with the detection antibodies, the secreted proteins are then visualised as coloured spots. In the end, qualitative results of the secreted protein and semi-quantitative results regarding the frequency of the secreting cells is available. However, it takes a considerable amount of time (from several hours up to days) until proteins are detectable and multiplexing is limited to 1-3 analytes [158, 162].

3.2.1 Detecting secreted proteins from single-cells in combination with micro-well arrays

Another promising strategy to detect proteins secreted by a single-cell is to combine a micro-well array with the general ELISA scheme. In the literature different approaches have been followed enabling both *end-point (static)* [36, 37, 163–167] or *dynamic* assays [38]. Another distinction that can be made is on the configuration of the micro-well, on whether it is open or closed, i.e. *open micro-well arrays* or *closed micro-well arrays*. Both configurations have advantages and disadvantages, which are summarised below:

- Open micro-well arrays offer accessibility to the cells during the measurement, i.e. it is possible to add any additional factor (e.g. stimulus) during the course of the experiment.
- In open micro-well arrays, larger amount of medium and as a result of nutrients is available, thus longer duration measurements are possible.
- Open micro-well arrays offer the possibility for dynamic measurements.
- In closed micro-well arrays signal loss is less in comparison to open arrays, where loss of signal due to persistent diffusion should be carefully manipulated.
- Closed micro-well arrays can introduce perturbations in the biological system as secretion events from the cells will affect the local concentration of analytes or other soluble factors that will affect cellular response in an autocrine fashion. Thus, the typical duration of a measurement in a closed array is 3-4 hours.
- Usually quantification of the closed micro-well arrays is easier with more standard setups required (like a microarray reader, or an epi-fluorescence microscope). While, dynamic quantification using total internal reflection fluorescence (TIRF) microscopy is a set-up not available to every research laboratory.
- The open micro-well configuration due to persistent diffusion of the secreted material out of the micro-wells, and due to constraints imposed by thermodynamics and mass transport is less useful for quantitative measures. For that, the open micro-well array configuration

is better for rapid screening of highly productive cells (antibody secreting cells, manufacturing cell lines) since biases toward high secretors and high affinity interactions [168].

3.2.2 Objective

Within the framework of this thesis, we mainly focused on the development of an open micro-well array since it will also enable the dynamic analysis of cytokine secretion. However, we also kept in mind that closed arrays appear to be a more established format in the literature, providing high statistics i.e. a large numbers of single-cells can be interrogated simultaneously, even though not a direct monitoring of the secretion event. We believe that both formats are complementary to each other and are both useful for an all-around investigation of a biological phenomenon. Statistics can be obtained with the closed array format and then a model of a possible secretion mechanism can be proposed. This proposed model can be directly interrogated with the open micro-well array format and a total internal reflection fluorescence (TIRF) microscope (see figure 3.3).

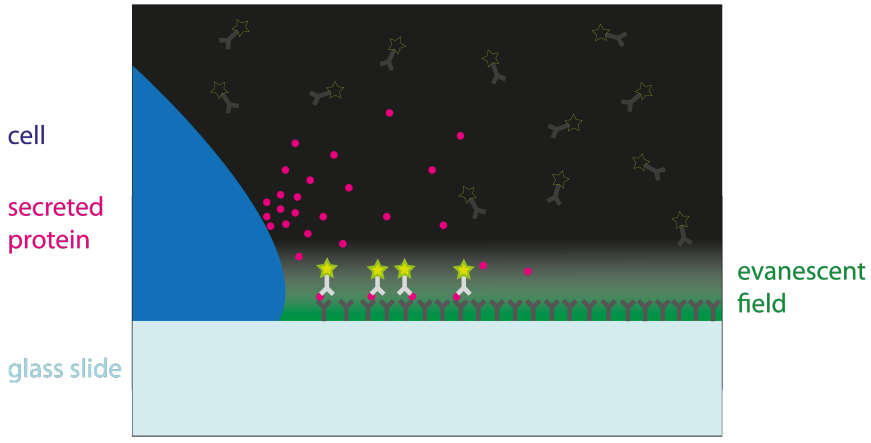

Figure 3.3: Illustration of a *dynamic open* array. A cell sits on a glass slide coated with *capture* antibodies; in the medium *detection* antibodies are diluted. The cell secretes the cytokine and ELISA sandwiches are formed. By utilizing a TIRF microscope setup only the bottom of the micro-well will be illuminated, permitting in this way a direct monitoring of the secretion event.

3.3 Experimental results

3.3.1 Antibody immobilization strategies - Background

Passive adsorption

To coat a surface with a biomolecule different strategies can be followed. The simplest is *passive adsorption*, which is the accumulation of particles (adsorbate) on a surface (adsorbent or substrate). The reverse process is called *desorption*. There are two main classes of adsorption, namely *physisorption* and *chemisorption*. In *physisorption* the forces involved are long range weak intermolecular attraction forces, van der Waals forces, between the adsorbate and the substrate. On the other hand, in *chemisorption* a molecule adheres to a surface through the formation of a chemical bond, which means that in this case we have strong modifications in the electron density of the adsorbate molecule.

Passive adsorption is the simplest way of immobilizing an antibody on a surface. It is the most widely used approach not only in the standard 96-well plate format of the assay, but also in many microfluidic devices [169]. In a 96-well plate adsorption occurs passively as the result of hydrophobic interactions between the amino acids side chains on the antibody and the plastic surface. On these hydrophobic plastic surfaces, the antibodies will have a distribution of different orientations on the surface namely *Fab-up, Fab-down, side-on, flat-on*, with Fab being the variable site of the antibody molecule [170] (figure 3.4). In this case the adsorption is dependent on time, temperature, and the pH of the coating buffer, as well as the concentration of the coating antibody. Usually coating of the capture antibody is done in pH 9.6 (most commonly with a carbonate/bicarbonate buffer) due to the isoelectric point of most antibodies, around 6 pH in most cases [171]. Moreover, a range of concentrations of coating the capture antibody is usually tested, since higher concentrations of antibody may actually have a negative effect on coating leading to over saturation of the wells which can inhibit antibody binding due to steric hindrance [171]. On the other hand, at low surface coverage antibodies adsorb on the substrate with a *flat on* orientation and are unable to capture their antigen [170, 171]. Moreover, even though antibodies adsorb on hydrophilic surfaces, such as borosilicate glass which is most commonly used for laboratory equipment and microscopy glass slides, with the *flat on* orientation predominately, the surface packing density of the antibody is the most important parameter to determine the available binding sites for the antigens. Additionally, at a fixed surface excess electrostatic repulsions between the antibodies and the surface, caused by increasing the pH value, can increase the available binding sites [172].

In many applications, such as microarrays but also cell culture, the substrates are coated with poly-L-lysine (PLL), a bio-compatible cationic polymer. Under physiological conditions the amine group and the lysine molecules of PLL are protonated. This cationic nature facilitates the adhesion of negatively charged biomolecules such as DNA but also of cells, since the cell surface is known to be negatively charged. PLL coating has also been used to enhance antibody coating on glass slides [36].

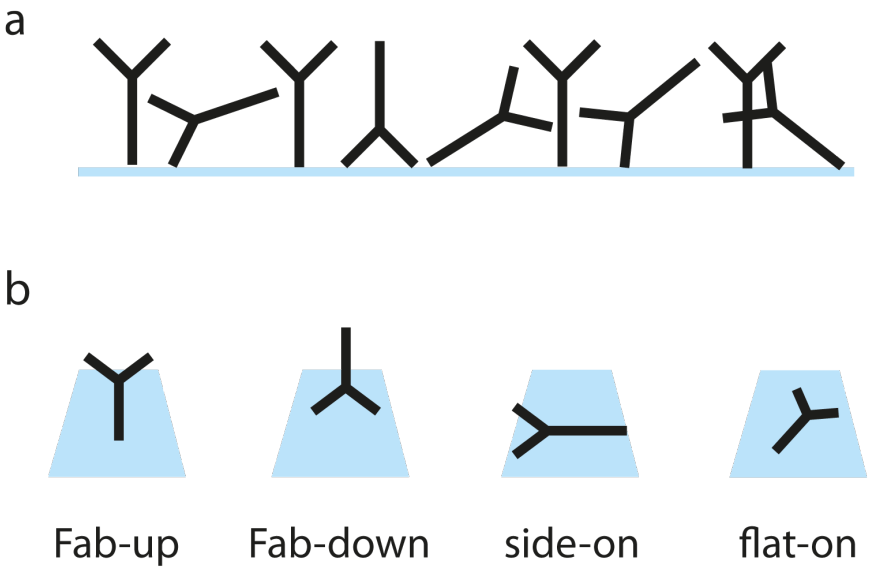

Figure 3.4: (a) Immobilization of an IgG antibody on a surface via *passive adsorption*. (b) Different orientations of an antibody on a surface, namely *Fab-up, Fab-down, side-on, flat-on*.

Bio-affinity immobilization

As it has been mentioned before (see section 2.2.2), in many applications it is preferential to orient the coated antibodies. In the case of an ELISA assay, this would in theory lead to a more sensitive assay [169]. The use of the biotin-avidin interaction to immobilize biomolecules in an oriented way is commonly known as *bioaffinity immobilization* [173]. The basic scheme is to coat the substrate with biotinylated *bovine serum albumin* (BSA), then with *avidin* and lastly use a biotinylated antibody as the *capture* one. In this case we have a combination of passive adsorption (BSA on the substrate) with affinity binding (biotin with avidin). The *biotin-avidin* interaction has been utilised in numerous applications due to its favourable features [174]

Biotin, or vitamin H, is found in all living cells. The bicyclic ring of the biotin molecule will bind with avidin, while the carboxyl group on the valeric acid side chain is free to be modified for the generation of biotinylated reagents that are used for conjugation with proteins. The most commonly used biotinylation reagent is the NHS ester of the biotin molecule that targets amine groups [175]. Moreover, antibody biotinylation is a widely-used rapid and specific process that does not perturbs the antibody's binding capacity due to biotin's small size (MW 244.31 g/mol).

Avidin is homotetrameric glycoprotein found in egg white, it is soluble in aqueous solutions and remains stable over a wide pH and temperature range. Four molecules of biotin can bind to one avidin. The non covalent interaction between biotin and avidin is very strong with a disassociation constant (K_d) of approximately $10^{-15}M$ [176], by far the strongest interaction reported, about 10^3 to 10^6 times stronger than the interaction between an antibody and its antigen. The bond formation is also very stable, resistant to pH and temperature changes, organic solvents, and enzymatic proteolysis. Several other homologs of avidin are available for use, such as streptavidin found in the *streptomyces avidinii* bacterium and being more resistant to non-specific substrate binding [177], deglycosylated forms (NeutrAvidin) [178] and forms of which the binding to biotin is pH-dependent (Nitroavidin) [179]. In figure 3.5 a schematic representation of the bio-affinity immobilization of an antibody on glass is shown.

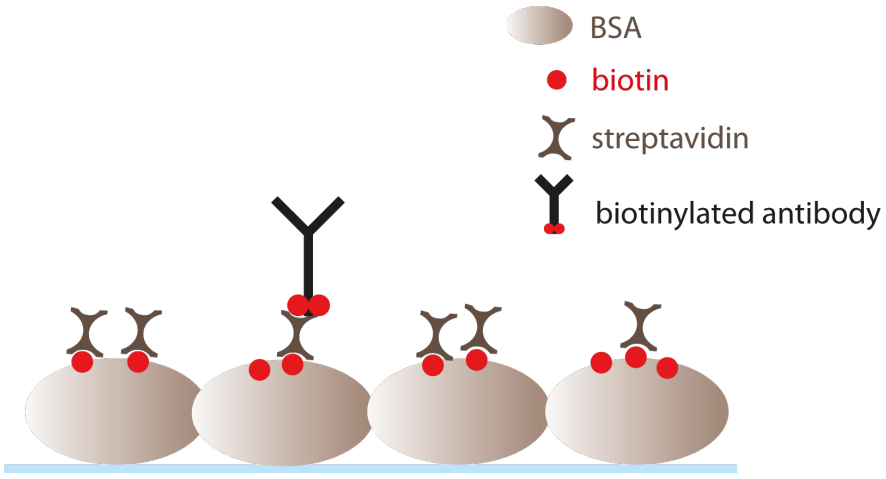

Figure 3.5: Bio-affinity immobilization of a biotinylated IgG antibody on glass. The combination of passive adsorption of BSA with affinity binding of the biotin-streptavidin complex can improve the orientation of the antibody molecule.

Covalent binding

In general, due to the need of protein arrays for proteomic and diagnostic tools, many strategies to covalently bind proteins on biochip substrates have been proposed [180, 181]. The covalent bonds are most commonly formed between side-chain-exposed functional groups of the protein molecule with substrates that have been suitably modified, resulting in a irreversible binding and a high surface coverage. The chemical binding can be random, *nonspecific immobilization*, when the residues are present usually on the exterior surface of the protein or can be specific, *site-specific immobilization*, which should result in a more controlled orientation of the immobilized biomolecule. The main strategies proposed for both types of immobilization are:

- nonspecific immobilization
  - amine chemistry
  - thiol chemistry
  - carboxyl chemistry
  - epoxy chemistry
  - photoactive chemistry
- site-specific immobilization
  - diels-alder cycloaddition
  - "click" chemistry
  - α-oxo semicarbazone ligation
  - peptide ligation
  - staudinger ligation

Covalent immobilization has also been used for antibodies, the majority of the applications has utilised surface silanization [169]. The proposed approaches include TiO_2 nanofibers treated with (3-glycidoxypropyl) methyldiethoxysilane (GPDES) [182], graphene nanosheets treated with 3-glycidyloxypropyl trimethoxysilane (GOPS) [183], glass slides silanized with epoxysilane [184, 185] and functionalization with (3-aminopropyl)-triethoxysilane (APTES) [186]. Yet, covalently immobilizing the antibody usually involve more complex surface chemistry, resulting in longer and more complex immobilizing protocols, without the guarantee that the immobilized antibody will be correctly oriented, at least for the nonspecific immobilization strategies [187, 188].

3.3.2 Antibody coating of glass slides

In order to develop a single-cell protein secretion assay utilising the ELISA scheme, the first step is to coat the substrate with the *capture* antibody. Antibodies can be coated via adsorption onto many surfaces such as glass, plastic, silicon or PDMS. We chose to use glass due to its optimal optical properties. In theory, adsorption of biomolecules on glass occurs mainly due to electrostatic interactions. Since antibodies tend to form multilayers on glass, which results in polar interactions between the adsorbed molecules, covalent binding of the antibodies onto the glass substrate is preferred, especially for quantitative immunoassays [169].

Our first approach was to covalently bind the capture antibodies on the glass substrate and then make the microwells on top. In this way, only the bottom of the micro-wells will be coated with the antibody. To covalently bind the antibodies on the glass we used VECTABOND^{TM},

a silane-based reagent, and Dimethyl pimelimidate (DMP) a membrane-permeable crosslinker, which contains an amine-reactive imidoester group at each end of a 7-atom spacer arm. Even though the coating of the glass slides was successful, making the PEG-DA micro-wells on top was not, since the coated antibody interfered with the adhesion of PEG-DA on the substrate. Furthermore, when making the PEG-DA micro-wells a PDMS stamp is placed on the substrate (see protocol in A.1), this PDMS stamp adsorbed almost all the coated antibodies of the glass (see figure 3.6). As a result, this approach was excluded as an option.

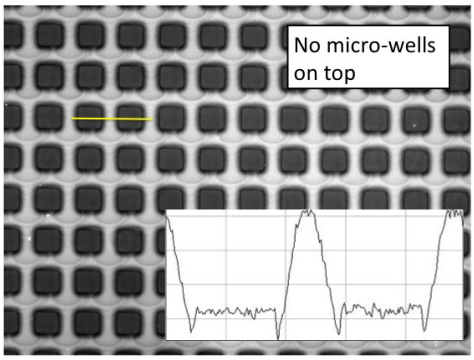

Figure 3.6: Coating the glass slide with VECTABOND^{TM} and then cross-linking the capture antibodies with DMP was successful, however PEG-DA micro-wells could not be formed on top. The squares are the imprint of the PDMS stamp during the fabrication of the micro-wells. The PDMS stamp adsorbed the antibodies coated on the glass substrate, resulting in a bottom that was not anymore coated with antibodies. The brighter areas are still coated with antibodies, as seen in the lower-right plot of the fluorescence intensity. The yellow line corresponds at the area plotted in the intensity plot (lower-right inset). These antibodies interfered with the adhesion of the PEG-DA micro-wells, which were lifted-off together with the PDMS stamp during the fabrication process. An anti-CD33 antibody conjugated with Alexa Fluor 488®, was used in the presented trial.

Apart from the covalent immobilization of the antibody on a glass slide, we further tested and compared the immobilization of an antibody on a PLL coated substrates (enhanced *passive adsorption* with the *bioaffinity immobilization* scheme. The substrates tested were bare ibidi®glass slides, glass slides silanized with 3-(Trimethoxysilyl)propyl methacrylate (TMSPMA) and ibidi®polymer foils. The results are presented in figure 3.7. The *bioaffinity immobilization* appear to be the best solution for all substrates, at least for the amount of antibody immobilised.

3.3.3 Antibody coating of PEG-DA micro-wells

The second approach that was followed was to first fabricate the micro-wells and the coat the bottom of them with the *capture* antibody. As mentioned above the molecular weight of the PEG chain determines its degree of protein and cell repellence and its attachment on the substrate. The longer the molecular weight the more protein and cell repellent the PEG is, but the smaller the molecular weight of PEG is, the better the attachment on the substrate. For the current approach three different PEG derivatives were tested, PEG-DA (MW 258), PEG-DA (MW 575) and PEG-DMA (MW 550) on glass silanized with TMSPMA and on ibidi®polymer

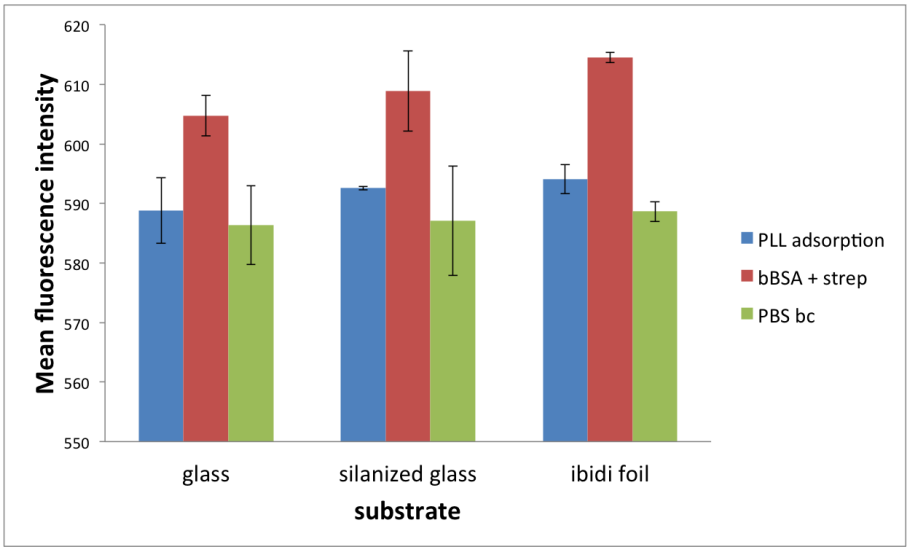

Figure 3.7: Coating various substrates with an antibody via *passive adsorption* enhanced with PLL or *bioaffinity immobilization*. The green bars stand for the background signal, only PBS was added in these samples. The antibody used in all cases was a biotinylated rabbit antibody and for detection a secondary anti-rabbit conjugated with AlexaFluor647®antibody was used. The error bars show the standard deviation of two independent trials. As a positive control for the PLL coated glasses, PLL conjugated with AlexaFluor 488®was used (data not shown).

foils both uncoated and treated. The best candidate resulted to be PEG-DA (MW 258), mainly due to the well attachment on all substrates, and its lower protein repellence was regarded as an acceptable characteristic. Coated with antibody via *passive adsorption* PEG-DA micro-wells are shown in figure 3.8.

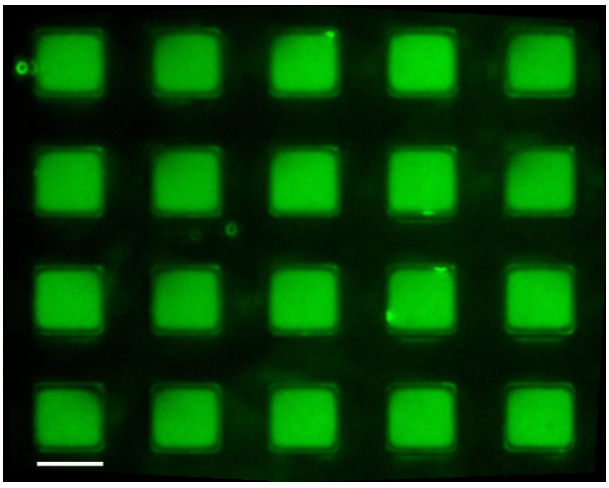

Figure 3.8: PEG-DA (MW 258) micro-wells coated with an Alexa Fluor 488®conjugated antibody via *passive adsorption* (see also figures 3.4). The scale bar corresponds to 50μm. The micro-wells were incubated with the antibody for 1 hour in room temperature at a concentration of 100μg/mL.

Since we are also interested in immobilising the antibodies on a substrate via the bio-affinity immobilisation, we further coated the PEG-DA (MW 258) micro-wells with BSA and NeutrAvidin and calculated the ratio of the biomolecule adsorbed on the silanized glass bottom versus the PEG-DA planar surface and walls. For the three biomolecules tested the ratios were 2.0 for the antibody, 1.3 for BSA and 2.0 for NeutrAvidin. The results are shown in figure 3.9, for BSA four different experimental conditions are averaged since the results were similar, while for the antibody and the NeutrAvidin the optimal experimental conditions are shown, which are 100 μg/mL and 20 μg/mL respectively with 1 hour incubation in room temperature for both. The experimental conditions averaged for BSA are 1 mg/mL and 50 μg/mL both for 10 and 30 minutes.

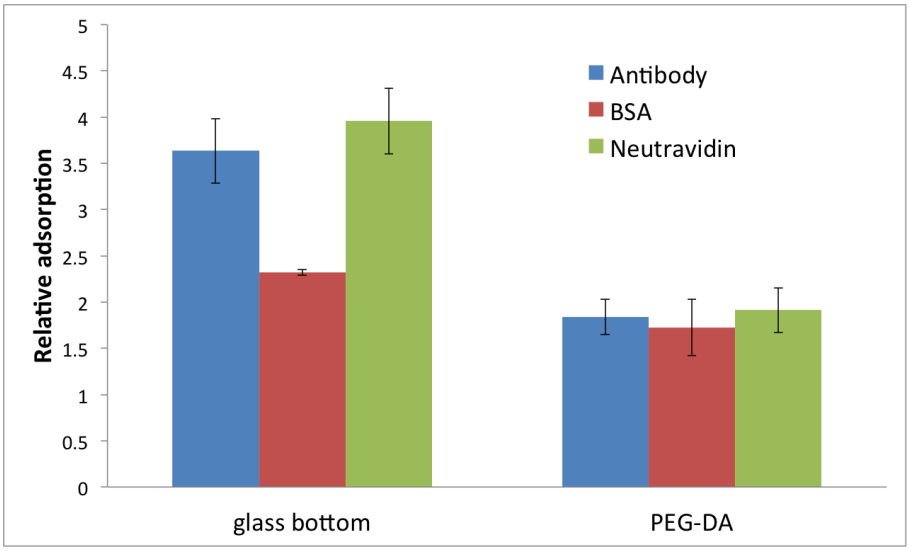

Figure 3.9: Relative adsorption denotes the quantity of a biomolecule adsorbed on a surface if we normalise with the control (background autofluorescence signal of the surface). The antibody used in these trials is an Alexa Fluor 488®conjugated antibody, BSA is conjugated with Alexa Fluor 488®and NeutrAvidin is conjugated with Oregon Green®. For the antibody and the NeutrAvidin the optimal conditions are plotted while for BSA four different conditions are averaged since the results were similar. The error bars for the antibody and NeutrAvidin trials show the standard deviation of three different samples.

In order to increase the sensitivity of the assay a reasonable approach is to improve the orientation of the *capture* antibody. The possibility of using an IgM antibody (as in section 2.2) is not feasible for detection assays mainly due to availability and cost issues. The most abundant antibody isotype in the market is the IgG, while it is possible that an IgM antibody against a specific antigen may not be available. Moreover, each ELISA antibody pair needs to be optimised due to unspecific binding of certain antibodies with other antibodies, or due to *cross-reactivity* i.e. when antibodies bind also to antigens other than the one they are specific to [189,190]. Taking the above into consideration, our third approach was to coat the bottom of the micro-wells with biotinylated antibodies via the *bio-affinity immobilization*. Most available antibody pairs are commercially available in a kit (ELISA kit), where the *capture* antibody is in its native form while the *detection* is biotinylated. The preliminary tests for cross-reactivity are done the two specific antibodies are guaranteed to function well for the sandwich ELISA format. In the case of the bio-affinity immobilization we exchange and use the biotinylated antibody as the *capture* antibody. Coated with antibody via *bio-affinity immobilization* PEG-DA micro-

wells are shown in figure 3.10. The concentration of the coated antibody is 8 μg/mL in all cases, while two concentrations of the secondary fluorescence antibody used for visualisation are shown (10 and 1 μg/mL).

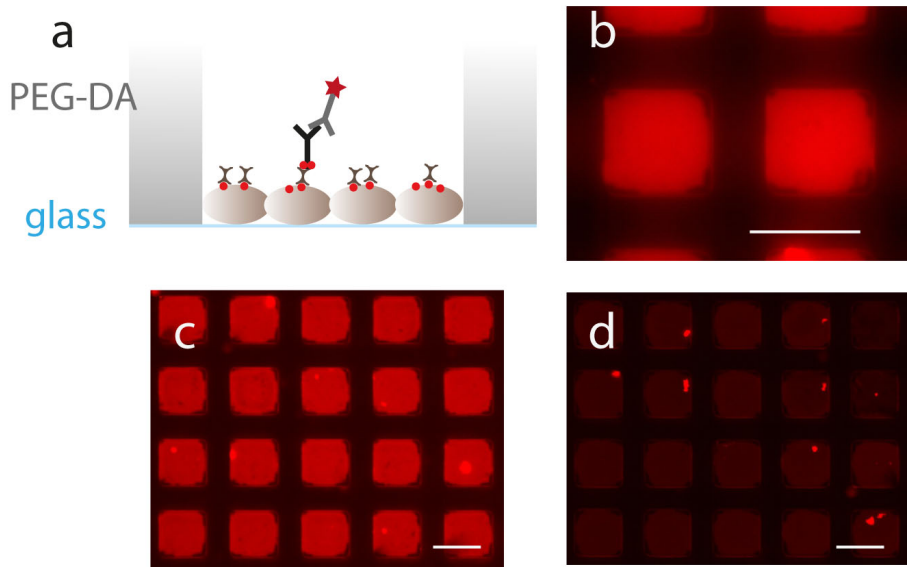

Figure 3.10: PEG-DA (MW 258) micro-wells coated with a goat anti-human biotinylated antibody via *bio-affinity immobilization*. (a) Schematic representation of the *bio-affinity coating* (biotinylated BSA on the bottom, streptavidin in the middle and on top the biotinylated antibody). For visualization a secondary fluorescently labeled antibody is used. Scale bars corresponds to 75μm in all images, and are equal to the side length of each micro-well. The biotinylated antibody was incubated for 30 minutes in room temperature in a concentration of 8μg/mL in all cases. The samples were blocked for 1 hour and the secondary used was an anti-goat conjugated with Alexa Fluor 647®antibody (10 μg/mL for (b), (c) and 1 μg/mL for (d)). (b) acquisition with a 40x objective, (c) and (d) with a 10x.

3.3.4 In-micro-well ELISA calibration assay

After coating the *capture* antibody on the bottom of the micro-wells, the following step is to build the whole sandwich ELISA complex on top. Since for this type of measurements our sample is a solution with a known concentration of the protein to be detected, we call this type of assay *standard ELISA assay*. In the end, a calibration curve will be produced, which we can use to translate our signals from cells to concentrations. In these trials two ELISA kits were utilised (from PeproTech®), one for human interleukin 2 (IL-2) and one for interleukin 1 beta (IL-1β). For each kit a certain range of the interrogated protein can be detected, for the IL-2 the range is 31 to 8000 pg/mL and for IL-1β is 12 to 1500 pg/mL. This dynamic range is optimised and validated by the provider as well as the suitability of the two antibodies for being used as the *capture* and *detection* antibody respectively. The micro-wells were made with PEG-DA (MW 258) on silanized with TMSPMA glass ibidi®slides.

Detection systems

The colorimetric is the most commonly used detection system in ELISA assays of the 96-well plate format. Colorimetric assays result in a coloured reaction product that absorbs light

in the visible range. The optical density of the reaction product is typically proportional to the amount of the protein being measured. The most commonly used enzymes are horseradish peroxidase (HRP) and alkaline phosphatase. These enzymes are usually conjugated to an avidin or streptavidin molecule which will bind to the biotinylated *detection* antibody. HRP is a small molecule (MW $\approx$ 44 kDa) and as a result it rarely causes steric hindrance problems with the antibody/antigen complex bound on the surface. Then, the final stage is the addition of the enzyme substrate. The most common substrates for HRP that produce soluble reaction products are dual function substrate tetramethylbenzidine (TMB) and 2,2'-azino-di [3-ethyl-benzthiazoline] sulfonate (ABTS). TMB is a highly sensitive substrate and due to its rapid reaction rate, it is ideally suited for a kinetic analysis. It produces a blue colour that can be measured at a wavelength of 650 nm. TMB can also be used in endpoint assays by stopping the reaction with 1M phosphoric acid. A yellow reaction product is formed upon acidification that can be measured at 450 nm. On the other hand, ABTS is considered an all-purpose substrate. Although it is less sensitive than either TMB, it has the widest working range of any substrate currently available for peroxidase. The reaction product for ABTS is a blue-green compound that can be measured between 405 to 410 nm. Its reaction rate is suitable for endpoint assays and is easily stopped with 1% SDS (sodium dodecyl sulfate), which does not change the colour or the absorbance of the reaction product.

To detect the captured cytokine on the bottom of the PEG-DA (MW 258) micro-wells, we used fluorescence-based detection, either with an epi-fluorescence microscope or a TIRF setup. The sandwich complex was the common one i.e. the capture antibody coated on the bottom, the protein and the biotinylated detection antibody on top. To visualise the complex we used NeutrAvidin conjugated with Oregon Green®or streptavidin conjugated with Alexa Fluor®660.

Total Internal Reflection Fluorescence Microscopy (TIRFM) is used to image fluorescent molecules on a transparent substrate and single molecule resolution can also be achieved [191, 192]. Instead of direct illumination, during TIRFM the sample is selectively illuminated by an evanescent field of a totally internal reflected laser beam. Eliminating the background fluorescence that originates from outside of the focal plane improves considerably the signal-to-noise ratio. For total reflection and generation of an evanescent field, the incidence angle of the excitation beam must be greater than the *critical angle*. The critical angle is determined by the refraction indices n_1 and n_2 of the two different media, typically the glass coverslip and the sample (water), and is given by $a_c = \arcsin\left(\frac{n_2}{n_1}\right)$, where $n_2 < n_1$. The evanescent field decreases exponentially in intensity along the z-axis of penetration:

$$I(z) = I_0 e^{-\frac{z}{d}} \tag{3.1}$$

where d is the *depth of penetration* given by:

$$d = \frac{\lambda_t}{4\pi\sqrt{n_1^2 \sin^2 \alpha - n_2^2}} \tag{3.2}$$

Typically, the depth of penetration is 100 to 200 nm, thus only fluorophores inside this volume will be excited, resulting in a much lower background noise, even 2,000-fold lower than normal epifluorescence microscopy.

Results

To generate a calibration curve inside the PEG-DA (MW 258) micro-wells, our first approach was to coat the capture antibody from the IL-1β ELISA kit on the bottom of the micro-wells via *passive adsorption*. As we know (see figure 3.9) PEG-DA walls are also coated with

antibodies but with less amount than the glass bottom. Six different trials were executed with varying experimental conditions, the key points are summarised in table 3.1. In these trials the concentrations of the *capture* and *detection* antibodies was 1 μg/mL, which is proposed by the kit manufacturer's protocol. In figure 3.11 representative epifluorescence images of these trials are shown together with the sandwich ELISA scheme. The images were analysed using *Microwell Analysis (MA)*, a custom made in-house ImageJ [193] plugin. With the MA plugin, the user can align a grid of regions of interest (ROIs) on the image of the micro-patterned surface. In this case, the grid is aligned over the bottom of the micro-wells. Then, the user can select which micro-wells can be included in the analysis or not. The mean fluorescence intensity over each ROI is calculated and the results are exported into a text file, which is further analysed with MATLAB®(Mathworks®, Natick MA, USA).

Trial	IL-1β range (pg/mL)	Fluorophore (μg/mL)	side length (μm)	Desiccation
1	(15 - 500)x 1000	NeutrAvidin Oregon Green®(5)	50	-
2	1.5 - 3000	NeutrAvidin Oregon Green®(5)	50	-
3	1.5 - 6000	NeutrAvidin Oregon Green®(5)	50	-
4	1.5 - 6000	Strepatvidin AlexaFluor660®(5)	50	-
5	1.5 - 6000	Strepatvidin AlexaFluor660®(6.6)	50	-
6	1.5 - 6000	Strepatvidin AlexaFluor660®(6.6)	75	30 minutes

Table 3.1: Experimental parameters of the *In-micro-well ELISA calibration trials*. Desiccation was performed before every incubation step in order to make sure that the bottom of the micro-wells is wetted with the corresponding solution of each different ELISA step, as it may be possible that during the washing steps, air may be trapped inside the micro-wells.

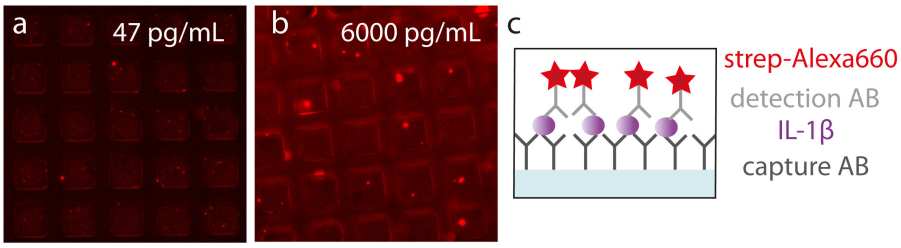

Figure 3.11: PEG-DA (MW 258) micro-wells with silanized glass bottom are challenged with human IL-1β; Epifluorescence image acquisition. In (a) the concentration of IL-1β is 47 pg/mL, while in (b) is 6000 pg/mL. In (c), a schematic representation of the ELISA sandwich on the glass bottom of the micro-well is shown. The capture and detection antibody were from the IL-1β ELISA kit from PeproTech®as well as the standard IL-1β protein. NeutrAvidin conjugated with OregonGreen®or streptavidin conjugated with Alexa Fluor®660 (shown here) were used for visualisation.

In our first trial, the micro-wells were challenged with a maximum IL-1β concentration of 500 ng/mL, based on [194]. However, the signal did not increase with increasing IL-1β concentration (figure 3.12). One possible reason is the ELISA kit's detection range; the kit used has a detection range of 12-1500 pg/mL. The concentrations tested in this trial where

far beyond the upper limit of detection which means that either we are at the saturation area or that the sandwich is not functional anymore, i.e. we have multilayers of proteins and their quantification is not possible anymore.

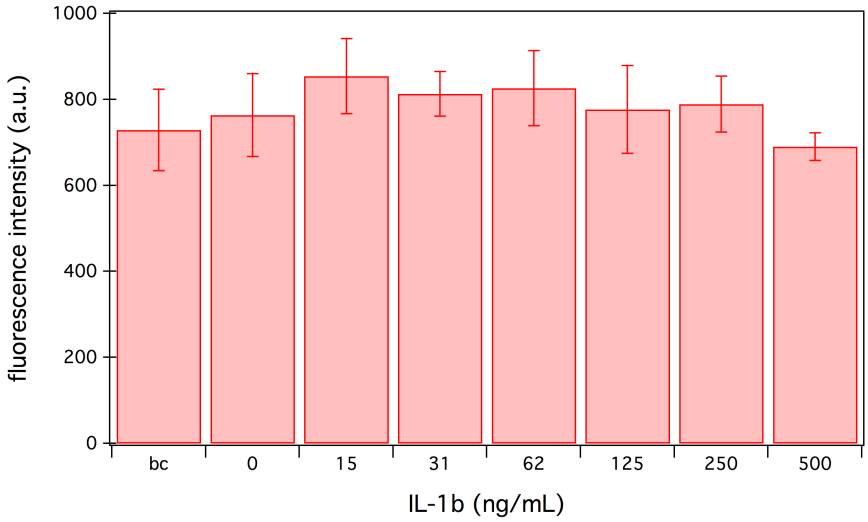

Figure 3.12: Calibration curve inside the micro-wells (trial 1). Fluorescence intensity was quantified over the bottom of the tested micro-wells. The error bars show the standard deviation of $\sim$ 1200 micro-wells tested in each condition.

We then continued by challenging the micro-wells with IL-1β in the concentration range of the ELISA kit. The second trial produced better results, but the signal increase was corresponding to IL-1β concentration increase only for 750 pg/mL and above. In figure 3.13, the results from trial 2 are plotted and the data are fitted with the Hill equation.

The subsequent trials (see figure 3.14) were part of an effort to improve the results of the second trial and produce an acceptable calibration curve. However, only the sixth trial produced equivalent results with the second. Again the lowest IL-1β concentrations could not be distinguished from the signal generated when no IL-1β was added. The lowest concentration of trial 6 that could be distinguished was 3000 pg/mL.

Samples from trials 3 to 6 were also tested with a TIRF microscope. For trials 4 to 6 TIRF setup 1 (Olympus microscope) was used. Setup 1 compromises a red excitation laser (at 662 nm) and an emission filter of 700/50 nm. The sample stage is small and as a result only the 4 central wells of the 8-well slide (from ibidi®), where the micro-wells were made, could be imaged. For sample 3 a second TIRF setup was used, setup 2 (Nikon Ti Eclipse microscope). Setup 2 compromised a green laser, the emission filter used was 515/35 nm and the objective was an oil immersed, 60x with NA 1.49. Since both fluorophores, Oregon Green®and Alexa Fluor®660, bleached very fast when illuminated, for acquiring the image the focus plane was set in one position with one random micro-well and then the stage was moved to the adjacent micro-well, of which immediately an image was acquired. TIRFM images of the setup 1 are shown in figure 3.15. In figure 3.16 the results from the TIRF acquisition are presented, in accordance with the epifluorescence images, the average fluorescence intensity on the bottom of each micro-well was calculated. Again, not a monotonous increase of the signal is observed with increasing IL-1β concentration, even though TIRF is more sensitive than epifluorescence microscopy. One possible explanation may be the heterogeneity of the sample, as shown in figure 3.17. Across one sample there are certain areas with compromised signal, possibly during TIRF acquisition, images from such areas where acquired in some samples. On the contrary, with

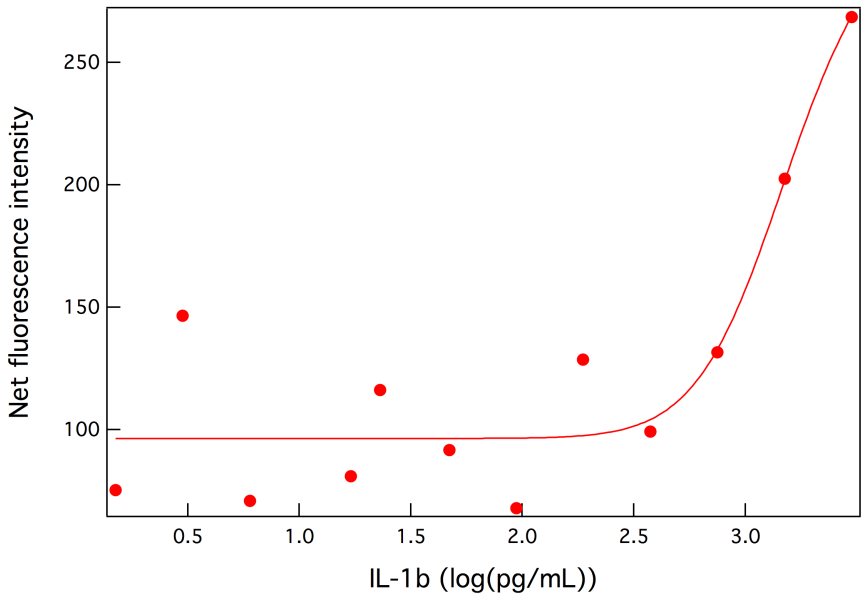

Figure 3.13: Calibration curve inside the micro-wells (trial 2). Fluorescence intensity was quantified over the bottom of the tested micro-wells. The background fluorescence intensity (micro-wells filled with PBS only) was subtracted from all data points. Data points are fitted with the Hill equation.

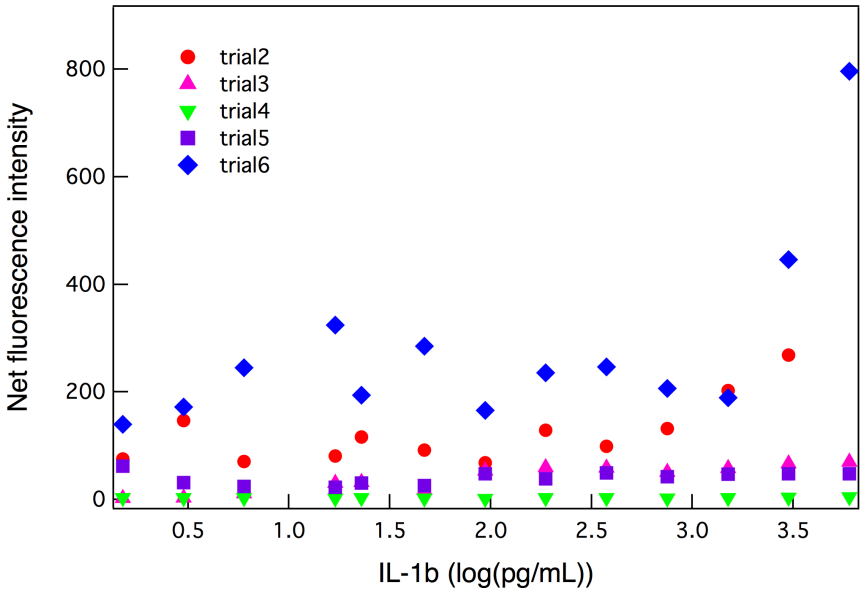

Figure 3.14: Calibration curves inside the micro-wells (trials 2 to 6); Epifluorescence image acquisition. Fluorescence intensity was quantified over the bottom of the tested micro-wells. The background fluorescence intensity (micro-wells filled with PBS only) was subtracted from all data points.

epifluorescence microscopy the number of micro-wells analysed is big (potentially up to 6,800 micro-wells per condition for this experimental setup) and even if such areas with compromised

signal are included, this did not affect the final average signal for each sample.

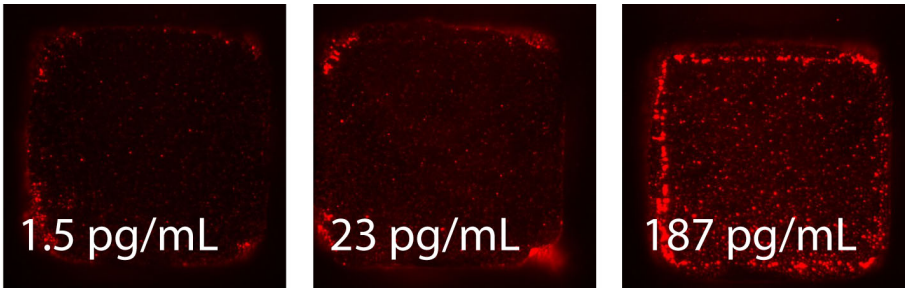

Figure 3.15: PEG-DA (MW 258) micro-wells with silanized glass bottom are challenged with human IL-1β; TIRF image acquisition. The side length of the micro-well is 75 μm. The concentration of IL-1β is shown on each image.

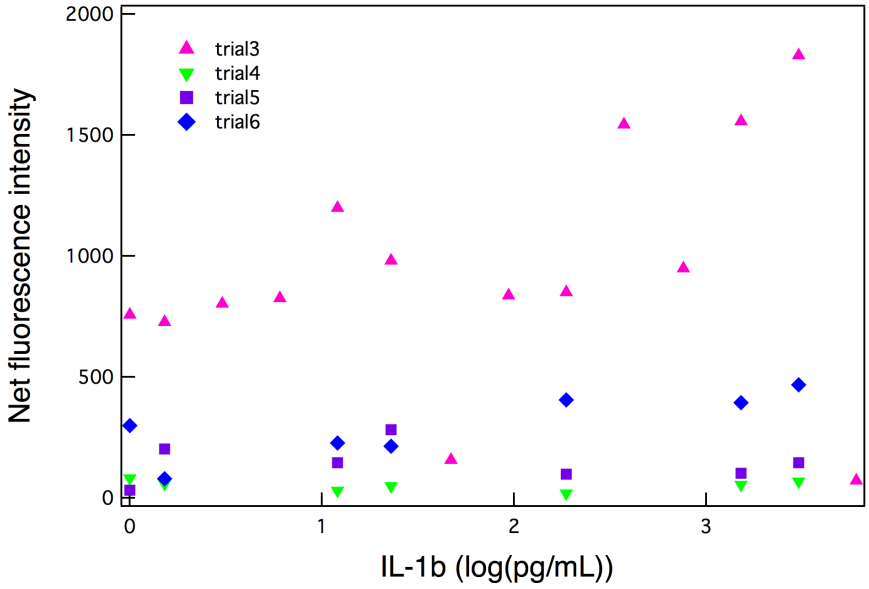

Figure 3.16: Calibration curves inside the micro-wells (trials 3 to 6); TIRF image acquisition. Fluorescence intensity was quantified over the bottom of the tested micro-wells. The background fluorescence intensity (micro-wells filled with PBS only) was subtracted from all data points.

To better understand the variability of the fluorescence signal on the bottom of the micro-wells across one given sample and how these signals differ across different samples i.e. different IL-1β concentration, we plot the histograms of the fluorescence intensity signals for trial 2 (figure 3.13). For these histograms, $\sim$ 160 micro-wells per sample are analysed. The histograms are plotted in figure 3.18 and indeed we see that distinguishing the signals of the lowest concentrations is not trivial.

Next, to enhance the sensitivity of the assay we tried immobilising the *capture antibody* at the bottom of the micro-wells via *bio-affinity immobilisation* (see figure 3.10). The results are shown in figure 3.19. In this trial an antibody ELISA pair for IL-2 detection was used (BioLegend®). As *capture antibody* we used the biotinylated antibody, which is normally used as the detection antibody, at a concentration of 8 μg/mL. As a *detection antibody* we used the

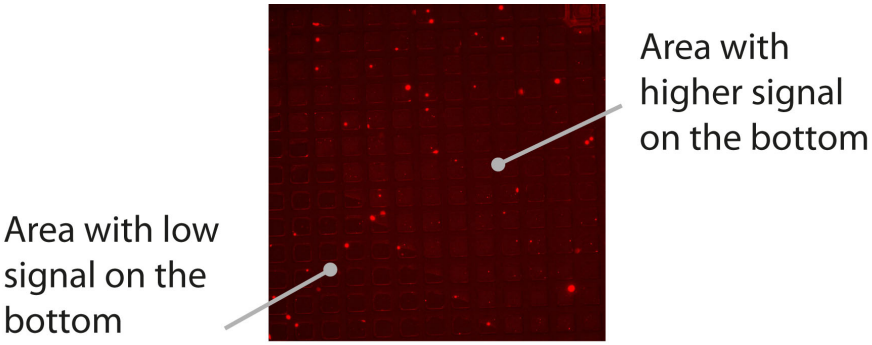

Figure 3.17: Diversity of the fluorescence signal along a sample. In a certain sample there are areas with micro-wells with compromised signal on their bottom.

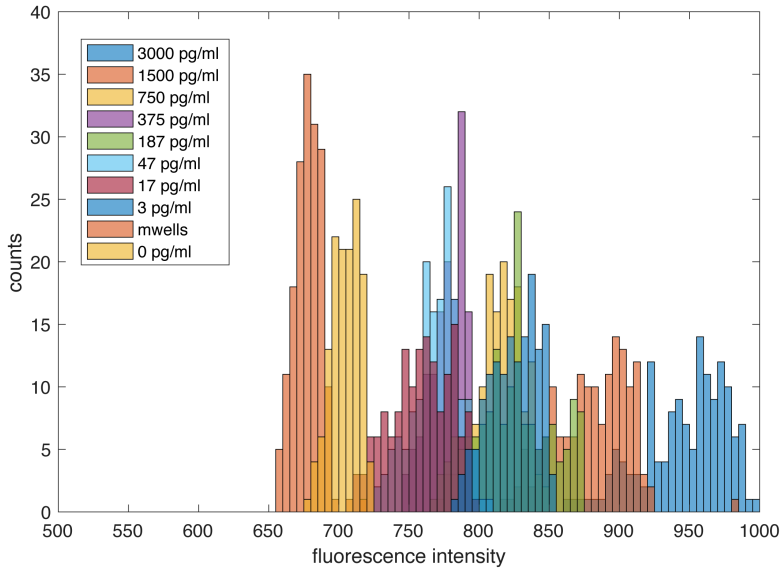

Figure 3.18: Histograms of the fluorescence intensity over the bottom of the micro-wells ($N \approx$ 160 micro-wells per sample).

antibody normally used as the capture one, in a labeled with FITC (fluorescein isothiocyanate) form (1 μg/mL). The IL-2 standard protein was from the IL-2 ELISA kit (PeproTech®). In accordance to figure 3.12 the mean fluorescence intensity on the bottom of the micro-wells was calculated. The data shown were acquired with a 10x objective, to be in accordance with the absorbance trials (see figures 3.12 and 3.14). Images were also acquired with the 4x, 40x and 100x objectives but without any difference in the results. In this case, the *bio-affinity immobilisation* scheme did not improve the results.

A potential idea to improve the sensitivity of the calibration assay is to utilise biotinylated DNA nanoparticles (NPs) conjugated with fluorophores for visualisation of the ELISA sandwich complexes, instead of using NeutrAvidin OregonGreen®or streptavidin Alexa Fluor®660 as above. This idea is applicable only when the capture antibody is adsorbed on the bottom (not for *bio-affinity immobilisation*). However, one should take into consideration the size of the DNA NPs, which is $60 \times 90nm$, with the size of the antibody molecule, $\sim 10 \times 2.5 \times 15nm$.

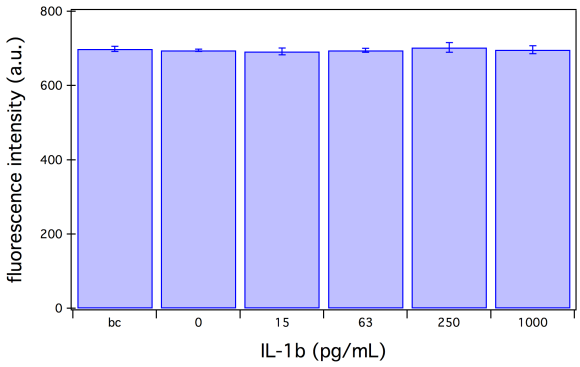

Figure 3.19: Calibration curve inside the micro-wells using the *bio-affinity* mode to immobilise the *capture antibody*. Fluorescence intensity was quantified over the bottom of the tested micro-wells. The error bars show the standard deviation of $\sim$ 140 micro-wells tested in each condition.

Moreover, such DNA NPs need a buffer with high salt concentration, which should be tested with the ELISA protocol.

Sensitivity of the epifluorescence microscope

Based on the above results, we observed that we cannot distinguish our signal from the background noise and that our *lower limit of detection (LLoD)* was 750 pg/mL in the second trial of the ELISA calibration assays (see figure 3.13). For that we performed an adsorption test in order to unravel the sensitivity of our epifluorescence microscope setup. In this test, we used a secondary antibody conjugated with AlexaFluor®647 and let this antibody adsorb on the bottom of the micro-wells in a wide range of concentrations. The epifluorescence microscope setup was the same used in the above trials (with a 10x objective). We selected a red fluorophore as in this region PEG-DA has the lowest autofluorescence (see figure 2.10), which is the best case scenario in our experimental setup. In figure 3.20, the images show the adsorption of certain different concentrations of the secondary antibody on the bottom of the micro-wells, while in figure 3.21, the calculated fluorescence intensity on the bottom of the micro-wells is plotted for all the different concentrations tested. The image analysis was done the same way as in the above ELISA calibration trials and on average $\sim$55 micro-wells were analysed for each different antibody concentration. Below the 100 ng/mL concentration, the signal is indistinguishable from the background noise.

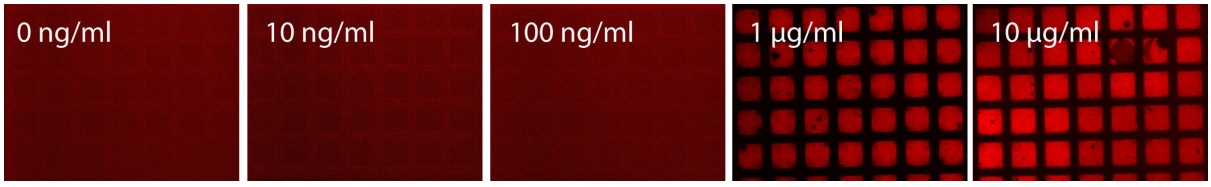

Figure 3.20: Different concentrations of a secondary conjugated with AlexaFluor®647 are adsorbed on the bottom of the micro-wells. The side length of each micro-well is 100 μm.

In the literature [36, 37, 166, 168], usually a laser microarray scanner is used to visualise ELISA complexes formed on glass slides. In general, most microarray scanners fall into two main categories. The first one is based on confocal microscope optics with a photomultiplier

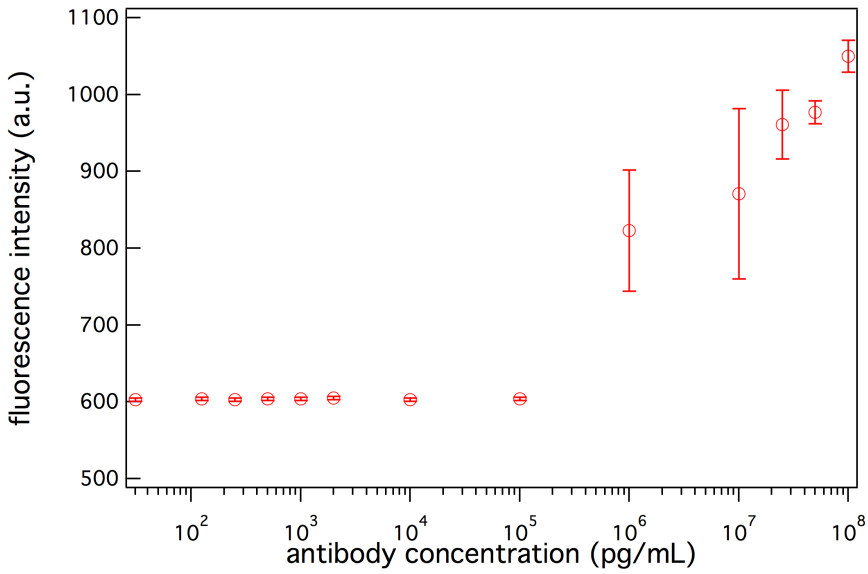

Figure 3.21: Sensitivity of the epifluorescence microscope. Different concentrations of a secondary conjugated with AlexaFluor®647 are adsorbed on the bottom of the micro-wells and the fluorescence intensity is then measured.

tube (PMT) and the second is based on standard microscope optics with a charge-coupled device (CCD) camera as a sensor [195]. Devices of the second category are usually referred to as microarray readers. Regarding the excitation there are three types of illumination technologies, the best being the gas laser, the next most common type uses diode or "solid-state" lasers and very few systems in use are based on controlled halogen bulb light sources. In the publications mentioned above the first type of microarray scanners is used namely with laser excitation and PMT, thus herein when referring to microarray scanners we refer to this type. A comparison of the signal-to-noise ratio between a fluorescence microscope and a laser microarray scanner can be found in the supplementary material of Zhou et al. 2012 [196]. In the two channels tested, Cy3 (green channel) and Cy5 (red channel), the laser microarray scanner had a better signal-to-noise ratio than the fluorescence microscope, 50 and 10 times more in the green and red channel respectively. Also the detection of nuclear localisation of SMAD1 and SMAD2 in human mesenchymal cells was tested and the laser microarray scanner was proven to have larger dynamic range and better detection sensitivity. In practice, microarray readers can typically detect between one copy in 100,000 and one copy in 500,000 [197, 198]. The sensitivity required for such a low-level fluorescence detection is $\sim$ 2 to 5 molecules per square micrometer with a linear dynamic range of five orders of magnitude.

By making a rough estimation based on our experimental results from trial 2 of the calibration assay, the corresponding numbers of our fluorescence microscope set up are 50 molecules per square micrometer for a best case scenario or 200 molecules per square micrometer for a safe scenario. These numbers were calculated as follows, our minimum detected concentration of IL-1β was 750 pg/mL. The molecular weight of IL-1β is 17.5 kDa or 17,500 g/mol, which means that the concentration of IL-1β in the volume is 0.04 nM. Our working volume was 200 μL, so by multiplying with the *Avogadro's number*, we have $\sim 5 \times 10^9$ molecules in this volume. The area of our substrate is 1 square centimetre, so if all the molecules are projected on this surface we get the number 50 molecules per square micrometer. Similarly, if we start with the 3000 pg/mL instead of the 750 pg/mL concentration, we get the number 200 molecules per

square micrometer.

Importance of signal-to-noise ratio

From the above, we conclude that the concentration range of the calibration ELISA assay is already near our limit of detection with our fluorescence microscope setup. Furthermore, we need to keep in mind that our modified surface with the PEG-DA micro-wells has a higher fluorescence background noise than that of bare glass. The main reason is the autofluorescence of PEG-DA walls, which results in stray light when the sample is illuminated with the epi-fluorescence mode. TIRF illumination in theory should have had better results, however that was not the case due to the rapid bleaching of the fluorophores but also probably due to the heterogeneity across the sample. Nevertheless, the TIRF illumination approach is not rejected but further adjustments of the assay is needed to be suitable for detection with the TIRF setup.

Another promising strategy to enhance the very low signal of cytokine secretion from single cells is to use the single molecule arrays (SiMoAs) [164,199,200]. This assay compromises the use of sealed micro-wells (with dimensions 4.5 $\times$ 3.25 μm) with bead-based ELISA and enzymatic reporters. Due to the small volume of the micro-wells the fluorophores generated by individual enzymes are confined, resulting in a very high concentration of the product molecules that can be detected. Then, by using standard microscope optics, it is even possible to distinguish micro-wells associated with a single enzyme molecule from those not associated with an enzyme, i.e. empty micro-wells. This strategy led to an improved sensitivity in comparison to standard ELISAs as detection could be achieved even in $\sim 10^{-19}$ M concentration of the target molecule and also allowed detection of proteins in serum at $\sim 10^{-15}$ M [164]. SiMoA was also combined with single cells and both high and low protein expression levels of intracellular prostate specific antigen (PSA) were detected [200].

3.3.5 Cell secretion

The next section focuses on experimental trials done with cells. To develop a single-cell ELISA secretion assay, we need a model cell line or even primary cells, that secrete a known protein for testing our assay. The available cell lines in our case were the HuH-7 and the Jurkat cell lines. The HuH-7 is a well differentiated hepatocyte derived cellular carcinoma cell line that was originally taken from a liver tumour in a 57-year-old Japanese male in 1982. The line was established by H. Nakabayshi and J. Sato. Based on previous work [201], we expected that HuH-7 will secrete IL-1β after stimulation with interleukin 6 (IL-6) and tumour necrosis factor alpha (TNFa).

The Jurkat cells are immortalised T lymphocytes, established from the peripheral blood of a 14 year old boy with acute lymphoblastic leukemia (ALL) at first relapse in 1976. Jurkat cells are able to robustly produce interleukin-2 (IL-2). The Jurkat clone that we used in the following trials is equivalent to the Jurkat ACC 282 clone from DSMZ (Leibniz-Institut DMSZ-Deutsche Sammlung von Mikroorganismen und Zellkulturen GmbH). Under steady-state resting conditions, IL-2 is mainly produced by $CD4^+$ T-cells in secondary lymph organs. The secreted IL-2 is then consumed by cells, mostly by regulatory T-cells (Treg), at the site with the CD25 receptor (IL-2Ra). During the immune response activated antigen-specific $CD4^+$ and $CD8^+$ T-cells produce large amounts of IL-2, which is then consumed by $CD25^+$ effector T-cells and Treg cells [202]. In general, Jurkat cells have been shown to be a suitable in-vitro model for studying the expression of the IL-2 receptor but also the secretion of IL-2 [203]. As every T-cell, they need two synergistic signals for full activation, namely one from a monoclonal antibody against the $CD3$ T-cell receptor (TCR) surface proteins or a lectin such as phytohaemaglutinin (PHA) and one by a phorbol ester, such as phorbol 12-myristate 13-acetate (PMA). PMA activates

protein kinase C (PKC) and hence NF-κB. PHA is a well-known selective T cell mitogen [204]. PHA binds to sugars on glycosylated surface proteins, including TCR, and thereby cross-linking them. This triggers calcium-dependent signalling pathways leading to NFAT (nuclear factor of activated T cells) activation.

Colorimetric bulk sandwich ELISA measurements

To test whether the above mentioned cell lines that were available, indeed secrete the aforementioned cytokines, traditional bulk ELISA measurements in 96-well plates were performed. HuH-7 were seeded in 96-well plate (5,000 cells per condition) and were stimulated with IL-6 or TNF-a (both 100 ng/mL [201]) for overnight. Supernatants were then collected and were diluted 1:1 with PBS. For the ELISA, the kit's manufacturer's protocol (PeproTech®) was followed. For detection the enzyme used was the HRP and the substrate was ABTS. Colour development was monitored using a plate reader at 430 nm with wavelength correction set at 650 nm. Huh-7 secreted IL-1β under stimulation with IL-6 and TNFa but the secretion level was quite low, $\sim$ 2 pg/mL in both cases while for the unstimulated condition, referred to as "medium", the secretion was $\sim$ 5 pg/mL (figure 3.22).

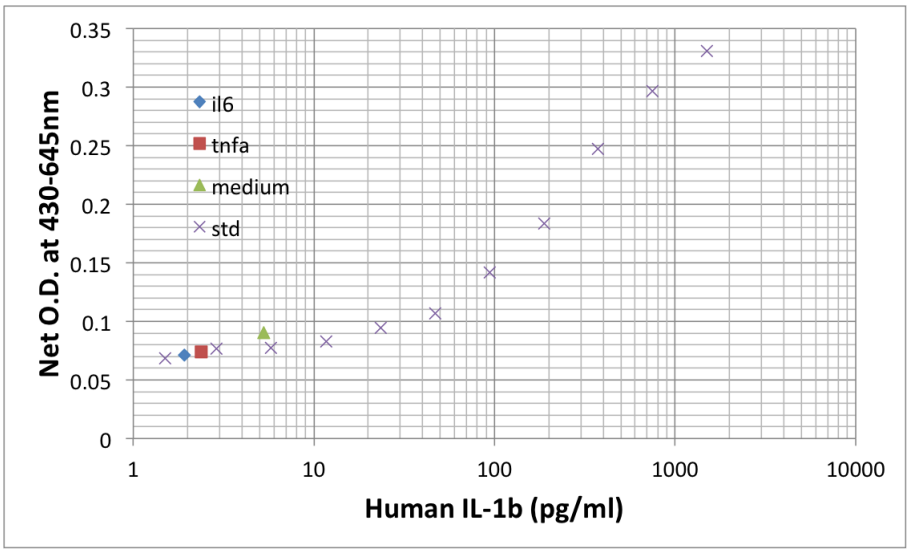

Figure 3.22: Huh-7 secrete low levels of IL-1β under stimulation with IL-6 (blue diamond) or TNFa (red square). In the unstimulated condition (green triangle), the cells secreted even more IL-1β. The standard curve is depicted with the purple points, for which recombinant IL-1β was used. For the standard curve each point is the mean value of a triplicate, while for the samples each point is the mean value of a tetraplicate.

The MOLM-13 cell line was also tested for secretion of IL-1β under stimulation with IL-6 and TNFa, however these cells did not secrete IL-1β at any condition. Since, our longterm goal is to perform an ELISA in real-time, to study the dynamics of the secretion event, an important aspect of this experiment is the performance of the ELISA assay under cell culturing conditions i.e. within the cell culture media. We tested whether substituting the buffer normally used during ELISA incubation steps, with cell medium would affect the assay performance. For that, we performed in parallel two standard (using recombinant IL-1β) ELISA colorimetric assays. The first one was done according to the manufacturer's protocol while in the second the incubations of the standard (recombinant IL-1β) and the *detection antibody* were done in cell

medium. For detection the enzyme used was the HRP and the substrate was ABTS. Indeed the assay sensitivity is affected, since the LLoD (lower limit of detection) of the assay done solely with assay buffer was 11.7 pg/mL (blue diamonds in figure 3.23), while the LLoD of the assay done with cell medium during two of the incubations was 93.75 pg/mL (red squares in figure 3.23).

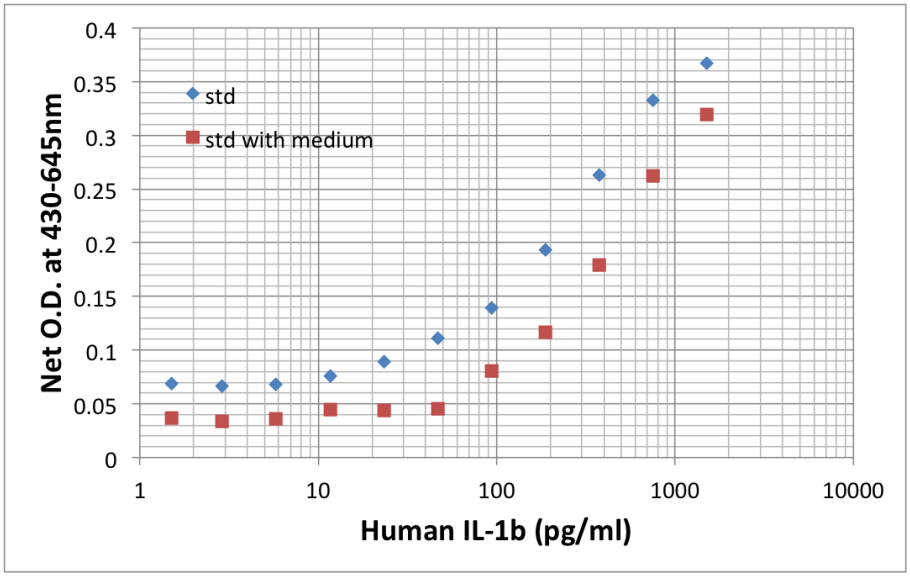

Figure 3.23: Cell medium affects the sensitivity of the ELISA colorimetric assay. For both standard curves recombinant IL-1β was used. The LLoD of the assay done solely with assay buffer was 11.7 pg/mL (blue diamonds), while the LLoD of the assay done with cell medium during two of the incubations was 93.75 pg/mL (red squares). For the standard curve each point is the mean value of a triplicate.

Next, we tested the secretion of IL-2 from the available Jurkat cells under different activation conditions. The optimal activation condition was found to be co-stimulation with PMA (100 ng/mL) and PHA (10 μg/mL) (see figure 3.24).

In-micro-well ELISA with cells

With regard to the dynamic secretion assay we would like to develop (figure 3.3), our first approach for an ELISA secretion assay inside the PEG-DA micro-wells, was to implement an *end point protocol* for detection of secretion events. The basic idea is that the micro-wells will be pre-coated with the *capture* antibody, then the cells will be seeded in the micro-wells and will be let to secrete the proteins. After this incubation period the following ELISA steps will be executed with the cells in the micro-wells [38, 168]. The core steps of the protocol are the following:

1. Coat micro-wells with capture antibody.
2. Block with BSA.
3. Add cells and stimuli, incubate for 2, 4 or 24 hours (pre-stimulated cells can be also used).
4. Wash x4 (cells stay in the micro-wells).

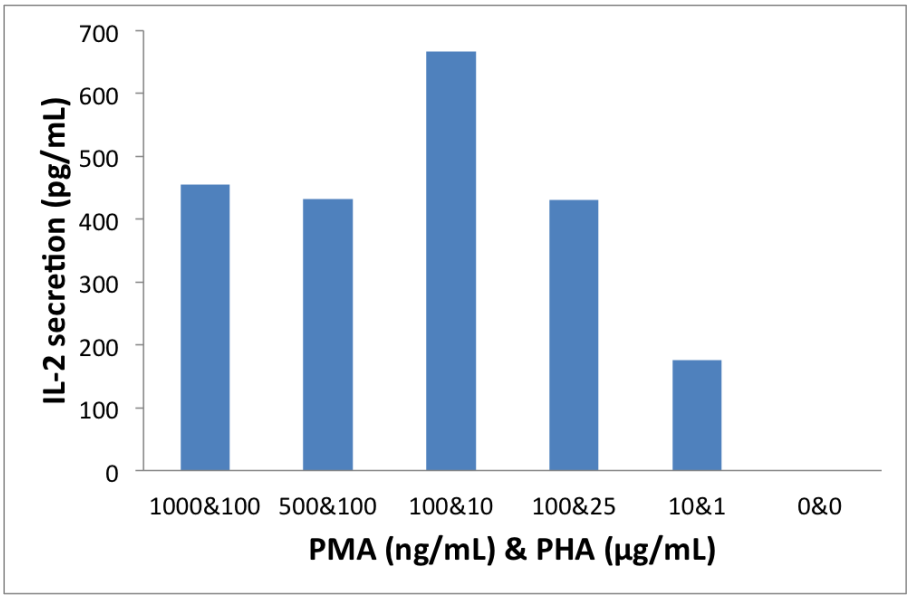

Figure 3.24: IL-2 secretion of Jurkat cells under different concentrations of PMA and PHA.

5. Add detection antibody (biotinylated) and marker for dead cells, incubate for 1 hour.

6. Wash x4.

7. Add labeled NeutrAvidin (or Streptavidin), incubate for 15 minutes.

8. Wash x4.

9. Image under the epifluorescence microscope.

The main challenges of these protocol is firstly to compromise between cell survival and unspecific binding. On the one hand, the buffer used during the ELISA incubation times must be substituted with the cell medium, otherwise cells won't survive for more than approximately half an hour. In this case, shorter incubation times may help to reduce unspecific binding of the cell medium components that may interfere with the ELISA antibodies. Secondly, during the washes in an ELISA assay a "detergent" buffer is typically used. This buffer most often contains Tween-20, which is a surfactant that decreases the background binding and also enhances reagent spreading. However, Tween-20 is also used to lyse the cells (at 0.5-5% v/v concentration), consequently its use with living cells is not ideal. In our case, the wash buffer used in the previous ELISA experiments contained Tween-20 at 1% v/v concentration. In the current trials with the cells we substituted the typical wash buffer (containing Tween-20) with PBS (Phosphate-buffered saline).

The cell lines HuH-7 and MOLM-13 were tested for IL-1β secretion with the above in-micro-well ELISA protocol. The cells were stimulated with TNF-a and IL-6 (both 100 ng/mL) for 2, 4 or 24 hours. During imaging L-15 medium supplemented with 10% FBS (Fetal Bovine Serum) and l-glutamine was used. However, no secretion events could be detected in these trials and the signal from the standard controls, samples that were incubated with IL-1β (1.5 ng/mL), was very weak.

ELISA-on-cell

Another very promising approach to detect secretion events at the single-cell level is to measure the secreted cytokines at the surface of the cell i.e. perform an *ELISA-on-cell*. In general, even for population based assays measuring as close as possible to the cells is highly desirable due to the much higher concentration of the secreted proteins near the cell layer surface. This concept is usually referred to as *Near-cell-ELISA*. The *Near-cell-ELISA* scheme is inspired by the *autocrine* and *paracrine* types of cell communication that have been described above (see section 3.1). The proteins captured and measured in this case are much higher in numbers, not only because they can be captured before they will come back to the same cell or bind on a receptor of an adjacent cell, but also due to measuring closer to the "source". If we think the cell as a spherical source due to diffusion, the closer to the cell we can measure the higher the concentration of the secreted protein will be.

As far as the single-cell scheme *ELISA-on-cell*, the same higher concentration of the secreted protein near the cell surface can be exploited in order to detect secretion events of low abundance, such as the secretion of cytokines. In this case the *capture* antibody can be immobilised on the surface of the cell via its constant domain (Fc). A similar approach has been developed and kits are commercially available from ©Miltenyi Biotec. Even though, the developed kits so far available are for a limited number of proteins, namely interferon gamma (IFNg) and interleukins 2, 4, 5, 10 (IL-2, -4, -5, -10), they are practical and reliable. The principle of the Miltenyi *ELISA-on-cell* designed for leukocytes is as follows (see figure 3.25); A "catch reagent", a double antibody of which the one end binds on a cell surface molecule while the other end targets the desirable protein to measure, is attached to the cell surface. Next, the cells are incubated in 37^oC for a short period of time to secrete the proteins. The secreted protein will then bind on the "catch reagent". After this incubation period, the cells are labeled with a *detection* antibody which is conjugated with a fluorophore. At that time the cells are tested using flow cytometry and the cells bearing an ELISA complex on their surface are detected. The sensitivity of the assay lies on the fact that since viable cells are analysed, non-specific background can be minimised by dead cell exclusion.

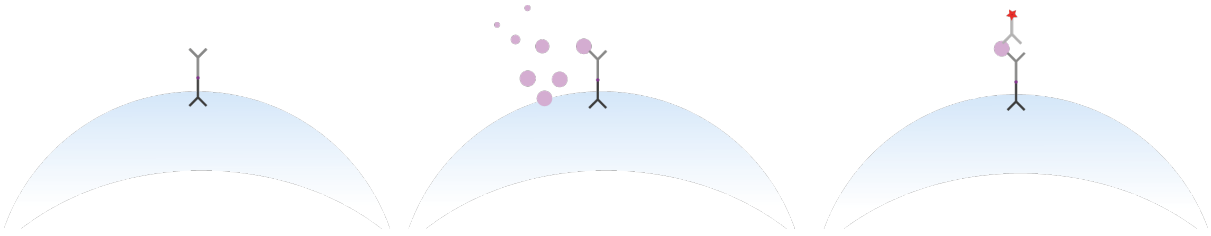

Figure 3.25: Principle of the *ELISA on cell assay* (©Miltenyi Biotec). A "catch reagent", a double antibody of which the one end binds on a cell surface molecule while the other end targets the desirable protein to measure, is attached to the cell surface. Then, the cells are incubated for a short amount of time to secrete the proteins. The secreted protein will bind on the "catch reagent". After this incubation period, cells are labeled with a *detection* antibody which is conjugated with a fluorophore.

In our case, we followed two approaches of the *ELISA on cell assay*, one end-point analysis based on the protocol from ©Miltenyi Biotec and one time-lapse protocol for dynamic analysis of cytokine secretion [205]. We used an "IL-2 Secretion Assay" (©Miltenyi Biotec) to detect the secreted IL-2 from the Jurkat cell line but also from primary T-cells. These primary cells were kindly offered from the K. P. Hopfner lab, and were expanded T-cells from PBMCs (peripheral

blood mononuclear cells). The expansion procedure lasted 18 days and resulted in a population of T-cells over 90% of the total number of cells. Moreover, the *detection antibody* of the kit was conjugated to APC (allophycocyanin). The main steps of the end-point analysis are the following:

1. Stimulate cells.
2. Label cells with the IL-2 "catch reagent".
3. IL-2 secretion period; Seed cells in the micro-wells and incubate cells for 45 minutes.
4. Label cells with the IL-2 detection antibody.
5. Image cells under the microscope.

The main steps of the time-lapse protocol for dynamic analysis of IL-2 secretion are the following:

1. Stimulate cells (optional).
2. Label cells with the IL-2 "catch reagent".
3. Seed cells in the micro-wells together with stimuli (activation factors).
4. Add detection antibody.
5. Image cells under the microscope with 20x objective for 4 to 24 hours every 5 minutes.

IL-2 plays a key part to many T-cell processes such as their response to bacterial infection, it also activates them to proliferate and differentiate and in general it is relevant in all autoimmune disorders, since it is required in the process of separating self from non-self. To study in a dynamic fashion the activation of T-cells using PHA, we performed a time-lapse dynamic monitoring of IL-2 secretion from Jurkat cells, with various PHA concentrations. After labelling the cells with the "catch reagent", we seeded them in PEG-DA (MW 258) micro-wells of 35 μm diameter coated with fibronectin, and then monitored the cells under the microscope using a 20x objective for 24 hours. To detect dead cells, we used the Sytox®Green stain. During the monitoring the detection antibody labeled with APC was present in the cell medium. When an IL-2 protein was secreted by the cell and was captured by the "catch reagent", the detection antibody bound on the IL-2 protein, thus forming the complete ELISA sandwich complex. Due to the red fluorescence signal these cells could be detected 3.26.

Images were then analysed using the in-house ImageJ plugin MA (see section 3.3.4) to extract the fluorescence intensities over the bottom of the micro-wells. Images were background corrected using the "Clustering Based Well Analysis" ImageJ plugin (Laura Lechtenberg's master thesis, which is based on a previously published method [206]). Figure 3.27 shows an exemplary plot of the fluorescence intensity over time. Each curve corresponds to one single cell, in this case we see that two cells secreted IL-2 (i.e. red fluorescence increased) in one field of view, indicating the high sensitivity of the assay.

We also performed an identical monitoring procedure with starved cells (using 5% FBS instead of 10% that it is typically used) to see whether their response would be higher. Starved cells were more stressed and for that they were monitored for 12 hours. In figure 3.28, the results of this monitoring for both cell populations, starved and normal, is presented. It is clear that starved cells are more stressed (light green curve) and that in both cases the IL-2 secreting cells fraction is below 10%. Error bars were calculated as in section 5.3.2.

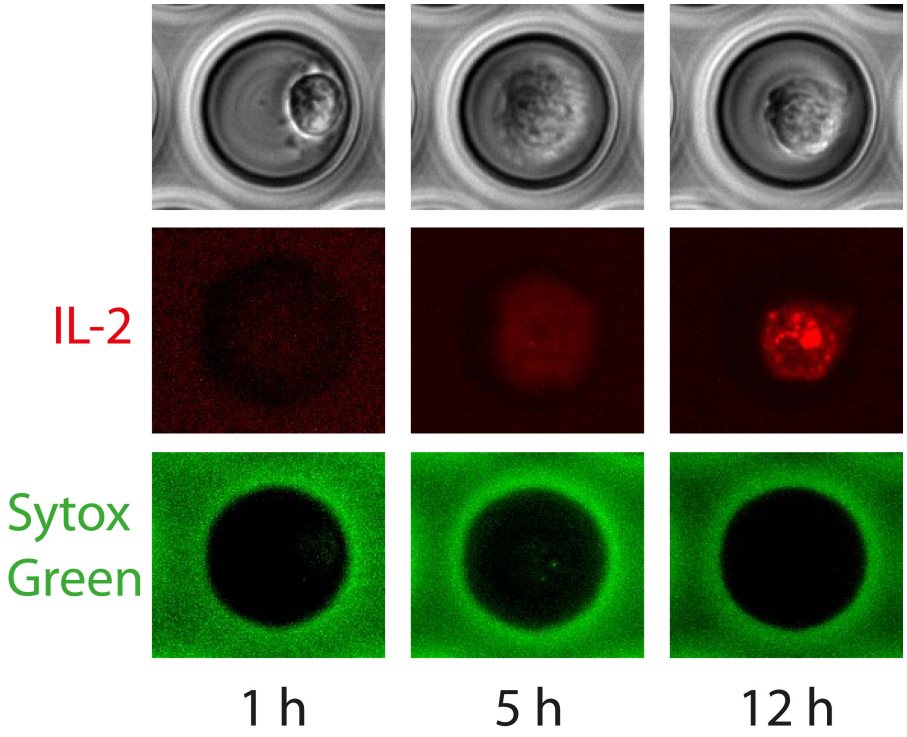

Figure 3.26: A Jurkat cell secreting IL-2. The first raw shows phase contrast images, the second raw shows images of the red fluorescence channel that correspond to the APC signal from the detection antibody, while the third raw shows the signal in the green channel for the Sytox®Green stain for dead cells. This cell was monitored for 12 hour during which it was activated with PMA (25 ng/mL) and PHA (1000 ng/mL). The diameter of the micro-well is 35 μm. At the second column, we observe that when the IL-2 secretion initiates (2nd raw) the cell obtains an adherent phenotype (1st raw).

Next in the same manner, we monitored the activation of the Jurkat cell line using a combination of PHA together with PMA. The concentration of PMA was the same across the different conditions (25 ng/mL) while PHA concentration varied. In figure 3.29 the results are presented for both cell populations (starved and in complete medium). In this case, again starved cells are more stressed (light green curve), however the fraction of IL-2 secreting cells is double than the population monitored in complete medium. Starved cells were monitored for 6 hours while the cells in complete medium were monitored for 12 hours.

After monitoring the activation of the Jurkat cell line using either PHA or PHA in combination with PMA, we observed that IL-2 secretion coincided with cell death at a great extent. Across all PHA concentrations, the average percentage of IL-2 secreting cells that also underwent cell death was $\sim 89\%$, while across all conditions with PHA in combination with PMA activation the average percentage was $\sim 85\%$. An exemplary cell that secretes IL-2 and dies is shown in figure 3.30.

Primary T-cells were also monitored in a similar manner. This sample, as mentioned above, was derived from PBMCs from a healthy donor. An expansion protocol was followed for 18 days and T-cells (more than 90%) compromised the final population. Due to their higher vulnerability these cells were seeded in bigger micro-wells (square-shaped with 50 μm side length). The cell size distribution was much broader in comparison to the Jurkat cell line indicating the much

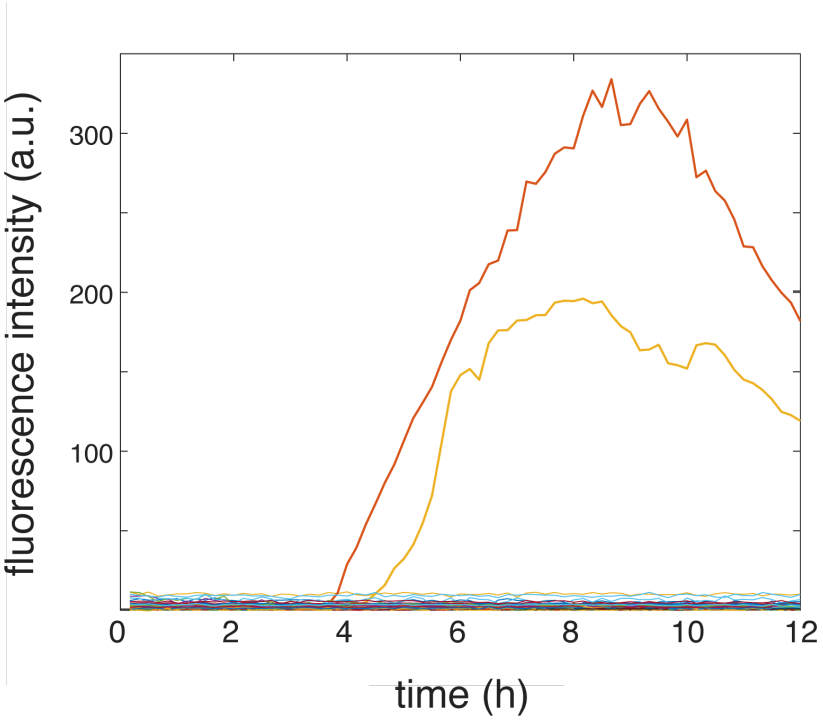

Figure 3.27: Fluorescence intensity profile over time of IL-2 secretion from Jurkat cells, in PEG-DA micro-wells of 35 μm diameter. Two of cells are secreting IL-2; each curve corresponds to one single cell (total number of cells plotted N = 36).

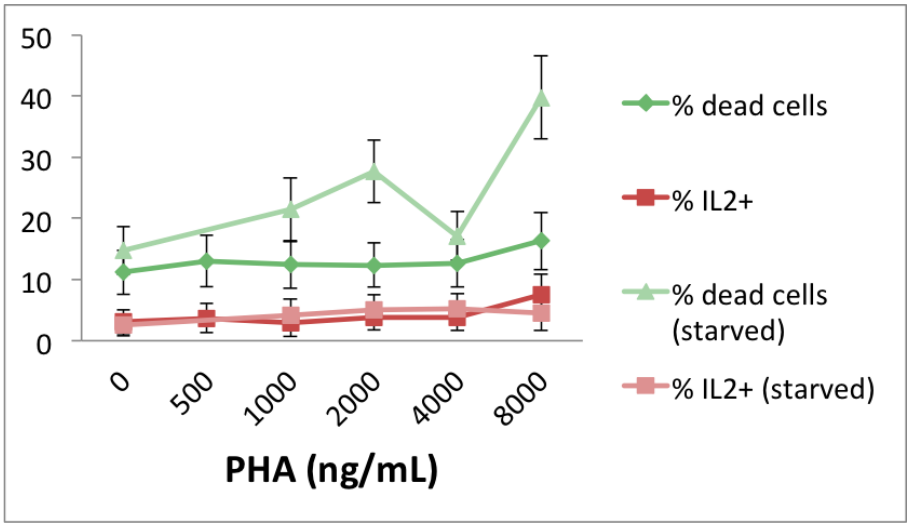

Figure 3.28: Activating Jurcat cells with various PHA concentrations results in low percentages of IL-2 secreting cells. Starved cells (light-coloured curves were monitored for 12 hours, while cells in complete medium were monitored for 24 hours.

higher heterogeneity of this sample. Image analysis in this case proved to be more challenging mainly due to the small cell size of the cells compared to the micro-well and the high background signal. Because of that, extracting the average fluorescence intensity over the bottom of the

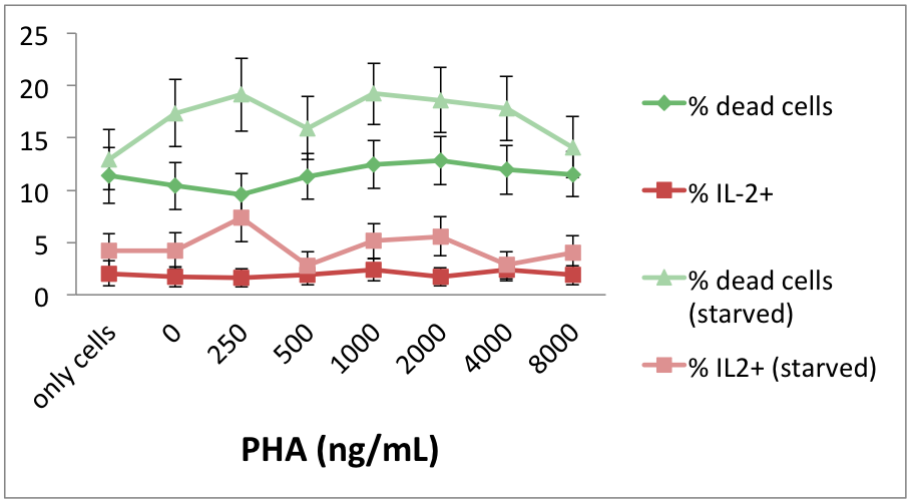

Figure 3.29: Activating Jurcat cells with PMA (25 ng/mL) and various PHA concentrations results in low percentages of IL-2 secreting cells. Starved cells (light-colored curves) were monitored for 6 hours, while cells in complete medium were monitored for 12 hours. The fraction of IL-2 secreting cells is double than the population monitored in complete medium.

micro-wells did not led to the detection of the activated cells (IL-2 secreting cells). In this case, it is essential to extract the fluorescence intensity over the cell area only, however this implies the necessity of cell tracking, since most of the cells were highly motile. In our case, we analysed the data manually however automatising the image analysis will require the implementation of a cell tracking module if the use of bigger micro-wells is required. The cells were pre-stimulated with a cytokine cocktail of TNFa (10 μg/mL) and IL-6 (10 μg/mL) or activated with PMA (5 ng/mL) and PHA (1 μg/mL) for an overnight. The following day the stimulated cells were divided into two samples. The cells were seeded in the micro-wells and IL-2 secretion was either monitored for 4 hours or quantified using the end-point analysis procedure. The cells that were monitored for 4 hours were subdivided into four different subgroups depending on whether they secreted IL-2 and whether they underwent apoptosis or not. The results are presented in figure 3.31. During the measurement the apoptosis marker Cell Event™Caspase 3/7 was included for the detection of apoptotic cells.

The second half of the sample was analysed using the end-point protocol, immediately after the overnight incubation. The results are shown in figure 3.32. A very small fraction of the cells secreted IL-2 (yellow component) below 1% in all three conditions. The majority of the cells remained inactive (light purple) and a high percentage of cells (46%) underwent apoptosis when cells were activated with PMA and PHA (light orange).

An advantage of the time-lapse over the end-point analysis is its higher sensitivity due to the longer observation period. Even though the total number of cells analysed with the end-point protocol is higher (see table 3.2) the percentage of the detected IL-2 secreting cells was lower (see figures 3.31, 3.32). The most probable reason may be the short time window during which the secretion event can be detected on the surface of the cell, which is 45 minutes for the end-point protocol (step 3). On the other hand, if a time-lapse observation is possible, it is desirable as the observation window can be as long as 24 hours. In our case, the 4-hour time-lapse was enough to detect the small fraction of the IL-2 secreting cells out of the pre-stimulated primary T-cells.

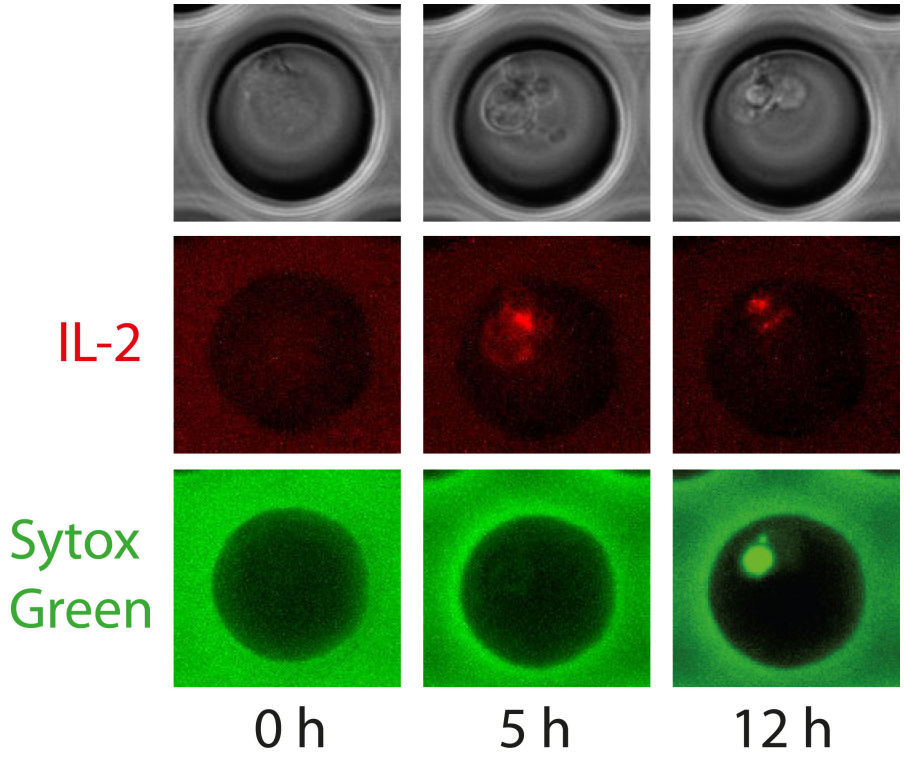

Figure 3.30: A Jurkat cell secretes IL-2 and then undergoes cell death. The first raw shows phase contrast images, the second raw shows images of the red fluorescence channel that correspond to the APC signal from the detection antibody, while the third raw shows the signal in the green channel for the Sytox®Green stain for dead cells. This cell was monitored for 12 hour during which it was activated with PMA (25 ng/mL) and PHA (8000 ng/mL). The diameter of the micro-well is 35 μm. At the second column, we observe that IL-2 secretion initiates (2nd raw) during the first stages of cell death, when the cell has started blebbing (1st raw) but before the signal from the nucleus stain is detectable (3rd raw).

Condition	End-point analysis	Time-lapse analysis
PMA/PHA	514	376
TNFa / IL-6	1051	288
no stimulation	706	406

Table 3.2: Total number of primary T-cells analysed in each different condition in the two different versions of the *ELISA-on-cell* assay, end-point and time-lapse analysis.

Conclusion

From the above experimental trials it is concluded that the most promising approach is the detection on the cell surface, *ELISA-on-cell*, over detecting the secreted protein on the bottom of the micro-well. This was determined by the specific parameters of the micro-well platform used, namely the relatively high background signal due to PEG-DA autofluorescence, in combination with the very low signal generated from the concentration range of the standard assays (ELISA calibration assays, section 3.3.4) but also from the small number of molecules secreted

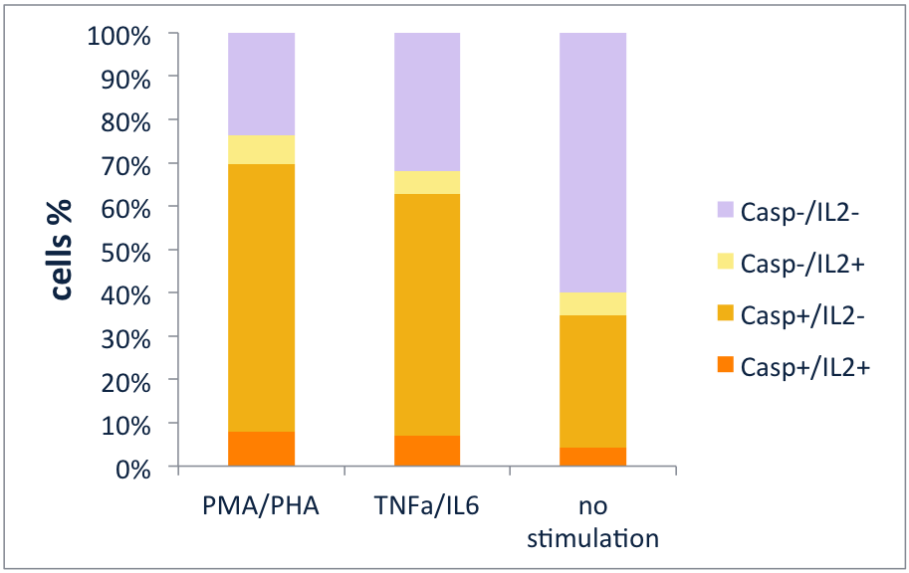

Figure 3.31: Pre-stimulated T-cells were monitored for IL-2 secretion. Cells were pre-stimulated for an overnight with either a cytokine cocktail (TNFa and IL-6 each at 10 μg/mL) or with PMA (5 ng/mL) and PHA (1 μg/mL). During the 4 hour monitoring few cells secreted IL-2 (yellow and dark orange components), while the majority of the cells either remained inactive (light purple) or underwent apoptosis without IL-2 secretion (light orange).

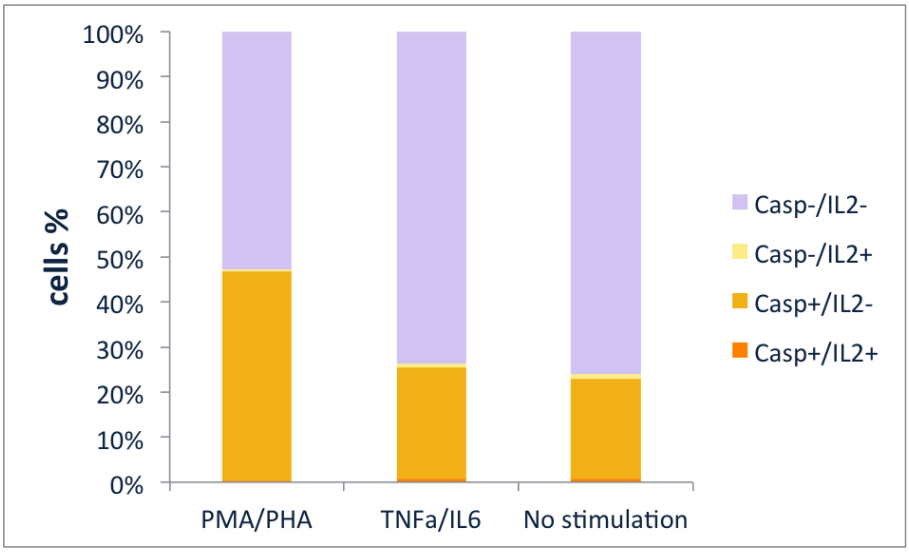

Figure 3.32: Pre-stimulated T-cells were tested for IL-2 secretion using the end-point analysis protocol. Cells were pre-stimulated for an overnight with either a cytokine cocktail (TNFa and IL-6 each at 10 μg/mL) or with PMA (5 ng/mL) and PHA (1 μg/mL). Very few cells secreted IL-2 (yellow and dark orange components), while the majority of the cells either remained inactive (light purple) or underwent apoptosis without IL-2 secretion (light orange).

by cytokine-secreting cells ([168] and *In-micro-well ELISA* trials, section 3.3.5).

Other promising approaches reported in the literature are, as mentioned above, the SiMoAs technology [200], a method combining PDMS micro-wells and bead-based ELISA [207] and

finally the well-established *microengraving* method [36,37,39]. Each one of them has its advantages and disadvantages but they manage to detect low secretion levels such as the secretion of cytokines from single-cells. The SiMoAs based method [200] so far has been shown to quantify only intracellular proteins however without any amplification steps. Both the SiMoAs based method and microengraving offer an end-point analysis while the bead-based ELISA in PDMS micro-wells offers real-time measurements of secretion events. In the bead-based ELISA in PDMS micro-wells the lowest concentration that could be detected on the bead baring the *capture* antibodies was 2.5 ng/mL of IFNg, when the coated beads were challenged with different IFNg concentrations (calibration curve). In our *in-micro-well ELISA* calibration assays, our detection limit on the bottom of the PEG-DA micro-well was 750 pg/mL to 3000 pg/mL (see section 3.3.4) which is equivalent. However, even though using beads permitted the detection of cytokine secreting cells, in our case it was not possible (see section 3.3.5). One reason may be that in our cell population the frequency of secreting cells is very low. Another reason may be the fact that the surface area of the bead coated with antibodies is smaller compared to the bottom of a micro-well (it can be smaller up to 30 times depending on the size of the bead), hence the surface concentration of the captured protein is higher for a given number of secreted molecules resulting in a detectable signal for lower numbers of molecules. Moreover, by passivating PDMS with PEG passive adsorption of the secreted protein on the PDMS surface was minimised. And finally because PDMS is less autofluorescent than PEG-DA (see figure 2.10), the background noise was lower in this case.

3.4 Theoretical description of transfer phenomena and binding kinetics

In this section, numerical simulations using the COMSOL Multiphysics®software were carried out to better understand the distribution of the secreted molecules inside the micro-wells. We tested and compared two general approaches that have emerged, namely open micro-well and closed micro-well arrays (see section 3.2.1). For our experimental setup, important points to evaluate are the quantity of the secreted protein that escapes the micro-well due to the persistent diffusion in an open array, whether cross-contamination exists between adjacent micro-wells and finally how much time we need to incubate our cells in order to obtain a detectable signal. Three different geometries were applied to elucidate these points, the first is an axisymmetric model of a cylindrical micro-well and the rest are 3D geometries of cubic micro-wells.

3.4.1 Mathematical model and boundary conditions

The mathematical description of our experimental setup is the same for all different geometries. In all cases a cell is placed on the bottom of a micro-well and secretes a protein with a constant rate. In both the 2D and 3D geometries our models include the mass transport of the secreted proteins via diffusion, since there is no fluid flow inside our micro-well platform, and the binding reaction between the secreted protein and the *capture* antibody. The secreting cell is modelled as a sphere with a diameter of 15 μm, placed at the centre of the bottom of the micro-well. The micro-well and the surrounding volume is filled with water, which is a good approximation for cell medium. The cell is assumed to secrete proteins at a constant rate radially into the medium:

$$N_{total} = \kappa t \tag{3.3}$$

where N_{total} is the total number of secreted molecules, κ is a constant describing the rate of secretion, and t is the time. Even though in reality the secretion rate is not constant and

depends on various parameters such as the cell cycle phase, the secretory capacity of the cell but also on environmental cues [208, 209], assuming a constant rate simplifies the problem and gives us a better idea on the relationship between the quantities of the secreted proteins and those that are captured. The secretion rate for cytokines is 5-50 molecules/s, while for antibody producing cell lines the secreting rate of a cell can be up to 2000 molecules/s [36, 209].

The transport of the secreted protein in the liquid phase is described using the diffusion equation:

$$\frac{\partial C}{\partial t} = D\nabla^2 C \tag{3.4}$$

where C is the protein concentration and D is the diffusion coefficient.

We assumed that the *capture* antibody is uniformly coated on the bottom of the micro-well. Based on our experimental results (see figure 3.9), we also assumed that antibodies adsorb also on the PEG-DA walls, but on the walls the available binding sites are half the available binding sites on the glass bottom. The binding reaction on the coated surfaces is described by a reversible equilibrium process:

$$\mathrm{C} + \mathrm{B} \underset{\mathrm{k_{off}}}{\overset{\mathrm{k_{on}}}{\rightleftharpoons}} \mathrm{C_s} \tag{3.5}$$

where B are the free binding sites on the coated surface and C_s is the concentration of the antibody-protein complex on the surface, k_{on} and k_{off} are the association and disassociation constants respectively.

For the bottom and PEG-DA surfaces, the reaction and diffusion at the surface is described by a first order Langmuir adsorption model, where the diffusive flux is balanced against the reaction rate:

$$\vec{n} \cdot (-D\nabla C) = D_s\nabla^2 C_s + k_{on}C(B_0 - C_s) - k_{off}C_s \tag{3.6}$$

where B_0 is the initial concentration of the *capture* antibody i.e. binding sites and $(B_0 - C_s)$ is the concentration of the available binding sites. We assume that the antibodies do not diffuse on the surface, hence the diffusion term (D_s) is equal to 0. As a result the equation describing the boundary conditions on the coated surfaces becomes:

$$\vec{n} \cdot (-D\nabla C) = k_{on}C(B_0 - C_s) - k_{off}C_s \tag{3.7}$$

We also assumed that the binding of the antibody with the secreted protein occurs at 1:1 stoichiometry. The initial concentration (or Cauchy boundary condition) at $t = 0$ of free and bound protein is negligible ($C = 0$, $C_s = 0$). For the boundary condition at the edges of the medium above the micro-well, both a negligible concentration (C=0, Dirichlet boundary conditions), or the gradient of the concentration (Neumann boundary conditions) or a combination of the two at different surfaces (surface above and at the side) was tested. The parameters with a constant value across all model geometries are summarised in table 3.3.

Since this problem cannot be solved analytically, we will solve it numerically using the Finite Element Method (FEM), a short description of which is presented below.

3.4.2 Finite Element Method (FEM) basic concepts

A plethora of boundary value problems cannot be solved analytically. In such cases, approximate solutions can be obtained with various discretisation methods. One type of discretisation is directly applicable to the differential equations governing the problem. This approach includes

Parameter	Value
Density of total binding sites, B_0	$10^{-9}\ mol/m^2$
Density of total binding sites on PEG-DA walls, B_{0w}	$5 \times 10^{-10}\ mol/m^2$
Initial concentration of free protein, C_0	$0\ pmol/m^3$
Initial concentration of bound protein, C_{s0}	$0\ pmol/m^2$
Cell diameter	$15\ \mu m$
Diffusion coefficient, D	$3 \times 10^{-11}\ m^2/s$
Temperature	$310.15\ K$

Table 3.3: Constant parameter values across all models

methods such as the *finite differences approximations* [210, 211], various weighted residual procedures [212], or collocation methods [213, 214]. Another widely used approach is the *Finite Element Method (FEM)* where a weak form of the governing equations is interrogated.

The core idea of FEM analysis is to replace a continuous geometry with a set of objects with a finite number of degrees of freedom (DOF). These objects are called *elements* and they are connected with each other at the *nodes*. Typically, FEM analysis is divided into the following steps:

- Mesh generation which involves discretising the geometry of the PDE domain.
- Element definition; typically 3, 4, 8, or 9 node elements are used.
- Solving the system of equations with unknown variables the values of the desired field variable at the nodes of the elements.
- Interpolation of the desired field variable in the whole domain using the interpolation functions of the elements according to: $u = \sum N_i \overline{u_i}$

where u is the approximated field variable at any point in the integrated domain, $\overline{u_i}$ denotes the value of u at the nodes i, and N_i are the basis (or shape) functions.

In our case the function to be solved is the diffusion equation (see equation 3.4) which is of the general form:

$$Lu(x) = f(x) \tag{3.8}$$

Where L is the elliptic partial differential operator such as the Laplacian:

$$L = \frac{\partial^2}{\partial x^2} + \frac{\partial^2}{\partial y^2} + \frac{\partial^2}{\partial z^2} \tag{3.9}$$

The unknown variable u is discretised as: $u = \sum_{j=1}^{n} c_j u_j$, where $u(j)$ are the values at the nodes.

Then according to Galerkin - Ritz, we obtain the weak form of this equation by choosing a weight function v, multiply both sides of 3.8 with v and integrate across the domain:

$$\langle \nabla^2 u, v \rangle = \langle f, v \rangle \tag{3.10}$$

which becomes:

$$\langle u, v \rangle = \iint_{\Omega} u(x,y)v(x,y)dxdy \tag{3.11}$$

where the domain $\Omega \in \mathbb{R}^2$

3.10 is the weak form of 3.8. Even though a solution to the weak form may not be identical to the strong form 3.8, it has several advantages, including a lower order (1st order instead of 2nd order which was the original strong form). The lower order relaxes the requirement for continuity of the basis functions N_i, to C1 (1st derivative to be continuous) instead of C2, thus allowing us to use 1st order polynomials.

3.4.3 Results

Below the results from the different models will be presented. All models are based on the above equations and the specific parameters are given in each case.

Axisymmetric geometry

The first geometry tested is a simple axisymmetric model of a cylindrical micro-well of 35 μm diameter with a cell lying on the centre of the bottom of the micro-well (see figure 3.33). The affinity of the *capture* antibody was set to nanomolar range ($K_d = 10nM$). The secretion of the cell was set in the range of cytokine secretion, either low or high (9 or 50 molecules/s respectively). The PEG-DA walls were set to be either completely impermeable or baring half of the binding sites in comparison to the bottom, as it was concluded experimentally (see figure 3.9). The upper boundary of the micro-well was either set with a negligible concentration (C=0) or with negligible gradient of the concentration ($\nabla C = 0$). Since we are interested in the dynamic state of the system, a time-dependent study was executed for 4 or 24 hours, which is what is experimentally feasible. Apart from the experimentally available height of the micro-well, which is 30 μm, we also tested a height of 60 μm to explore whether it is a preferable solution. The range of the above parameters tested are summarised in tables 3.4, 3.5, 3.6, 3.7, and 3.8.

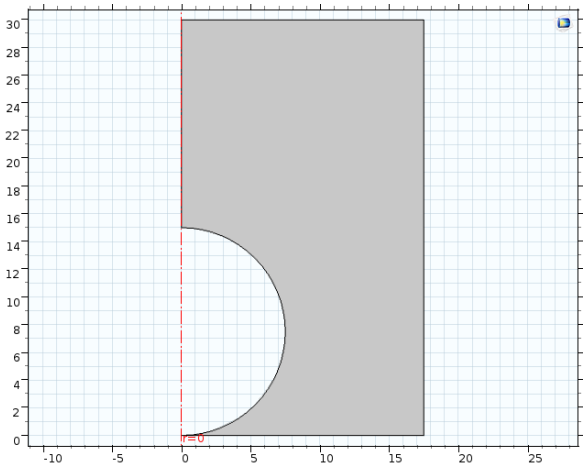

Figure 3.33: Geometry of the axisymmetric model. The height of the micro-well shown here is 30 μm and its diameter is 35 μm, which are the dimensions of our experimental setup.

Indicative results from these simulations are shown in figure 3.34. We also calculated at each time point the integrated concentration at the bottom of the micro-well, which is what we can measure experimentally. The most important parameter is the cell secretion rate (see figure 3.35), since only when the rate is increased in simulations 4 and 5 the protein captured on the bottom of the micro-well is also increased. At the first time points, the calculated

Parameter	S1
Cytokine secretion (molecules/s)	9
Upper boundary condition	$C = 0$
Micro-well wall boundary condition	impermeable
Micro-well height (μm)	30
Time (h)	4 or 24

Table 3.4: Parameter values for the axisymmetric geometry in simulation 1

Parameter	S2
Cytokine secretion (molecules/s)	9
Upper boundary condition	$C = 0$
Micro-well wall boundary condition	half binding sites
Micro-well height (μm)	30
Time (h)	4 or 24

Table 3.5: Parameter values for the axisymmetric geometry in simulation 2

Parameter	S3
Cytokine secretion (molecules/s)	9
Upper boundary condition	$\nabla C = 0$
Micro-well wall boundary condition	half binding sites
Micro-well height (μm)	30
Time (h)	4 or 24

Table 3.6: Parameter values for the axisymmetric geometry in simulation 3

Parameter	S4
Cytokine secretion (molecules/s)	50
Upper boundary condition	$\nabla C = 0$
Micro-well wall boundary condition	half binding sites
Micro-well height (μm)	30
Time (h)	4 or 24

Table 3.7: Parameter values for the axisymmetric geometry in simulation 4

concentrations are negative, which is most probably due to numerical instabilities caused by the geometry (sphere on surface) or by high concentration gradients at the initial time points. Even though the axisymmetric geometry offers quick solutions, since the cell has a size comparable with the micro-well, the axisymmetric models are not very precise for quantitative calculations. Moreover, cross contamination to adjacent micro-wells cannot be tested. Hence, we continued our calculations using more suitable 3D geometries.

Parameter	Simulation 5
Cytokine secretion (molecules/s)	50
Upper boundary condition	$\nabla C = 0$
Micro-well wall boundary condition	half binding sites
Micro-well height (μm)	60
Time (h)	4 or 24

Table 3.8: Parameter values for the axisymmetric geometry in simulation 5

Open well model

To address the points mentioned above, namely more precise quantitative calculations and testing the potential cross contamination to adjacent micro-wells, we also used a 3D geometry for our computational analysis. In this case, as available in our experimental set up, the micro-wells had a cubic shape with 50×50×50 μm dimensions. Two micro-wells were included in the model to test the potential cross-contamination. The volume above the micro-wells is 350 μm, so the total height of the medium volume from the bottom of the micro-well is 400 μm, which the experimental height of the medium if the micro-wells are made in a 6-channel ibidi®slide (see figure 3.36). The equations of the model remain the same as in the axisymmetric model (see section 3.4.1).

However, the boundary conditions used at the edges of the medium volume are not straightforward to set. In one study, the Dirichlet boundary condition was used ($C = 0$) [168], assuming that the concentration far from a secreting cell is negligible. The Neumann boundary condition ($\nabla C = 0$) can also be used [215]. We believe that the Neumann boundary condition should be more suitable in our situation, but at this point we test both Neumann and Dirichlet boundary conditions as the latter might also be a good approximation. The parameters used in our first simulation are shown in table 3.9.

Parameter	Simulation 1
Cytokine secretion (molecules/s)	50
Upper boundary condition of medium	$C = 0$
Side boundary conditions of medium	$C = 0$
Micro-well wall boundary condition	half binding sites
Medium volume height (μm)	400
K_d (nM)	10
Time (h)	4

Table 3.9: Parameter values for the 3D geometry in simulation with Dirichlet boundary conditions.

By averaging the captured protein on the different surfaces we see that cross-contamination, i.e. captured protein on the adjacent micro-well, is negligible (see figure 3.37). Next, we compare the amount of protein captured on the bottom of the micro-well with the amount that diffused away. To approximate the amount of protein that diffused away, we integrate the amount of protein in the medium. In figure 3.38, we see that most of the protein is captured on the bottom.

Next we test the exactly same model using Neumann boundary conditions for the edges of the volume of the medium. The parameter values for this second simulation are shown in

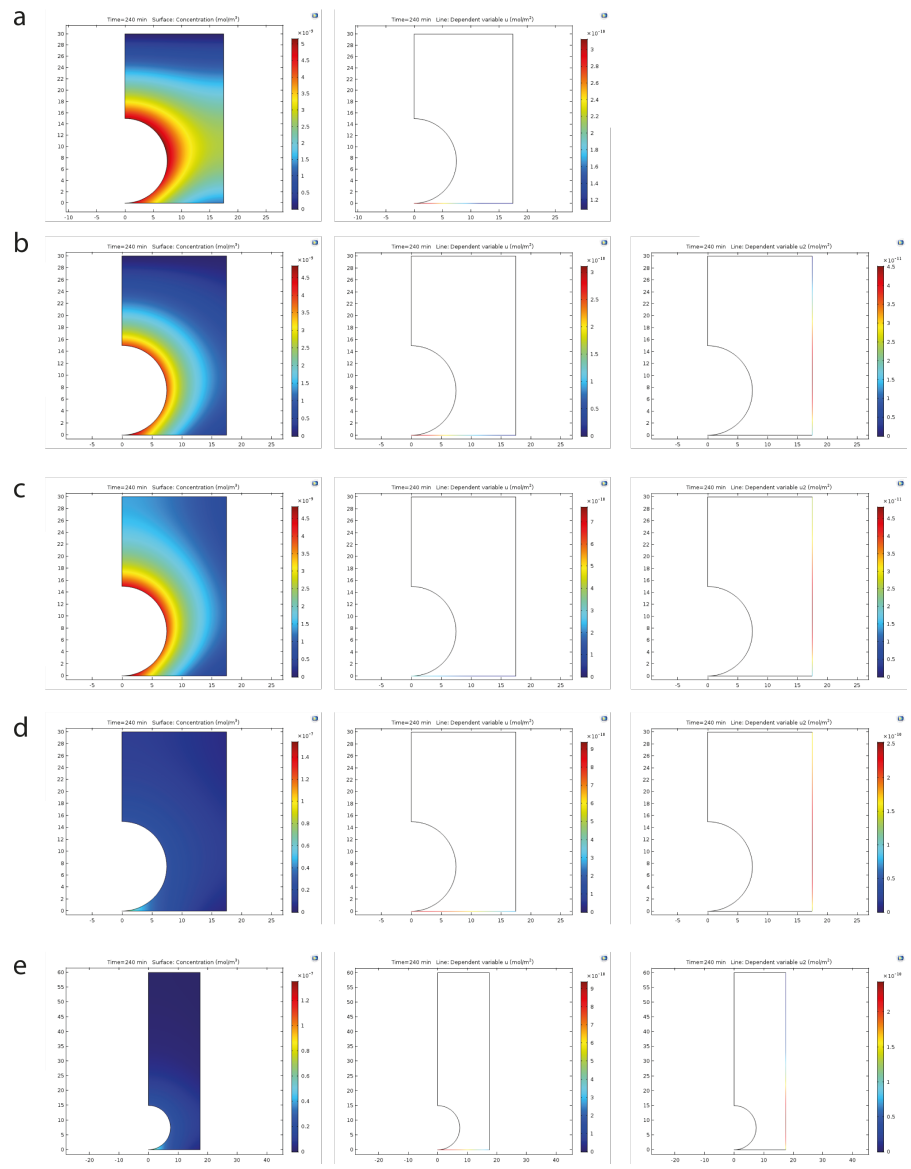

Figure 3.34: Spatial distribution of the secreted protein concentration after 4 hours of secretion, in the micro-well volume (left image), at the bottom of the micro-well (middle image) and at the micro-well wall (right image), (a) for simulation 1, (b) for simulation 2, (c) for simulation 3, (d) for simulation 4, and (e) for simulation 5.

table 3.10. The amount of captured protein on each different surface of the model (see figure 3.39) does not reach a plateau in this case, while the amount captured on the bottom of the micro-well is much less than the amount that diffused away (figure 3.40). From the above, we observe that the results are quite sensitive on the boundary condition used and thus selecting the most proper one is not trivial.

From the above results, the sensitivity of the results on the boundary condition used at the edges of the medium is obvious. The amount of secreted protein captured on the bottom is affected by the boundary condition chosen. For instance, when the Dirichlet boundary condition is used, it appears that more protein is captured on the bottom and less escapes in the bulk (see figure 3.38), while when the Neumann boundary conditions are used more protein escapes and

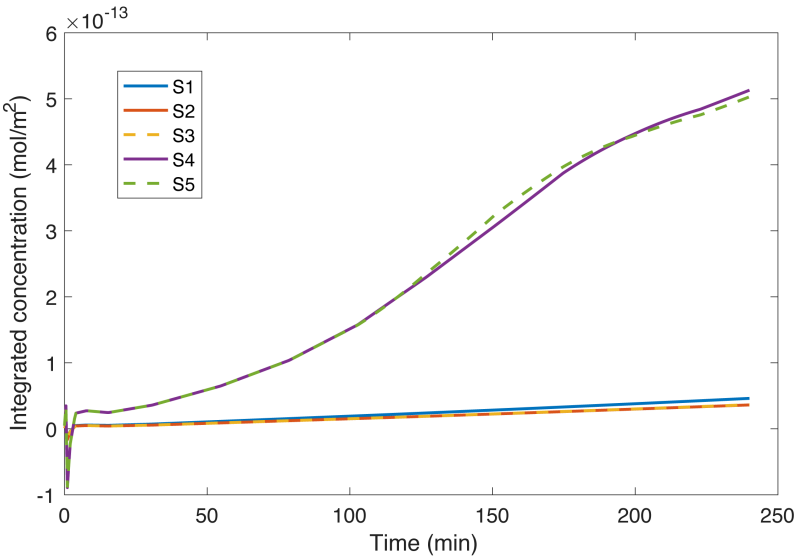

Figure 3.35: Secreted protein captured on the bottom of the micro-well as calculated in 5 different simulations. The most important parameter is the secretion rate of the cell.

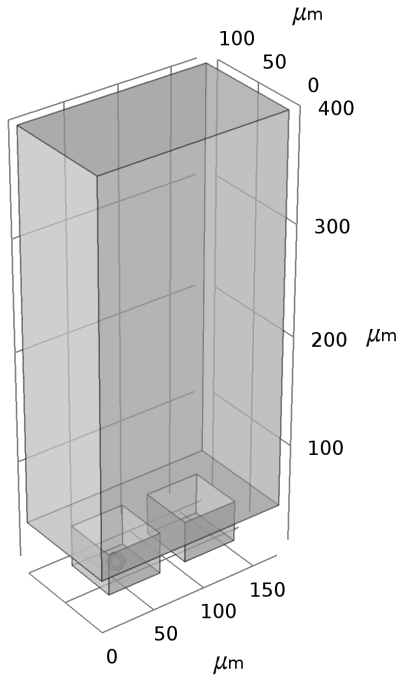

Figure 3.36: Geometry of the 3D open micro-well model.

less is captured on the bottom of the micro-well (see figure 3.40). Moreover, when the Dirichlet boundary conditions are used, we have an artefact, the concentration of the captured protein on any surface reaches a plateau after 4 hours, without saturating the available binding sites on the surfaces (see figure 3.37). Also, we observe that the absolute number of the concentration captured on the bottom of the micro-well is lower than when using Neumann boundary condi-

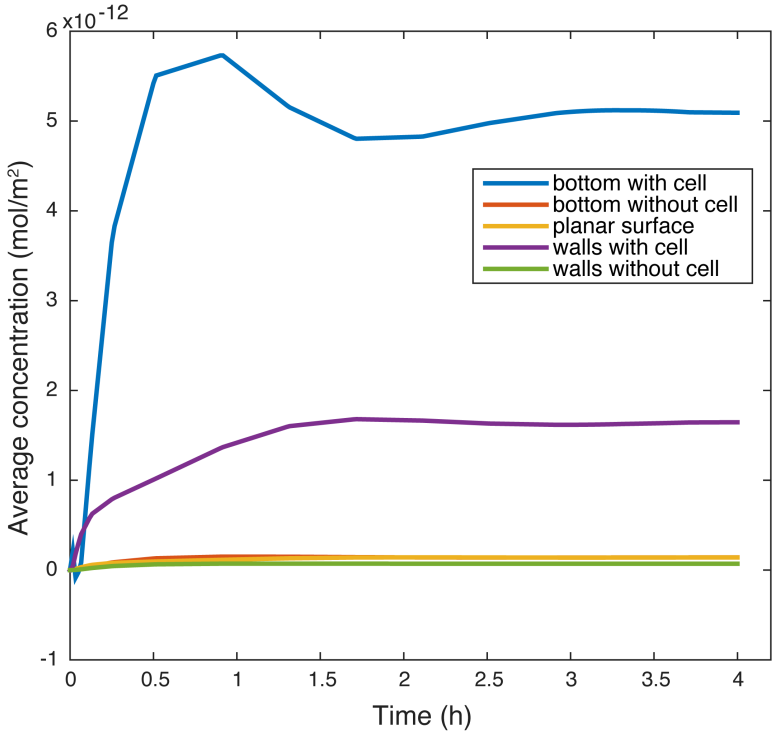

Figure 3.37: Average surface concentration over time on the different surfaces of the model with parameters presented in table 3.9. Most of the captured protein is on the bottom of the micro-well with the cell (blue curve) and a significant amount is also captured on the walls of the same micro-well. The amount of protein captured on the planar surface and in the adjacent micro-well is negligible. On the bottom of the micro-well with the cell, 0.5% of the total binding sites are occupied. 50 molecules/s that we test here is the theoretical maximum secretion rate of a cell that secretes cytokines.

Parameter	Simulation 1
Cytokine secretion (molecules/s)	50
Upper boundary condition of medium	$\nabla C = 0$
Side boundary conditions of medium	$\nabla C = 0$
Micro-well wall boundary condition	half binding sites
Medium volume height (μm)	400
K_d (nM)	10
Time (h)	4

Table 3.10: Parameter values for the 3D geometry in simulation with Neumann boundary conditions.

tions (see figures 3.38, 3.40). This means that the Dirichlet boundary condition acts like a sink which adsorbs the proteins strongly, or at least at a comparable level with the antibodies on the surface. This is not true and as a result using Dirichlet boundary conditions does not lead to a model that captures sufficiently the phenomenon.

Next, we test a combination of the Neumann and Dirichlet boundary conditions, i.e. at

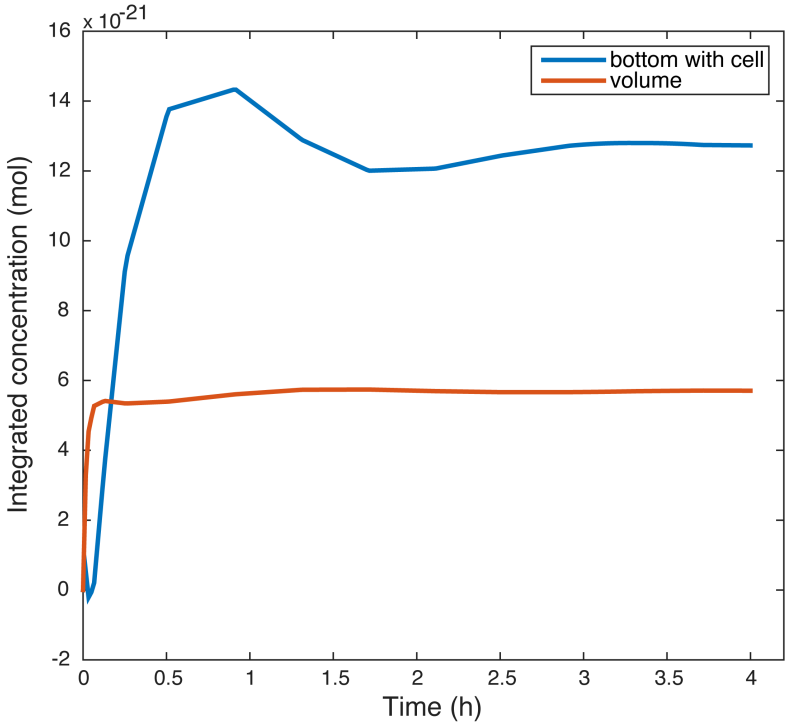

Figure 3.38: The captured protein on the bottom of the micro-well over time is plotted (blue curve) together with the unbound free protein in the volume (orange curve). The amount of protein captured on the bottom is 2.2 times higher than the free unbound protein.

the side edges of the medium we used Neumann boundary conditions while at the upper edge we used the Dirichlet boundary conditions with the assumption that the concentration of the protein far from the cell is negligible. The parameter values for this third simulation are shown in table 3.11. The amount of captured protein on each different surface of the model (see figure 3.41), now reaches a plateau the same as when only Dirichlet boundary conditions are used (see figure 3.37). However, in this case the amount captured on the bottom of the micro-well is much less than the amount that diffuses away, (figure 3.42), same as when only Neumann boundary conditions are used (figure 3.40). From the above, we observe again that the results are quite sensitive on the boundary condition used and thus selecting the most proper one is not trivial.

Using this model, which combines Neumann and Dirichlet boundary conditions, we test the next two very important parameters i.e. the affinity of the capture antibody to the secreted protein and the cell secretion rate. Here we test an antibody with higher affinity for the secreted protein, i.e. with lower Kd value. Also we use lower secretion rate, 5 molecules/s, which the lowest theoretical rate for cytokine secretion. The parameter values for this simulation are shown in table 3.12. In this case, although some numerical instabilities at the first time points, the amount of protein captured on the bottom is more than the one escaped in the bulk (see figure 3.43), indicating the importance of the affinity of the antibody and the cell secretion rate.

Next, using the higher affinity antibody we test the higher secretion rate i.e. 50 molecules/s. However, the results are not reliable due to very high numerical instabilities which led to negative concentrations on the bottom of the micro-well. These numerical instabilities are most probably due to the fact that our sink is very close to our source, i.e. the cell that secretes the proteins

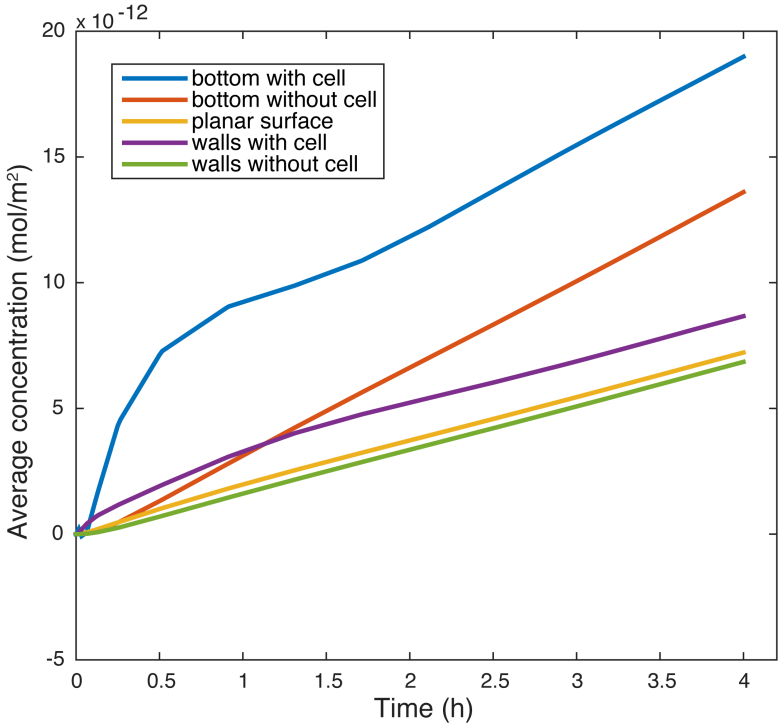

Figure 3.39: Average surface concentration captured over time on the different surfaces of the model (Neumann boundary conditions, see parameter values in table 3.10). Here the differences are not that pronounced as in the previous model (Dirichlet boundary conditions, see parameter values in table 3.9).

Parameter	Simulation 1
Cytokine secretion (molecules/s)	50
Upper boundary condition of medium	$C = 0$
Side boundary conditions of medium	$\nabla C = 0$
Micro-well wall boundary condition	half binding sites
Medium volume height (μm)	400
K_d (nM)	10
Time (h)	4

Table 3.11: Parameter values for the 3D geometry in simulation with both Neumann and Dirichlet boundary conditions.

sits on the bottom of the micro-well, on which proteins bind on the antibodies, resulting in very high gradients. Also, the geometry cannot be differentiated, since we have a sphere on a surface. These arithmetic instabilities, caused by the above reasons, are prominent when we reduce the Kd of the antibody i.e. when our sink gets stronger.

For the above reasons we conclude that more accurate calculations are needed and that the assumption of negligible protein concentration far from the cell (i.e. Dirichlet boundary conditions at the upper edge of the medium) is not enough for reliable and quantitative results.

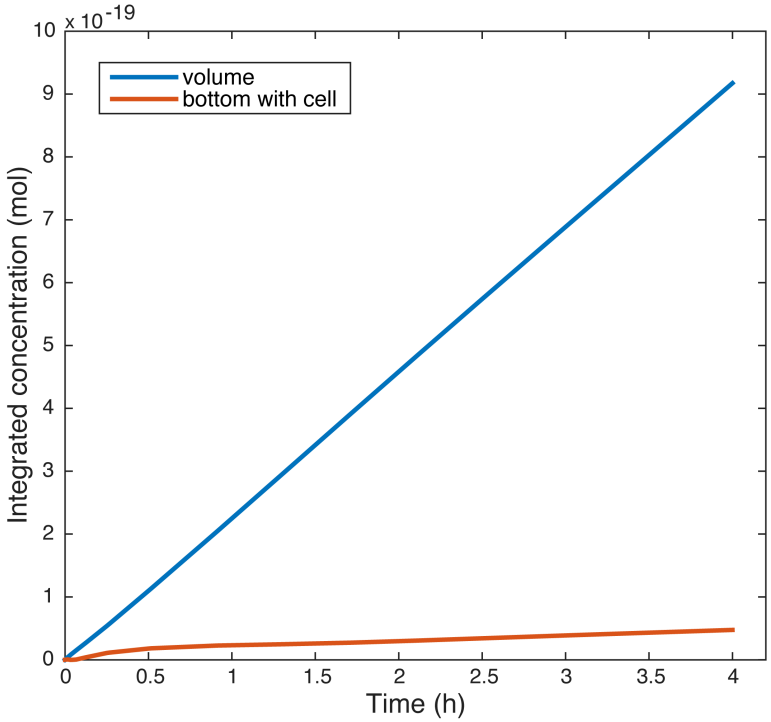

Figure 3.40: The captured protein on the bottom of the micro-well over time is plotted (orange curve) together with the unbound free protein in the volume (blue curve), for the model with Neumann boundary conditions, see parameter values in table 3.10. At the last time point the amount of protein bound on the surface is 5.1% the amount of the free unbound protein.

Parameter	Simulation 1
Cytokine secretion (molecules/s)	5
Upper boundary condition of medium	$C = 0$
Side boundary conditions of medium	$\nabla C = 0$
Micro-well wall boundary condition	half binding sites
Medium volume height (μm)	400
K_d (nM)	0.1
Time (h)	6

Table 3.12: Parameter values for the 3D geometry in simulation with both Neumann and Dirichlet boundary conditions.

For that we use a much smaller time step and the finest possible mesh in order to avoid arithmetic instabilities. Since these calculations are demanding we use a fairly small geometry (see figure 3.44) and we calculate for 60 min. The parameter values used in these simulations are presented in table 3.13.

Indeed, the above strategy leads to meaningful results, which are summarised below. The Kd value of the antibody determines how much of the secreted protein will be lost by diffusion. If the antibody has a Kd value of 10 nM (affinity at nanomolar range) the quantity of the lost

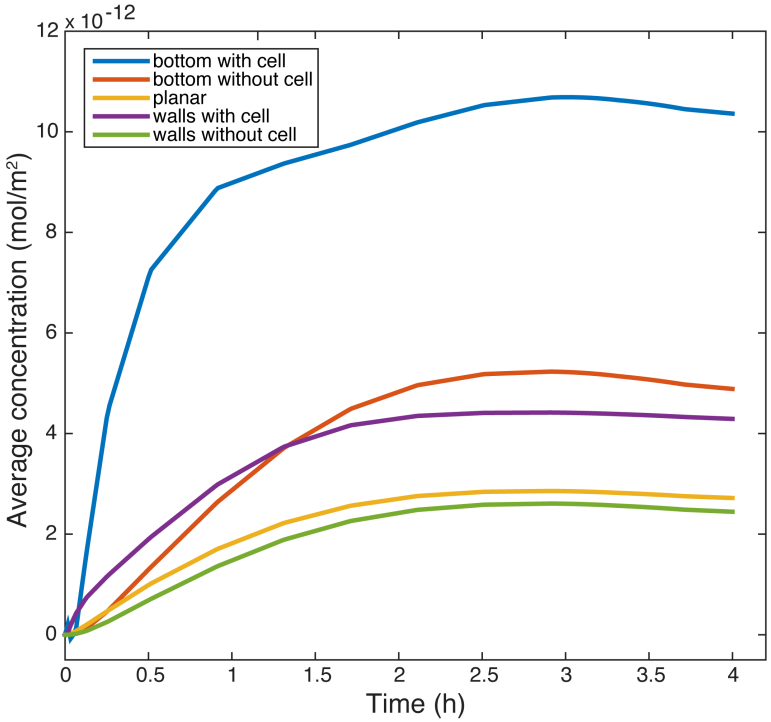

Figure 3.41: Average surface concentration captured over time on the different surfaces of the model with Neumann boundary conditions at the side edges of the medium and Dirichlet boundary conditions at the upper edge of the medium (see parameter values in table 3.11). Here a plateau is reached but slower than in the first model (Dirichlet boundary conditions, see parameter values in table 3.9).

Parameter	Simulation 1
Cytokine secretion (molecules/s)	5 or 50
Upper boundary condition of medium	$\nabla C = 0$
Side boundary conditions of medium	$\nabla C = 0$
Micro-well wall boundary condition	half binding sites
Medium volume height (μm)	150
K_d (nM)	0.1 or 10
Time (h)	1

Table 3.13: Parameter values for the smaller 3D geometry in simulations with Neumann boundary conditions.

protein is 6 times more than the captured one (see figure 3.45). On the other hand, if the antibody has a Kd value of 0.1 nM (affinity at picomolar range) the amount of protein captured on the bottom is 15 times more than the amount lost by diffusion (see figure 3.46). In the case of antibody with Kd value of 0.1 nM and cell secretion rate of 50 molecules/s, the surface distributions of the captured protein are shown in figure 3.47.

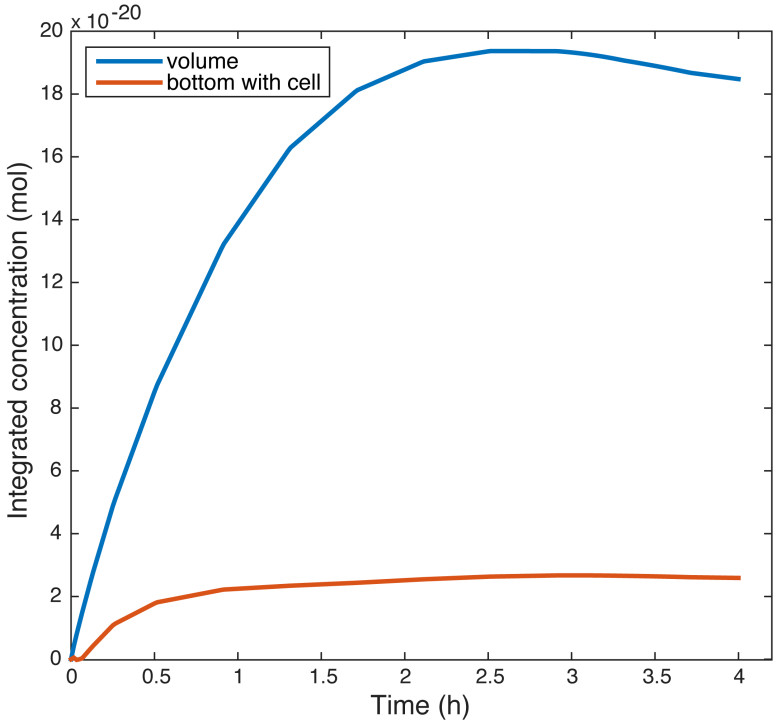

Figure 3.42: The captured protein on the bottom of the micro-well over time is plotted (orange curve) together with the unbound free protein in the volume (blue curve), for the model with Neumann boundary conditions at the side edges of the medium and Dirichlet boundary conditions at the upper edge, see parameter values in table 3.11. At the last time point the amount of protein bound on the surface is $\sim$ 14% the amount of the free unbound protein. Here we observe saturation also in the volume.

Closed well model

Herein, we compare the results of an open array, presented above, with the closed arrays for detection of single-cell secretion events (such as the microengraving method [36]). In this case, our model compromises a cubic micro-well, as tested above for the open array model, with dimensions 50×50×50 μm (see figure 3.48). The micro-well is closed with a glass slide coated with *capture* antibodies. In the case of the closed array, PDMS is used to make the micro-wells, which is then coated with BSA to both prevent passive adsorption of the capture antibodies on it and to prevent cells from sticking on it. For this reason, the micro-well walls are modelled without any antibodies coated on them. The equations of the model remain the same as in the previous models (see section 3.4.1). Similarly, we assume that the initial concentration (at $t = 0$) of free (C) or bound protein (C_s) are negligible ($C = 0$, $C_s = 0$). The tested K_d values are again 0.1 and 10 nM and various secretion rates close to the range of cytokine secretion (5 to 50 molecules/s) are tested.

An exemplary distribution of the concentration of the captured protein on the glass slide on top of the micro-well is shown in figure 3.49. The average concentration of captured protein on the glass surface on top of the micro-well after 4 hour of constant secretion is presented in figures 3.50 and 3.51 for K_d values 0.1 and 10 nM respectively. Obviously, higher captured concentrations are observed in the case of the antibody with higher affinity (K_d= 0.1 nM).

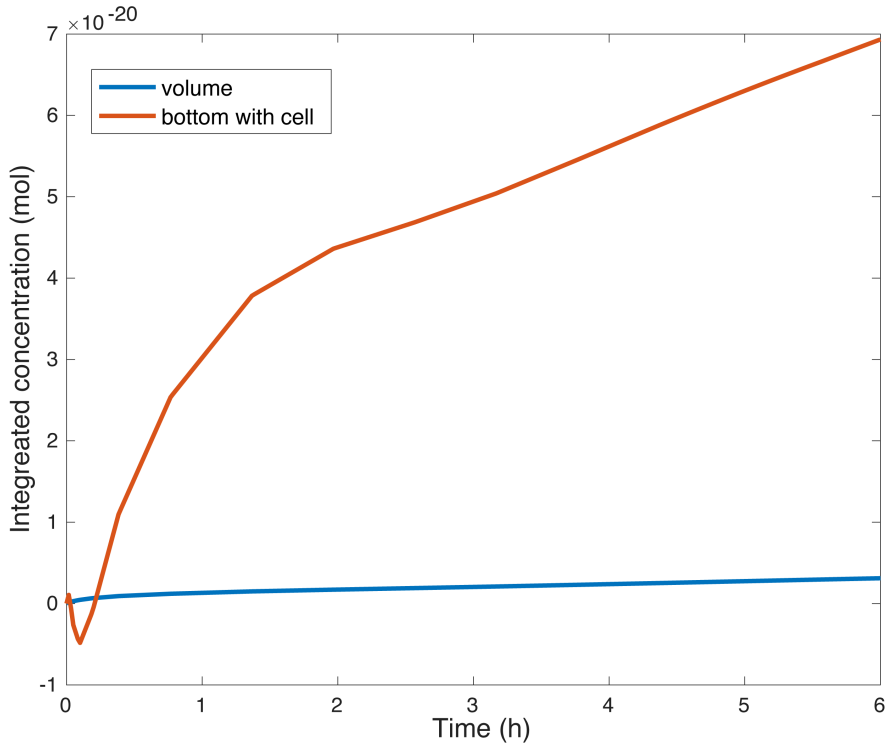

Figure 3.43: The captured protein on the bottom of the micro-well over time is plotted (orange curve) together with the unbound free protein in the volume (blue curve), for the model with Neumann boundary conditions at the side edges of the medium and Dirichlet boundary conditions at the upper edge, see parameter values in table 3.12. At the last time point the amount of protein bound on the surface is larger than the amount of the free unbound protein.

In the same way as in the open array configuration, we compare the amount of protein captured on the glass with the secreted unbound protein still in the medium inside the micro-well volume. For the closed array the amount captured on the glass slide is always higher than the free unbound protein (see figure 3.52 for Kd value of 0.1 nM and 3.53 for 10 nM).

In table 3.14, the ratio of the captured concentration on the bottom vs the concentration of the unbound protein in the volume are summarised for both the open and the closed array. It is now evident that the most important parameter for the open array is the affinity of the capture antibody (K_d value) but for the closed array the most important parameter is the cell secretion rate.

3.4.4 Comparison with the experimental results

With the above simulation results at hand the question that arises is whether it is possible to detect cytokines secreted by a single cell in an open well format (or open array format). Let's test our worst case scenario, we have a cell that secretes at a very low rate (5 molecules/s) but we have a capture antibody with a K_d value of 0.1 nM. In one hour, based on the above simulations (parameters in table 3.13), the captured concentration at the bottom of the micro-well will be 1.5235×10^{-10} mol/m^2 or 92 molecules/μm^2, which is below our detection limit in a safe scenario (200 molecules/μm^2, see section 3.3.4). If the K_d of the capture antibody is

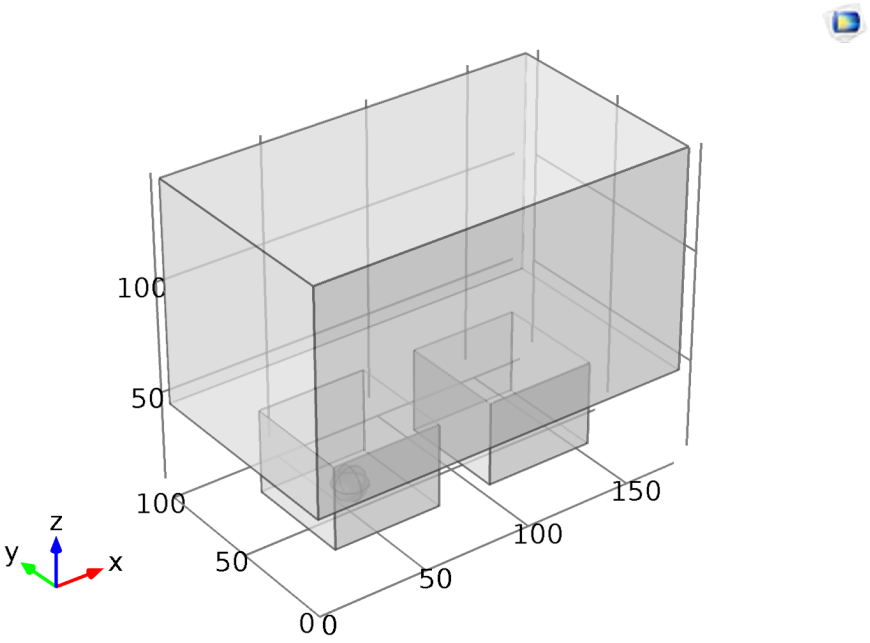

Figure 3.44: Smaller 3D geometry.

$\frac{[captured]}{[unbound]}$	Open array	Closed array
K_d = 10 nM, 5 molecules/s	0.16	87
K_d = 10 nM, 50 molecules/s	0.16	55
K_d = 0.1 nM, 5 molecules/s	15	87
K_d = 0.1 nM, 50 molecules/s	15	55

Table 3.14: Ratio of the captured protein concentration on the glass surface vs the free unbound protein in the medium volume for open and closed arrays. The ratios were calculated based on the simulation results.

10 nM then in one hour, we will have 1.0867×10^{-12} mol/m^2 captured protein on the bottom, which is 0.65 molecules/μm^2, and thus we need to wait at least 77 to 308 hours for a detectable signal (depending on how we set our sensitivity limit, best case scenario or safe, see section 3.3.4).

Now, for the Jurkat cells we had at hand, if we assume uniform secretion among the population, every cell secretes 15,000 molecules per hour (calculated from the experiments in 3.3.5). If a Jurkat cell is in a cubic (50×50×50 μm) micro-well, we will have 6 molecules/μm^2 captured proteins in one hour, which means that with a capture antibody with a K_d value of 0.1 nM we need 9 hours (or 36 hours for the safe scenario) for a detectable signal, while for a K_d of 10 nM we need 50 hours (or 200 hours for the safe scenario).

3.4.5 Conclusion and Outlook

In this chapter a single-cell secretion assay based on micro-well arrays in combination with ELISA was developed. Two main formats were studied, an open micro-well and a closed micro-

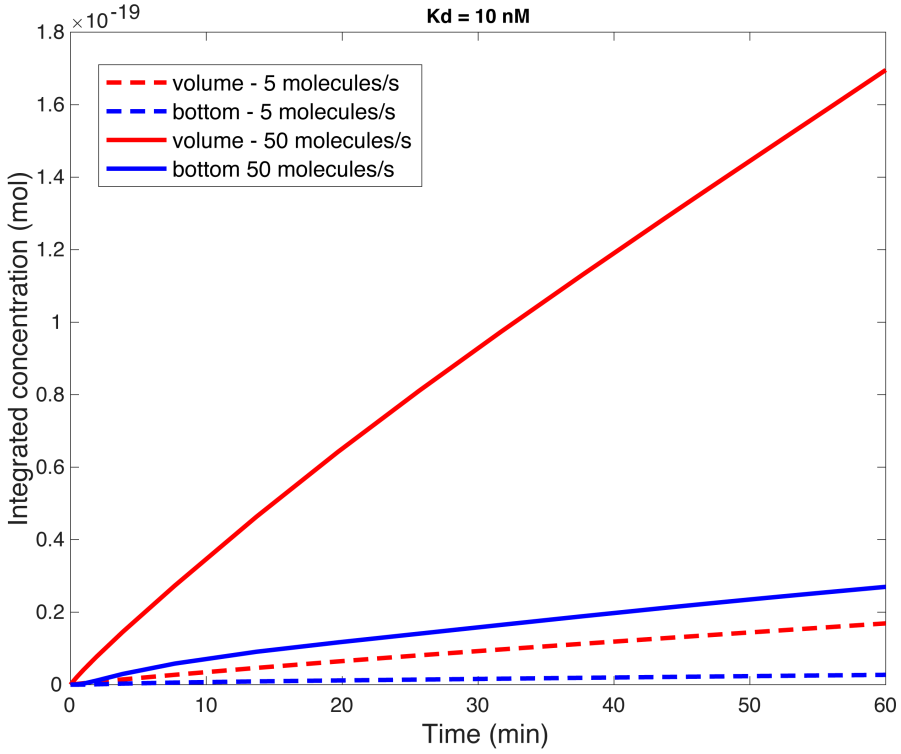

Figure 3.45: For a *capture* antibody at the nanomolar range (Kd = 10 nM), the secreted protein captured on the bottom of the micro-well (blue curves) is 6 times less than the amount of protein lost by diffusion (red curves). Solid lines correspond to a cell secretion rate of 50 molecules/s, while dashed lines correspond to 5 molecules/s.

well format. Herein, we focused on the open micro-well format as it has certain key advantages, such as the potential for (i) a dynamic readout of secretion events, (ii) longer observation times and also (iii) adding any additional factor during the course of the readout.

Our first approach was to capture the secreted protein at the bottom of the micro-well. However, it was challenging to detect the small amounts of proteins that are within the range of the used sandwich ELISA format (see section 3.3.4). Due to the autofluorescence of the micro-well material (PEG-DA), during epi-fluorescence illumination stray light creates an enhanced background noise that interferes with the signal. Detection with TIRF illumination was also challenging mainly due to the fast bleaching of the fluorophores (see section 3.3.4). Capturing the secreted protein at the surface of the secreting cell, proved to be a more sensitive approach leading to detectable signals (see section 3.3.5), thus we were able to detect in a dynamic fashion the secretion of IL-2 from Jurkat cells. Our current experimental setup offers the potential to monitor up to 12,000 single-cells in parallel in one single measurement that can comprise up to 8 different conditions.

We then performed numerical simulations using FEM to better understand the diffusive transfer properties inside our open micro-well setup and to compare the amount of captured protein with the closed micro-well format. We realized that the boundary conditions in our model strongly affect the results, and we concluded that the Neumann boundary conditions ($\nabla C = 0$) better describe our problem of how the secreted protein distributes. Based on this model, we found that in the open-well format the affinity of the capture antibody greatly

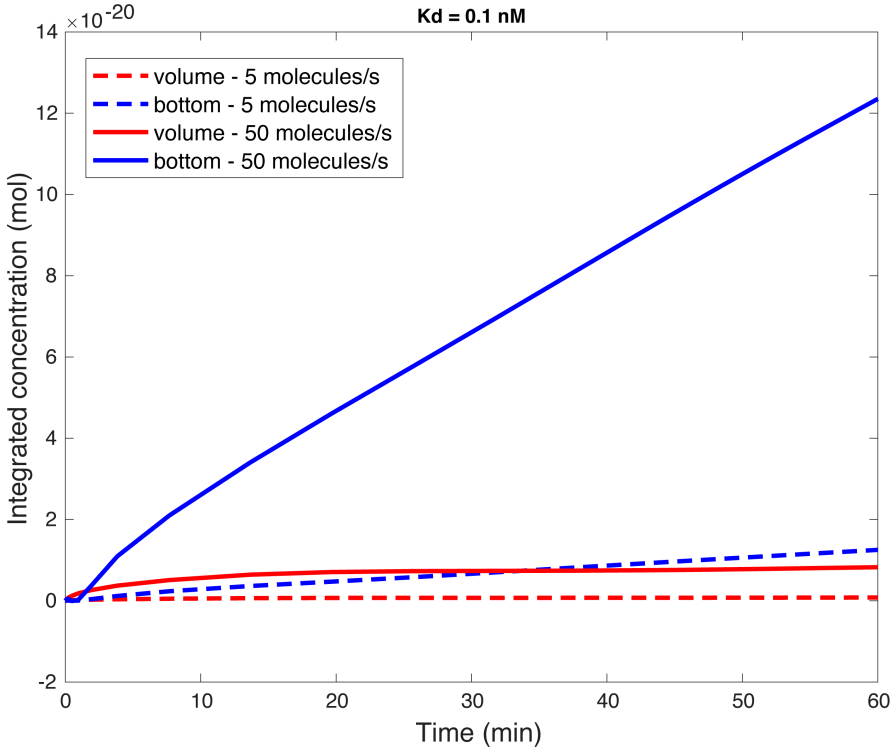

Figure 3.46: For a *capture* antibody at the picomolar range (Kd = 0.1 nM), the secreted protein captured on the bottom of the micro-well (blue curves) is 15 times more than the amount of protein lost by diffusion (red curves). Solid lines correspond to a cell secretion rate of 50 molecules/s, while dashed lines correspond to 5 molecules/s.

determines the concentration of the captured protein and hence the amount of the protein that escaped the micro-well due to diffusion. When antibodies in the nanomolar range are used the amount of protein lost is 6 times greater than the one captured, while for antibodies in the picomolar range the amount of protein captured on the bottom is 15 times greater than the amount lost by diffusion. On the other hand, for the closed micro-well format, in which the secreted proteins are captured on the top surface of the micro-well, for a capture antibody in the nanomolar range, the amount of protein captured is 55 times greater than the amount of the unbound protein. Nevertheless, the most important parameter for the amount of protein captured in the closed micro-well format is the cell secretion rate.

Detecting secreted proteins at the single-cell level is of great importance for a variety of different applications, but especially for highly heterogenous response such as in the case of immune cells. For instance, a single-cell secretion assay can provide useful data to investigate the mechanism of IL-1β secretion from monocytes, which is still an open question [216–218] besides its central role during inflammation [219]. NK cells, another class of immune cells, interrogate target cells and either lyse them or secrete inflammatory cytokines. A single-cell secretion assay can shed light on the functional responses of NK cells [39, 40] i.e. whether an NK cell can both lyse a target and secrete a cytokine or whether it biases towards one function only.

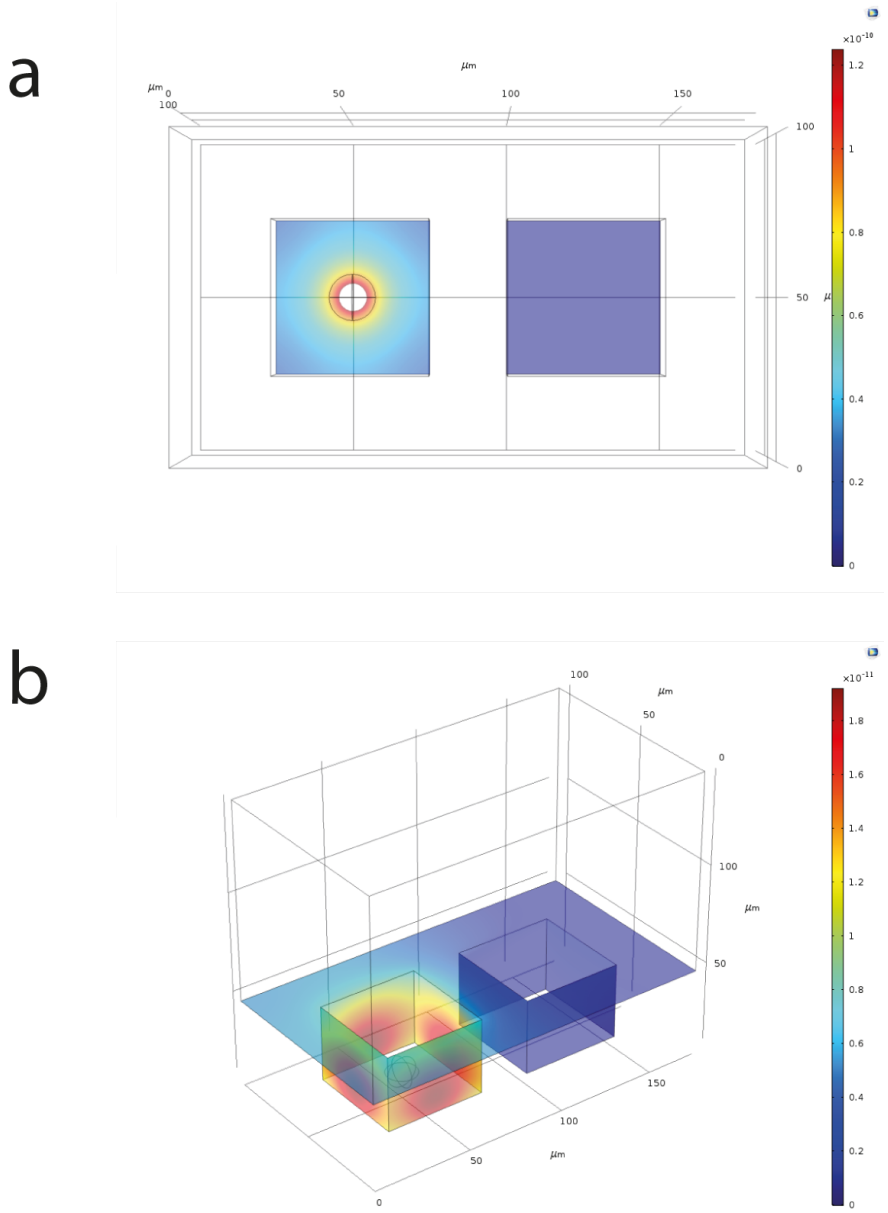

Figure 3.47: Surface distributions of the captured protein for a *capture* antibody with Kd value of 0.1 nM and cell secretion rate of 50 molecules/s. (a) Top view of the model: captured protein distribution at the bottom of the micro-wells. No cross-contamination to the adjacent micro-well is observed (b) Captured protein distribution at the walls of the micro-wells and the planar surface.

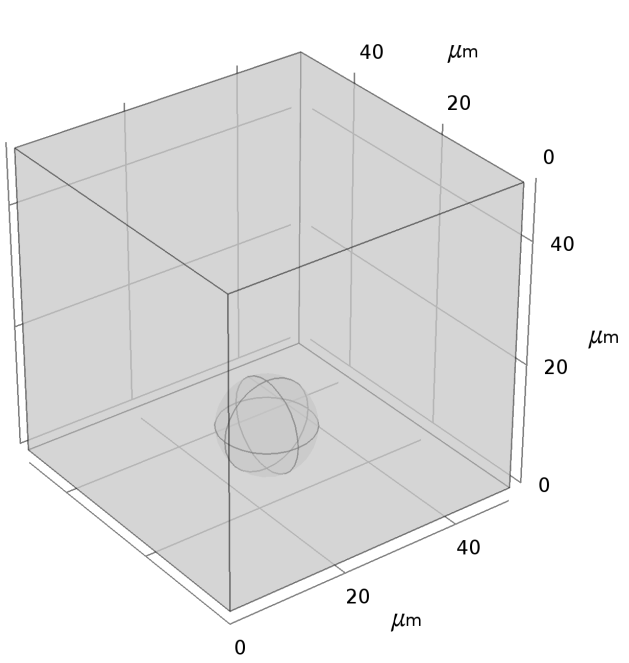

Figure 3.48: Geometry of the closed array model.

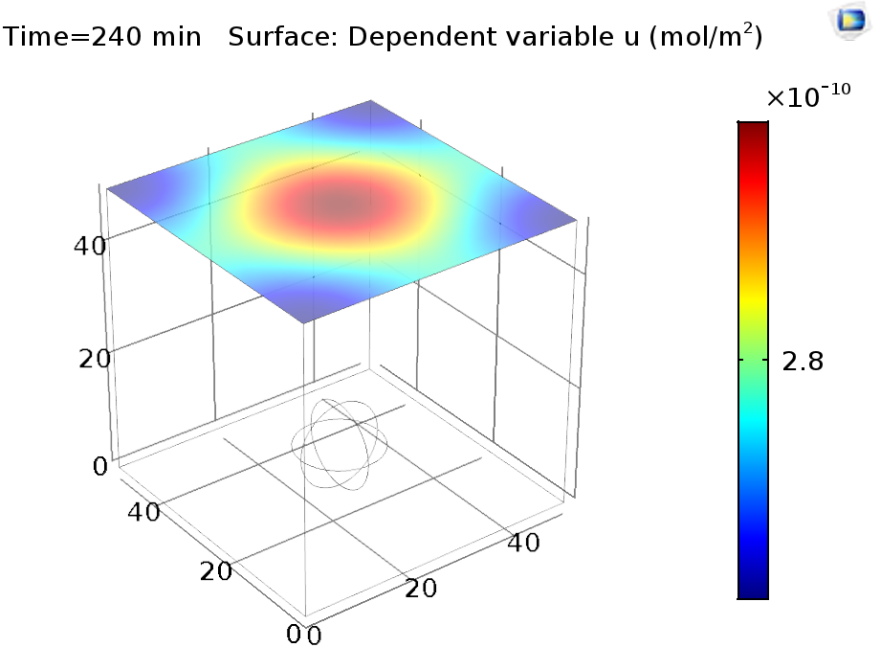

Figure 3.49: Distribution of the captured protein on the glass surface on top of the micro-well, for secretion rate 50 molecules/s and K_d value of the capture antibody equal to 10 nM.

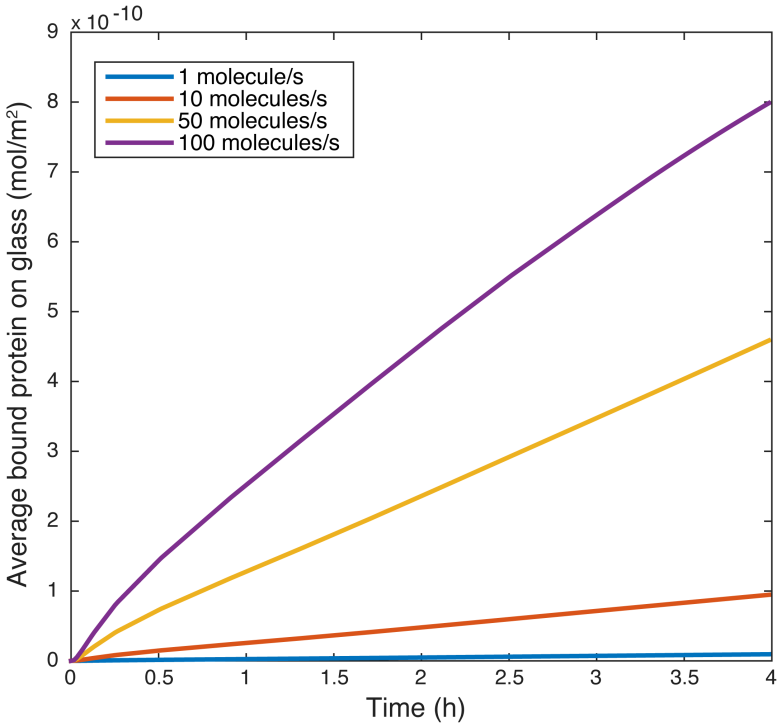

Figure 3.50: Captured protein on the glass surface on top of the micro-well. The glass surface is coated with antibodies with $K_d = 0.1$ nM, different secretion rates at the range of cytokine secretion are plotted.

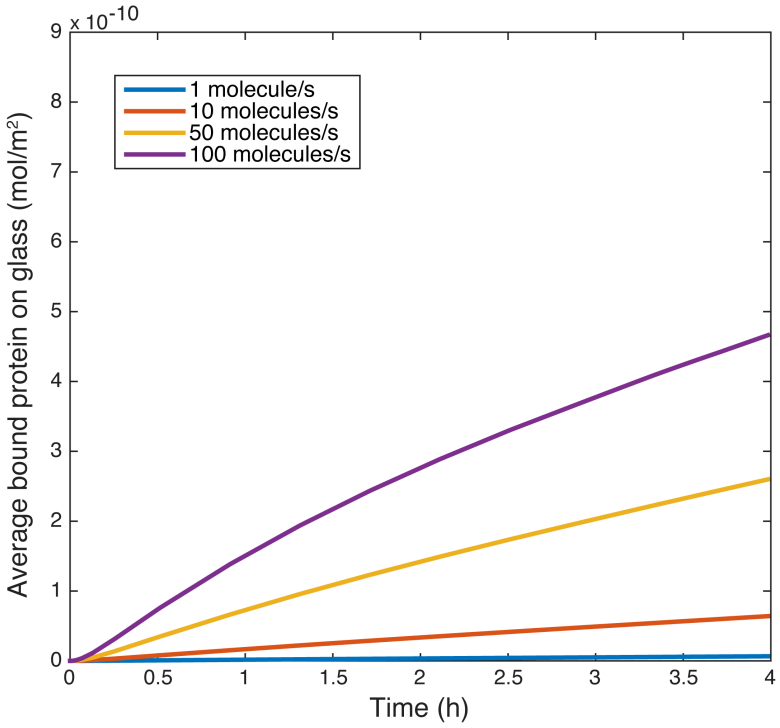

Figure 3.51: Captured protein on the glass surface on top of the micro-well. The glass surface is coated with antibodies with $K_d = 10$ nM, different secretion rates at the range of cytokine secretion are plotted.

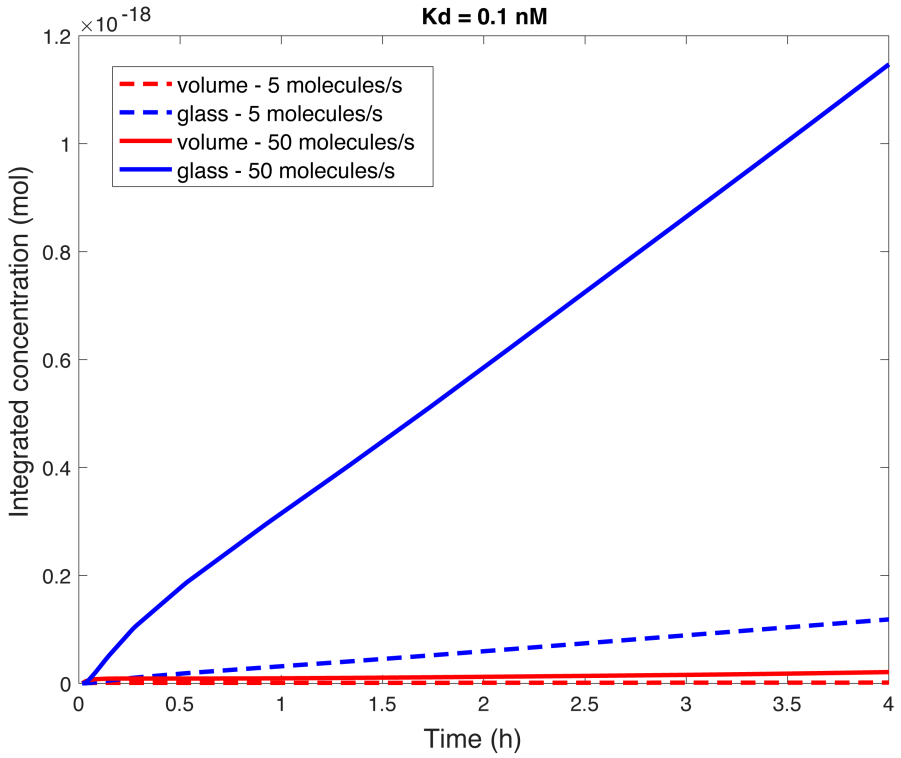

Figure 3.52: In a closed array, for a *capture* antibody at the picomolar range (Kd = 0.1 nM), the secreted protein captured on the glass on top of of the micro-well (blue curves) is higher than the amount of free unbound protein in the micro-well volume (red curves). Solid lines correspond to a cell secretion rate of 50 molecules/s, while dashed lines correspond to 5 molecules/s.

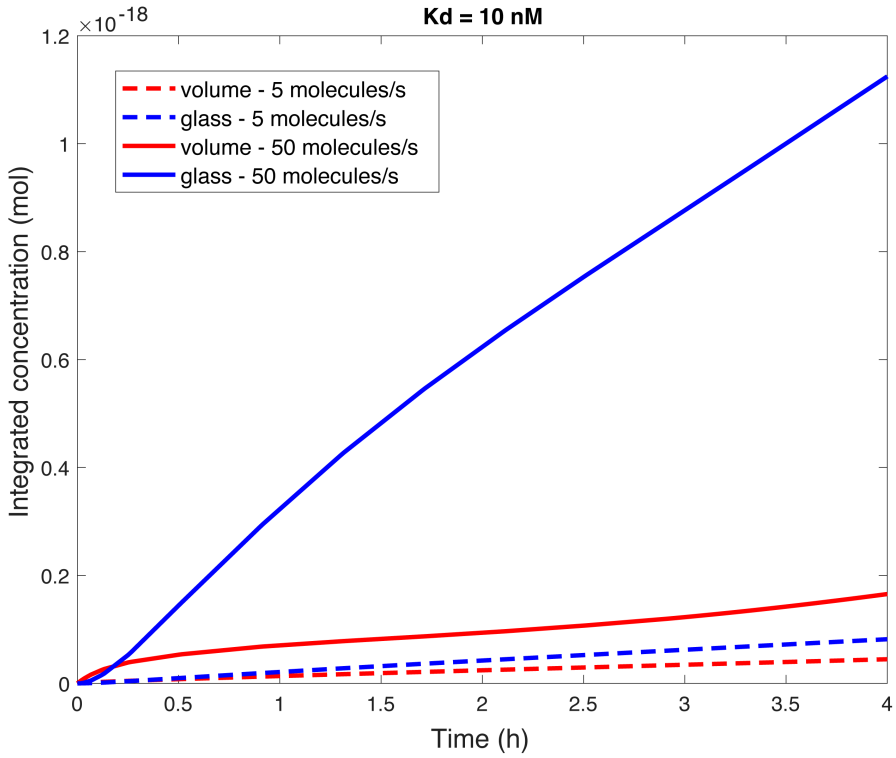

Figure 3.53: In a closed array, for a *capture* antibody at the nanomolar range (Kd = 10 nM), the secreted protein captured on the glass on top of the micro-well (blue curves) is higher than the amount of free unbound protein in the micro-well volume (red curves). Solid lines correspond to a cell secretion rate of 50 molecules/s, while dashed lines correspond to 5 molecules/s.

Chapter 4

Application in Cancer Immunotherapy

4.1 Cancer immunotherapy basic concepts

Mutations in the genome can result in the transformation of a normal cell to a tumour cell. Our bodies possess both *internal-* and *external-checking systems* to monitor what happens in our cells [220]. The *internal-checking system* comprises mostly of tumour suppressor genes, that suppress tumour cells in a process called *programmed cell death* or *apoptosis*. In essence, cells are programmed to die if any mutations are detected in their genes. If the tumour cells escape the internal check they will face the *external-checking system* mediated by the immune system. *Cancer immunotherapy* refers to any type of therapy that uses substances to stimulate the immune system to help the body fight cancer. Types of immunotherapy include cytokines, vaccines, and monoclonal antibodies or antibody derivatives.

Our immune system is able to detect even tiny changes in cells, by using receptors on their surface that specifically bind to certain molecules. Usually these molecules are proteins expressed by tumour cells. Tumour cells bear a lot of abnormal proteins due to errors in the genome, or due to uncontrolled production of certain proteins that should have stopped being expressed at earlier stages of cell maturation. Immune cells patrol our body and when they detect cells with such transformed proteins, they are activated and eventually lyse the tumour cell. Provided that our immune cells can recognise tumour cells, tumour cells cannot accumulate and develop into a disease. Indeed, cancer can be described as a disease caused by unlimited growth of tumour cells that escaped the immune system.

The idea of immunotherapy was first introduced in the 19th century when William Coley, today acknowledged as the "Father of Immunotherapy", attempted to utilise the immune system for treating cancer [221]. He injected mixtures of live and inactivated Streptococcus pyogenes and Serratia marcescens into patients and achieved even complete remission in several types of malignancies, including sarcoma, lymphoma, and testicular carcinoma. However, the lack of a known mechanism of action for "Coley's toxins" and the risks of infecting cancer patients with pathogenic bacteria caused oncologists to adopt surgery and radiotherapy as standard treatments early in the 20th century [222]. The idea of immunotherapy in cancer drew attention again when Thomas and Burnet first proposed the theory of *cancer immunosurveillance* in 1957 [223]. In the 1970s, Milstein and Koehler were the first to produce monoclonal antibodies in the laboratory. They used hybridomas, antibody-secreting cell lines formed by the fusion of lymphocytes with myeloma cell lines, which facilitated the use of antibodies in cancer immunotherapy [224]. Rituximab was the first monoclonal antibody approved by the FDA for the treatment of a cancer, non-Hodgkin's lymphoma, and was introduced in 1997. Rituximab

binds to CD20 on the surface of immature B cells and targets them for elimination by natural killer cells (NK cells) [225]. In conclusion, immunotherapy regimens do not directly kill cancer cells but enhances the immune system to recognise and eliminate them.

4.2 Cytotoxic immune cells

The main types of cytotoxic cells in our organism are the cytotoxic T-lymphocytes (CTL), the natural killer (NK) cells and macrophages [226]. All of these cells can lyse malignant host and foreign cells but they vary regarding their origin, phenotype, morphology and target cell specificity. CTL cells play a critical role during the *adaptive immune response*. Adaptive immune cells in general have a very limited specificity in recognising their targets and usually have a delayed response since they need time to proliferate and produce the essential molecules to attack their targets. CTLs recognise specific antigens presented together with molecules of class I major histocompatibility complex (MHC). They contain typical lysosomal granules and express a characteristic pattern of surface molecules. On the other hand, macrophages and NK cells are a part of the *innate immune response*. Innate immune cells lack precise specificity in recognising their targets but they respond fast against them. They recognise target cells based on the general patterns of molecules expressed by target cells or pathogens. In the study described in this chapter, NK cells were used as effector cells and they will be described in more detail in the following section.

Natural Killer cells

NK cells recognise and eliminate infected and cancerous cells. All the cells in our body, except from red blood cells, bare on their surface certain molecules called MHC-I. Infected and cancerous cells usually stop expressing this molecular complex. NK cells recognise these cells, form a specific one-to-one immune synapse with them, and ultimately eliminate them mainly through the perforin/granzyme pathway [227, 228]. Perforin is a membrane-disrupting protein that creates pores on the plasma membrane of the target cell [229,230]. Granzymes are a family of structurally related serine proteases with various substrate specificities. They are released by cytoplasmic granules and induce the apoptosis of the target cell either through the activation of caspases (apoptotic cysteine proteases), or in the absence of activated caspases [230, 231].

4.3 NK-cell cytolytic activity is enhanced by antibody-derived proteins

Therapeutic antibodies are an established component of current clinical protocols for the treatment of cancer, inflammatory and autoimmune disorders. Used in cancer therapy, they operate essentially through one of the following mechanisms (or combinations of these): perturbation of signaling for proliferation and survival of cancer cells; activation of complement dependent cytotoxicity (CDC); induction of antibody dependent cellular cytotoxicity (ADCC); and induction of an adaptive systemic immune response ("tumor vaccination effect") [232]. So far monoclonal antibodies, antibody-drug conjugates (ADCs), and radio-immunoconjugates (RICs) are the most widely used formats, quite few of which have received approval for clinical use in oncology [233,234]. These agents can mediate a preferential elimination of tumour cells and at the same time maintain an acceptable toxicity profile by targeting tumours through tumour-specific or tumour-associated antigens. Although unmodified antibodies in the classic immunoglobulin (IgG) format have been successful for selected types of cancer, including certain types of

leukemias, lymphomas and breast cancer, their broader use for solid tumours is limited. Engineering of antibodies has led to the development of more broadly applicable derivatives such as Fc-engineered and glyco-engineered antibodies, ADCs, RCs, bispecific antibodies, tandem diabodies, single-chain triplebodies and a variety of bi- and multi-specific agents [235–238]. Such modified antibody-derived proteins frequently offer advantageous properties and function with increased efficacy and selectivity. Some of these new molecular formats no longer carry the full antigen-binding-domains of classic IgGs (Fv-domains), but employ engineered antibody fragments, termed "single-chain Fragment variables" (scFvs), as recognition domains.

A first member of a class of such agents termed "bispecific tandem diabodies", Blinatumomab, has received drug approval in 2014 [239–242]. These agents carry one scFv domain specific for a target antigen on a tumour cell connected to a second scFv domain specific for a trigger molecule on an effector cell, such as a cytolytic T-lymphocyte or an NK cell. These agents bind in multiple copies to the cancer cell and connect it with an effector cell by formation of a synapse. This leads to an activation of the effector cell and lysis of the target cell. Bispecific tandem diabodies are monospecific for the cancer cell ("mono-targeting") and for the effector cell. An extension of this molecular format are the "single-chain tandem triplebodies" (in short triplebodies), which carry two scFv recognition modules for target antigens on the cancer cell plus one scFv module specific for a trigger molecule on an effector cell. They can be designed to bind either two copies of the same target antigen or one copy of each of two different target antigens on the same cancer cell [243, 244]. The latter "dual-targeting" mode of binding leads to an increased selectivity of lysis of cancer cells bearing both antigens in high combined cell surface density in the presence of other cells carrying the same target antigens, either alone or in combination, but in lower surface density [245]. This enhanced selectivity of lysis is a unique and useful property of dual-targeting triplebodies, not shared with most other cancer therapeutics. Another useful property of this molecular format is the option to design triplebodies for the recruitment of a chosen type of effector cells, such as NK-cells, T-cells or others [246, 247].

Triplebody SPM-2 (33-16-123) was designed for the elimination of acute myeloid leukemia (AML) cells. It carries one binding site for CD16 and two binding sites for the tumor-antigens CD123 and CD33, present on AML cells [244–246] (see figure 4.1). Triplebodies can bind their target cells either mono-valently with only one of the two target binding modules, leaving the other non-engaged, or bi-valently, employing both target binding modules simultaneously. In the latter case, an avidity-like, synergistic effect occurs and the overall affinity for bivalent binding is greater than the combined monovalent affinities of the two component target-specific scFvs. The equilibrium binding constant (K_d) drops by more than 2-fold, indicating co-operativity of binding [243]. For a prototype triplebody the K_d value was about 3-fold lower for the bivalent than for the monovalent binding mode. Surprisingly however, in this case the cytolytic activity was improved by far more than 3-fold. Half-maximum lytic activity was reached for the triplebody at approximately 25-fold lower concentrations than for the corresponding tandem diabodies [243]. The half maximal effective concentrations (EC50) were 4 pM for this triplebody and 110 pM for the corresponding tandem diabody in a redirected lysis (RDL) experiment [243]. It is not clear, how a 3-fold increase in the overall binding affinity (avidity) of a triplebody to the tumour cell, relative to the corresponding tandem diabody, produces a 25-fold reduction in the EC50 concentrations. Possibly the stronger binding leads to the generation of a more intimate, "tighter", less leaky synapse with a more efficient delivery of granzymes and perforins from the effector into the target cell. The efficiency of lysis conceivably could be influenced more by the tightness of the synapse than by the affinity/avidity of binding. Alternatively, dynamic properties of the lytic process may be affected more than proportionally by the increased binding avidity between effector and target cell mediated by the triplebody compared to the tandem

diabody. A parallel between this situation and the case of the Fc-engineered antibodies may be seen, where the increased cytolytic activity of the modified antibodies was explained by a dynamic effect, the "kinetic boosting" of NK cells, a reduction of the average length of time between two consecutive lytic events by the same killer cell [248].

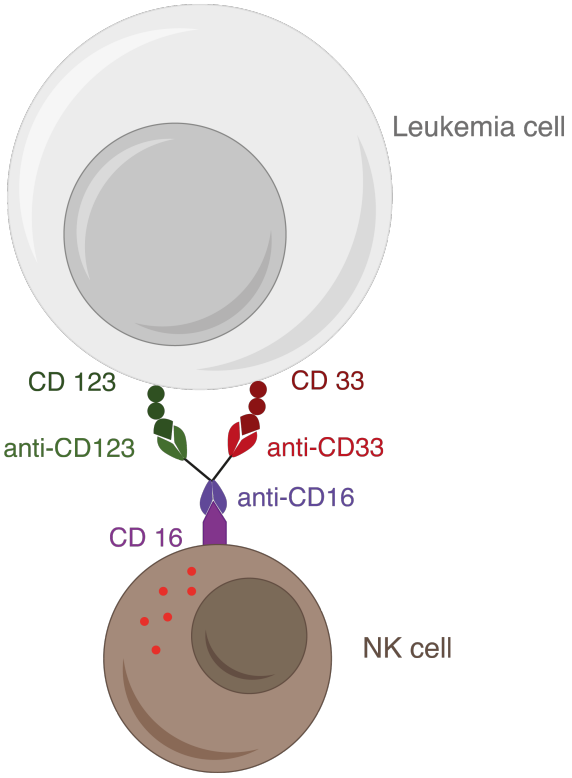

Figure 4.1: SPM-2 triplebody mode of action; SPM-2 carries one binding site for CD16 and two binding sites for the tumour-antigens CD123 and CD33, present on AML cells ("dual-targeting" concept).

4.4 Utilisation of the 2D array to study Natural Killer cell mediated lysis

4.4.1 Conventional assays for measurements of NK-cell activity

Conventional cytolysis assays can be used for this purpose, but they require significant numbers of the effector cells and are limited in the type of information they deliver. Standard bulk assays, such as chromium 51- or calcein-release assays [245, 249, 250], produce statistically valid data, because the results are averaged over approximately 5 x 10^4 target cells in one reaction plus a corresponding number of effector cells, typically used in a 2- to 10-fold numerical excess. For one measurement point, $10^5 - 10^6$ effector cells are needed, and about 10^7 cells for a complete experiment. Normal NK cell counts are 2.5 x $10^8/L$ in peripheral blood (PB). To obtain 10^7 NK cells from a healthy donor, 50 mL of PB are typically drawn for one complete cytotoxicity experiment. At diagnosis, the counts of normal leukocytes in the bone marrow (BM) and PB of an AML patient are often reduced by 10- to 20-fold. Consequently, monitoring the functional activity of the remaining normal NK cells of an AML patient in the early stages of treatment

with standard bulk assays would require either far more than 50 mL of PB for each assay, or the use of BM samples, which are difficult to procure. Therefore, new assays are needed, which produce the equivalent information with far smaller numbers of effector cells.

Apart from these logistic limitations, release assays are difficult to use for reaction periods longer than 4 hours, because spontaneous release of the label from target cells increases with length of the assay and creates an unacceptably large background [245, 249, 250]. In addition, these bulk assays lack detailed information about the interaction dynamics between individual target and effector cells as well as the role of antibody-derived agents in this process. A direct visualisation of specific synapses between individual cytotoxic cells and their targets, followed by cellular lysis, was first achieved through the combined use of fluorescent antibodies specific for cell surface marker proteins and confocal microscopy [251, 252]. Sequential lysis of successive targets by single effector cells was observed [253–255], but direct observation and quantitative analysis of serial lysis remained difficult [256, 257] . Initially, cytotoxicity tests were mainly performed with bulk assays such as ^{51}Cr release, or with endpoint methods such as flow cytometry [258, 259], which do not permit a dynamic analysis at the single-cell level. Data acquisition with single-cell imaging techniques was slow, and these techniques were used in a low-throughput mode [251, 252]. High-resolution microscopy methods added later, permitted more detailed studies of immunological synapses, but these methods produced only static images of individual events and were not suited for high throughput analysis and studies of dynamic processes [260–262].

4.4.2 Imaging approaches to visualise natural killing mode and ADCC

To overcome these limitations and to visualise cytolytic processes with small numbers of cells and in great detail, time-lapse microscopy methods were implemented [248, 263–265]. These methods permit investigators to follow lysis of individual target cells by individual effectors at high throughput and for observation periods of 15 hours and beyond. A key improvement enabling this progress was the design of structured micro-arrays of biocompatible polymers such as PDMS on a microscope carrier surface [248,264,265]. Target cells were made to adhere to such arrays and effector cells were allowed to move across the targets in the fluid phase. Effector- and target-cells were confined to very small reaction volumes, and in combination with automated time-lapse fluorescence microscopy, thousands of effector-target cell interactions were monitored by imaging individual wells of the arrays. Such single-cell cytometry (SSC) methods have been used to study both T-CTL and NK-cells [248, 264–266] and have produced important new insights. For example, it was discovered that the release of interferon γ by T-CTL in contact with virus-infected target cells, which is consistently detected as a correlate of T-cell activation in conventional bulk assays, was not a tight correlate of T-cell activation when studied at the single cell level [264]. Similarly, Fc-engineered antibodies were found in this way to have gained their enhanced cytolytic potential by "kinetic boosting" of NK-cells, i.e. by shortening of the time between serial lytic events [248].

The lysis of cancer cells by NK cells in their natural killing mode (in the absence of added mediator proteins such as antibodies) was analysed in detail with SSC methods [266]. Low magnification imaging was used to continuously track large numbers of individual NK cells and to reveal statistics of lysis. In addition, low effector-to-target cell (E:T) ratios in the range from 1:10 - 1:100 were used to follow serial lysis by individual NK cells. New parameters characterising the lytic process emerged, including the "time to first kill" (the time needed for an NK cell between first contact with a target cell and the onset of lysis); the "time to subsequent lysis" in a sequence of serial lytic events; and the average and maximum numbers of serial lytic events achieved by a single NK cell. NK cells, which had completed a first lytic event on a confluent layer of targets, required a shorter length of time to the next event when

they were still in contact with the previous victim than when this contact was lost. Therefore, a "memory for prior lytic acts" appeared to exist in NK-cells, which were simultaneously in contact with the previous and the next target cells, and this effect disappeared when contact with the previous target was lost. This memory effect may reflect a state of preparedness of an NK cell for lysis, augmented by continued contact with the previous target, an important biological insight gained exclusively through the use of this new method. SSC techniques were further used to classify NK cell subsets based on their migration behaviour and details of their cytolytic activity [40, 267]. Differences in the cytolytic potential of NK cells, in their migration behaviour, and in their contact dynamics between IL-2-stimulated and non-stimulated cells have been uncovered with SSC methods [40]. Different NK cell subsets and NK cell lines were analysed in this manner, as well as IL-2-activated and unstimulated NK cells isolated from healthy donors [41].

4.4.3 Time-resolved fluorescence microscopy for live cell monitoring

To explain the surprisingly strong increase in the cytolytic potential mediated by triplebodies relative to the corresponding tandem diabodies, the use of SCC methods is expected to contribute significantly. For this reason, here we have asked, whether SCC methods can be employed to study of the mode of cytolytic action of NK cells mediated by triplebody SPM-2. In the first stage of adapting the method to this problem and to simplify the experimental setup, only the CD123-specific binding site of this agent was employed.

We used SCC to assess the efficacy of SPM-2-mediated killing of adherent human target cells by primary human NK cells in a time-lapse mode (see figure 4.2). The main objective was to establish an assay using arrayed target cells and to validate it by comparing results with results obtained from standard calcein release assays. Comparable dose-response functions were indeed obtained. Importantly, the SCC assay allowed for measurement of killing rates, which vary with time and could not be measured so far by bulk release assays. Our results open the possibility for future use of the assay to study not only the quality of primary effector cells from human donors, but also to study mechanistic details of the mode of action of the therapeutic agent on different subsets of target cells, including both bulk leukemia cells and minimum residual disease (MRD) cells, considered to be closely related to the relapse-initiating leukemia stem cells (LSCs).

4.5 Dynamic analysis of Natural Killer cell activation and killing

4.5.1 Experimental design

To quantify redirected lysis (RDL) of adherent target cells by NK cells mediated by triplebody SPM-2, we developed a single-cell assay based on fluorescence microscopy and structured microarrays. We produced arrays of adhesion sites spaced by 60 μm and deposited on carrier surfaces suited for microscopic observation. Adherent epithelial cells, the established human cell line HEK293.123, were seeded on the micro-structured surfaces (figure 4.3a,b) and attached in the desired pattern (figure 4.3c). A standardised batch of effector cells from a healthy human donor was used. These were peripheral blood mononuclear cells (PBMCs) expanded in culture for 20 days in the presence of IL-2, so-called LAK cells (Lymphokine Activated Killer cells), a mixture of T-, NKT- and NK-cells containing 25% of activated NK cells [245, 246, 268]. Image acquisition started immediately after addition of the NK cells plus the therapeutic agent or controls. Images were acquired in 12 min intervals over a time course of 16 hours. The time-lapse sequences were analysed by using custom-made image-analysis software integrating the fluorescence intensities from each individual cell adhesion site at each time-point. The onset of

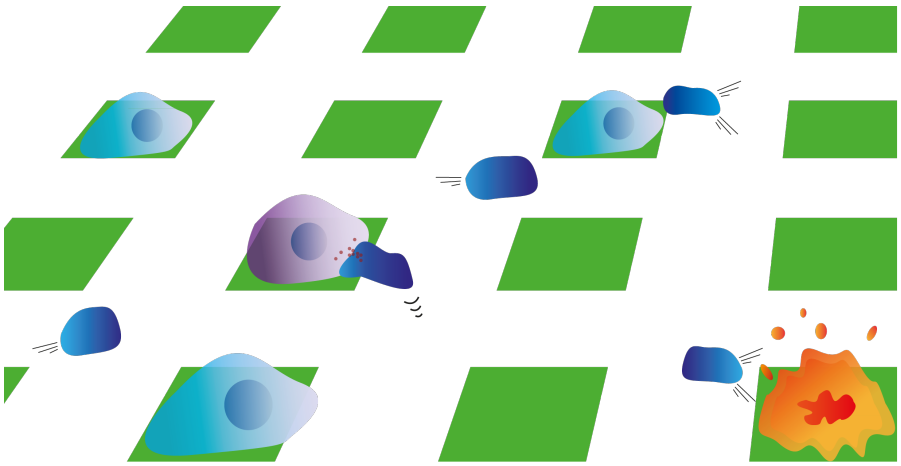

Figure 4.2: Principle of the proposed SCC assay: target cells are arranged in arrays by micro-structured adhesion sites, hence allowing for a facilitated assessment of the fraction of cells specifically lysed by NK cells, which are added to the assay. We take time-lapse movies over a period of 16 hours and follow the action of SPM-2 by detecting the fluorescence signal of the cell death marker propidium iodide (PI).

cell death (apoptosis) was detected when a rapid increase in fluorescence intensity of the red marker dye propidium iodide (PI) was recorded after it entered dying cells (figure 4.3e).

4.5.2 Comparison with the data from the bulk release assay validates the SSC assay

To validate data acquired with the new assay, results produced with this assay and with the standard calcein release assay were compared in benchmark experiments. When the same reagents (batches of target cells, NK cells, mediator protein, buffers, cell culture media) and and other conditions (same operators, same laboratory) were used in comparative experiments, comparable data were obtained with both assays. To allow for better comparability, the NK-cells used in both assays were preparatively enriched from IL-2-stimulated LAK-cells with the help of immunomagnetic (MACS) beads. The enriched population contained (83.3 ± 4.6)% of CD56 ^{bright}CD16 ^{bright} NK cells, which were used in a 2:1 effector-to-target cell (E:T) ratio. Over a 16 hour measurement period, a maximum of about 35% of the cells analysed were lysed in the SSC assay in the presence of triplebody SPM-2 (figure 4.4a, red open bars). This number represents the "overall lysis" achieved by NK cells, i.e. the sum of their lytic activity obtained in the "natural killer" mode (in the absence of added mediator proteins), plus the incremental lysis achieved by addition of the mediator protein. The differential owed to the mediator protein is referred to as the "specific lysis". The fraction of specifically lysed cells (% specific lysis) steadily increased with triplebody concentration and reached a plateau at about 25% for concentrations from 1 nM upwards (figure 4.4a, red closed bars). As a negative control the triplebody SPM-1 (19-16-19; [243]) was used, a protein in the same molecular format as SPM-2 and carrying the same scFv binding site for CD16, but with specificity for the target antigen CD19, which is absent from the surface of HEK293.123 cells. In separate experiments with CD19-positive target cells this control triplebody mediated cytolysis by NK cells [243], (but it did not produce specific lysis of HEK293.123 targets in the SSC assay (figure 4.4a, black open bars).

The fraction of specific lysis induced by SPM-2 showed a comparable dose dependence in

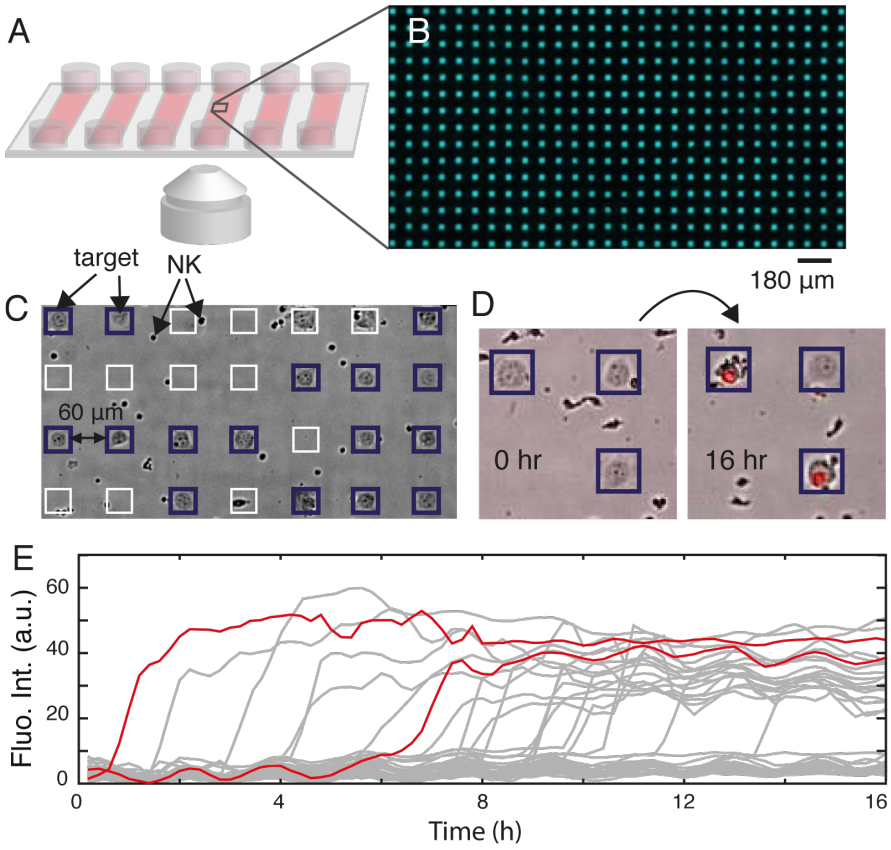

Figure 4.3: Experimental set-up of the single-cell cytometry (SCC) assay. Chemically modified patterned surfaces (arrays) were prepared on 6-channel microscope slides (A). Protein-coated arrays were generated by plasma-induced patterning. B: Squares with a side-length of 30 μm were coated with fibronectin (here fibronectin labeled with Alexa Fluor 488) and the backfilling (black) area with PLL(20k)-g(3.5)-PEG(2k) (PEG(2)). Each channel on the carrier surface, shown in (A), contained 4400 adhesive squares for cell attachment. In (B) a part of an overview microscopic scan of one coated channel of the slide is shown. C: Arrays of adherent HEK293.123 target cells were prepared on the chemically modified surfaces (surfaces seeded with cells have adhesive squares with unlabelled fibronectin). NK cells were added and squares occupied by single target cells (framed in blue) were selected and tracked in a time-lapse mode. NK cells were identified cinematographically by their size and motility. The distance between the squares was 60 μm in our experiments, but arrays with different spacing can be produced. D: The cell-impermeable red fluorescent marker PI (propidium iodide) was used to identify dead cells. Overlay of brightfield and PI emission is presented for the first and last frame of a measurement. E: The mean fluorescence intensity of 40 cells over time is plotted (in the presence of 10 nM SPM-2 triplebody). Each track ("fate plot") represents the fluorescence intensity of one cell in the PI channel. Tracks exceeding an intensity threshold represent lysed cells. Two exemplary time-courses of two target cells that were lysed are highlighted in red. Reprinted with permission from [269].

the SSC- and the calcein-release assays (figure 4.4b). In both cases specific lysis reached plateau values for concentrations from 1 nM upwards, and the shape of the curves was similar. The EC50 values derived from both curves were (10.2 $\pm$ 8.0) and (12.2 $\pm$ 0.12) pM for the calcein-

and the SCC assays, respectively. The errors represent the standard deviation computed by statistical modelling of the two assays (see in [269]). While the EC50 values derived from both data sets were very similar, the maximum fractions of specifically lysed cells were (48.1 ± 2.3)% for the calcein assay and (24.5 ± 1.4)% for the SCC assay. This difference most likely is explained by the fact that in the calcein assay both effector and target cells were present in the fluid phase, whereas in the SSC assay the targets were anchored to the substrate and were for this reason less accessible to the effector cells. In addition, in the SCC assay the density of cells per unit volume was less than half of the density reached in the calcein assay. However, this quantitative difference in the maximum levels of specific lysis recorded with both assays does not affect the key conclusion that the SSC assay is validated by this comparison, because it captured the dose dependence of the triplebody's killing potential in the same qualitative manner as the calcein assay.

The dependence of specific lysis on the E:T ratio was measured with both assays, to further characterise the quality of cytolysis assays (figure 4.5). For this experiment the triplebody was used in a constant saturating concentration of 1 nM, while the E:T ratios were varied. Effector cells were MACS enriched LAK cells with a (90.2 ± 3.0)% content of CD56 ^{bright}CD16 ^{bright} NK cells. The fraction of specifically lysed cells increased with the E:T ratio up to the largest ratio measured (5:1) in a steady manner, similar dependence was observed in other cytolysis assays (figure 4.5). A further increase for even greater E:T ratios may still be observed. The extent of specific lysis for E:T values <1 was lower than expected based on the landmark study of NK cells in their natural killer mode [266], where serial lysis was readily observed for E:T values as low as 1:10 and 1:20. The difference is probably due to the far lower density of target cells in our SSC assays than in the landmark study, where confluent monolayers of target cells were used. In the published study the "memory for prior lytic events" [266] was significant, whereas under our SSC conditions it was probably less important due to the greater spacing of the target cells. The dependency of the calcein assay on the E:T ratio was not measured here again, because the results were known and were qualitatively similar to those shown for the SSC assay (figure 4.5, [244]). From this similarity we conclude, that the typical dependency of specific lysis on the E:T ratio is another experimental result validating the SSC assay.

4.5.3 Changes in the rate of lysis occur over the duration of a 16 hour reaction

The SCC assay allows us to monitor target cell lysis over long periods of time. Taking advantage of this new capability, we measured not only the cumulative number of lysed cells integrated over the entire measurement interval, but also killing rates, i.e. the number of lytic events per unit of time, for example lytic events per hour (figure 4.6). The assay allowed us to follow the kinetics of induction of death of individual target cells ("fate plots") by measuring the fluorescence intensity emitted by the red marker PI as a function of time (figure 4.6a,b). The discrete measurement values recorded at times $t_1, t_2, t_3, t_4, t_5, t_6$ etc. were fitted by a curve, and for different individual cells these "fate plots" had different shapes. The transition to cell death was accompanied by a stepwise increase in PI fluorescence intensity shown for 3 randomly selected individual cells (figure 4.6b). For one of these cells (red curve in figure 4.6b) the corresponding time-lapse frames at selected time points are shown in figure 4.6a. From such data, the cumulative fraction (percentage) of lysed cells was computed and plotted for 3 different concentrations of SPM-2: 0, 1 and 100 nM (figure 4.6c). The percentage of lysed cells is the number of cells lysed relative to the total number of target cells analysed for this experimental condition. The level of lysis seen for 0 nM of the agent represents natural killing by the NK cells present in the reaction, and the cumulative percentage of these natural killing events also increased with time (figure 4.6c, yellow plot). By subtracting this value from the "overall lysis"

values, the cumulative percentage of "specifically lysed cells" is computed. The curves shown in figure 4.6c represent the cumulative fraction of overall lysed cells before subtraction of this contribution. For the purpose of computing rates of lysis, it is sufficient to work with the "overall lysis" values, because the amount of natural killing by the NK cells is a constant background, which does not influence the rate of specific lysis. Rates of specific lysis were computed from the cumulative curves such as those shown in figure 4.6c by computing the first derivative with respect to time. Rates of specific lysis determined in this manner are plotted in figure 4.6d over the course of 16 hours for various SPM-2 concentrations and for constant numbers of NK cells. In the absence of NK cells (left panel in figure 4.6d labeled "medium") the rate of lysis by NK-cells was obviously zero. In the absence of SPM-2 and for low concentrations of the agent (0.01-0.1 nM) the killing rate of the NK cells was almost constant, with about 40-50 cells killed per hour (figure 4.6d, 2nd, 3rd and 4th panels from the left). At higher concentrations, from 1-100 nM, the triplebody clearly affected the activation of the effector cells and the killing rate. The killing rates increased until a maximum was reached after several hours and then gradually decreased. This maximum rate was greater for higher concentrations of SPM-2 (50 and 100 nm, last 2 panels to the right in figure 4.6d) than for intermediate concentrations (0.1 to 10 nM; central panels in figure 4.6d), and therefore, the agent clearly influenced the maximum killing rate of the NK cells. The maximum rate also occurred earlier at high concentrations of the agent than at lower concentrations (figure 4.6d).

Importantly, the rates of lysis measured for the 1st hour of the reaction were elevated (highlighted in yellow in figure 4.6d) and dropped strongly in the 2nd hour for all tested concentrations of the mediator protein, even without added mediator protein (figure 4.6d, 2nd panel from the left). Thereafter the rates slowly increased until maximum rates were reached between 5 to10 hours into the reaction, and subsequently the rates were reduced again.

Interpretation of the observed changes in cytolytic reaction rates

The high reaction rates observed in the 1st hour must be due to an activity of the NK cells in their natural killer mode, because they were observed even in the absence of added triplebody (figure 4.6d, 2nd panel from the left). The likely explanation is, that the NK-cells used in these experiments were pre-activated LAK cells, stimulated by 20 days of culture in the continued presence of IL-2. They were "ready to kill" and loaded with granules filled with perforins and granzymes [230]. We observed that the NK cells settled down during the first hour of the reaction and after 1 hour almost all were deposited on the carrier surface. We propose that upon first contact with the target cells, the NK cells degranulated in a first burst in their "natural killing" mode, without any influence of added mediator protein. Thereafter the NK cells were likely exhausted and must have replenished their storage granules. The triplebody must have played a role either in the replenishment process or the subsequent lytic events or both, because the maximum rates of lysis were clearly augmented by the triplebody in a dose-dependent manner (figure 4.6d). The observed increase in lytic rates with time suggests an influence of the triplebody on the speed of replenishment of the lytic granules, or on other metabolic processes preparing the NK cell for the next degranulation event and on an acceleration of the cadence of lytic bursts. If we were to determine the mean interval between first and subsequent killing events for individual NK cells used in E:T ratios much less than 1, then we would expect to find a shortening of these intervals in function of the dose of added triplebody, a "kinetic boosting" of NK cytolysis as previously reported [248, 266]. The decline of reaction rates observed after the maximum values were reached a few hours into the reaction is more difficult to explain. A possible influence may come from the internalisation of CD123 from the surface of the target cells mediated by the triplebody [270]. At the 1 nM concentration of triplebody used in these experiments, 600 million molecules of triplebody are present per microliter of reaction fluid.

If a few hundrets of target cells are covered by 1 microliter of fluid, each carrying 360,000 copies of CD123 on its surface, then this would amount to a few million molecules of CD123 initially exposed on the surface of this pool of targets facing 600 million molecules of triplebody. Consequently, under these saturating concentrations, an approximately 100-fold (or greater) numerical excess of triplebody in the fluid phase is present over the number of target antigens on the target cell surface. Under these circumstances, most CD123 molecules on the surface will be occupied by a triplebody molecule and will be internalized within approximately 30 to 60 minutes, a process called "down-modulation of the target antigen". Some of the internalised CD123 molecules will be recycled to the surface, and new synthesis of CD123 will also occur, but these resurfacing molecules will again be rapidly re-internalised, because the 100-fold excess of triplebody in the fluid phase will not be exhausted. This recycling and re-internalisation will occur continuously over the 16 hour measurement period, and it is therefore not obvious, how this process could contribute to the observed reduction of reaction rates after the maximum has been reached. As only less than half of the target cells are killed over the entire reaction period, it is difficult to conceive that the number of available target cells, which was reduced by less than 2-fold over this time, would explain the observed 2-fold drop in the rate of lysis. More likely, in addition to the contribution by the loss of target cell numbers, the targets must also be in a state of "preparedness" for lysis, and this preparedness may decrease with time in a manner influenced by the concentration of the triplebody. A mechanistic explanation for the decrease in reaction rates after reaching the observed maximum a few hours into the reaction interval is presently not obvious. If the explanation offered above for the increase in rates during the first few hours of the observation interval (on the way to the maximum) is correct, namely that a "kinetic boosting" occurs with a concurrent shortening of the time interval between successive lytic events of a single NK cell, than the observed slowing down of the reaction rates after reaching the maximum may be accompanied by a corresponding "kinetic dampening" of the NK cells, i.e. an increase in the median length of time between two consecutive lytic events of a single NK cell. The time-resolved SSC method presented here is sufficiently powerful to permit a direct experimental test of the validity of this hypothesis.

Another advantage made possible by the use of these time-resolved SSC methods is, that we now have learned that the initial burst in lysis during the first hour is due to a natural killing process, and not to a specific effect of the added mediator protein. Therefore, we can now subtract this contribution and study the specific effect of the mediator protein with greater precision. The use of a standard release assay would not have permitted us to make this observation and to correct the data for this effect. The uncorrected data would have been skewed and would have informed us with lesser precision about the effects of the triplebody than the corrected data obtained with the new method.

The first hypothesis proposed above was, that the enhanced cytolytic activity of dual-targeting triplebodies over the corresponding mono-targeting bispecific diabodies was due to "kinetic boosting", for example by a shortening of the median length of time between two successive lytic events of a single NK cell. A second hypothesis to explain this enhanced activity is also based on a dynamic argument. It proposes that the dual-targeting agents enhance the probability for a "productive encounter" between an NK cell and a target cell and similar to the first hypothesis, it can only be tested by experiments employing time-resolved methods. We define as "productive encounter" a long-lasting association between an NK and a target cell, while a non-productive encounter, describes that an NK cell made brief contact with a target cell, then detached, and cell death did not follow. In our microscopic time-lapse studies of single NK cells only about 1/3 of all documented encounters were productive. The second hypothesis posits, that the percentage of productive encounters increases with increasing concentrations of the triplebody and is greater for the triplebody than for the corresponding mono-targeting

bispecific diabodies. We have not yet measured this dependence directly, but these measurements are now possible with the available method. Binding of the two cells can be described by an "on-rate" and an "off-rate", and it appears to be intuitively plausible that these rates should be influenced by the triplebody, because it acts like a glue and should reduce the off-rate. As the triplebody has a higher avidity for the target cell than the corresponding bispecific diabodies carrying only one binding site for the target cell, it appears further likely that the off-rate should be lower for the triplebody than for the mono-targeting corresponding tandem diabodies, because the affinity expressed through the equilibrium rate constant of binding is the ratio between off-rate and on-rate of binding. As the on-rate almost always remains constant, the key variable affecting K_d and affinity is the off-rate, and therefore, for the triplebody with the greater avidity of binding to the target cell, we would anticipate to see a slower off-rate of the NK cell from the target, and thus a higher percentage of productive encounters.

However, this argument, although it is intuitively appealing, is not correct, because the known affinities and avidities of the triplebody describe only its binding to the target cell, but not the binding of an NK-cell to a target cell decorated with the triplebody. Other parameters than the mere affinity of the triplebody for the target cell will likely affect the efficacy of binding of an NK cell to the decorated target cell, such as the affinity of the CD16-binding module of the triplebody for the NK cell and others. It is quite conceivable that the triplebody once bound to the target cell induces secondary changes in the surface density of receptors and ligands on the target cell, which then indirectly influence the establishment of a productive encounter with the NK cell. Consequently, in order to test the validity of this second hypothesis, it remains necessary to perform direct measurements of the success rate of the encounters and of the influence of a triplebody on this rate as opposed to the corresponding tandem diabodies and other control proteins. The new assay therefore offers the opportunity to make the direct experimental observations needed for a critical test of this second hypothesis.

4.5.4 Natural killing dynamic analysis against non-adherent AML target cells

Samples of primary cancer cells derived from hematologic malignancies consist of non-adherent cells. To render the proposed assay suitable for non-adherent cells we used a second version of the chip, in which instead of fibronectin square patterns we have patterns coated with antibodies of the IgM isotype (see section 2.2.2). To test this second version we measured the natural killing potency of primary NK cells from another healthy donor on the human AML-derived target cell line MOLM-13.

A suitable antibody candidate for capturing the MOLM-13 cells on the micro-patterns, without interfering with the NK cells, is an anti-CD15 antibody. The CD15 myeloid marker is present on the surface of the MOLM-13 cells [80] but not on the primary NK cells (see section 2.2.2). Square patterns of 25 μm were used for the MOLM-13 cell line, as its size is smaller and smaller square patterns lead to a higher percentage of single-cell occupied patterns. Even though in the case of non-adherent cells smaller distances among the square patterns would be possible to be used, we chose the 60 μm distance to be consistent with the measurements of the adherent target cells. In figure 4.7a an array of MOLM-13 cells is presented with NK cells added. Since, the size and the morphology of the MOLM-13 cells is very similar to the one of the NK cells, their staining is essential to successfully distinguish them.

We measured the natural killing of NK cells alone without addition of a mediating protein to test the proof of principle of the above-described version of the assay for non-adherent cells. For these measurements, NK cells were derived from a second healthy donor and activated as previously described [245, 268]. Preparation of the samples, image acquisition and analysis were performed as for the measurements with the adherent HEK293.123 cell line. The E:T

ratio was 2:1 and after a 16-hour measurements period 2.6% of the cells analysed were lysed (figure 4.7c). This percentage was lower than the average natural killing of the first donor at the same E:T ratio (8.4%, figure 4.4a) which probably reflects donor-to-donor variability issues and the different type target cells used. Time-lapse frames of an NK cell killing a MOLM-13 are presented in figure 4.7b. The variation of the killing rate over the course of 16 hours for the natural killing of the NK cells measured is presented in figure 4.7d. A slightly higher killing rate during the 1st hour is also observed in this case and reflects the preceding stimulation of the NK cells with IL-2 as was extensively discussed above.

4.5.5 Conclusions and Outlook

Herein, single cell arrays combined with time-resolved fluorescence microscopy methods were used to study the interaction of primary human NK cells with human target cells mediated by triplebody SPM-2, an antibody-derived protein, which recruits NK cells for target cell lysis. The arrayed pattern of target cells allowed for automated counting of lytic events. Lysis depended on the dose of the agent and the E:T ratio in a manner typical for standard cytolysis assays, and consequently this new assay was validated relative to existing standard procedures (calcein release assay) by direct comparative analysis. Use of the new SCC assay revealed so far unreported changes in the killing rate over long-term reaction periods (16 hours). These changes may be explained by changes in the median length of time between two successive lytic events of a single NK cell, achieved through the action of the triplebody, similar to the "kinetic boosting" of NK cells proposed previously to explain the enhanced cytolytic potential of Fc-engineered therapeutic IgG antibodies [248].

The dependence of target cell lysis on the dose of a therapeutic agent and on the E:T ratio are important characteristics of standard cytotoxicity assays and both properties are routinely monitored in academic research and commercial drug development. However, the standard assays are so-called "bulk assays", as they produce data averaged over a population as well as a time period. In contrast, the SSC assay produces data with spatial as well as temporal single cell resolution. The former provides detailed information on the interaction between a target and an effector, while the latter unveils the dynamics of this interaction. To better understand the mode of action of novel therapeutics based on the recruitment of effector cells and the functional properties of the effector cells involved, it is essential to have the ability to study also the dynamics of these processes. An important example illustrating this need is the "kinetic boost" of the NK cell function, a shorter time interval between sequential lysis events, induced by Fc-engineered antibodies [248]. This dynamic phenomenon could only be discovered by using time-resolved methods, but not with the standard static cytotoxicity assays or affinity measurements of optimised antibodies. An additional advantage of single cell assays is that they generate statistically significant data with substantially smaller numbers of effector cells. For an SCC assay typically only 2 x 10^4 of NK cells are needed per measurement point, 5-times fewer than the $>10^5$ cells needed for each measurement point in a calcein release assay. Patient-derived NK cells are a scarce resource, in particular to monitor disease status and therapy outcome for AML patients, as outlined in the introduction. Further miniaturisation of the new method is possible, so that reliable measurements may become possible with as few as 5,000 - 10,000 NK cells. Hence chip-based single cell assays are valuable for clinical monitoring of the patients NK response and for the choice of personalised treatment for individual AML patients. They can also be applied to T-CTL as effector cells and triplebodies and other antibody-derived proteins recruiting T-cells as cytolytic effectors [240, 271, 271].

Assays employing spatially arrayed target cells can also be useful to scrutinise questions regarding the timing in cell-cell recognition and immune response, such as the "memory" effect described for NK cells [248]. Also, in the experiments presented here the full potential of the

dual-targeting triplebody SPM-2 has not yet been analysed. Here we have so far only used the CD123-binding site of this agent. The effect of simultaneous engagement of both binding sites by one copy each of CD33 and CD123 on the lytic activity of NK cells can be studied. Dual-targeting renders SPM-2 agent particularly promising for the therapy of AML because virtually all patients expressed either one or the other of the two antigens [272]. Indeed, in cell culture cytolysis assays with primary cells from a broad range of AML patients with different subtypes of AML and with a standard batch of NK cells from an unrelated healthy donor, all samples showed very effective lysis. This is an unusually high degree of responsiveness, considering that the response rate to one of the best antibody-derived agent available so far for the treatment of AML (Mylotarg™, [273]) was in the range of 40% for blasts from patients with different subtypes of AML [274]. Even blasts from patients with AML subtypes that typically show a poor response to conventional chemotherapy were lysed efficiently by SPM-2 plus NK cells (T. Braciak, unpublished data). Moreover, the pair of (CD33 plus CD123) is highly expressed on AML leukemia stem cells (AML-LSCs) but far less on normal haematopoietic stem cells (HSCs [275–277]). Consequently, a therapeutic window appears to exist, which may permit a preferential elimination of the AML-LSCs over the normal HSCs of the patient and a reconstitution of the patient's haematopoietic system after the end of therapy from the patient's own HSCs, without the need for an allogeneic or autologous stem cell transplantation. If this could be achieved, then this result would constitute major progress in the therapy of AML. For this reason, in the future it is important to study in detail not only how a patient's autologous NK cells in conjunction with this agent lyse the patient's bulk AML blasts, but also whether and how they lyse subsets of blasts progressively closer and closer to the leukemia initiating cells (LICs) and relapse initiating MRD cells, which are likely to be encompassed in the $CD34^{+}CD34^{-}CD123^{high}$ compartment of BM and PB cells, which comprises between 0.01 and 67% of all malignant cells for different AML patients [278]. To this end, cytolysis assays with rare subsets of patient-derived AML cells and NK- or T cells are required, which will be available in small numbers only. Finally, agents targeting the same pair of antigens, but recruiting T-cells as cytolytic effectors are also under development [279], and similar experiments as those outlined above will also need to be performed with the corresponding T-cell-recruiting agents in order to find the best suited agent for individual patients in the sense of a personalised medicine. Developments are well under way that personalised medicine will clearly become more prevalent in the future. Time-resolved SSC assays and their further refinements are likely to unravel the capabilities of Fc engineered antibodies and other bi- and tri-specific antibody-derived agents such as the triplebodies described here for enhanced target cell lysis. For all these reasons, they offer the potential to assist treatment decisions and monitoring of treatment success in cancer therapy.

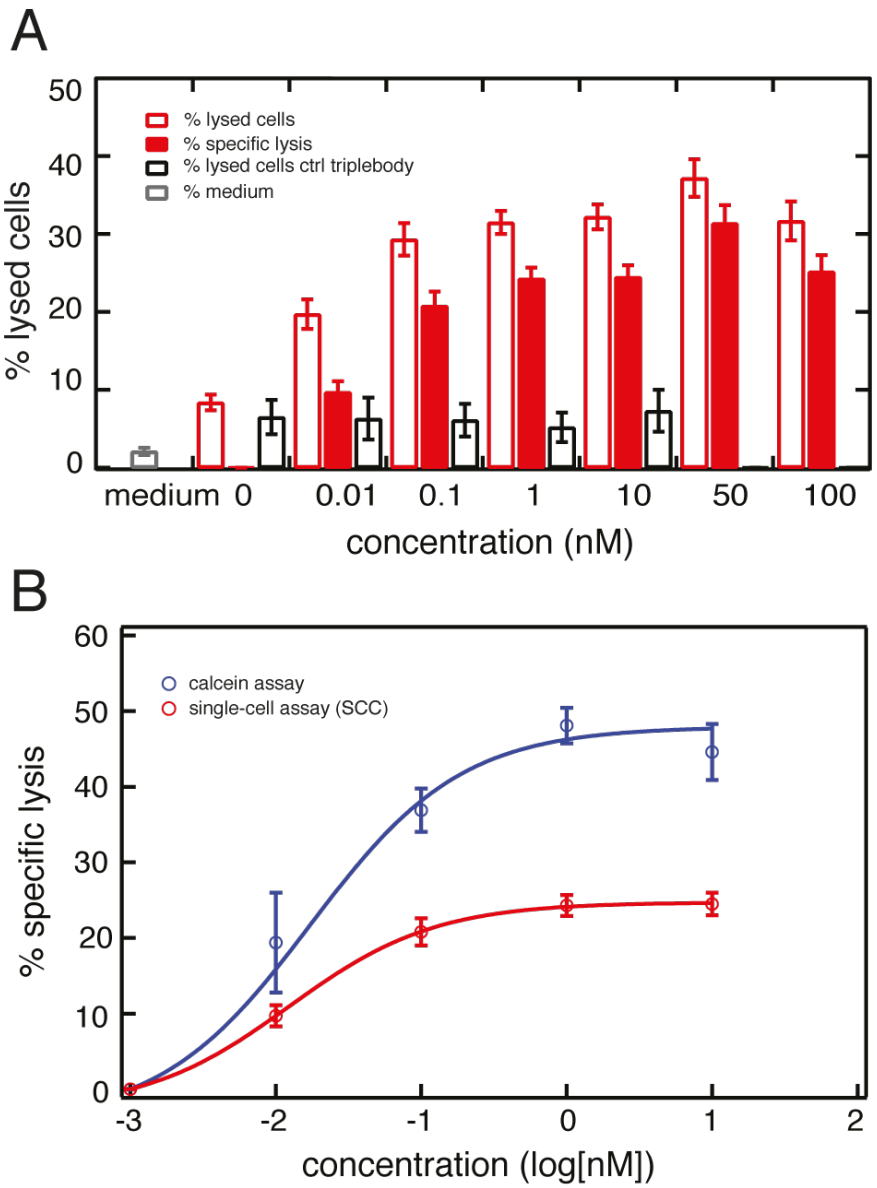

Figure 4.4: Validation of the SCC assay by direct comparison with the bulk assay. (A) Data obtained with the SCC assay. Red open bars: percentage of dead target cells relative to the total number of target cells analysed ("overall lysis"). Red filled bars: percentage of specific lysis induced by SPM-2 after subtraction of natural killing by NK cells alone (the numbers shown for 0 nM concentration). Black open bars: overall lysis produced by addition of control triplebody SPM-1 (19-16-19), a triplebody in the same molecular format as SPM-2, but recognising the target antigen CD19, which is absent from HEK293.123 cells. This control was not performed for 50 and 100 nM concentrations of the control protein. Medium control: without added NK cells and triplebodies; this control measures the extent of spontaneous death of target cells over the measurement interval. The averaged value of all the dose-dependent measurements is shown. (B) Comparison of data obtained with the SCC assay (red circles) over a 16 hour measurement and the bulk assay (calcein release assay; blue circles) over a 4 hour period. Data points of the calcein assay represent the mean value of the percentage of specific lysis averaged over triplicate reaction wells on the same microtiter plate, and error bars represent the SEM (standard error of the mean). Effector cells were MACS-purified NK cells from a healthy donor, pre-stimulated with IL-2 (LAK cells), and seeded at an E:T ratio of 2:1. Reprinted with permission from [269].

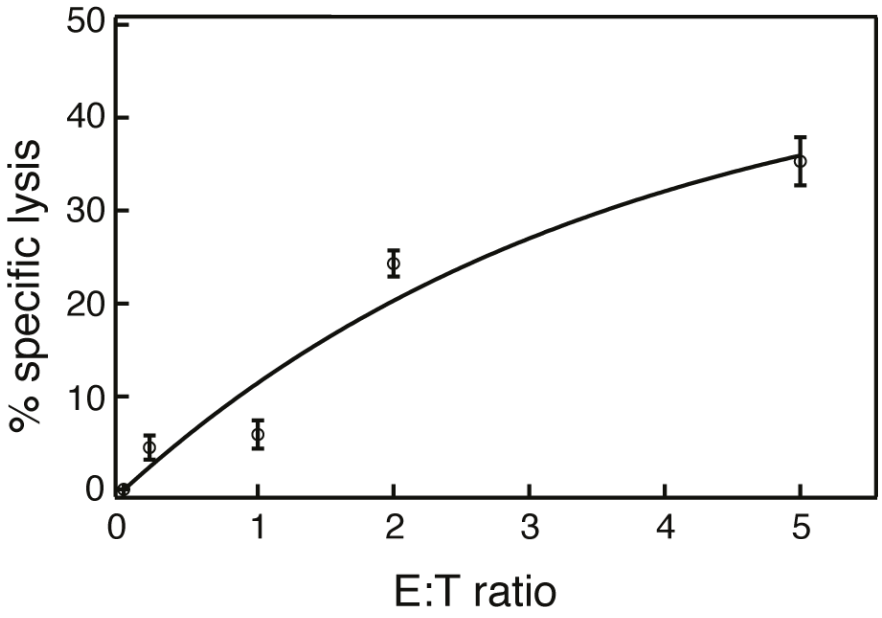

Figure 4.5: Dependence of specific lysis measured with the SCC assay on the E:T ratio. Lysis induced over a range of different Effector to Target (E:T) cell ratios by SPM-2 at a 1 nM saturating concentration. Data points are fitted to an exponential curve. Effector cells were MACS-purified NK cells from a healthy donor, pre-stimulated with IL-2 (LAK cells). Reprinted with permission from [269].

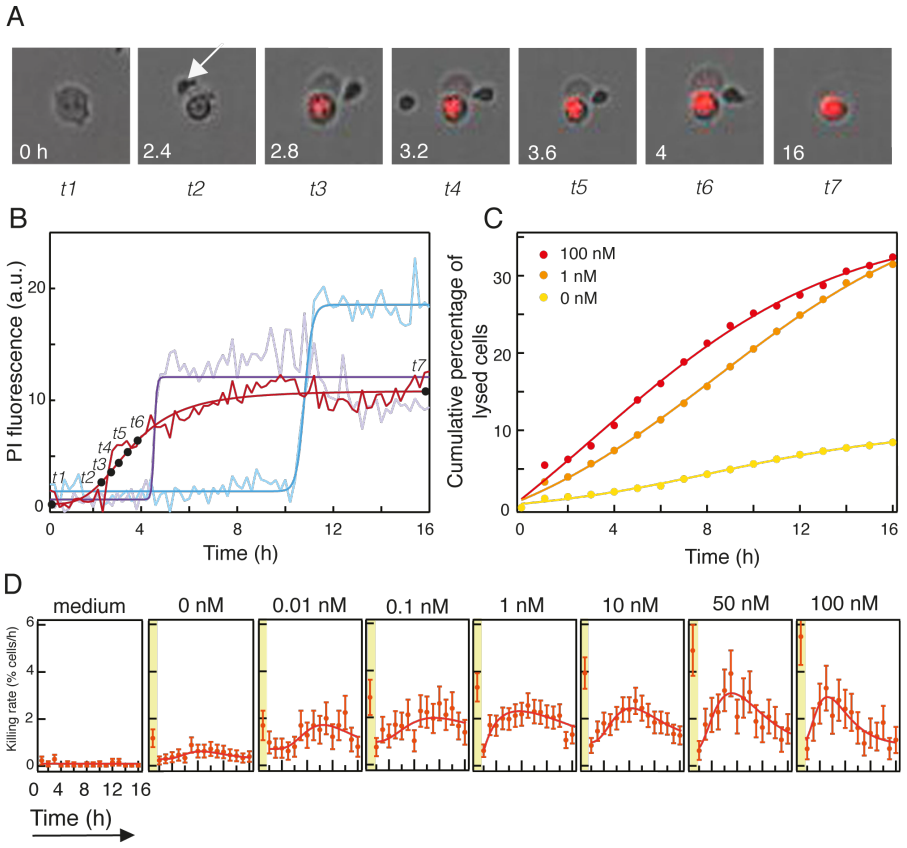

Figure 4.6: Dynamic analysis of lytic events with the SCC assay. (A) Time-lapse images of an exemplary target cell being killed by an NK cell (arrow). The progressively increased PI fluorescence intensity reflects progressive nuclear membrane disintegration (irreversible apoptosis). (B) PI fluorescence intensity of 3 exemplary target cells over the course of 16 hours, including the cell shown in (A) (red curve). Raw intensities were fitted with the Hill Equation. (C) Cumulative percentage of lysed target cells for 3 different concentrations of SPM-2: 0, 1 and 100 nM. Data points were fitted with the sigmoid function. (D) Killing rate as a function of time for increasing concentrations of SPM-2 by a constant number of NK cells. The left panel ("medium") shows the dynamic of spontaneous cell death events, in the absence of NK cells. Data points were fitted with a log normal distribution curve. Data points for the first hour of the reaction (highlighted in yellow) represent natural killing by the NK cells but not specific lysis mediated by the triplebody. These events also occurred in the absence of added triplebody (2nd panel from the left), and were therefore excluded from the fitting. Reprinted with permission from [269].

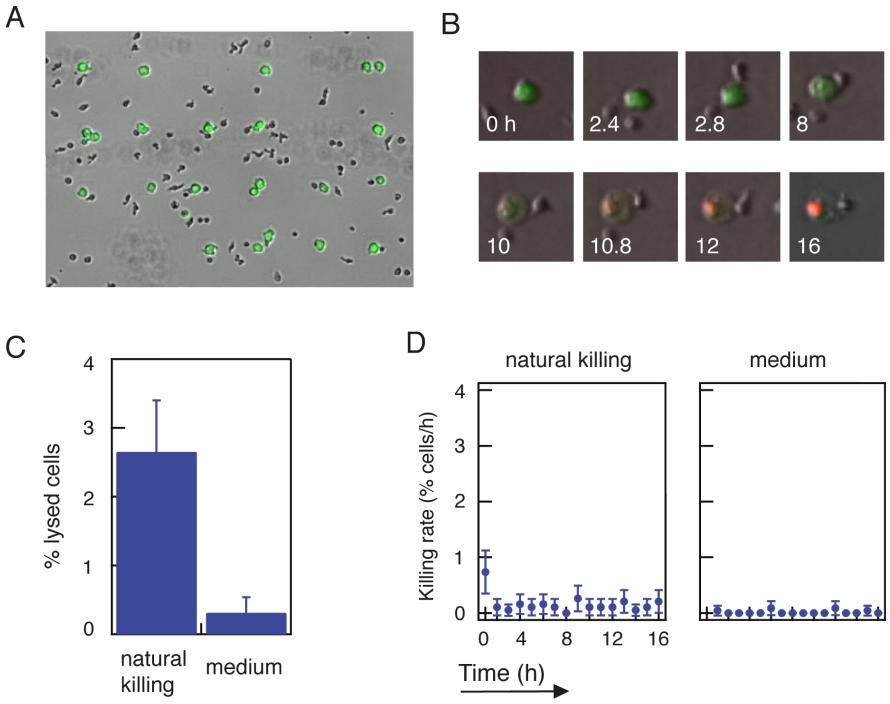

Figure 4.7: Variant of the SCC assay adapted to non-adherent target cells. Arrays of antibody-coated square patterns were generated with the same procedure as the fibronectin arrays, by substituting fibronectin with an anti-human CD15 antibody. Arrays of stained MOLM-13 cells (CellTracker™Green CMFDA) were prepared on the chemically modified surfaces and then NK cells (unstained) were added (A). (B) Time-lapse images of an exemplary MOLM-13 target cell (green) being killed by an NK cell (unstained). The progressively increased PI fluorescence intensity reflects progressive nuclear membrane disintegration (irreversible apoptosis). (C) Data obtained with the SCC assay showing the natural killing potency of NK cells against MOLM-13 cells. The bars represent the percentage of dead target cells relative to the total number of target cells analysed. (D) Dynamic analysis of the natural killing mode of NK cells against the MOLM-13 target cells. The right panel ("medium") shows the dynamic of spontaneous cell death events, in the absence of NK cells. Reprinted with permission from [269].

Chapter 5

Application in Cell Cycle and Chemotherapy

5.1 Cell Cycle

Cell division enables the generation of a whole organism from just a single cell, and it is a fundamental part of the *cell cycle*. As simply stated by Paul Nurse (Nobel Prize in 2001 shared with Leland Hartwell and Timothy Hunt for groundbreaking discoveries on the eukaryotic cell control on its reproduction), the cell cycle is a series of events from the "birth" of a cell to its later division into two cells. In every cycle the cell has to precisely replicate all of its genes and then separate them precisely into two progeny cells. If these two steps are not executed accurately, the outcome is the generation of genetic unstable cells, i.e. cells with wrong number of chromosomes, or with chromosomes with altered or rearranged parts, which can lead to cancer.

5.1.1 Normal cell cycle

In somatic cells the cell cycle is divided into four main periods, the G1 phase (G comes from *gap*), the S phase (S comes from *synthesis)*, the G2 and the mitotic (M) phase (see figure 5.1). The G1, S and G2 phases consist the *interphase*, which accounts for about 90% of the cycle. During the interphase the cell grows by producing proteins and organelles and accumulates the nutrients needed for mitosis. Especially, during the S phase, the DNA synthesis phase, the cell duplicates its chromosomes. Thus, a cell grows (G1), continues to grow as it copies its chromosomes (S), grows more as it completes preparations for cell division (G2) and divides (M). The daughter cells may repeat the process. A human cell might divide every 24 hours. For that cell cycle duration the M phase will last only for 1 hour, while the S phase might take about 10 to 12 hours or about half the cycle. The rest of the time will be for the gap phases both G1 and G2. The G2 phase usually takes 4 to 6 hours, while the G1 phase is the most variable in length in different types of cells.

Even though a lot of molecular changes occur during the interphase the morphology of the cell remains the same during this period. On the other hand during mitosis the morphology of the dividing cell start to change. Mitosis refers to the division of the nucleus and it is followed by *cytokinesis*, which is the division of the cytoplasm. It is conventionally separated into five stages, namely *prophase, prometaphase, metaphase, anaphase* and *telophase*. Overlapping with the latter stages of mitosis, cytokinesis completes the mitotic phase. During *prophase*, the replicated chromosomes, which consist of two closely associated sister chromatids, condense. Outside the nucleus, the mitotic spindle assembles between the two centrosomes that have begun

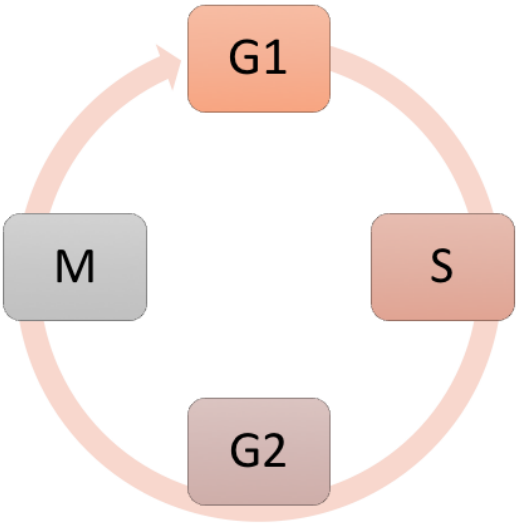

Figure 5.1: Schematic representation of the cell cycle. The cell cycle starts with the G1 phase and then the S, G2 and M phases follow.

to move apart. Then *prometaphase* starts abruptly with the breakdown of the nuclear envelope. Chromosomes can now attach to spindle microtubules via their kinetochores (specialised proteins located at the centromere) and undergo active movement. Next, during the longest stage of mitosis, i.e. the *metaphase*, the chromosomes are aligned at the equator of the spindle, midway between the spindle poles. The paired kinetochore microtubules on each chromosome attach to opposite poles of the spindle. Then follows the *anaphase*, during which the sister chromatids synchronously separate, and each is pulled slowly toward the spindle pole it is attached to. The kinetochore microtubules get shorter, and the spindle poles also move apart, both contributing to chromosome segregation. Anaphase is the shortest stage of mitosis, often lasting only a few minutes. During *telophase*, the two sets of chromosomes arrive at the poles of the spindle. A new nuclear envelope reassembles around each set, completing the formation of two nuclei and marking the end of mitosis. The division of the cytoplasm begins with the assembly of the contractile ring. In the end, at *cytokinesis*, the cytoplasm is divided in two by the contractile ring made of actin and myosin filaments, which pinches in the cell to create two daughters, each with one nucleus.

Molecular control system of the cell cycle

But how is the cell cycle regulated in each individual cell? We know for a fact that the frequency of cell division varies with the type of cell. For example, human skin cells divide frequently while on the other hand some of the most specialised cells, such as muscle and nerve cells, do not divide at all in a mature human. The timing and rate of cell division of each different cell type is crucial to normal growth, development and maintenance. These cell cycle differences among different cell types in one organism are regulated at the molecular level. Indeed, the cell cycle is driven by specific signalling molecules present in the cytoplasm. This cyclically operating set of molecules triggers and coordinates key events in the cell cycle. The *cell cycle control system* is

subject to both internal control and external adjustment, being regulated at certain checkpoints by both internal and external signals.

A *checkpoint* in the cell cycle is a control point where stop and go-ahead signals can regulate the cycle. Many signals registered at checkpoints come from cellular surveillance mechanisms inside the cell; the signals report whether crucial cellular processes that should have occurred by that point have in fact been completed correctly and thus whether or not the cell cycle should proceed. Checkpoints also register signals from outside the cell. In mammalian cells the most important checkpoint is the G1 one (also called restriction point). If a cell receives a go-ahead signal at the G1 checkpoint, it will usually complete G1, S, G2 and M phases and divide. If it does not receive a go-ahead signal at that point, it will exit the cycle, switching into a non dividing state called the *G0 phase*. Most cells in the human body are in the G0 phase.

The cell cycle is actually coordinated by rhythmic fluctuations of the abundance and activity of the cell cycle control molecules present in the cytoplasm. These regulatory molecules are mainly two types of proteins, namely *protein kinases* and *cyclins*. *Protein kinases* are enzymes that activate and inactivate other proteins by phosphorylating them. Specific protein kinases give the go-ahead signals at the G1 and G2 checkpoints. Many of these kinases are present at a constant concentration in the growing cell, but much of the time they are in an inactive form. To be active such a kinase must be attached to a *cyclin*, a protein that its concentration cyclically fluctuates in the cell. Because of this requirement, these kinases are called *cyclin-dependent kinases (cdks)*. The activity of a cdk rises and falls with changes in the concentration of its cyclin partner. For the G1 checkpoint, animal cells have at least three cdk proteins and several different cyclins that operate at this checkpoint. The fluctuating activities of different cyclin-Cdk complexes are crucial to control all the stages of the cell cycle.

5.1.2 Disruptions of the cell cycle during cancer

The normal cell cycle described above is disrupted during cancer, as cancer cells grow and divide out of control. Cancer cells exhibit neither *density-dependent inhibition* nor *anchorage dependence*. *Density-dependent inhibition* is when crowded cells stop dividing while *anchorage dependence* refers to the fact that normal cells in order to divide must be attached on a substrate. Moreover, cancer cells do not stop dividing when growth factors are depleted, indicating that they may produce growth factors themselves or that they may have an abnormality in the signalling pathway that conveys the growth factor's signal to the cell cycle control system even in the absence of this growth factor. Another possibility is that the cell possesses an abnormal cell cycle control system. Important differences between normal cells and cancer cells indicate derangements of the cell cycle. If and when they stop dividing, cancer cells do so at random points in the cycle, rather than at the normal checkpoints. Furthermore, cancer cells can go on diving indefinitely in culture if they are given a continuous supply of nutrients. Conversely, nearly all normal mammalian cells growing in culture divide only about 20 to 50 times before they stop dividing, age and die.

The abnormalities and variations in cell cycle kinetics result in various clinical responses. For that reason, cell cycle specific chemotherapy is a promising approach for improved clinical outcomes by focusing on the continuously changing vulnerability of cancer cells. Typically cancer cells over express cyclins and loose the expression of cdks [280]. Because of the importance of cdks in the regulation of growth, many therapeutic strategies involve the development of specific kinase inhibitors that would block cell cycle progression and induce growth arrest. In addition, cancer cells acquire an incompetent checkpoint control system, resulting in aberrant responses to cell damage. For example, despite cellular damage a cancer cell will pass to the S or M phase producing in that way a malignant daughter cell. However, cells with compromised checkpoint control usually are more sensitive to further DNA or microtubule damage.

Uncontrolled cell cycle progression in the presence of such a damage is usually fatal, possibly being the reason of the increased sensitivity of some cancer cells to DNA-damaging treatments. Thus, targeting intact cell cycle components can be a promising therapeutic strategy next to conventional chemotherapy and radiation. Typical strategies include the following [280]:

- Inhibition of cdk activity during G1 phase [281, 282]
  - Ectopic cdk inhibitor replacement and growth arrest [283, 284]
  - Cdk inhibitor replacement and cytotoxicity [285, 286]
  - Pharmacologic cdk inhibitors [287]
  - Second generation cdk inhibitors [288, 289]
- Targeting S phase events
  - S phase progression [290]
- Abrogation of the G2 checkpoint
  - G2/M transition [291, 292]
  - G2 checkpoint inhibitors [293, 294]

The potential of cell cycle phase specific drugs has also led to the development of various mathematical models to improve the design of scheduling of such drugs [295].

5.2 Chemotherapy basic concepts

Modern conventional chemotherapy began in the 1940s with the advent of molecular medicine in the latter half of the twentieth century. Before that, therapeutic strategies mainly included surgical interventions [296]. One of the first families of drugs used to fight malignancies constitutes molecules with a structure related to mustard gas, which was used as a weapon in World War I. Single drug treatments were widely practiced until the 1960s when the term *combination chemotherapy* was first introduced by DeVita and coworkers [297] who extended to lymphomas the actual first clinically curative combination chemotherapy for childhood ALL by Holland, Frei and Freireich. The main idea of combination chemotherapy is to combine drugs with different modes of actions to increase the likelihood of synergistic anticancer effects.

Two main classes of antineoplastic drugs can be distinguished, conventional molecules and target specific molecules [298]. Targeted therapies were first introduced in the 1990s, after various molecular and genetic approaches led to the discovery of new signalling networks that regulate cellular processes altered in cancer such as proliferation and survival. Possible targets include various growth factors, signalling molecules, cell cycle proteins, apoptosis modulators and molecules promoting angiogenesis [299]. Despite the fact that are considered more promising due to their increased precision and reduced side effects, conventional antineoplastic drugs are still widely used. Conventional antineoplastic drugs are highly chemically active, which results in their anticancer activity but also constitutes their main drawback, which is excessive toxicity. Based on their action on the DNA molecule, conventional antineoplastic drugs can be categorised in three main different subgroups:

- Molecules acting on DNA synthesis (antimetabolites)
- Molecules directly affecting DNA (alkylating agents, intercalating agents and topoisomerase inhibitors)

- Molecules affecting mitosis (antitubulin agents)

Below the classes of conventional chemotherapy drugs used in the present chapter, namely *topoisomerase inhibitors* and *vinca alkaloids* will be briefly presented.

5.2.1 Topoisomerase inhibitors

Topoisomerases enzymes are mainly responsible for the cleavage and annealing of the DNA molecule during replication and transcription. Two types of topoisomerases exist, namely type I and II. Type I acts on one strand of the DNA molecule, while type II acts on both strands of the DNA. Inhibitors of these enzymes are widely used as anticancer agents. Two types of topoisomerase II inhibitors are the podophyllotoxins and the most widely used anthracyclines. The anthracycline antibiotics are produced by the fungus *Streptomyces percetus* var *caesius*. They share a common chemical structure, with a basic anthracycline structure containing a glycoside bound to an amino sugar, daunosamine. Anthracyclines have several modes of actions. They are potent inducers of double strand breaks in DNA, and can cause cell cycle arrest at the G2 phase, the latter occurring by disrupting the interaction between topoisomerase II and cdks. Topoisomerase II inhibitors can cause a wide range of chromosomal aberrations, and can act by either stabilising topoisomerase II - DNA complexes, or by interfering with the catalytic activity of the enzyme, both resulting in double-strand breaks in the DNA.

In the present study we used Daunorubicin (DNR), an anthracycline antibiotic, which stabilises the topoisomerase II complex after it has broken the DNA chain for replication, preventing the DNA double helix from being released and thereby stopping the process of replication. DNR is thus expected to act throughout the whole cell cycle and especially strongly during DNA replication in S-phase. Among various neoplasms, DNR is most commonly used to treat Acute Myeloid Leukemia (AML), Acute Lymphoblastic Leukemia (ALL) and Acute Promyelocytic Leukemia (APL) [300, 301].

5.2.2 Vinca alkaloids

Vinca alkaloids are derived from the *Vinca rosea* plant and they target tubulin, which polymerise into microtubules, a major component of the eukaryotic cytoskeleton. Upon entering the cell, vinca alkaloids bind rapidly to tubulin. Blocking microtubule polymerisation results in a impaired mitotic spindle formation during the M phase [302, 303]. The mitotic spindle is the macromolecular machine that segregates chromosomes to two daughter cells during mitosis. The major structural elements of the spindle are microtubules, whose intrinsic polarity and dynamic properties are critical for bipolar spindle organisation and function. Vinca alkaloids are also thought to increase apoptosis by increasing concentrations of p53 (cellular tumour antigen p53) and p21 (cyclin-dependent kinase inhibitor 1) and by inhibiting Bcl-2 activity [304–308]. Increasing concentrations of p53 and p21 lead to changes in protein kinase activity, phosphorylation of Bcl-2 subsequently inhibits the formation Bcl-2-BAX heterodimers, resulting in decreased anti-apoptotic activity. Nevertheless, cells have developed resistance against the vinca alkaloids by utilising drug efflux.

Herein, we used Vincristine (VCR) as an M-phase dependent drug. VCR was isolated in 1961 [309] and it is used to treat many types of cancer, including ALL, AML, Hodgkin's disease, neuroblastoma, and small cell lung cancer among others. VCR works partly by binding to the tubulin protein, thus stopping the cell from separating its chromosomes during the metaphase; the cell then undergoes apoptosis. Since VCR's mechanism of action targets all rapidly dividing cell types, it not only inhibits cancerous cells but can also affect the intestinal epithelium and bone marrow. At high concentrations, it stimulates microtubule depolymerisation and mitotic

spindle destruction. At lower clinically relevant concentrations, VCR blocks mitotic progression. Upon VCR addition, progression from metaphase to anaphase is blocked and cells enter a state of mitotic arrest. The cells may then undergo one of several fates [46]. Tetraploid cells may undergo unequal cell division producing aneuploid daughter cells. Alternatively, they may exit the cell cycle without undergoing cell division, a process termed mitotic slippage or adaptation. These cells may continue progressing through the cell cycle as tetraploid cells (Adaptation I), may exit G1 phase and undergo apoptosis or senescence (Adaption II), or may escape to G1 and undergo apoptosis during interphase (Adaptation III). Another possibility is cell death during mitotic arrest. Alternatively, mitotic catastrophe may occur and cause cell death.

5.2.3 Heterogeneity of cancer cell populations and in drug response

Cell-to-cell response variability is prominent during numerous cell processes, even in clonal cell populations [4]. The potential sources of this heterogeneity in responses are not well defined. They can be genetic or epigenetic differences, differences in the cell cycle phase, or stochastic fluctuations in biochemical reactions. Cell heterogeneity is also prominent in cancer. Cancer is an intrinsically highly diverse disease; tumours of any different histological type not only exhibit genetic diversity but also display their variation when exposed to all forms of chemotherapy [43, 44, 310–312]. Even within the same tumour, different cell subpopulations are found. How these different subpopulations contribute to the disease progression but also how differently they respond to any given therapeutic intervention is still not clear. Nonetheless, drug resistance is often attributed to this intra-tumour heterogeneity [313]. This heterogeneity is also evident in the molecular make up of the each tumour cell, since a tumour cell might be aneuploid, i.e. having abnormal number of chromosomes, it may have gene deletions or amplifications and it generally might be characterised by extensive genetic instability [314]. Variations in cell cycle kinetics are dynamic in time and include different cell cycle durations, different proliferation and apoptosis rates but also differences of the S-phase and quiescent cell fraction.

Intra-tumour heterogeneity is often modelled using evolutionary principles [49, 315, 316]. In this type of models, the tumour is regarded to have derived from a single cell that acquired a mutation in a critical gene and that this mutation passed on the offsprings that continue to acquire more genetic or epigenetic mutations that ultimately result in a fully transformed malignancy compromising numerous clonal variants. Two are the main tumour evolution models that have been proposed, namely the *cancer stem cell model* and the *clonal evolution model* [316, 317]. According to the *cancer stem cell model* differentiated cancer cells are progeny of cancer stem cells and they are not able to undergo self-renewing cell division. Consequently, only cancer stem cells can accumulate additional genetic changes that can drive tumour progression and drug resistance. Data from patients with AML strongly support this model [318, 319]. On the other hand, based on the *clonal evolution model* tumour cell phenotypes are determined based on the combination of cell type of origin of the tumour-initiating cell, acquired genetic and epigenetic alterations, and paracrine signals from surrounding cells. Cellular phenotypes are unstable, thus can change as the tumour evolves. In this case, all tumour cells can undergo self-renewing division. As a result, any tumour cell has the potential to contribute to tumour progression and drug resistance. These two models are not mutually exclusive and their combination is also possible.

Furthermore, mathematical models have been developed to describe the intrinsic heterogeneity and growth of cancer cells [320, 321]. The intrinsic heterogeneity is the other side of the coin, of which heterogenous responses even in clonal populations are not cancer related, but arise from stochastic biological processes, which are nevertheless tightly regulated in nature. Because of these intrinsic mechanisms the system, the cell uses to integrate information and respond, becomes even more complex. One such example is the cell cycle, which is regulated

by many different components (as mentioned above in section 5.1.1). However, these components operate under different conditions and external cues that continuously change. In order to maintain an ordered cell cycle mechanism variations in gene expression [322], cell cycle duration [323], cell size [324] and time to death [325, 326] must exist. In the two models reported in Greene et al. [320], the growth of cancer cells is described as a dynamic transition between proliferative and quiescent states. These models predict variations in growth as a function of the intrinsic heterogeneity i.e. heterogeneity originating from the durations of the cell cycle and apoptosis, cellular densities dependencies are also included. Based on these models, it is shown that the duration of the cell cycle has a noticeable impact on the growth dynamics. However, experimental data to investigate this dependency are still needed.

In conclusion, intra-tumour heterogeneity relates to the variation in genome, epigenome, proteome and cell and tissue behaviour found in an individual tumour and its stromal constituents i.e. its micro-enviroment. In addition, identical clones inside a tumour are also heterogenous due to stochastic variations [313]. Analysing sister cells in parallel is a useful strategy to study the sources of heterogeneity, whether or to what extent it originates from proteome and stochastic variations or genetic differences (see next section 5.2.4). It is essential to understand the sources of this heterogeneous response of the cancer cell population, in order to design (but also combine) novel and potent agents that target with high specificity the malignant cells and at the same time they do not cause adverse toxicities. Apart from targeted therapeutics, chemotherapy drugs are still widely used and resistance to chemotherapy is a key factor of whether a treatment will be successful or not, thus single-cell platforms able to track how heterogeneity affects and is affected by a given treatment are needed.

5.2.4 Sister cell heterogeneity

Sister cells response variability is a hot topic lately since it can shed light on whether different phenotypes stem from genetic or epigenetic differences or from differences in the protein state of the cells. There have been contradictory results depending on the cell process that was interrogated. For instance, it has been previously reported that sister cells undergo apoptosis synchronously [327, 328]. However, in response to anti-mitotic drugs the fate of one sister is independent of the fate of the other [46]. In another study, sister cell fate in response to TRAIL-induced apoptosis correlated, as did also the time-to-death between HeLa sister cells but this correlation decayed as a function of time since division, the time period tested was 8 hours. Based on this observation, the *transient heritability* in fate model was proposed, which states that protein synthesis promotes cell divergence so that sister cells soon become no more similar to each other than random paired cells [326].

5.3 Micro-trenches array

As explained above, cell population heterogeneity is not only prominent in cancer and in the response to a given drug but also in almost every cell process. Yet it is not clear whether this observed heterogeneity contains any relevant information. For example, one might hypothesise that ensemble averages might reflect the dominant biological mechanism operating within each single cell of a population. However, it is known that population distributions can obscure rare or small subpopulations of cells [15, 18].

In addition, variability in the onset of apoptosis among cells even in clonal populations has been reported before [325–330]. As mentioned above, the apoptotic activity is tightly synchronized among related cells, since nearby cells underwent apoptosis at similar times [327] and that heterogeneity in response to TRAIL-induced apoptosis between sister cells has been

also observed [326]. In this case, it was suggested that cell-to-cell difference in the timing and probability of death is transiently heritable and subsequent heterogeneous responses emerge from cell-to-cell differences in protein levels that exist before drug exposure. Sister cells have identical genetic material; thus, studying the responses between sister cells can straightforwardly indicate whether the response variability stems from genetic/epigenetic differences or not.

Nevertheless, tracking of single cells in time-lapse microscopy movies is still a challenging problem, especially for non-adherent cells, since they loosely attach on the surface, and disappear from the field-of view very fast, within a few hours. Different automatic methods have been proposed and compared [331], but due to quick cell movement, high cell densities, and difficult cell identification e.g. due to shape, time intensive manual tracking becomes necessary to achieve accurate tracks [332]. Moreover, manual tracking remains the only reliable way to distinguish sister cells among a cell population. The confinement of single cells into well-defined spatial structures can remedy the situation and allow for the application of automatic tracking with high accuracy. Consequently, platforms that confine a family of cells derived from one single cell are a useful tool to enable the automatisation of the image analysis and to yield in a faster and effortless way data that can address these questions regarding the sources of cell-to-cell response variability.

Here we introduce a platform that enables the continuous observation of families of cells derived from individual cells. The platform employs arrays of micro-trenches optimised to observe cells for two consecutive generations. Micro-trenches have a size of 30x120 μm and are made of PEG-DA (MW 258). Thus, they accommodate four to six cells. By seeding a low concentration of cells we could have trenches occupied with only one single cell that divided over time, as a result we efficiently compartmentalised the cell population into genetically identical cell families. Moreover, compartmentalisation of the cell population not only reduces the error of mixing the identities of adjacent cells but also the time and computational power needed for tracking.We demonstrate that automated image analysis is feasible and enables determination of cell cycle duration distribution functions and sister cell correlations. A key feature of the platform is the direct and parallel observation of many cells with individual cell cycles in parallel (see figure 5.2).

A phase contrast image of the micro-trenches array occupied with cell families is shown in figure 5.2a and an illustration of the micro-trenches with cells inside in figure 5.2b. A single-cell divides twice and forms of a genetically identical cell family (see figure 5.2c). The ratio of the width of a micro-trench to the diameter of a cell, which is around 1.5-2, prevents any confinement stress on it. The division time point is indicated with t_0 and the second one with t_1. In figure 5.2d, the representative time-lapse frames illustrate the tracking procedure over the time of two divisions, from one mother to four granddaughters. The tracking algorithm can successfully discriminate the different daughter cells, provided that cells keep their initial alignment, which is indeed kept to a great extent due to the small width of the micro-trench. Applying automated tracking in the phase contrast images, we successfully tracked 50% of the total cell population tested.

5.3.1 Monitoring cell clones for consecutive generations

Theoretical models of cell division

In bacteria it was hypothesised that cell growth and division are coupled through a cell size threshold, however recent experimental observations suggest that cells attempt to add a constant volume from the time of initiation of DNA replication to the next initiation event [333] or that cells divide after growing on average a certain amount, irrespective of the length at birth [334]. On the contrary, in somatic cells such a regulation may not exist at all, since their size regulation

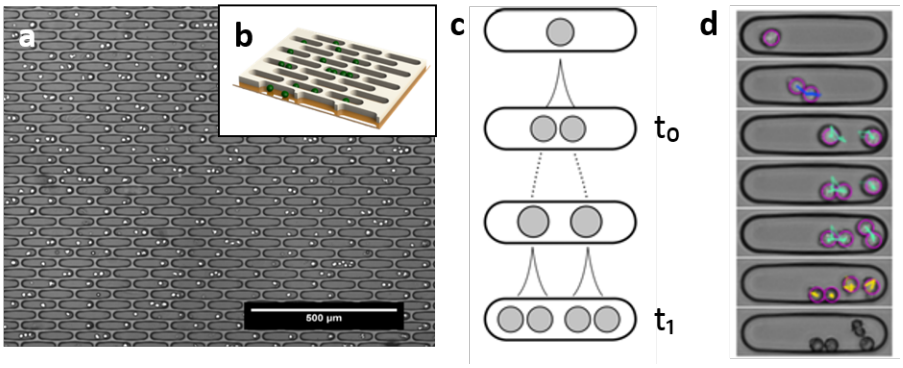

Figure 5.2: The micro-trenche array enables long-term observation of cell lineages derived from a single cell. (a) Phase contrast image of micro-trenches loaded with cells. (b) Schematic 3D representation of the 20 μm deep trenches. (c) Schematic diagram of cell division events at times t_0 and t_1 within a single micro-trench. (d) Time-lapse phase contrast images and cell time traces showing that the identity of single cells within the family tree can be followed over time.

might be a result of external growth or mitogenic signals from their microenvironment. However, after observing cells for 50 hours, it has been shown that the volume added across the cell cycle is independent of cell birth size and it is proposed that this type of size regulation can arise from various types of coupling between cell size, cell growth and cell cycle progression [335]. It has also been proposed, based on a coupled mathematical model of mammalian cell cycle and circadian clock, that the circadian clock triggers critical size control in the mammalian cell cycle and that it is more readily observed in cell lines that contain circadian rhythms [336]. Microfluidic devices have facilitated single-cell studies and boosted the collection of quantitative experimental data, such as the measurement of single-cell mass with high accuracy [337]. Measuring the cell size or the volume added to the cell after its mother division are crucial quantitative data to elucidate the underlying mechanisms that drive cell division. The micro-trenches array coupled with time-lapse microscopy and automated image analysis is a step toward this direction.

Pearson's correlation coefficient

In statistics, correlation coefficients are used to measure how strong a relationship between two variables may be. In linear regression the most commonly used correlation coefficient is the *Pearson's correlation coefficient* or (*Pearson Product Moment Correlation (PPMC)*). The greek letter ρ is used to represent the Pearson correlation coefficient of a population and the letter r is used for a sample. The most common formulas to calculate the Pearson's correlation coefficient are:

$$r = \frac{N\sum x_i y_i - (\sum x_i \sum y_i)}{\sqrt{[N\sum x_i^2 - (\sum x_i)^2][N\sum y_i^2 - (\sum y_i)^2]}} \tag{5.1}$$

where,

- N is the sample size
- x_i, y_i are the single samples indexed with i

or

$$r = \frac{s_{xy}}{s_x s_y} \tag{5.2}$$

where,

- s_x, s_y is the sample standard deviations
- s_{xy} is the sample covariance

For the population correlation coefficient we have:

$$\rho = \frac{\sigma_{xy}}{\sigma_x \sigma_y} \tag{5.3}$$

The population correlation coefficient has the σ_x and σ_y as the population standard deviations and σ_{xy} as the population covariance.

The formulas return a value between -1 and 1, where 1 indicates a strong positive relationship, -1 indicates a strong negative relationship and 0 indicates no correlation at all.

Lognormal distribution

A *lognormal distribution*, also known as *log-normal* or *Galton distribution*, is a continuous probability distribution of a random variable whose logarithm is normally distributed. Skewed distributions with low mean values, large variance, and with all values positive often fit the lognormal distribution. The probability density function of this distribution is:

$$\mathrm{LogNorm}(x, \mu, \sigma, p) = \frac{N}{c_{\mathrm{LN}}} \frac{1}{x^p} \exp\left(-\frac{\ln(x/\mu)^2}{2\sigma^2} \right) \tag{5.4a}$$

$$c_{\mathrm{LN}} = \sqrt{2\pi}\, \sigma\, \mu^{1-p} \exp\left((1-p)^2 \frac{\sigma^2}{2} \right) \tag{5.4b}$$

where σ is the width parameter, p a shape parameter, μ is the location parameter. c_{LN} is chosen so that $\int_0^\infty \mathrm{LogNorm}(x, \mu, \sigma, p)\, dR = N$. The mode of the distribution is defined as

$$x_{\mathrm{mode}} = \mu e^{-p\sigma^2} \tag{5.5}$$

and the n^{th} moment $\langle X^n \rangle$ of the `LogNorm` distribution as

$$\langle X^n \rangle = \frac{\int X^n \,\mathrm{LogNorm}(X)\, dX}{\int \mathrm{LogNorm}(X)\, dX} = \mu^n\, e^{\frac{1}{2}\sigma^2 n(2-2p+n)} \tag{5.6}$$

Gamma distribution

A *gamma distribution* is a general type of statistical distribution that arises naturally in processes for which the waiting time between Poisson distributed events are relevant. Gamma distributions have two free parameters, namely α and θ. The general formula for the probability density function of the gamma distribution is:

$$f(x) = \frac{(\frac{x-\mu}{\beta})^{\gamma-1} \exp\left(-\frac{x-\mu}{\beta}\right)}{\beta \Gamma(\gamma)}, x \geq \mu, \gamma, \beta > 0 \tag{5.7}$$

where γ is the shape parameter, μ is the location parameter, β is the scale parameter and Γ is the gamma function:

$$\Gamma(a) = \int_0^\infty s^{a-1} e^{-s} ds \tag{5.8}$$

When μ=0 and β=1, we have the *standard gamma distribution*, which is:

$$f(x) = \frac{x^{\gamma-1} \exp\{x\}}{\Gamma(\gamma)}, x \geq 0, \gamma > 0 \tag{5.9}$$

Cell cycle duration determination

The cell cycle duration has the most significant effect on the growth dynamics of the tumour [320]. Using the micro-trenches array, we detected cell division time points of two consecutive cell divisions and studied the distribution of the cell cycle duration. In this array, sister cells are compartmentalised and can be easily distinguished, permitting the straightforward correlation of the cell cycle duration between sister cells. After the first division of a single starting cell, a micro-trench contains two daughter cells that can be separately tracked (see figure 5.3). For each cell, we determine the first division time point t_0, the division of the first daughter cell at time t_1, and the division of the second daughter cell at t_2 (Figure 5.3a). In our experiments 320 MOLM-13 starting cells were observed for 40 hours and at least two divisions. The cell cycle duration distribution with a mean of 19.7 ± 2.6 (mean ± std, n=320 cells) hours is well described by both a log-normal distribution and a gamma distribution (Figure 5.3b). For clones where both t_1 and t_2 were observed (n=320), we analysed the difference between the cell cycle durations for sister cells. The distribution of sister cell differences has a mean of 2.3 ± 2.7 hours (mean ± std, n=85 pairs of sister cells) and is well fitted with an exponential distribution (Figure 5.3c). Compared to randomly paired cells, the cell cycle duration of sister cells is highly correlated, with a Pearson correlation coefficient of r=0.85 ± 0.04 as compared to r=0.25 ± 0.09 for randomly paired cells (Figure 5.3d), in agreement with a previous study [338].

Herein, we observed that the cell cycle duration distribution falls into a lognormal distribution and it has also been reported that the size of mammalian cells also falls into a lognormal distribution [339, 340]. Cell size distributions should be determined by the growth and division processes [341] and the kinetics of division fragmentation processes are known to yield lognormal distributions under certain conditions [342].

5.3.2 Monitoring cell response to chemotherapeutic drugs

Cell cycle components are altered in cancer and depending on the phase of the cell cycle when a drug is administered, it can be either cytostatic or cytotoxic [280]. For that, we further utilised the micro-trench array as a clocking device to assess the phase of the cell cycle without the use of a molecular indicator. The main principle is that if we monitor one single cell until it divides, we then can roughly assess the cell cycle phases of the two daughter cells. In this way, we can test whether the activity of standard chemotherapeutic drugs is affected by the phase of the cell cycle in a quantitative manner. To test this hypothesis we chose two widely used chemotherapeutic drugs; VCR and DNR. Vincristine (see details in 5.2.2), an antitumor vinca alkaloid, binds to the tubulin protein and thus stops the cell from separating its chromosomes during metaphase, due to this mitotic arrest cell death follows. For that reason it is considered an M-phase dependent drug. On the other hand, daunorubicin (see details in 5.2.1), an anthracycline aminoglycoside antineoplastic, intercalates on DNA and inhibits the function of the enzyme topoisomerase II during transcription and replication, so it is expected to act throughout the whole cell cycle. Both drugs, among other neoplasms, are used to tackle many types of leukaemia such as Acute

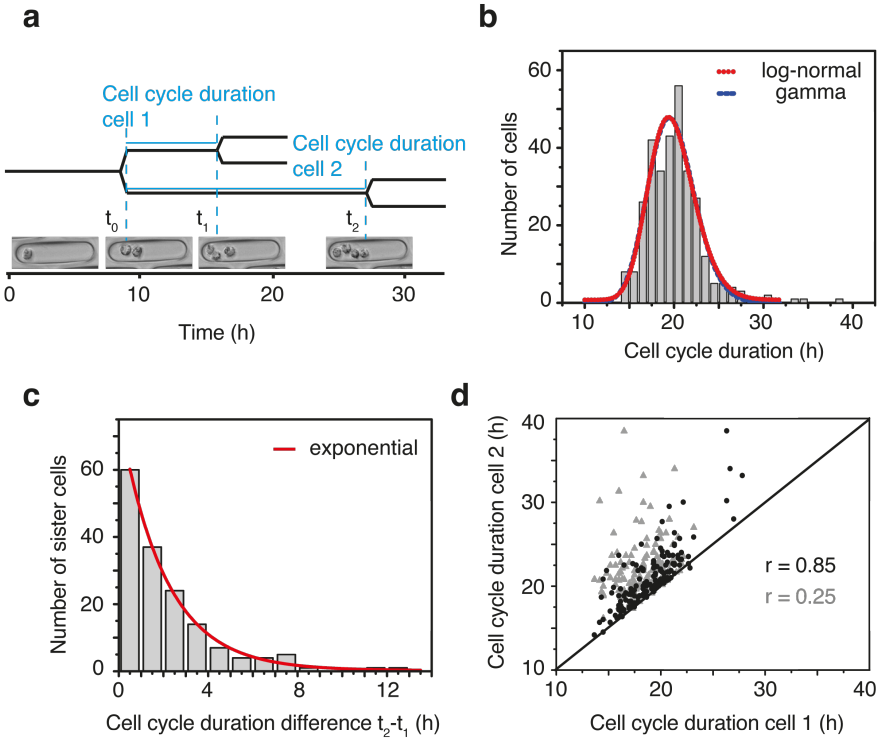

Figure 5.3: Cell cycle duration distribution. (a) Schematic representation of the individual time spans from one cell division event to the next. The axis at the bottom indicates the time in hours and shows the corresponding phase contrast images at selected time-points. (b) Measured distribution of the cell cycle duration from an ensemble of 320 cells (MOLM-13) showing mean cell cycle duration of 19.7 hours and standard deviation 2.6 hours. The dotted red line corresponds to a log-normal fit and the dashed blue line to a gamma distribution fit. (c) Distribution of the difference between the cell cycle duration of sister cells. The difference in the cell cycle duration time is fitted with an exponential curve (red line). (d) Correlation of the cell cycle duration for sister cells (black dots) is higher (Pearson correlation coefficient r = 0.85 ± 0.04) than randomly paired cells (grey triangles, r = 0.25 ± 0.09).

Myeloid Leukeamia (AML) [343, 344]. In figure 5.4 a schematic of the cell cycle and where exactly VCR and DNR are expected to act is presented.

Unsynchronised cell population

We utilised the micro-trench array to observe and study the dependence of VCR/DNR induced apoptosis on the cell cycle phase of a heterogeneous, in terms of synchronisation, MOLM-13 cell population directly from the cell culture flask. Mother cell mitosis, i.e. the division time (t_0), is used as a reference point of the cell-phase indication. In order to obtain the background of each individual cell, we let the cells to divide at least once and added at the 20th hour of the measurement, based on the division time distribution (Figure 5.3b), the drugs (VCR or DNR). In this way, we analysed the fate of the daughter cells, for which we knew their mother's division time point. To track the cells we used out of focus (-20 μm) phase contrast images before adding the drug. For detecting the death times we used fluorescence images of the propidium iodide (PI) marker for the VCR data and of the Cell Event™Caspase 3/7 marker for the DNR data, since

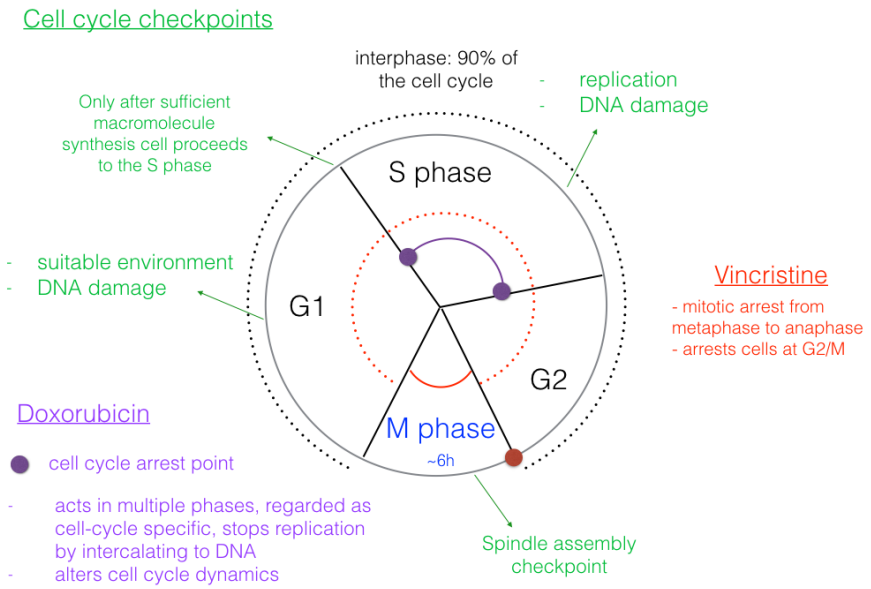

Figure 5.4: Depiction of VCR and DNR effects on the cell cycle.

DNR is auto-fluorescent in the red region. A timeline of the experimental procedure is shown in figure 5.5a. Plots in figure 5.5b show for each different drug concentration the distribution of the time-to-death of the single cells tracked i.e. the time passed after adding the drug until the cell died. The black curves represent the Kernel density estimation of the probability density function of each histogram. As expected only a few cells are dead in the control, when no drug is added, while the percentage of dead cells rises with increasing vincristine concentration. For 10 and 100 nM vincristine concentrations, the number of dead cells increases after 12 hours, indicating that cells can be resistant for the first hours after drug exposure. In figure 5.5c, for each different drug concentration, a scatter plot of the time passed in the cell cycle, i.e. the time passed from the division until the drug was added, with the time-to-death. The blue lines are best linear fits and show the dependence of the time-to-death on the time spent in the cell cycle. While in the control the correlation is slightly positive, with increasing vincristine concentration the correlation gets increasingly negative. At the highest concentration, 1000 nM, no correlation is observed. Phase independent apoptosis induced by microtubule targeting agents have been reported in previous studies utilising cell lines and relatively high drug concentrations [345–347], alternatively the reason for no correlation in the 1000 nM vincristine might be that side effect toxicities are prominent. The coloured areas indicate the cell cycle phase based on the division distribution in figure 5.3b, the duration for each phase is calculated based on the phase durations proposed in T. S. Weber et al. 2014 [348]. Green denotes the G1 phase, pink the S phase and blue the G2/M phases. The negative correlation between the time spent in the cell-cycle and the time-to-death in the case of vincristine is expected, since it is known that at high concentration vincristine stimulates microtubule depolymerisation and mitotic spindle destruction, while at lower clinically relevant concentrations, it blocks mitotic progression. Hence, a cell that spent a large amount of time in the cell-cycle should be closer to the M-phase so it should have a shorter time-to-death. On the other hand, in the daunorubicin induced cell death the no correlation is observed between the time the cell passed in the cell cycle and the time-to-death (see figure

5.6).

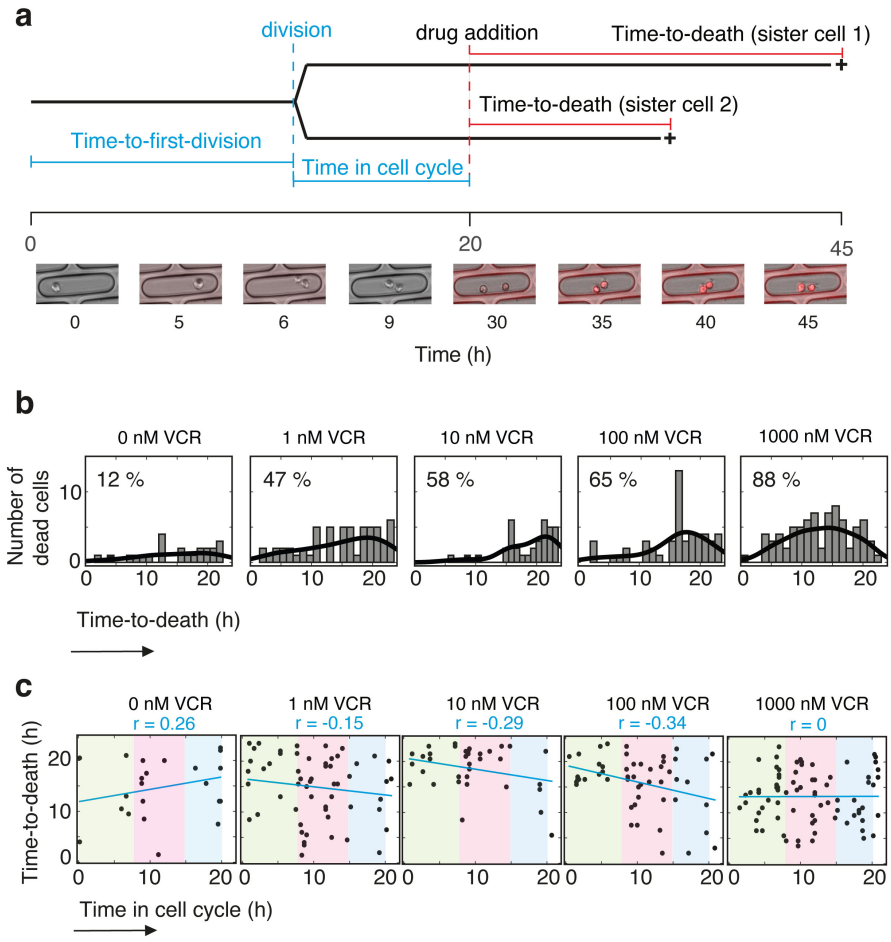

Figure 5.5: Unsynchronised cell population: distributions of the time-to-death induced by Vincristine. (a) Schematic description of the experimental procedure. Image acquisition starts at time 0 h and after a set time (20 hours), vincristine is added. Tracking of the individual cells gives the division time of each mother cell, which is different in each micro-trench, and the time-to-death of the two daughter cells. Images show an exemplary cell dividing before drug addition; both of its daughter cells die (overlay of the in-focus phase contrast and PI fluorescence images). (b) Distribution of the time-to-death for all tracked cells. The black lines represent the Kernel density estimation of the probability density function in each drug treatment. The overall percentage of dead cells is given at upper left corner of each plot. (c) Correlation plots between the time passed in the cell cycle and the time-to-death. The blue line is a linear fit to the scatter plot in each drug treatment. The Pearson correlation coefficient (r) is shown for each drug concentration on top of each graph. The coloured areas denote the different cell cycle phases based on the average division time presented in figure 5.3b. Green stands for the G1, pink for the S and blue for the G2/M phase.

Synchronised cell population and comparison

Next, we compare our results of the unsynchronised MOLM-13 cells with a cell population synchronised using a standard protocol. We employed the "double thymidine block" synchro-

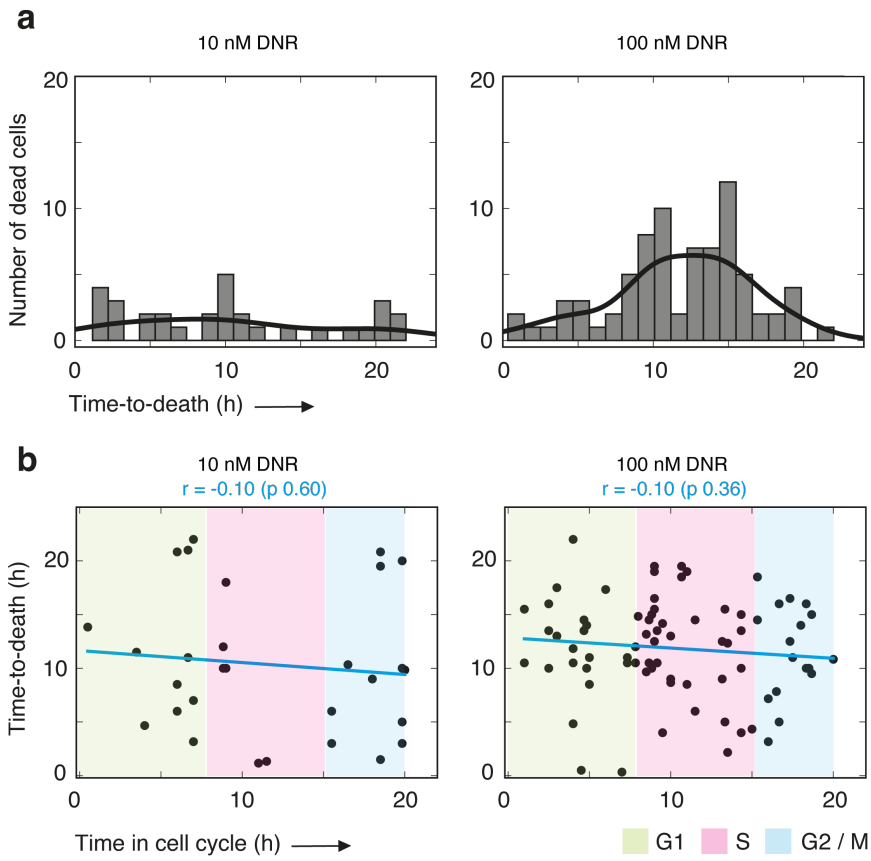

Figure 5.6: Unsynchronised cell population: concentration dependent effects on the time-to-death induced by daunorubicin. (a) Distribution of the time-to-death for all tracked cells. The black lines represent the Kernel density estimation of the probability density function in each drug treatment. (b) No correlation is observed between the time passed in the cell cycle and the time-to-death. The blue line is a linear fit to the scatter plot in each drug treatment. The Pearson correlation coefficient (r) is shown for each drug concentration on top of each graph together with the p-value of the correlation test (in parenthesis). The coloured areas denote the different cell cycle phases based on the average division time presented in figure 5.3b.

nisation procedure [349] on our model cell system, MOLM-13, and performed a cytotoxic test on the micro-trench array. Thymidine is a pyrimidine deoxynucleoside. Deoxythymidine is the DNA nucleoside T, which pairs with deoxyadenosine (A) in double-stranded DNA. High concentration of thymidine interrupts the deoxynucleotide metabolism pathway, by halting DNA replication. As treatment with thymidine arrests cells throughout the S phase, a double thymidine block procedure, which involves releasing cells from a first thymidine block before trapping them with a second thymidine block, is generally used to induce a more synchronised early S phase blockade. Thus thymidine arrests cells at the G1/S border, which is after the division time point t_0 within the length of G1 phase. In our setup, cells were released 3 hours before the start of imaging. We seeded the cells in micro-trenches and we added the drug just before the beginning of imaging. In figure 5.7a, we show a timeline of the experimental procedure. In figure 5.7b, we plot the distributions of the time-to-death for each drug concentration. The black curves represent the Kernel density estimation of the probability density function of each histogram. For all vincristine concentrations the maximum of these distributions is near the

15th hour after starting imaging, indicating that synchronised cells are resistant to vincristine treatments and indeed more than the unsynchronised population (see figure 5.5b), while for the daunorubicin only in the higher 100 nM concentration we observe a maximum round the 12th hour (see figure 5.8a).

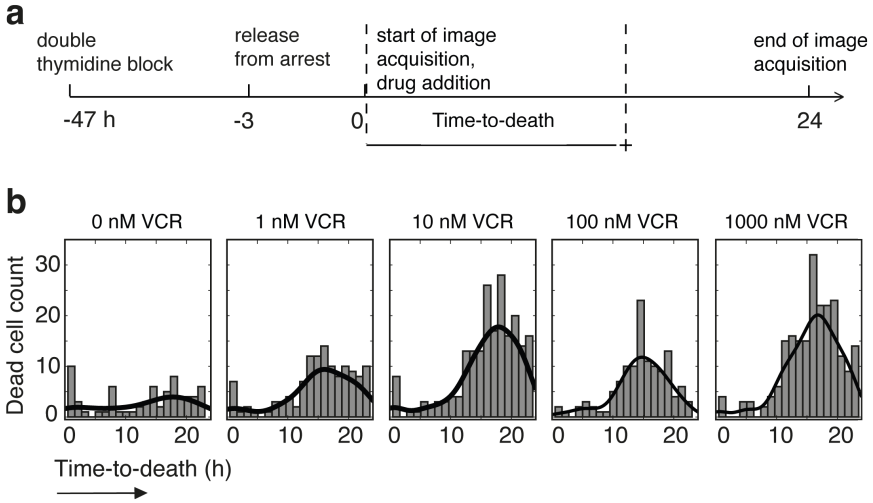

Figure 5.7: Synchronised cell population: distributions of the time-to-death induced by vincristine. (a) Timeline of the experimental procedure. (b) For each drug concentration, the plots show the time-to-death distribution of synchronised cells. The black lines represent the Kernel density estimation of the probability density function in each case.

In figure 5.9 we compare our results of the unsynchronised cell population (see figure 5.5) with a cell population synchronised with thymidine block (see figure 5.7) for the population treated with VCR. For both the unsynchronised and the synchronised population, the total number of dead cells increases with increasing drug concentration (figure 5.9a). For the error bars: we hypothesised that the data follow the binomial distribution; for a confidence level of 95% the error is [350]:

$$\sqrt{1.96\frac{p}{(1-p)N_t}} \tag{5.10}$$

where,

- p is the proportion of dead cells,
- N_t is the total number of cells.

The time-to-death distributions of the unsynchronised (red) and synchronised (blue) population are similar (figure 5.9b). The distributions plotted are the normalised number of cells in all drug treatments, for all cells tracked. Apart from a peak at the beginning of the measurement in the synchronised population, the shape of the two distributions is equivalent. The synchronisation protocol did not affect the shape of the time-to-death distribution also for the cells treated with DNR (see figure 5.8b). In all drug treatments, in the unsynchronised population sister cells are correlated in the time-to-death (Pearson correlation coefficient r = 0.54, p-value: 1.15×10^{-7}), while in the synchronised population, where the cells occupying the same trench are not related, no correlation is observed (r = 0.05, p-value: 0.05). The ellipses indicate the directionality of the correlation (see figure 5.9c).

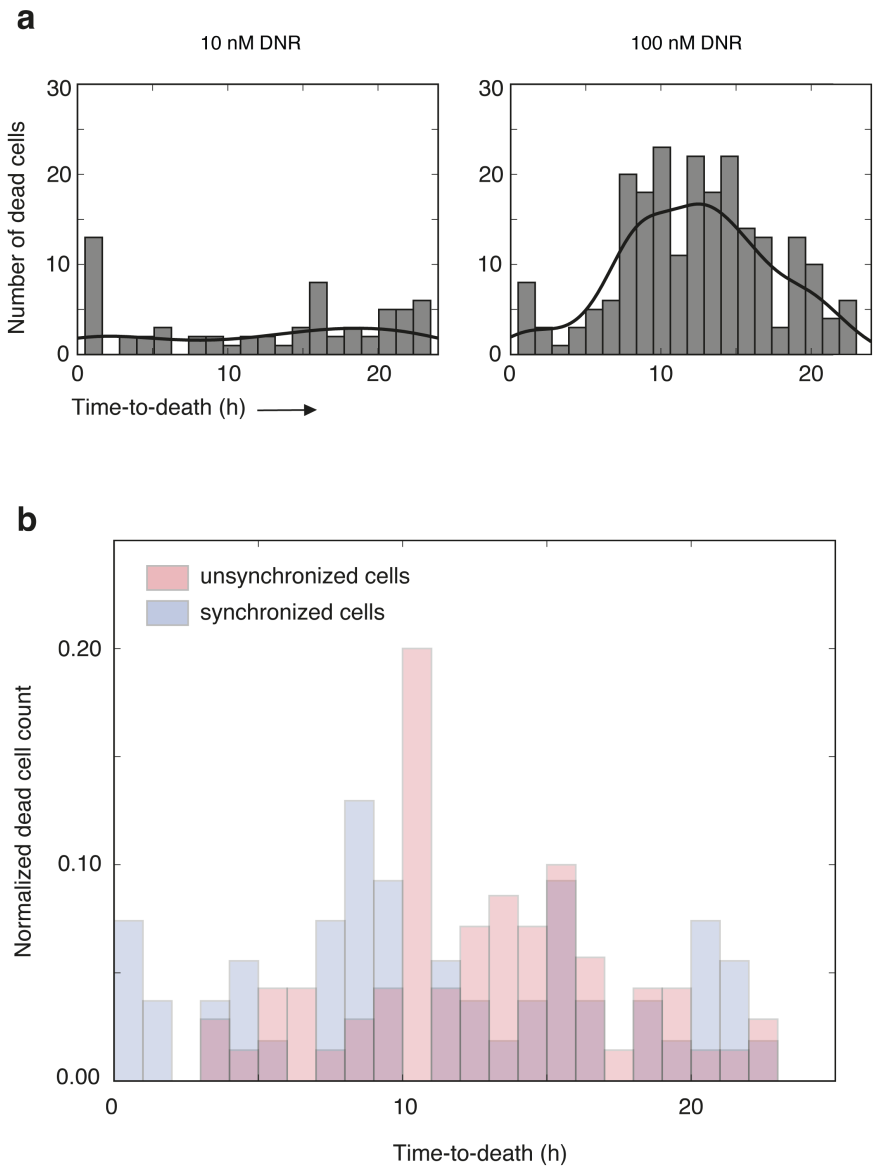

Figure 5.8: Synchronised cell population: distributions of the time-to-death induced by daunorubicin. (a) The time-to-death of all cells is analysed, whether they divided after drug addition or not. For each drug concentration, the plots show the time-to-death distribution of synchronised cells. The black lines represent the Kernel density estimation of the probability density function in each case. (b) The synchronisation protocol does not affect the time-to-death; the shape of both distributions is equivalent.

Herein, we observed similar response between sister cells in the unsynchronised experiment as far as the death time is concerned during an observation period of 24 hours after the addition of the drugs. At the same time the distributions of the death time (average of all different drug concentrations) of the unsynchronised and the synchronised populations are similar, which suggests that synchronising the cells with the double thymidine block does not affect their response to both tested drugs.

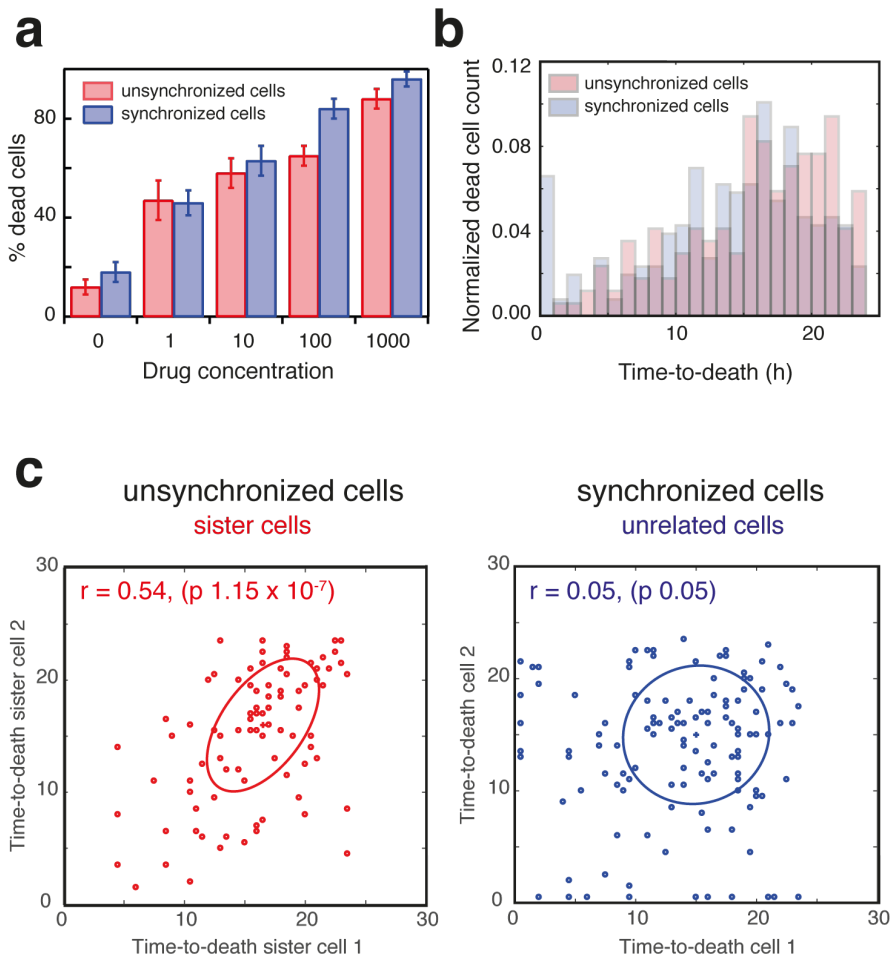

Figure 5.9: The time-to-death between sister cells is correlated in the unsynchronised population. (a) Dose response curve, i.e. percentage of dead cells versus drug concentration for unsynchronised and unsynchronised cells. (b) Distributions of time-to-death of the normalised number of cells across all drug concentrations for both the unsynchronised and the synchronised population. The synchronisation did not affect the death time distribution. (c) Sister cells of the unsynchronised population (n=93 pairs of sister cells) are correlated in the time-to-death (r = 0.54, p-value: 1.15 x 10^{-7}), while for the unrelated cells in the synchronised population (n=129 pairs) no correlation is observed (r = 0.05, p-value: 0.05). The ellipses indicate the directionality of the correlation.

5.3.3 Conclusions and Outlook

Micro-trenches enable a label-free method for tracking cells and for estimating the cell cycle phase without the use of molecular indicators. To our experience, such a label-free approach overcomes the main drawbacks we encountered when tested other popular indicators such as the FUCCI marker [351]. Namely, the low transfection efficiency of 20-40%, generally short duration of the staining (about 15 hours), which was not sufficient for our long-time measurements, and finally insufficient reliability since only around 5% of the cells tested, demonstrated the expected change of colours that correspond to the change of the cell cycle phase. In parallel, by compartmentalising the cell population in small groups, we could boost the image-based

cell tracking. Without the use of such an array, time-lapse observation of cell population for many hours, even beyond 48 hours, is impossible for both adherent and non-adherent cells since they escape from the field of view very fast, within a few hours. Moreover, confining the cells remedies the high error rate of distinguishing two different cells that are moving toward the same direction. By using a phase contrast objective and out of focus acquisition, we could successfully automatically track half of the total cell population and robustly determine the division time points. We further utilised the micro-trenches array to determine the death times of cells after inducing cell death with VCR and DNR, and showed that in the unsynchronised population the death time of sister cells is correlated. In the future, the micro-trenches array can be used with more than one drug, namely for combination therapy, to determine the optimal administration timing of each drug.

Appendix A

Important protocols

A.1 Micromolding in capillaries (MIMIC)

The MIMIC protocol was first introduced in the group of George Whitesides in 1995 [352].
Materials

- Poly(ethylene glycol)-diacrylate (PEG-DA MW 258 g/mol or 575 g/mol), poly(ethylene glycol)-dimethacrylate (PEG-DMA MW 550 g/mol)
- 2-hydroxy-2-methylpropiophenone (photoinitiator)
- PDMS monomer
- Silicon elastomer curing agent (crosslinker)
- 8-well- or 6-channel slide (ibidi®)
- ibidi®coverslips (uncoated) or ibidi®glass slides (# 1.5 H (170 ± 5 μm D 263 Scott glass))

Equipment

- Si wafer with desired structures

Procedure

- Work under the hood (membrane lab) as much as possible, it gives you cleaner final structures.
- Cleaning and wetting steps are critical to have healthy cells in the end.

1. Prepare PDMS stamp by mixing PDMS with the crosslinker (10:1 ratio) and then curing it in 50 °C for 4 hours or overnight. To get rid of bubbles in the PDMS/crosslinker mixture use the desiccator before baking it. A thin (approximately 5mm), flexible PDMS is preferable since it will adhere to the surface better and detach easier.
2. Prepare ibidi®coverslips/glasses: Sonicate to clean 10 mins with 70% ethanol, 10 min with distilled water, blow dry with pressurized air gun (at Zeiss microscope).
3. Plasma treatment: Follow plasma cleaner steps, put PDMS upside down (structures exposed) + ibidi®foil. Use argon, 20% power (set the nob at 1.00) for 18 seconds (0.3 minutes).

4. PEG-DA preparation: Mix 98 μL of monomer with 2 μL the of photo activation agent (2%). Monomer is in the fridge (PEG-DA) and photo initiator is in toxic-chemical cabinet (2-Hydroxy-2-methylpropiophenone). Vortex for 15 seconds.

5. Cut the PDMS stamp into the appropriate size and shape based on the type of the ibidi®slide used. The optimal is to have two structured areas per PDMS stamp. Clean the blade with a tissue and isopropanol after every cut. Using a scotch tape clean the PDMS stamps to remove any small particles on the surface. Place the PDMS stamps at the appropriate positions, put a drop of PEG-DA at the side of each stamp (in front of the structured area) and wait until it flows inside. Make sure there is minimum excess as a wall will be formed at the side, which will prevent proper attachment of the ibidi®sticky slides.

6. Cure PEG-DA under UV light for 15 minutes (UV cleaner).

7. Remove PDMS and cure PEG-DA further in the oven (50 °C) for at least 5 hours (or overnight).

8. Clean the structures with sonication as step 2.

9. Attach the ibidi®sticky slide to the foil, incubate in the oven overnight (this is recommended by ibidi®).

10. Wet the structures at least 2 hours before use. If you are using it right-away use the same medium for incubation. Otherwise PBS is better, exchange it with the medium around 30 min before seeding the cells.

11. Alternatively put the medium in the channels, sonicate it for 3 minutes (this will get rid of bubbles) and exchange with fresh medium.

- PEG-DA or PEG-DMA do not adhere on bare glass, but do so on silanized glass. Use TMSPMA (3-(Trimethoxysilyl)propyl methacrylate) to silanize the glass surface: put a drop of TMSPMA on a tissue in a petri-dish together with the glass and let in a desiccator overnight.

- DO NOT DO the plasma step for silanized glass, it destroys the coating.

- You CAN do an Ar-plasma after the structures are cured: instead of step 8.

- Some cell lines prefer the PEG-DA structures coated with fibronectin (e.g. MOLM-13). Coating with fibronectin: After step 9, incubate with 70% ethanol in the desiccator for 2 hours, wash with PBS. Then incubate the structures with a 35 μg/mL fibronectin solution (in PBS) for 45 minutes in the desiccator. Wash the structures with PBS taking care that they are always covered with liquid. Desiccate again for 10 minutes.

A.2 Plasma-induced protein patterning

Materials

- PLL-PEG (2) (2mg/mL) in 150 mM NACL and 10 mM Hepes (ccpro), pH = 7,4 (PLL (20)-g (3.5)- PEG (2), abbreviated PLL-PEG(2), SuSoS)

- FN (1 mg/mL) in PBS (Yoproteins) or anti-human CD15 IgM isotype (BioLegend®)

- PDMS monomer
- Silicon elastomer curing agent (crosslinker)
- Phosphate Buffered Saline (PBS)
- 8-well- or 6-channel slide (ibidi®)
- ibidi®coverslips (uncoated)

Equipment

- Si wafer with desired structures

Procedure

- Prepare PDMS stamp by mixing PDMS with the crosslinker (11:1 ratio), and then curing it in 50 °C for 4 hours or overnight. To get rid of bubbles in the PDMS/crosslinker solution use the desiccator before baking it. A thin (approximately 3-5 mm), flexible PDMS is preferable since it will adhere to the surface better and detach easier.
- Cut with a scalpel the PDMS out of the Si wafer and then using a blade cut it further to the appropriate shape and size depending on the ibidi®slide used. Clean the blade with a tissue and isopropanol after every cut. Using a scotch tape clean the PDMS stamps to remove any small particles on the surface. Place the PDMS stamps at the appropriate positions on the ibidi®coverslips.
- Plasma treatment: Follow plasma cleaner steps, place the iibidi®coverslips together with the PDMS stamps in the chamber. Use oxygen, 70% power (set the nob at 4.50) for 3 minutes.
- After the plasma treatment is over, place the stamps under the hood and add a drop PLL-PEG(2) close to each stamp (4 μL per stamp); The liquid will flow under the stamp due to capillary action. Do not touch the stamp with the tip of your pipette. Incubate for 30 min.
- Prepare protein solution:
  - Target concentration for fibronectin: 35-50 μg/mL, incubation: 45-60 minutes in room temperature
  - Target concentration for IgM antibody: 15 μg/mL, incubation: 60 minutes in room temperature
- Rinse the substrate with PBS and remove the PDMS stamps. Wash additionally two times with PBS. Add the protein solution and incubate for the appropriate time.
- Rinse the substrate several times without letting the surface to dry. After the last washing step, let PBS remain in the dish for at least 5 minutes, then you can exchange with medium and seed your cells.

Bibliography

[1] Walter M Elsasser. Outline of a theory of cellular heterogeneity. *Proceedings of the National Academy of Sciences*, 81(16):5126–5129, 1984.

[2] Sui Huang. Non-genetic heterogeneity of cells in development: more than just noise. *Development*, 136(23):3853–3862, 2009.

[3] Dinesh Kumar Singh, Chin-Jen Ku, Chonlarat Wichaidit, Robert J Steininger, Lani F Wu, and Steven J Altschuler. Patterns of basal signaling heterogeneity can distinguish cellular populations with different drug sensitivities. *Molecular systems biology*, 6(1):369, 2010.

[4] Steven J Altschuler and Lani F Wu. Cellular heterogeneity: do differences make a difference? *Cell*, 141(4):559–563, 2010.

[5] Jeffrey M Levsky, Shailesh M Shenoy, Rossanna C Pezo, and Robert H Singer. Single-cell gene expression profiling. *Science*, 297(5582):836–840, 2002.

[6] Alex Sigal, Ron Milo, Ariel Cohen, Naama Geva-Zatorsky, Yael Klein, Yuvalal Liron, Nitzan Rosenfeld, Tamar Danon, Natalie Perzov, and Uri Alon. Variability and memory of protein levels in human cells. *Nature*, 444(7119):643, 2006.

[7] N Takasuka, MRH White, CD Wood, WR Robertson, and JRE Davis. Dynamic changes in prolactin promoter activation in individual living lactotrophic cells. *Endocrinology*, 139(3):1361–1368, 1998.

[8] Katsuhiko Hayashi, Susana M Chuva de Sousa Lopes, Fuchou Tang, and M Azim Surani. Dynamic equilibrium and heterogeneity of mouse pluripotent stem cells with distinct functional and epigenetic states. *Cell stem cell*, 3(4):391–401, 2008.

[9] Arjun Raj and Alexander van Oudenaarden. Nature, nurture, or chance: stochastic gene expression and its consequences. *Cell*, 135(2):216–226, 2008.

[10] Nicholas Navin, Jude Kendall, Jennifer Troge, Peter Andrews, Linda Rodgers, Jeanne McIndoo, Kerry Cook, Asya Stepansky, Dan Levy, Diane Esposito, et al. Tumour evolution inferred by single-cell sequencing. *Nature*, 472(7341):90, 2011.

[11] Jianbin Wang, H Christina Fan, Barry Behr, and Stephen R Quake. Genome-wide single-cell analysis of recombination activity and de novo mutation rates in human sperm. *Cell*, 150(2):402–412, 2012.

[12] Michael J McConnell, Michael R Lindberg, Kristen J Brennand, Julia C Piper, Thierry Voet, Chris Cowing-Zitron, Svetlana Shumilina, Roger S Lasken, Joris R Vermeesch, Ira M Hall, et al. Mosaic copy number variation in human neurons. *Science*, 342(6158):632–637, 2013.

[13] Takashi Nagano, Yaniv Lubling, Tim J Stevens, Stefan Schoenfelder, Eitan Yaffe, Wendy Dean, Ernest D Laue, Amos Tanay, and Peter Fraser. Single-cell hi-c reveals cell-to-cell variability in chromosome structure. *Nature*, 502(7469):59, 2013.

[14] Ian Chambers, Jose Silva, Douglas Colby, Jennifer Nichols, Bianca Nijmeijer, Morag Robertson, Jan Vrana, Ken Jones, Lars Grotewold, and Austin Smith. Nanog safeguards pluripotency and mediates germline development. *Nature*, 450(7173):1230, 2007.

[15] Hannah H Chang, Martin Hemberg, Mauricio Barahona, Donald E Ingber, and Sui Huang. Transcriptome-wide noise controls lineage choice in mammalian progenitor cells. *Nature*, 453(7194):544, 2008.

[16] Amar M Singh, Takashi Hamazaki, Katherine E Hankowski, and Naohiro Terada. A heterogeneous expression pattern for nanog in embryonic stem cells. *Stem cells*, 25(10):2534–2542, 2007.

[17] Taeko Kobayashi, Hiroaki Mizuno, Itaru Imayoshi, Chikara Furusawa, Katsuhiko Shirahige, and Ryoichiro Kageyama. The cyclic gene hes1 contributes to diverse differentiation responses of embryonic stem cells. *Genes & development*, 23(16):1870–1875, 2009.

[18] Anne Wilson, Elisa Laurenti, Gabriela Oser, Richard C van der Wath, William Blanco-Bose, Maike Jaworski, Sandra Offner, Cyrille F Dunant, Leonid Eshkind, Ernesto Bockamp, et al. Hematopoietic stem cells reversibly switch from dormancy to self-renewal during homeostasis and repair. *Cell*, 135(6):1118–1129, 2008.

[19] James E Ferrell and Eric M Machleder. The biochemical basis of an all-or-none cell fate switch in xenopus oocytes. *Science*, 280(5365):895–898, 1998.

[20] Sui Huang, Yan-Ping Guo, Gillian May, and Tariq Enver. Bifurcation dynamics in lineage-commitment in bipotent progenitor cells. *Developmental biology*, 305(2):695–713, 2007.

[21] Frank B Dean, Seiyu Hosono, Linhua Fang, Xiaohong Wu, A Fawad Faruqi, Patricia Bray-Ward, Zhenyu Sun, Qiuling Zong, Yuefen Du, Jing Du, et al. Comprehensive human genome amplification using multiple displacement amplification. *Proceedings of the National Academy of Sciences*, 99(8):5261–5266, 2002.

[22] Chenghang Zong, Sijia Lu, Alec R Chapman, and X Sunney Xie. Genome-wide detection of single-nucleotide and copy-number variations of a single human cell. *Science*, 338(6114):1622–1626, 2012.

[23] Guoji Guo, Mikael Huss, Guo Qing Tong, Chaoyang Wang, Li Li Sun, Neil D Clarke, and Paul Robson. Resolution of cell fate decisions revealed by single-cell gene expression analysis from zygote to blastocyst. *Developmental cell*, 18(4):675–685, 2010.

[24] Yosef Buganim, Dina A Faddah, Albert W Cheng, Elena Itskovich, Styliani Markoulaki, Kibibi Ganz, Sandy L Klemm, Alexander van Oudenaarden, and Rudolf Jaenisch. Single-cell expression analyses during cellular reprogramming reveal an early stochastic and a late hierarchic phase. *Cell*, 150(6):1209–1222, 2012.

[25] Arjun Raj, Patrick Van Den Bogaard, Scott A Rifkin, Alexander Van Oudenaarden, and Sanjay Tyagi. Imaging individual mrna molecules using multiple singly labeled probes. *Nature methods*, 5(10):877, 2008.

[26] Ehud Shapiro, Tamir Biezuner, and Sten Linnarsson. Single-cell sequencing-based technologies will revolutionize whole-organism science. *Nature Reviews Genetics*, 14(9):618, 2013.

[27] Jan Philipp Junker and Alexander van Oudenaarden. Every cell is special: genome-wide studies add a new dimension to single-cell biology. *Cell*, 157(1):8–11, 2014.

[28] Sean C Bendall, Erin F Simonds, Peng Qiu, D Amir El-ad, Peter O Krutzik, Rachel Finck, Robert V Bruggner, Rachel Melamed, Angelica Trejo, Olga I Ornatsky, et al. Single-cell mass cytometry of differential immune and drug responses across a human hematopoietic continuum. *Science*, 332(6030):687–696, 2011.

[29] Karl-Johan Leuchowius, Carl-Magnus Clausson, Karin Grannas, Yücel Erbilgin, Johan Botling, Agata Zieba, Ulf Landegren, and Ola Söderberg. Parallel visualization of multiple protein complexes in individual cells in tumor tissue. *Molecular & Cellular Proteomics*, 12(6):1563–1571, 2013.

[30] Bruno Vanherberghen, Per E. Olofsson, Elin Forslund, Michal Sternberg-Simon, Mohammad Ali Khorshidi, Simon Pacouret, Karolin Guldevall, Monika Enqvist, Karl-Johan Malmberg, Ramit Mehr, and Björn Önfelt. Classification of human natural killer cells based on migration behavior and cytotoxic response. *Blood*, 121(8):1326–1334, 2013.

[31] Pratip K Chattopadhyay and Mario Roederer. Good cell, bad cell: Flow cytometry reveals t-cell subsets important in hiv disease. *Cytometry part A*, 77(7):614–622, 2010.

[32] Pratip K Chattopadhyay, Todd M Gierahn, Mario Roederer, and J Christopher Love. Single-cell technologies for monitoring immune systems. *Nature immunology*, 15(2):128, 2014.

[33] Chao Ma, Rong Fan, Habib Ahmad, Qihui Shi, Begonya Comin-Anduix, Thinle Chodon, Richard C Koya, Chao-Chao Liu, Gabriel A Kwong, Caius G Radu, et al. A clinical microchip for evaluation of single immune cells reveals high functional heterogeneity in phenotypically similar t cells. *Nature medicine*, 17(6):738, 2011.

[34] PV Moonsamy, T Williams, P Bonella, CL Holcomb, BN Höglund, G Hillman, D Goodridge, GS Turenchalk, LA Blake, DA Daigle, et al. High throughput hla genotyping using 454 sequencing and the fluidigm access array? system for simplified amplicon library preparation. *HLA*, 81(3):141–149, 2013.

[35] Farzad Sekhavati, Max Endele, Susanne Rappl, Anna-Kristina Marel, Timm Schroeder, and Joachim O Rädler. Marker-free detection of progenitor cell differentiation by analysis of brownian motion in micro-wells. *Integrative Biology*, 7(2):178–183, 2015.

[36] J Christopher Love, Jehnna L Ronan, Gijsbert M Grotenbreg, Annemarthe G van der Veen, and Hidde L Ploegh. A microengraving method for rapid selection of single cells producing antigen-specific antibodies. *Nature biotechnology*, 24(6):703, 2006.

[37] Qing Han, Neda Bagheri, Elizabeth M Bradshaw, David A Hafler, Douglas A Lauffenburger, and J Christopher Love. Polyfunctional responses by human t cells result from sequential release of cytokines. *Proceedings of the National Academy of Sciences*, 109(5):1607–1612, 2012.

[38] Yoshitaka Shirasaki, Mai Yamagishi, Nobutake Suzuki, Kazushi Izawa, Asahi Nakahara, Jun Mizuno, Shuichi Shoji, Toshio Heike, Yoshie Harada, Ryuta Nishikomori, et al. Real-time single-cell imaging of protein secretion. *Scientific reports*, 4:4736, 2014.

[39] Yvonne J Yamanaka, Christoph T Berger, Magdalena Sips, Patrick C Cheney, Galit Alter, and J Christopher Love. Single-cell analysis of the dynamics and functional outcomes of interactions between human natural killer cells and target cells. *Integrative Biology*, 4(10):1175–1184, 2012.

[40] Bruno Vanherberghen, Per E Olofsson, Elin Forslund, Michal Sternberg-Simon, Mohammad Ali Khorshidi, Simon Pacouret, Karolin Guldevall, Monika Enqvist, Karl-Johan Malmberg, Ramit Mehr, et al. Classification of human natural killer cells based on migration behavior and cytotoxic response. *Blood*, 121(8):1326–1334, 2013.

[41] Per Erik Olofsson, Elin Forslund, Bruno Vanherberghen, Ksenia Chechet, Oscar Mickelin, Alexander Rivera Ahlin, Tobias Everhorn, and Björn Önfelt. Distinct migration and contact dynamics of resting and il-2-activated human natural killer cells. *Frontiers in immunology*, 5:80, 2014.

[42] Jun Wang, Douglas Tham, Wei Wei, Young Shik Shin, Chao Ma, Habib Ahmad, Qihui Shi, Jenkan Yu, Raphael D Levine, and James R Heath. Quantitating cell–cell interaction functions with applications to glioblastoma multiforme cancer cells. *Nano letters*, 12(12):6101–6106, 2012.

[43] I What. Tumor heterogeneity. *Cancer research*, 44:2259–2265, 1984.

[44] Harry Rubin. The significance of biological heterogeneity. *Cancer and Metastasis Reviews*, 9(1):1–20, 1990.

[45] Alexander RA Anderson, Alissa M Weaver, Peter T Cummings, and Vito Quaranta. Tumor morphology and phenotypic evolution driven by selective pressure from the microenvironment. *Cell*, 127(5):905–915, 2006.

[46] Karen E Gascoigne and Stephen S Taylor. Cancer cells display profound intra-and interline variation following prolonged exposure to antimitotic drugs. *Cancer cell*, 14(2):111–122, 2008.

[47] Ivana Bozic, Johannes G Reiter, Benjamin Allen, Tibor Antal, Krishnendu Chatterjee, Preya Shah, Yo Sup Moon, Amin Yaqubie, Nicole Kelly, Dung T Le, et al. Evolutionary dynamics of cancer in response to targeted combination therapy. *elife*, 2, 2013.

[48] Daniel P Cahill, Kymberly K Levine, Rebecca A Betensky, Patrick J Codd, Candice A Romany, Linsey B Reavie, Tracy T Batchelor, P Andrew Futreal, Michael R Stratton, William T Curry, et al. Loss of the mismatch repair protein msh6 in human glioblastomas is associated with tumor progression during temozolomide treatment. *Clinical cancer research*, 13(7):2038–2045, 2007.

[49] Li Ding, Timothy J Ley, David E Larson, Christopher A Miller, Daniel C Koboldt, John S Welch, Julie K Ritchey, Margaret A Young, Tamara Lamprecht, Michael D McLellan, et al. Clonal evolution in relapsed acute myeloid leukaemia revealed by whole-genome sequencing. *Nature*, 481(7382):506, 2012.

[50] Chris Hunter, Raffaella Smith, Daniel P Cahill, Philip Stephens, Claire Stevens, Jon Teague, Chris Greenman, Sarah Edkins, Graham Bignell, Helen Davies, et al. A hypermutation phenotype and somatic msh6 mutations in recurrent human malignant gliomas after alkylator chemotherapy. *Cancer research*, 66(8):3987–3991, 2006.

[51] Peter J Campbell, Shinichi Yachida, Laura J Mudie, Philip J Stephens, Erin D Pleasance, Lucy A Stebbings, Laura A Morsberger, Calli Latimer, Stuart McLaren, Meng-Lay Lin, et al. The patterns and dynamics of genomic instability in metastatic pancreatic cancer. *Nature*, 467(7319):1109, 2010.

[52] Dan A Landau, Scott L Carter, Petar Stojanov, Aaron McKenna, Kristen Stevenson, Michael S Lawrence, Carrie Sougnez, Chip Stewart, Andrey Sivachenko, Lili Wang, et al. Evolution and impact of subclonal mutations in chronic lymphocytic leukemia. *Cell*, 152(4):714–726, 2013.

[53] Mel Greaves and Carlo C Maley. Clonal evolution in cancer. *Nature*, 481(7381):306, 2012.

[54] Charles Swanton. Intratumor heterogeneity: evolution through space and time. *Cancer research*, 72(19):4875–4882, 2012.

[55] Marco Gerlinger, Stuart Horswell, James Larkin, Andrew J Rowan, Max P Salm, Ignacio Varela, Rosalie Fisher, Nicholas McGranahan, Nicholas Matthews, Claudio R Santos, et al. Genomic architecture and evolution of clear cell renal cell carcinomas defined by multiregion sequencing. *Nature genetics*, 46(3):225, 2014.

[56] Elza C de Bruin, Nicholas McGranahan, Richard Mitter, Max Salm, David C Wedge, Lucy Yates, Mariam Jamal-Hanjani, Seema Shafi, Nirupa Murugaesu, Andrew J Rowan, et al. Spatial and temporal diversity in genomic instability processes defines lung cancer evolution. *Science*, 346(6206):251–256, 2014.

[57] Nicholas McGranahan and Charles Swanton. Biological and therapeutic impact of intratumor heterogeneity in cancer evolution. *Cancer cell*, 27(1):15–26, 2015.

[58] Robert A Gatenby, Ariosto S Silva, Robert J Gillies, and B Roy Frieden. Adaptive therapy. *Cancer research*, 69(11):4894–4903, 2009.

[59] Sakshi Gulati, Pierre Martinez, Tejal Joshi, Nicolai Juul Birkbak, Claudio R Santos, Andrew J Rowan, Lisa Pickering, Martin Gore, James Larkin, Zoltan Szallasi, et al. Systematic evaluation of the prognostic impact and intratumour heterogeneity of clear cell renal cell carcinoma biomarkers. *European urology*, 66(5):936–948, 2014.

[60] Andrea Sottoriva, Inmaculada Spiteri, Sara GM Piccirillo, Anestis Touloumis, V Peter Collins, John C Marioni, Christina Curtis, Colin Watts, and Simon Tavaré. Intratumor heterogeneity in human glioblastoma reflects cancer evolutionary dynamics. *Proceedings of the National Academy of Sciences*, 110(10):4009–4014, 2013.

[61] Cassandra L Hodgkinson, Christopher J Morrow, Yaoyong Li, Robert L Metcalf, Dominic G Rothwell, Francesca Trapani, Radoslaw Polanski, Deborah J Burt, Kathryn L Simpson, Karen Morris, et al. Tumorigenicity and genetic profiling of circulating tumor cells in small-cell lung cancer. *Nature medicine*, 20(8):897, 2014.

[62] Evan Z Macosko, Anindita Basu, Rahul Satija, James Nemesh, Karthik Shekhar, Melissa Goldman, Itay Tirosh, Allison R Bialas, Nolan Kamitaki, Emily M Martersteck, et al. Highly parallel genome-wide expression profiling of individual cells using nanoliter droplets. *Cell*, 161(5):1202–1214, 2015.

[63] Allon M Klein, Linas Mazutis, Ilke Akartuna, Naren Tallapragada, Adrian Veres, Victor Li, Leonid Peshkin, David A Weitz, and Marc W Kirschner. Droplet barcoding for single-cell transcriptomics applied to embryonic stem cells. *Cell*, 161(5):1187–1201, 2015.

[64] H Christina Fan, Glenn K Fu, and Stephen PA Fodor. Combinatorial labeling of single cells for gene expression cytometry. *Science*, 347(6222):1258367, 2015.

[65] Todd M Gierahn, Marc H Wadsworth II, Travis K Hughes, Bryan D Bryson, Andrew Butler, Rahul Satija, Sarah Fortune, J Christopher Love, and Alex K Shalek. Seq-well: portable, low-cost rna sequencing of single cells at high throughput. *Nature methods*, 14(4):395, 2017.

[66] Melody K Morris, An Chi, Ioannis N Melas, and Leonidas G Alexopoulos. Phosphoproteomics in drug discovery. *Drug discovery today*, 19(4):425–432, 2014.

[67] Regina K Cheung and Paul J Utz. Screening: Cytof?the next generation of cell detection. *Nature Reviews Rheumatology*, 7(9):502, 2011.

[68] Xiao-Mei Zhao, Younan Xia, and George M. Whitesides. Soft lithographic methods for nano-fabrication. *J. Mater. Chem.*, 7:1069–1074, 1997.

[69] Felix Jakob Segerer, Peter Johan Friedrich Röttgermann, Simon Schuster, Alicia Piera Alberola, Stefan Zahler, and Joachim Oskar Rädler. Versatile method to generate multiple types of micropatterns. *Biointerphases*, 11(1):011005, 2016.

[70] Anna-Kristina Marel, Susanne Rappl, Alicia Piera Alberola, and Joachim Oskar Rädler. Arraying cell cultures using peg-dma micromolding in standard culture dishes. *Macromolecular bioscience*, 13(5):595–602, 2013.

[71] Matthias L Zorn, Anna-Kristina Marel, Felix J Segerer, and Joachim O Rädler. Phenomenological approaches to collective behavior in epithelial cell migration. *Biochimica et Biophysica Acta (BBA)-Molecular Cell Research*, 1853(11):3143–3152, 2015.

[72] Felix J Segerer, Florian Thüroff, Alicia Piera Alberola, Erwin Frey, and Joachim O Rädler. Emergence and persistence of collective cell migration on small circular micropatterns. *Physical review letters*, 114(22):228102, 2015.

[73] Christoph Schreiber, Felix J Segerer, Ernst Wagner, Andreas Roidl, and Joachim O Rädler. Ring-shaped microlanes and chemical barriers as a platform for probing single-cell migration. *Scientific reports*, 6:26858, 2016.

[74] Manuel Théry. Micropatterning as a tool to decipher cell morphogenesis and functions. *J Cell Sci*, 123(24):4201–4213, 2010.

[75] Qingzong Tseng, Eve Duchemin-Pelletier, Alexandre Deshiere, Martial Balland, Hervé Guillou, Odile Filhol, and Manuel Théry. Spatial organization of the extracellular matrix regulates cell–cell junction positioning. *Proceedings of the National Academy of Sciences*, 109(5):1506–1511, 2012.

[76] Farshid Guilak, Daniel M Cohen, Bradley T Estes, Jeffrey M Gimble, Wolfgang Liedtke, and Christopher S Chen. Control of stem cell fate by physical interactions with the extracellular matrix. *Cell stem cell*, 5(1):17–26, 2009.

[77] Mehrije Ferizi, Carolin Leonhardt, Christian Meggle, Manish K Aneja, Carsten Rudolph, Christian Plank, and Joachim O Rädler. Stability analysis of chemically modified mrna using micropattern-based single-cell arrays. *Lab on a Chip*, 15(17):3561–3571, 2015.

[78] Peter JF Röttgermann, Kenneth A Dawson, and Joachim O Rädler. Time-resolved study of nanoparticle induced apoptosis using microfabricated single cell arrays. *Microarrays*, 5(2):8, 2016.

[79] Bryan A Langowski and Kathryn E Uhrich. Microscale plasma-initiated patterning (μpip). *Langmuir*, 21(23):10509–10514, 2005.

[80] Y Matsuo, RAF MacLeod, CC Uphoff, HG Drexler, C Nishizaki, Y Katayama, G Kimura, N Fujii, E Omoto, M Harada, et al. Two acute monocytic leukemia (aml-m5a) cell lines (molm-13 and molm-14) with interclonal phenotypic heterogeneity showing mll-af9 fusion resulting from an occult chromosome insertion, ins (11; 9)(q23; p22p23). *Leukemia*, 11(9):1469, 1997.

[81] LJ Bendall, V Makrynikola, A Hutchinson, AC Bianchi, KF Bradstock, and DJ Gottlieb. Stem cell factor enhances the adhesion of aml cells to fibronectin and augments fibronectin-mediated anti-apoptotic and proliferative signals. *Leukemia*, 12(9):1375, 1998.

[82] K Kortlepel, LJ Bendall, and DJ Gottlieb. Human acute myeloid leukaemia cells express adhesion proteins and bind to bone marrow fibroblast monolayers and extracellular matrix proteins. *Leukemia*, 7(8):1174–1179, 1993.

[83] Takuya Matsunaga, Naofumi Takemoto, Tsutomu Sato, Rishu Takimoto, Ikuta Tanaka, Akihito Fujimi, Takehide Akiyama, Hiroyuki Kuroda, Yutaka Kawano, Masayoshi Kobune, et al. Interaction between leukemic-cell vla-4 and stromal fibronectin is a decisive factor for minimal residual disease of acute myelogenous leukemia. *Nature medicine*, 9(9):1158, 2003.

[84] O Hrušák and A Porwit-MacDonald. Antigen expression patterns reflecting genotype of acute leukemias. *Leukemia*, 16(7):1233, 2002.

[85] Nan Li and Chih-Ming Ho. Photolithographic patterning of organosilane monolayer for generating large area two-dimensional b lymphocyte arrays. *Lab on a Chip*, 8(12):2105–2112, 2008.

[86] Mirren Charnley, Marcus Textor, Ali Khademhosseini, and Matthias P Lutolf. Integration column: microwell arrays for mammalian cell culture. *Integrative biology*, 1(11-12):625–634, 2009.

[87] Sara Lindström and Helene Andersson-Svahn. Miniaturization of biological assays?overview on microwell devices for single-cell analyses. *Biochimica et Biophysica Acta (BBA)-General Subjects*, 1810(3):308–316, 2011.

[88] Emanuele Ostuni, Christopher S Chen, Donald E Ingber, and George M Whitesides. Selective deposition of proteins and cells in arrays of microwells. *Langmuir*, 17(9):2828–2834, 2001.

[89] Kirsty Leong, Anna K Boardman, Hong Ma, and Alex K-Y Jen. Single-cell patterning and adhesion on chemically engineered poly (dimethylsiloxane) surface. *Langmuir*, 25(8):4615–4620, 2009.

[90] Jacqueline R Rettig and Albert Folch. Large-scale single-cell trapping and imaging using microwell arrays. *Analytical chemistry*, 77(17):5628–5634, 2005.

[91] Marc R Dusseiller, Michael L Smith, Viola Vogel, and Marcus Textor. Microfabricated three-dimensional environments for single cell studies. *Biointerphases*, 1(1):P1–P4, 2006.

[92] Mirjam Ochsner, Marc R Dusseiller, H Michelle Grandin, Sheila Luna-Morris, Marcus Textor, Viola Vogel, and Michael L Smith. Micro-well arrays for 3d shape control and high resolution analysis of single cells. *Lab on a Chip*, 7(8):1074–1077, 2007.

[93] Marc R Dusseiller, Dominik Schlaepfer, Mirabai Koch, Ruth Kroschewski, and Marcus Textor. An inverted microcontact printing method on topographically structured polystyrene chips for arrayed micro-3-d culturing of single cells. *Biomaterials*, 26(29):5917–5925, 2005.

[94] Ali Khademhosseini, Lino Ferreira, James Blumling III, Judy Yeh, Jeffrey M Karp, Junji Fukuda, and Robert Langer. Co-culture of human embryonic stem cells with murine embryonic fibroblasts on microwell-patterned substrates. *Biomaterials*, 27(36):5968–5977, 2006.

[95] Daniel Day, Kim Pham, Mandy J Ludford-Menting, Jane Oliaro, David Izon, Sarah M Russell, and Min Gu. A method for prolonged imaging of motile lymphocytes. *Immunology and cell biology*, 87(2):154, 2009.

[96] Jeffrey C Mohr, Juan J de Pablo, and Sean P Palecek. 3-d microwell culture of human embryonic stem cells. *Biomaterials*, 27(36):6032–6042, 2006.

[97] Hannes-Christian Moeller, Matthew K Mian, Shamit Shrivastava, Bong Geun Chung, and Ali Khademhosseini. A microwell array system for stem cell culture. *Biomaterials*, 29(6):752–763, 2008.

[98] Myriam Cordey, Monika Limacher, Stefan Kobel, Verdon Taylor, and Matthias P Lutolf. Enhancing the reliability and throughput of neurosphere culture on hydrogel microwell arrays. *Stem Cells*, 26(10):2586–2594, 2008.

[99] Alexander Revzin, Kazuhiko Sekine, Aaron Sin, Ronald G Tompkins, and Mehmet Toner. Development of a microfabricated cytometry platform for characterization and sorting of individual leukocytes. *Lab on a Chip*, 5(1):30–37, 2005.

[100] Vicki I Chin, Philippe Taupin, Sandeep Sanga, John Scheel, Fred H Gage, and Sangeeta N Bhatia. Microfabricated platform for studying stem cell fates. *Biotechnology and bioengineering*, 88(3):399–415, 2004.

[101] Laura C Taylor and David R Walt. Application of high-density optical microwell arrays in a live-cell biosensing system. *Analytical biochemistry*, 278(2):132–142, 2000.

[102] Mordechai Deutsch, Assaf Deutsch, Orian Shirihai, Ihar Hurevich, Elena Afrimzon, Yana Shafran, and Naomi Zurgil. A novel miniature cell retainer for correlative high-content analysis of individual untethered non-adherent cells. *Lab on a Chip*, 6(8):995–1000, 2006.

[103] Yoshiharu Tokimitsu, Hiroyuki Kishi, Sachiko Kondo, Ritsu Honda, Kazuto Tajiri, Kazumi Motoki, Tatsuhiko Ozawa, Shinichi Kadowaki, Tsutomu Obata, Satoshi Fujiki, et al. Single lymphocyte analysis with a microwell array chip. *Cytometry Part A*, 71(12):1003–1010, 2007.

[104] Chad I Rogers, Jayson V Pagaduan, Gregory P Nordin, and Adam T Woolley. Single-monomer formulation of polymerized polyethylene glycol diacrylate as a nonadsorptive material for microfluidics. *Analytical chemistry*, 83(16):6418–6425, 2011.

[105] Frederik Kotz, Klaus Plewa, Werner Bauer, Norbert Schneider, Nico Keller, Tobias Nargang, Dorothea Helmer, Kai Sachsenheimer, Michael Schäfer, Matthias Worgull, et al. Liquid glass: a facile soft replication method for structuring glass. *Advanced Materials*, 28(23):4646–4650, 2016.

[106] A Poison. A theory for the displacement of proteins and viruses with polyethylene glycol. *Preparative biochemistry*, 7(2):129–154, 1977.

[107] H Walter, DE Brooks, and D Fisher. Partitioning in aqueous two-phase systems, 1985.

[108] Barry R Lentz. Polymer-induced membrane fusion: potential mechanism and relation to cell fusion events. *Chemistry and physics of lipids*, 73(1-2):91–106, 1994.

[109] Robert J Klebe and Melodee G Mancuso. Chemicals which promote cell hybridization. *Somatic cell genetics*, 7(4):473–488, 1981.

[110] Samuel Zalipsky and J Milton Harris. *Poly (ethylene glycol) Chemistry and Biological Applications*. ACS Publications, 1997.

[111] J Milton Harris. *Poly (ethylene glycol) chemistry: biotechnical and biomedical applications*. Springer Science & Business Media, 2013.

[112] JMHM Scheutjens and GJ Fleer. Statistical theory of the adsorption of interacting chain molecules. 1. partition function, segment density distribution, and adsorption isotherms. *Journal of Physical Chemistry*, 83(12):1619–1635, 1979.

[113] JMHM Scheutjens and GJ Fleer. Statistical theory of the adsorption of interacting chain molecules. 2. train, loop, and tail size distribution. *The Journal of Physical Chemistry*, 84(2):178–190, 1980.

[114] Mikael Bjoerling, Gunnar Karlstroem, and Per Linse. Conformational adaption of poly (ethylene oxide): a carbon-13 nmr study. *The Journal of Physical Chemistry*, 95(17):6706–6709, 1991.

[115] Mansoor Amiji and Kinam Park. Surface modification of polymeric biomaterials with poly (ethylene oxide), albumin, and heparin for reduced thrombogenicity. *Journal of Biomaterials Science, Polymer Edition*, 4(3):217–234, 1993.

[116] C-G Gölander, James N Herron, Kap Lim, P Claesson, P Stenius, and JD Andrade. Properties of immobilized peg films and the interaction with proteins. In *Poly (ethylene glycol) Chemistry*, pages 221–245. Springer, 1992.

[117] C-G Gölander, S Jönsson, T Vladkova, P Stenius, and J-Ch Eriksson. Preparation and protein adsorption properties of photopolymerized hydrophilic films containing n-vinylpyrrolidone (nvp), acrylic acid (aa) or ethyleneoxide (eo) units as studied by esca. *Colloids and Surfaces*, 21:149–165, 1986.

[118] Aigars Piruska, Irena Nikcevic, Se Hwan Lee, Chong Ahn, William R Heineman, Patrick A Limbach, and Carl J Seliskar. The autofluorescence of plastic materials and chips measured under laser irradiation. *Lab on a Chip*, 5(12):1348–1354, 2005.

[119] Skarphedinn Halldorsson, Edinson Lucumi, Rafael Gómez-Sjöberg, and Ronan MT Fleming. Advantages and challenges of microfluidic cell culture in polydimethylsiloxane devices. *Biosensors and Bioelectronics*, 63:218–231, 2015.

[120] Feng Hua, Yugang Sun, Anshu Gaur, Matthew A Meitl, Lise Bilhaut, Lolita Rotkina, Jingfeng Wang, Phil Geil, Moonsub Shim, John A Rogers, et al. Polymer imprint lithography with molecular-scale resolution. *Nano letters*, 4(12):2467–2471, 2004.

[121] Søren Balslev, AM Jorgensen, B Bilenberg, Klaus Bo Mogensen, Detlef Snakenborg, Oliver Geschke, Jörg Peter Kutter, and Anders Kristensen. Lab-on-a-chip with integrated optical transducers. *Lab on a Chip*, 6(2):213–217, 2006.

[122] Ren Yang, John D Williams, and Wanjun Wang. A rapid micro-mixer/reactor based on arrays of spatially impinging micro-jets. *Journal of Micromechanics and Microengineering*, 14(10):1345, 2004.

[123] J Carlier, S Arscott, V Thomy, JC Fourrier, F Caron, JC Camart, C Druon, and P Tabourier. Integrated microfluidics based on multi-layered su-8 for mass spectrometry analysis. *Journal of micromechanics and Microengineering*, 14(4):619, 2004.

[124] Ferdinand Walther, Polina Davydovskaya, Stefan Zürcher, Michael Kaiser, Helmut Herberg, Alexander M Gigler, and Robert W Stark. Stability of the hydrophilic behavior of oxygen plasma activated su-8. *Journal of Micromechanics and Microengineering*, 17(3):524, 2007.

[125] Maria Nordström, Rodolphe Marie, Montserrat Calleja, and Anja Boisen. Rendering su-8 hydrophilic to facilitate use in micro channel fabrication. *Journal of Micromechanics and Microengineering*, 14(12):1614, 2004.

[126] Michael Stangegaard, Zhenyu Wang, Jörg Peter Kutter, M Dufva, and Anders Wolff. Whole genome expression profiling using dna microarray for determining biocompatibility of polymeric surfaces. *Molecular Biosystems*, 2(9):421–428, 2006.

[127] Gabriela Voskerician, Matthew S Shive, Rebecca S Shawgo, Horst Von Recum, James M Anderson, Michael J Cima, and Robert Langer. Biocompatibility and biofouling of mems drug delivery devices. *Biomaterials*, 24(11):1959–1967, 2003.

[128] Marc Hennemeyer, Ferdinand Walther, Sandra Kerstan, Katrin Schürzinger, Alexander M Gigler, and Robert W Stark. Cell proliferation assays on plasma activated su-8. *Microelectronic Engineering*, 85(5-6):1298–1301, 2008.

[129] Ansgar Waldbaur, Holger Rapp, Kerstin Laenge, and Bastian E Rapp. Let there be chip?towards rapid prototyping of microfluidic devices: one-step manufacturing processes. *Analytical Methods*, 3(12):2681–2716, 2011.

[130] D Hülsenberg, A Harnisch, C Jakob, M May, and B Straube. High aspect ratio structures obtained by electroforming in microstructured glass. *Microsystem technologies*, 2(1):109–113, 1995.

[131] David A Herold, Katherine Keil, and David E Bruns. Oxidation of polyethylene glycols by alcohol dehydrogenase. *Biochemical pharmacology*, 38(1):73–76, 1989.

[132] James W Crook, Paul Hott, John T Weimer, Richard L Farrand, and Aubrey E Cooper. The acute toxicity of polyethylene glycol 200 in laboratory animals. Technical report, ARMY ARMAMENT RESEARCH AND DEVELOPMENT COMMAND ABERDEEN PROVING GROUND MD CHEMICAL SYSTEMS LAB, 1981.

[133] Henry F Smyth, Charles P Carpenter, and C Boyd Shaffer. The toxicity of high molecular weight polyethylene glycols; chronic oral and parenteral administration. *Journal of Pharmaceutical Sciences*, 36(5):157–160, 1947.

[134] FE Shideman and Leonard Procita. Some pharmacological actions of polypropylene glycols of average molecular weight 400, 750, 1200 and 2000. *Journal of Pharmacology and Experimental Therapeutics*, 103(3):293–305, 1951.

[135] Tian-Lu Cheng, Kuo-Hsiang Chuang, Bing-Mae Chen, and Steve R Roffler. Analytical measurement of pegylated molecules. *Bioconjugate chemistry*, 23(5):881–899, 2012.

[136] Christina Hassler, Tim Boretius, and Thomas Stieglitz. Polymers for neural implants. *Journal of Polymer Science Part B: Polymer Physics*, 49(1):18–33, 2011.

[137] Soumya Nag and Rajarshi Banerjee. Fundamentals of medical implant materials. *ASM handbook*, 23:6–17, 2012.

[138] Sylvie I Ertel, Buddy D Ratner, Amarjeev Kaul, Michael B Schway, and Thomas A Horbett. In vitro study of the intrinsic toxicity of synthetic surfaces to cells. *Journal of Biomedical Materials Research Part A*, 28(6):667–675, 1994.

[139] Jessamine Ng Lee, Xingyu Jiang, Declan Ryan, and George M Whitesides. Compatibility of mammalian cells on surfaces of poly (dimethylsiloxane). *Langmuir*, 20(26):11684–11691, 2004.

[140] Lin Wang, Bing Sun, Katherine S Ziemer, Gilda A Barabino, and Rebecca L Carrier. Chemical and physical modifications to poly (dimethylsiloxane) surfaces affect adhesion of caco-2 cells. *Journal of biomedical materials research Part A*, 93(4):1260–1271, 2010.

[141] Keil J Regehr, Maribella Domenech, Justin T Koepsel, Kristopher C Carver, Stephanie J Ellison-Zelski, William L Murphy, Linda A Schuler, Elaine T Alarid, and David J Beebe. Biological implications of polydimethylsiloxane-based microfluidic cell culture. *Lab on a Chip*, 9(15):2132–2139, 2009.

[142] Rafael Gomez-Sjoberg, Anne A Leyrat, Benjamin T Houseman, Kevan Shokat, and Stephen R Quake. Biocompatibility and reduced drug absorption of sol- gel-treated poly (dimethyl siloxane) for microfluidic cell culture applications. *Analytical chemistry*, 82(21):8954–8960, 2010.

[143] Yoshikazu Hirai, Ken-ichiro Kamei, Yoshihide Makino, Li Liu, Qinghua Yuan, Yong Chen, and Osamu Tabata. mesc and hipsc proliferation on negative photoresists for microfluidics. *Procedia Engineering*, 25:1233–1236, 2011.

[144] Elizabeth W LaPensee, Christopher R LaPensee, Sejal Fox, Sandy Schwemberger, Scott Afton, and Nira Ben-Jonathan. Bisphenol a and estradiol are equipotent in antagonizing cisplatin-induced cytotoxicity in breast cancer cells. *Cancer letters*, 290(2):167–173, 2010.

[145] Krishnamurthy V Nemani, Karen L Moodie, Jeoffry B Brennick, Alison Su, and Barjor Gimi. In vitro and in vivo evaluation of su-8 biocompatibility. *Materials Science and Engineering: C*, 33(7):4453–4459, 2013.

[146] A Deepu, VVR Sai, and S Mukherji. Simple surface modification techniques for immobilization of biomolecules on su-8. *Journal of Materials Science: Materials in Medicine*, 20(1):25–28, 2009.

[147] Sarah L Tao, Ketul C Popat, James J Norman, and Tejal A Desai. Surface modification of su-8 for enhanced biofunctionality and nonfouling properties. *Langmuir*, 24(6):2631–2636, 2008.

[148] Ning Bao, Balamurugan Jagadeesan, Arun K Bhunia, Yuan Yao, and Chang Lu. Quantification of bacterial cells based on autofluorescence on a microfluidic platform. *Journal of Chromatography A*, 1181(1-2):153–158, 2008.

[149] Shau-Chun Wang and Michael D Morris. Plastic microchip electrophoresis with analyte velocity modulation. application to fluorescence background rejection. *Analytical chemistry*, 72(7):1448–1452, 2000.

[150] Marek W Urban and Theodore Provder. *Multidimensional spectroscopy of polymers: vibrational, NMR, and fluorescence techniques*. ACS Publications, 1995.

[151] Kenneth R Hawkins and Paul Yager. Nonlinear decrease of background fluorescence in polymer thin-films–a survey of materials and how they can complicate fluorescence detection in μtas. *Lab on a Chip*, 3(4):248–252, 2003.

[152] Musundi B Wabuyele, Sean M Ford, Wieslaw Stryjewski, James Barrow, and Steven A Soper. Single molecule detection of double-stranded dna in poly (methylmethacrylate) and polycarbonate microfluidic devices. *Electrophoresis*, 22(18):3939–3948, 2001.

[153] Gary A Baker, Chase A Munson, Eric J Bukowski, Sheila N Baker, and Frank V Bright. Assessment of one-and two-photon excited luminescence for directly measuring o2, ph, na+, mg2+, or ca2+ in optically dense and biologically relevant samples. *Applied spectroscopy*, 56(4):455–463, 2002.

[154] Clyde V Owens, Yolanda Y Davidson, Satyajit Kar, and Steven A Soper. High-resolution separation of dna restriction fragments using capillary electrophoresis with near-ir, diode-based, laser-induced fluorescence detection. *Analytical Chemistry*, 69(6):1256–1261, 1997.

[155] N.A. Campbell, J.B. Reece, and M.R. Taylor. *Study Guide for Biology (unbound ValuePack Component)*. Pearson Education, Limited, 2009.

[156] Narendra Maheshri and Erin K. O'Shea. Living with noisy genes: How cells function reliably with inherent variability in gene expression. *Annual Review of Biophysics and Biomolecular Structure*, 36(1):413–434, 2007. PMID: 17477840.

[157] Kfir Oved, Eran Eden, Martin Akerman, Roy Noy, Ron Wolchinsky, Orit Izhaki, Ester Schallmach, Adva Kubi, Naama Zabari, Jacob Schachter, et al. Predicting and controlling the reactivity of immune cell populations against cancer. *Molecular systems biology*, 5(1):265, 2009.

[158] Meiye Wu and Anup K Singh. Single-cell protein analysis. *Current Opinion in Biotechnology*, 23(1):83 – 88, 2012. Analytical biotechnology.

[159] Stephen P. Perfetto, Pratip K. Chattopadhyay, and Mario Roederer. Seventeen-colour flow cytometry: unravelling the immune system. *Nature Reviews Immunology*, 4:648 EP –, 08 2004.

[160] Olga Ornatsky, Dmitry Bandura, Vladimir Baranov, Mark Nitz, Mitchell A. Winnik, and Scott Tanner. Highly multiparametric analysis by mass cytometry. *Journal of Immunological Methods*, 361(1):1 – 20, 2010.

[161] Meredith Slota, Jong-Baeck Lim, Yushe Dang, and Mary L Disis. Elispot for measuring human immune responses to vaccines. *Expert review of vaccines*, 10(3):299–306, 2011.

[162] Salix Boulet, Michel L Ndongala, Yoav Peretz, Marie-Pierre Boisvert, Mohamed-Rachid Boulassel, Cecile Tremblay, Jean-Pierre Routy, Rafick-P Sekaly, and Nicole F Bernard. A dual color elispot method for the simultaneous detection of il-2 and ifn-γ hiv-specific immune responses. *Journal of immunological methods*, 320(1-2):18–29, 2007.

[163] Stephanie M Schubert, Stephanie R Walter, Mael Manesse, and David R Walt. Protein counting in single cancer cells. *Analytical chemistry*, 88(5):2952–2957, 2016.

[164] David M Rissin, Cheuk W Kan, Todd G Campbell, Stuart C Howes, David R Fournier, Linan Song, Tomasz Piech, Purvish P Patel, Lei Chang, Andrew J Rivnak, et al. Single-molecule enzyme-linked immunosorbent assay detects serum proteins at subfemtomolar concentrations. *Nature biotechnology*, 28(6):595, 2010.

[165] Qiong Xue, Yao Lu, Markus R Eisele, Endah S Sulistijo, Nafeesa Khan, Rong Fan, and Kathryn Miller-Jensen. Analysis of single-cell cytokine secretion reveals a role for paracrine signaling in coordinating macrophage responses to tlr4 stimulation. *Sci. Signal.*, 8(381):ra59–ra59, 2015.

[166] Yao Lu, Qiong Xue, Markus R Eisele, Endah S Sulistijo, Kara Brower, Lin Han, Elad David Amir, Dana Pe?er, Kathryn Miller-Jensen, and Rong Fan. Highly multiplexed profiling of single-cell effector functions reveals deep functional heterogeneity in response to pathogenic ligands. *Proceedings of the National Academy of Sciences*, 112(7):E607–E615, 2015.

[167] Aishun Jin, Tatsuhiko Ozawa, Kazuto Tajiri, Tsutomu Obata, Sachiko Kondo, Koshi Kinoshita, Shinichi Kadowaki, Kazuo Takahashi, Toshiro Sugiyama, Hiroyuki Kishi, et al. A rapid and efficient single-cell manipulation method for screening antigen-specific antibody–secreting cells from human peripheral blood. *Nature medicine*, 15(9):1088, 2009.

[168] Alexis J Torres, Abby S Hill, and J Christopher Love. Nanowell-based immunoassays for measuring single-cell secretion: characterization of transport and surface binding. *Analytical chemistry*, 86(23):11562–11569, 2014.

[169] Ana I Barbosa and Nuno M Reis. A critical insight into the development pipeline of microfluidic immunoassay devices for the sensitive quantitation of protein biomarkers at the point of care. *Analyst*, 142(6):858–882, 2017.

[170] Meredith E Wiseman and Curtis W Frank. Antibody adsorption and orientation on hydrophobic surfaces. *Langmuir*, 28(3):1765–1774, 2012.

[171] Xiaoqiang Wang, Yuming Wang, Hai Xu, Honghong Shan, and Jian R Lu. Dynamic adsorption of monoclonal antibody layers on hydrophilic silica surface: a combined study by spectroscopic ellipsometry and afm. *Journal of colloid and interface science*, 323(1):18–25, 2008.

[172] Hai Xu, Xiubo Zhao, Jian R Lu, and David E Williams. Relationship between the structural conformation of monoclonal antibody layers and antigen binding capacity. *Biomacromolecules*, 8(8):2422–2428, 2007.

[173] Cassandra L Smith, Jaqueline S Milea, and Giang H Nguyen. Immobilization of nucleic acids using biotin-strept (avidin) systems. In *Immobilisation of DNA on Chips II*, pages 63–90. Springer, 2005.

[174] Eleftherios P Diamandis and Theodore K Christopoulos. The biotin-(strept) avidin system: principles and applications in biotechnology. *Clinical chemistry*, 37(5):625–636, 1991.

[175] Shufang Luo and David R Walt. Avidin-biotin coupling as a general method for preparing enzyme-based fiber-optic sensors. *Analytical Chemistry*, 61(10):1069–1072, 1989.

[176] N Michael Green. Avidin. In *Advances in protein chemistry*, volume 29, pages 85–133. Elsevier, 1975.

[177] Fred Tausig, Frank J Wolf, et al. Streptavidin-a substance with avidin-like properties produced by microorganisms. *Biochemical and biophysical research communications*, 14:205–209, 1964.

[178] Yaffa Hiller, Jonathan M Gershoni, Edward A Bayer, and Meir Wilchek. Biotin binding to avidin. oligosaccharide side chain not required for ligand association. *Biochemical journal*, 248(1):167–171, 1987.

[179] Ely MORAG, Edward A BAYER, and Meir WILCHEK. Reversibility of biotin-binding by selective modification of tyrosine in avidin. *Biochemical journal*, 316(1):193–199, 1996.

[180] Federica Rusmini, Zhiyuan Zhong, and Jan Feijen. Protein immobilization strategies for protein biochips. *Biomacromolecules*, 8(6):1775–1789, 2007.

[181] Dohyun Kim and Amy E Herr. Protein immobilization techniques for microfluidic assays. *Biomicrofluidics*, 7(4):041501, 2013.

[182] Won Seok Lee, Vijaya Sunkara, Ja-Ryoung Han, Yang-Seok Park, and Yoon-Kyoung Cho. Electrospun tio 2 nanofiber integrated lab-on-a-disc for ultrasensitive protein detection from whole blood. *Lab on a Chip*, 15(2):478–485, 2015.

[183] Juan Tang, Dianping Tang, Reinhard Niessner, Guonan Chen, and Dietmar Knopp. Magneto-controlled graphene immunosensing platform for simultaneous multiplexed electrochemical immunoassay using distinguishable signal tags. *Analytical chemistry*, 83(13):5407–5414, 2011.

[184] Jose L Garcia-Cordero and Sebastian J Maerkl. A 1024-sample serum analyzer chip for cancer diagnostics. *Lab on a Chip*, 14(15):2642–2650, 2014.

[185] Francesca Volpetti, Jose Garcia-Cordero, and Sebastian J Maerkl. A microfluidic platform for high-throughput multiplexed protein quantitation. *PLoS One*, 10(2):e0117744, 2015.

[186] MI Mohammed and MPY Desmulliez. Autonomous capillary microfluidic system with embedded optics for improved troponin i cardiac biomarker detection. *Biosensors and Bioelectronics*, 61:478–484, 2014.

[187] Ravi A Vijayendran and Deborah E Leckband. A quantitative assessment of heterogeneity for surface-immobilized proteins. *Analytical Chemistry*, 73(3):471–480, 2001.

[188] Anke K Trilling, Jules Beekwilder, and Han Zuilhof. Antibody orientation on biosensor surfaces: a minireview. *Analyst*, 138(6):1619–1627, 2013.

[189] Erik Björling and Mathias Uhlén. Antibodypedia, a portal for sharing antibody and antigen validation data. *Molecular & Cellular Proteomics*, 7(10):2028–2037, 2008.

[190] Jochen M Schwenk, Johan Lindberg, Mårten Sundberg, Mathias Uhlen, and Peter Nilsson. Determination of binding specificities in highly multiplexed bead-based assays for antibody proteomics. *Molecular & Cellular Proteomics*, 6(1):125–132, 2007.

[191] Kenneth N Fish. Total internal reflection fluorescence (tirf) microscopy. *Current protocols in cytometry*, pages 12–18, 2009.

[192] Seamus J Holden, Stephan Uphoff, Johannes Hohlbein, David Yadin, Ludovic Le Reste, Oliver J Britton, and Achillefs N Kapanidis. Defining the limits of single-molecule fret resolution in tirf microscopy. *Biophysical journal*, 99(9):3102–3111, 2010.

[193] Caroline A Schneider, Wayne S Rasband, and Kevin W Eliceiri. Nih image to imagej: 25 years of image analysis. *Nature methods*, 9(7):671, 2012.

[194] He Zhu, Gulnaz Stybayeva, Jaime Silangcruz, Jun Yan, Erlan Ramanculov, Satya Dandekar, Michael D George, and Alexander Revzin. Detecting cytokine release from single t-cells. *Analytical chemistry*, 81(19):8150–8156, 2009.

[195] Gary Hardiman. *Microarray innovations: technology and experimentation*. CRC Press, 2009.

[196] Jing Zhou, Yu Wu, Sang-Kwon Lee, and Rong Fan. High-content single-cell analysis on-chip using a laser microarray scanner. *Lab on a chip*, 12(23):5025–5033, 2012.

[197] M Shena. Microarray biochip technology. 2000.

[198] Zheng Luo and Daniel H Geschwind. Microarray applications in neuroscience. *Neurobiology of Disease*, 8(2):183–193, 2001.

[199] Trinh L Dinh, Kevin C Ngan, Charles B Shoemaker, and David R Walt. Using antigen–antibody binding kinetic parameters to understand single-molecule array immunoassay performance. *Analytical chemistry*, 88(23):11335–11339, 2016.

[200] Stephanie M Schubert, Stephanie R Walter, Mael Manesse, and David R Walt. Protein counting in single cancer cells. *Analytical chemistry*, 88(5):2952–2957, 2016.

[201] Ioannis N Melas, Alexander Mitsos, Dimitris E Messinis, Thomas S Weiss, and Leonidas G Alexopoulos. Combined logical and data-driven models for linking signalling pathways to cellular response. *BMC systems biology*, 5(1):107, 2011.

[202] Onur Boyman and Jonathan Sprent. The role of interleukin-2 during homeostasis and activation of the immune system. *Nature Reviews Immunology*, 12(3):180, 2012.

[203] Didier Mary, Jean-Franqois Peyron, Patrick Auberger, Claude Aussel, and Max Fehlmann. Modulation of t cell activation by differential regulation of the phosphorylation of two cytosolic proteins. implication of both ca2+ and cyclic amp-dependent protein kinases. *Journal of Biological Chemistry*, 264(24):14498–14502, 1989.

[204] Abolfazl Movafagh, Hassan Heydary, Seyed AbdolReza Mortazavi-Tabatabaei, and Eznollah Azargashb. The significance application of indigenous phytohemagglutinin (pha) mitogen on metaphase and cell culture procedure. *Iranian journal of pharmaceutical research: IJPR*, 10(4):895, 2011.

[205] Alon Oyler-Yaniv, Jennifer Oyler-Yaniv, Benjamin M Whitlock, Zhiduo Liu, Ronald N Germain, Morgan Huse, Grégoire Altan-Bonnet, and Oleg Krichevsky. A tunable diffusion-consumption mechanism of cytokine propagation enables plasticity in cell-to-cell communication in the immune system. *Immunity*, 46(4):609–620, 2017.

[206] Michael Schwarzfischer, Carsten Marr, Jan Krumsiek, P Hoppe, Timm Schroeder, and F Theis. Efficient fluorescence image normalization for time lapse movies. *Proc. Microscopic Image Analysis with Applications in Biology*, 5, 2011.

[207] Xingyue An, Victor G Sendra, Ivan Liadi, Balakrishnan Ramesh, Gabrielle Romain, Cara Haymaker, Melisa Martinez-Paniagua, Yanbin Lu, Laszlo G Radvanyi, Badrinath Roysam, et al. Single-cell profiling of dynamic cytokine secretion and the phenotype of immune cells. *PloS one*, 12(8):e0181904, 2017.

[208] Regis B Kelly. Pathways of protein secretion in eukaryotes. *Science*, 230(4721):25–32, 1985.

[209] Marc Charlet, Sandra J Kromenaker, and Friedrich Srienc. Surface igg content of murine hybridomas: direct evidence for variation of antibody secretion rates during the cell cycle. *Biotechnology and bioengineering*, 47(5):535–540, 1995.

[210] Richard Vynne Southwell. *Relaxation Methods in Theoretical Physics: A Continuation of the Treatise, Relaxation Methods in Engineering Science*, volume 2. The Clarendon Press, 1946.

[211] DN de G. Allen and RV Southwell. Relaxation methods applied to determine the motion, in two dimensions, of a viscous fluid past a fixed cylinder. *The Quarterly Journal of Mechanics and Applied Mathematics*, 8(2):129–145, 1955.

[212] Bruce A Finlayson. *The method of weighted residuals and variational principles*, volume 73. SIAM, 2013.

[213] Carsten Franke and Robert Schaback. Solving partial differential equations by collocation using radial basis functions. *Applied Mathematics and Computation*, 93(1):73–82, 1998.

[214] Oleg V Vasilyev and Christopher Bowman. Second-generation wavelet collocation method for the solution of partial differential equations. *Journal of Computational Physics*, 165(2):660–693, 2000.

[215] Guoqing Hu, Yali Gao, and Dongqing Li. Modeling micropatterned antigen–antibody binding kinetics in a microfluidic chip. *Biosensors and Bioelectronics*, 22(7):1403–1409, 2007.

[216] Moritz M Gaidt, Thomas S Ebert, Dhruv Chauhan, Tobias Schmidt, Jonathan L Schmid-Burgk, Francesca Rapino, Avril AB Robertson, Matthew A Cooper, Thomas Graf, and Veit Hornung. Human monocytes engage an alternative inflammasome pathway. *Immunity*, 44(4):833–846, 2016.

[217] Tessa Bergsbaken, Susan L Fink, and Brad T Cookson. Pyroptosis: host cell death and inflammation. *Nature Reviews Microbiology*, 7(2):99, 2009.

[218] Claudia Eder. Mechanisms of interleukin-1β release. *Immunobiology*, 214(7):543–553, 2009.

[219] Charles A Dinarello. Biologic basis for interleukin-1 in disease. *Blood*, 87(6):2095–2147, 1996.

[220] Haidong Dong. The basic concepts in cancer immunology and immunotherapy. In *The Basics of Cancer Immunotherapy*, pages 1–19. Springer, 2018.

[221] Edward F McCarthy. The toxins of william b. coley and the treatment of bone and soft-tissue sarcomas. *The Iowa orthopaedic journal*, 26:154, 2006.

[222] William K Decker and Amar Safdar. Bioimmunoadjuvants for the treatment of neoplastic and infectious disease: Coley's legacy revisited. *Cytokine & growth factor reviews*, 20(4):271–281, 2009.

[223] Gavin P Dunn, Allen T Bruce, Hiroaki Ikeda, Lloyd J Old, and Robert D Schreiber. Cancer immunoediting: from immunosurveillance to tumor escape. *Nature immunology*, 3(11):991, 2002.

[224] César Milstein. The hybridoma revolution: an offshoot of basic research. *Bioessays*, 21(11):966–973, 1999.

[225] Dominika Rudnicka, Anna Oszmiana, Donna K Finch, Ian Strickland, Darren J Schofield, David C Lowe, Matthew A Sleeman, and Daniel M Davis. Rituximab causes a polarization of b cells that augments its therapeutic function in nk-cell–mediated antibody-dependent cellular cytotoxicity. *Blood*, 121(23):4694–4702, 2013.

[226] Peter Groscurth. Cytotoxic effector cells of the immune system. *Anatomy and embryology*, 180(2):109–119, 1989.

[227] Alessandro Moretta, Cristina Bottino, Massimo Vitale, Daniela Pende, Roberto Biassoni, Maria Cristina Mingari, and Lorenzo Moretta. Receptors for hla class-i molecules in human natural killer cells. *Annual review of immunology*, 14(1):619–648, 1996.

[228] Hilary S Warren and Mark J Smyth. Nk cells and apoptosis. *Immunology & Cell Biology*, 77(1):64–75, 1999.

[229] Joseph A Trapani and Mark J Smyth. Functional significance of the perforin/granzyme cell death pathway. *Nature Reviews Immunology*, 2(10):735, 2002.

[230] Mark J Smyth, Erika Cretney, Janice M Kelly, Jennifer A Westwood, Shayna EA Street, Hideo Yagita, Kazuyoshi Takeda, Serani LH van Dommelen, Mariapia A Degli-Esposti, and Yoshihiro Hayakawa. Activation of nk cell cytotoxicity. *Molecular immunology*, 42(4):501–510, 2005.

[231] Mark J Smyth and Joseph A Trapani. Granzymes: exogenous porteinases that induce target cell apoptosis. *Immunology today*, 16(4):202–206, 1995.

[232] Louis M Weiner, Joseph C Murray, and Casey W Shuptrine. Antibody-based immunotherapy of cancer. *Cell*, 148(6):1081–1084, 2012.

[233] Andrew M Scott, Jedd D Wolchok, and Lloyd J Old. Antibody therapy of cancer. *Nature Reviews Cancer*, 12(4):278, 2012.

[234] Janice M Reichert. Antibodies to watch in 2014. *MAbs*, 6(1):5–14, 2014.

[235] Roland Kontermann. Dual targeting strategies with bispecific antibodies. *MAbs*, 4(2):182–197, 2012.

[236] Roland E Kontermann and Ulrich Brinkmann. Bispecific antibodies. *Drug discovery today*, 20(7):838–847, 2015.

[237] Christoph Spiess, Qianting Zhai, and Paul J Carter. Alternative molecular formats and therapeutic applications for bispecific antibodies. *Molecular immunology*, 67(2):95–106, 2015.

[238] Christoph Stein, Ingo Schubert, and Georg H Fey. Natural killer (nk)-and t-cell engaging antibody-derived therapeutics. *Antibodies*, 1(1):88–123, 2012.

[239] Patrick A Baeuerle and Carsten Reinhardt. Bispecific t-cell engaging antibodies for cancer therapy. *Cancer research*, 69(12):4941–4944, 2009.

[240] Ralf Bargou, Eugen Leo, Gerhard Zugmaier, Matthias Klinger, Mariele Goebeler, Stefan Knop, Richard Noppeney, Andreas Viardot, Georg Hess, Martin Schuler, et al. Tumor regression in cancer patients by very low doses of a t cell–engaging antibody. *Science*, 321(5891):974–977, 2008.

[241] Max S Topp, Peter Kufer, Nicola Gökbuget, Mariele Goebeler, Matthias Klinger, Svenja Neumann, Heinz-A Horst, Thorsten Raff, Andreas Viardot, Mathias Schmid, et al. Targeted therapy with the t-cell–engaging antibody blinatumomab of chemotherapy-refractory minimal residual disease in b-lineage acute lymphoblastic leukemia patients results in high response rate and prolonged leukemia-free survival. *Journal of clinical oncology*, 29(18):2493–2498, 2011.

[242] Max S Topp, Nicola Gökbuget, Anthony S Stein, Gerhard Zugmaier, Susan O'Brien, Ralf C Bargou, Hervé Dombret, Adele K Fielding, Leonard Heffner, Richard A Larson, et al. Safety and activity of blinatumomab for adult patients with relapsed or refractory b-precursor acute lymphoblastic leukaemia: a multicentre, single-arm, phase 2 study. *The Lancet Oncology*, 16(1):57–66, 2015.

[243] Christian Kellner, Joerg Bruenke, Julia Stieglmaier, Michael Schwemmlein, Michael Schwenkert, Heiko Singer, Kristin Mentz, Matthias Peipp, Peter Lang, Fuat Oduncu, et al. A novel cd19-directed recombinant bispecific antibody derivative with enhanced immune effector functions for human leukemic cells. *Journal of immunotherapy*, 31(9):871–884, 2008.

[244] Markus Kügler, Christoph Stein, Christian Kellner, Kristin Mentz, Domenica Saul, Michael Schwenkert, Ingo Schubert, Heiko Singer, Fuat Oduncu, Bernhard Stockmeyer, et al. A recombinant trispecific single-chain fv derivative directed against cd123 and cd33 mediates effective elimination of acute myeloid leukaemia cells by dual targeting. *British journal of haematology*, 150(5):574–586, 2010.

[245] Ingo Schubert, Domenica Saul, Stefanie Nowecki, Andreas Mackensen, Georg H Fey, and Fuat S Oduncu. A dual-targeting triplebody mediates preferential redirected lysis of antigen double-positive over single-positive leukemic cells. *MAbs*, 6(1):286–296, 2014.

[246] Todd A Braciak, Sarah Wildenhain, Claudia C Roskopf, Ingo A Schubert, Georg H Fey, Uwe Jacob, Karl-Peter Hopfner, and Fuat S Oduncu. Nk cells from an aml patient have recovered in remission and reached comparable cytolytic activity to that of a healthy monozygotic twin mediated by the single-chain triplebody spm-2. *Journal of translational medicine*, 11(1):289, 2013.

[247] Claudia C Roskopf, Christian B Schiller, Todd A Braciak, Sebastian Kobold, Ingo A Schubert, Georg H Fey, Karl-Peter Hopfner, and Fuat S Oduncu. T cell-recruiting triplebody 19-3-19 mediates serial lysis of malignant b-lymphoid cells by a single t cell. *Oncotarget*, 5(15):6466, 2014.

[248] Gabrielle Romain, Vladimir Senyukov, Nicolas Rey-Villamizar, Amine Merouane, William Kelton, Ivan Liadi, Ankit Mahendra, Wissam Charab, George Georgiou, Badrinath Roysam, et al. Antibody fc engineering improves frequency and promotes kinetic boosting of serial killing mediated by nk cells. *Blood*, 124(22):3241–3249, 2014.

[249] KT Brunner, J Mauel, J-C Cerottini, and B Chapuis. Quantitative assay of the lytic action of immune lymphoid cells of 51cr-labelled allogeneic target cells in vitro; inhibition by isoantibody and by drugs. *Immunology*, 14(2):181, 1968.

[250] David L Nelson, Carole C Kurman, and Deborah E Serbousek. 51cr release assay of antibody-dependent cell-mediated cytotoxicity (adcc). *Current protocols in immunology*, 8(1):7–27, 1993.

[251] Daniel M Davis, Isaac Chiu, Marlys Fassett, George B Cohen, Ofer Mandelboim, and Jack L Strominger. The human natural killer cell immune synapse. *Proceedings of the National Academy of Sciences*, 96(26):15062–15067, 1999.

[252] Arash Grakoui, Shannon K Bromley, Cenk Sumen, Mark M Davis, Andrey S Shaw, Paul M Allen, and Michael L Dustin. The immunological synapse: a molecular machine controlling t cell activation. *Science*, 285(5425):221–227, 1999.

[253] D Zagury, Jacky Bernard, Noelle Thierness, M Feldman, and G Berke. Isolation and characterization of individual functionally reactive cytotoxic t lymphocytes: conjugation, killing and recycling at the single cell level. *European Journal of Immunology*, 5(12):818–822, 1975.

[254] CJ Sanderson. The mechanism of t cell mediated cytotoxicity ii. morphological studies of cell death by time-lapse microcinematography. *Proc. R. Soc. Lond. B*, 192(1107):241–255, 1976.

[255] Thomas L Rothstein, Michael Mage, Gary Jones, and Louise L McHugh. Cytotoxic t lymphocyte sequential killing of immobilized allogeneic tumor target cells measured by time-lapse microcinematography. *The Journal of Immunology*, 121(5):1652–1656, 1978.

[256] Rauf Bhat and Carsten Watzl. Serial killing of tumor cells by human natural killer cells–enhancement by therapeutic antibodies. *PloS one*, 2(3):e326, 2007.

[257] Sylvie Isaaz, Kristin Baetz, Kristin Olsen, Eckhard Podack, and Gillian M Griffiths. Serial killing by cytotoxic t lymphocytes: T cell receptor triggers degranulation, re-filling of the lytic granules and secretion of lytic proteins via a non-granule pathway. *European journal of immunology*, 25(4):1071–1079, 1995.

[258] Jodi E Goldberg, Steven W Sherwood, and Carol Clayberger. A novel method for measuring ctl and nk cell-mediated cytotoxicity using annexin v and two-color flow cytometry. *Journal of immunological methods*, 224(1-2):1–9, 1999.

[259] Laurie Lamoreaux, Mario Roederer, and Richard Koup. Intracellular cytokine optimization and standard operating procedure. *Nature protocols*, 1(3):1507, 2006.

[260] Alice CN Brown, Stephane Oddos, Ian M Dobbie, Juha-Matti Alakoskela, Richard M Parton, Philipp Eissmann, Mark AA Neil, Christopher Dunsby, Paul MW French, Ilan Davis, et al. Remodelling of cortical actin where lytic granules dock at natural killer cell immune synapses revealed by super-resolution microscopy. *PLoS biology*, 9(9):e1001152, 2011.

[261] Alice CN Brown, Ian M Dobbie, Juha-Matti Alakoskela, Ilan Davis, and Daniel M Davis. Super-resolution imaging of remodeled synaptic actin reveals different synergies between nk cell receptors and integrins. *Blood*, 120(18):3729–3740, 2012.

[262] Jérémie Rossy, Sophie V Pageon, Daniel M Davis, and Katharina Gaus. Super-resolution microscopy of the immunological synapse. *Current opinion in immunology*, 25(3):307–312, 2013.

[263] John G Albeck, John M Burke, Bree B Aldridge, Mingsheng Zhang, Douglas A Lauffenburger, and Peter K Sorger. Quantitative analysis of pathways controlling extrinsic apoptosis in single cells. *Molecular cell*, 30(1):11–25, 2008.

[264] Navin Varadarajan, Boris Julg, Yvonne J Yamanaka, Huabiao Chen, Adebola O Ogunniyi, Elizabeth McAndrew, Lindsay C Porter, Alicja Piechocka-Trocha, Brenna J Hill, Daniel C Douek, et al. A high-throughput single-cell analysis of human cd8+ t cell functions reveals discordance for cytokine secretion and cytolysis. *The Journal of clinical investigation*, 121(11), 2011.

[265] Ivan Liadi, Jason Roszik, Gabrielle Romain, Laurence JN Cooper, and Navin Varadarajan. Quantitative high-throughput single-cell cytotoxicity assay for t cells. *Journal of visualized experiments: JoVE*, (72), 2013.

[266] Paul J Choi and Timothy J Mitchison. Imaging burst kinetics and spatial coordination during serial killing by single natural killer cells. *Proceedings of the National Academy of Sciences*, 110(16):6488–6493, 2013.

[267] Elin Forslund, Karolin Guldevall Guldevall, Per E Olofsson, Thomas Frisk, Athanasia Christakou, Martin Wiklund, and Björn Önfelt. Novel microchip-based tools facilitating live cell imaging and assessment of functional heterogeneity within nk cell populations. *Frontiers in immunology*, 3:300, 2012.

[268] Evren Alici, Tolga Sutlu, Bo Björkstrand, Mari Gilljam, Birgitta Stellan, Hareth Nahi, Hernan Concha Quezada, Gösta Gahrton, Hans-Gustaf Ljunggren, and M Sirac Dilber. Autologous antitumor activity by nk cells expanded from myeloma patients using gmp-compliant components. *Blood*, 111(6):3155–3162, 2008.

[269] Elisavet I Chatzopoulou, Claudia C Roskopf, Farzad Sekhavati, Todd A Braciak, Nadja C Fenn, Karl-Peter Hopfner, Fuat S Oduncu, Georg H Fey, and Joachim O Rädler. Chip-based platform for dynamic analysis of nk cell cytolysis mediated by a triplebody. *Analyst*, 141(7):2284–2295, 2016.

[270] Christoph Stein, Christian Kellner, Markus Kügler, Nina Reiff, Kristin Mentz, Michael Schwenkert, Bernhard Stockmeyer, Andreas Mackensen, and Georg H Fey. Novel conjugates of single-chain fv antibody fragments specific for stem cell antigen cd123 mediate potent death of acute myeloid leukaemia cells. *British journal of haematology*, 148(6):879–889, 2010.

[271] M Aigner, J Feulner, S Schaffer, R Kischel, P Kufer, K Schneider, A Henn, B Rattel, M Friedrich, PA Baeuerle, et al. T lymphocytes can be effectively recruited for ex vivo and in vivo lysis of aml blasts by a novel cd33/cd3-bispecific bite antibody construct. *Leukemia*, 27(5):1107, 2013.

[272] A Ehninger, M Kramer, C Röllig, C Thiede, M Bornhäuser, M Von Bonin, M Wermke, A Feldmann, M Bachmann, G Ehninger, et al. Distribution and levels of cell surface expression of cd33 and cd123 in acute myeloid leukemia. *Blood cancer journal*, 4(6):e218, 2014.

[273] Jacob M Rowe and Bob Löwenberg. Gemtuzumab ozogamicin in acute myeloid leukemia: a remarkable saga about an active drug. *Blood*, 121(24):4838–4841, 2013.

[274] Alan Burnett, Meir Wetzler, and Bob Löwenberg. Therapeutic advances in acute myeloid leukemia. *Journal of Clinical Oncology*, 29(5):487–494, 2011.

[275] CT Jordan, D Upchurch, SJ Szilvassy, ML Guzman, DS Howard, AL Pettigrew, T Meyerrose, R Rossi, B Grimes, DA Rizzieri, et al. The interleukin-3 receptor alpha chain is a unique marker for human acute myelogenous leukemia stem cells. *Leukemia*, 14(10):1777, 2000.

[276] AW Hauswirth, S Florian, D Printz, K Sotlar, M-T Krauth, G Fritsch, G-H Schernthaner, V Wacheck, E Selzer, WR Sperr, et al. Expression of the target receptor cd33 in cd34+/cd38-/cd123+ aml stem cells. *European journal of clinical investigation*, 37(1):73–82, 2007.

[277] Roland B Walter, Frederick R Appelbaum, Elihu H Estey, and Irwin D Bernstein. Acute myeloid leukemia stem cells and cd33-targeted immunotherapy. *Blood*, 119(26):6198–6208, 2012.

[278] François Vergez, Alexa S Green, Jerome Tamburini, Jean-Emmanuel Sarry, Baptiste Gaillard, Pascale Cornillet-Lefebvre, Melanie Pannetier, Aymeric Neyret, Nicolas Chapuis, Norbert Ifrah, et al. High levels of cd34+ cd38low/- cd123+ blasts are predictive of an adverse outcome in acute myeloid leukemia: a groupe ouest-est des leucémies aiguës et maladies du sang (goelams) study. *haematologica*, 96(12):1792–1798, 2011.

[279] C Arndt, A Feldmann, M Von Bonin, M Cartellieri, EM Ewen, S Koristka, I Michalk, S Stamova, N Berndt, A Gocht, et al. Costimulation improves the killing capability of t cells redirected to tumor cells expressing low levels of cd33: description of a novel modular targeting system. *Leukemia*, 28(1):59, 2014.

[280] Geoffrey I Shapiro and J Wade Harper. Anticancer drug targets: cell cycle and checkpoint control. *The Journal of clinical investigation*, 104(12):1645–1653, 1999.

[281] Charles J Sherr and James M Roberts. Cdk inhibitors: positive and negative regulators of g1-phase progression. *Genes & development*, 13(12):1501–1512, 1999.

[282] Sander van den Heuvel and Ed Harlow. Distinct roles for cyclin-dependent kinases in cell cycle control. *Science*, 262(5142):2050–2054, 1993.

[283] James A Eastham, Simon J Hall, Inder Sehgal, Jianxiang Wang, Terry L Timme, Guang Yang, Lisa Connell-Crowley, Stephen J Elledge, Wei-Wei Zhang, J Wade Harper, et al. In vivo gene therapy with p53 or p21 adenovirus for prostate cancer. *Cancer research*, 55(22):5151–5155, 1995.

[284] Xiaomei Jin, Dao Nguyen, Wei-Wei Zhang, Athanassios P Kyritsis, and Jack A Roth. Cell cycle arrest and inhibition of tumor cell proliferation by the p16ink4 gene mediated by an adenovirus vector. *Cancer research*, 55(15):3250–3253, 1995.

[285] Volker Sandig, Karsten Brand, Susanne Herwig, Jiri Lukas, Jiri Bartek, and Michael Strauss. Adenovirally transferred p16ink4/cdkn2 and p53 genes cooperate to induce apoptotic tumor cell death. *Nature medicine*, 3(3):313–319, 1997.

[286] Martha Schreiber, William J Muller, Gurmit Singh, and Frank L Graham. Comparison of the effectiveness of adenovirus vectors expressing cyclin kinase inhibitors p16 ink4a, p18 ink4c, p19 ink4d, p21 waf1/cip1 and p27 kip1 in inducing cell cycle arrest, apoptosis and inhibition of tumorigenicity. *Oncogene*, 18(9):1663, 1999.

[287] H Sedlacek, JÖRG Czech, RAMACHANDRA Naik, GURMEET Kaur, PETER Worland, MICHAEL Losiewicz, BERNARD Parker, BRADLEY Carlson, ADALINE Smith, ADRIAN Senderowicz, et al. Flavopiridol (l86 8275; nsc 649890), a new kinase inhibitor for tumor therapy. *International journal of oncology*, 9(6):1143–1168, 1996.

[288] K Lundgren, SM Price, J Excobar, A Huber, P O?Connor, W Chong, R Duvadie, L Li, SS Chu, J Nonomiya, et al. Novel cyclin-dependent kinase inhibitors with potent growth-inhibitory action. In *Proc. Am. Assoc. Cancer Res*, volume 40, page A2022, 1999.

[289] DH Walker, M Luzzio, J Veal, K Dold, M Edelstein, P Parker, D Rusnak, D Emerson, C Miller, J Onori, et al. The novel cyclin dependent kinase inhibitors, gw5181 and gw9499 regulate cell cycle progession and induce tumorselective cell death. In *Proc. Am. Assoc. Cancer Res*, volume 40, page A4783, 1999.

[290] Wilhelm Krek, Gangfeng Xu, and David M Livingston. Cyclin a-kinase regulation of e2f-1 dna binding function underlies suppression of an s phase checkpoint. *Cell*, 83(7):1149–1158, 1995.

[291] Ted Weinert. A dna damage checkpoint meets the cell cycle engine. *Science*, 277(5331):1450–1451, 1997.

[292] Todd Waldman, Christoph Lengauer, Kenneth W Kinzler, and Bert Vogelstein. Uncoupling of s phase and mitosis induced by anticancer agents in cells lacking p21. *Nature*, 381(6584):713, 1996.

[293] Jann N Sarkaria, Ericka C Busby, Randal S Tibbetts, Pia Roos, Yoichi Taya, Larry M Karnitz, and Robert T Abraham. Inhibition of atm and atr kinase activities by the radiosensitizing agent, caffeine. *Cancer research*, 59(17):4375–4382, 1999.

[294] Simon N Powell, Jeffrey S DeFrank, Paul Connell, Maeve Eogan, Frederic Preffer, David Dombkowski, Wei Tang, and Stephen Friend. Differential sensitivity of p53 (-) and p53 (+) cells to caffeine-induced radiosensitization and override of g2 delay. *Cancer research*, 55(8):1643–1648, 1995.

[295] Shea N Gardner. A mechanistic, predictive model of dose-response curves for cell cycle phase-specific and-nonspecific drugs. *Cancer research*, 60(5):1417–1425, 2000.

[296] Bruce A Chabner and Thomas G Roberts Jr. Chemotherapy and the war on cancer. *Nature Reviews Cancer*, 5(1):65, 2005.

[297] Vincent T DeVita and Philip S Schein. The use of drugs in combination for the treatment of cancer: rationale and results. *New England Journal of Medicine*, 288(19):998–1006, 1973.

[298] Nicolas Guichard, Davy Guillarme, Pascal Bonnabry, and Sandrine Fleury-Souverain. Antineoplastic drugs and their analysis: a state of the art review. *Analyst*, 142(13):2273–2321, 2017.

[299] Douglas Hanahan and Robert A Weinberg. The hallmarks of cancer. *cell*, 100(1):57–70, 2000.

[300] Xia Li, Xiufeng Yin, Huafeng Wang, Jiansong Huang, Mengxia Yu, Zhixin Ma, Chenying Li, Yile Zhou, Xiao Yan, ShuJuan Huang, et al. The combination effect of homoharringtonine and ibrutinib on flt3-itd mutant acute myeloid leukemia. *Oncotarget*, 8(8):12764, 2017.

[301] Maria Omsland, Øystein Bruserud, Bjørn T Gjertsen, and Vibeke Andresen. Tunneling nanotube (tnt) formation is downregulated by cytarabine and nf-κb inhibition in acute myeloid leukemia (aml). *Oncotarget*, 8(5):7946, 2017.

[302] Mary Ann Jordan and Leslie Wilson. Microtubules as a target for anticancer drugs. *Nature Reviews Cancer*, 4(4):253, 2004.

[303] Mohd Islam, Magdy N Iskander, et al. Microtubulin binding sites as target for developing anticancer agents. *Mini reviews in medicinal chemistry*, 4(10):1077–1104, 2004.

[304] Long G Wang, Xiao M Liu, Willi Kreis, and Daniel R Budman. The effect of antimicrotubule agents on signal transduction pathways of apoptosis: a review. *Cancer chemotherapy and pharmacology*, 44(5):355–361, 1999.

[305] Subrata Haldar, Nilamani Jena, and Carlo M Croce. Inactivation of bcl-2 by phosphorylation. *Proceedings of the National Academy of Sciences*, 92(10):4507–4511, 1995.

[306] Russell D Petty, IA Cree, LA Sutherland, EM Hunter, DP Lane, PE Preece, and PE Andreotti. Expression of the p53 tumor suppressor gene product is a determinant of chemosensitivity. *Biochemical and biophysical research communications*, 199(1):264–270, 1994.

[307] Christine C Zhang, Jin-Ming Yang, Eileen White, Maureen Murphy, Arnold Levine, and William N Hait. The role of map4 expression in the sensitivity to paclitaxel and resistance to vinca alkaloids in p53 mutant cells. *Oncogene*, 16(12):1617, 1998.

[308] Mikhail V Blagosklonny, Paraskevi Giannakakou, Wafik S El-Deiry, David GI Kingston, Paul I Higgs, Len Neckers, and Tito Fojo. Raf-1/bcl-2 phosphorylation: a step from microtubule damage to cell death. *Cancer research*, 57(1):130–135, 1997.

[309] Enrique Raviña. *The evolution of drug discovery: from traditional medicines to modern drugs*. John Wiley & Sons, 2011.

[310] Harry K Slocum, John C Parsons, Elva O Winslow, Lori Broderick, Hans Minderman, Károly Tóth, William R Greco, and Youcef M Rustum. Time-lapse video reveals immediate heterogeneity and heritable damage among human ileocecal carcinoma hct-8 cells treated with raltitrexed (zd1694). *Cytometry Part A*, 41(4):252–260, 2000.

[311] Ariel A Cohen, Naama Geva-Zatorsky, Eran Eden, Milana Frenkel-Morgenstern, Iirina Issaeva, Alex Sigal, Ron Milo, Cellina Cohen-Saidon, Yuvalal Liron, Zvi Kam, et al. Dynamic proteomics of individual cancer cells in response to a drug. *science*, 322(5907):1511–1516, 2008.

[312] Sreenath V Sharma, Diana Y Lee, Bihua Li, Margaret P Quinlan, Fumiyuki Takahashi, Shyamala Maheswaran, Ultan McDermott, Nancy Azizian, Lee Zou, Michael A Fischbach, et al. A chromatin-mediated reversible drug-tolerant state in cancer cell subpopulations. *Cell*, 141(1):69–80, 2010.

[313] Nicholas A Saunders, Fiona Simpson, Erik W Thompson, Michelle M Hill, Liliana Endo-Munoz, Graham Leggatt, Rodney F Minchin, and Alexander Guminski. Role of intratumoural heterogeneity in cancer drug resistance: molecular and clinical perspectives. *EMBO molecular medicine*, 4(8):675–684, 2012.

[314] Sridhar Ramaswamy and Todd R Golub. Dna microarrays in clinical oncology. *Journal of clinical oncology*, 20(7):1932–1941, 2002.

[315] Marco Gerlinger, Andrew J Rowan, Stuart Horswell, James Larkin, David Endesfelder, Eva Gronroos, Pierre Martinez, Nicholas Matthews, Aengus Stewart, Patrick Tarpey, et al. Intratumor heterogeneity and branched evolution revealed by multiregion sequencing. *New England journal of medicine*, 366(10):883–892, 2012.

[316] Kornelia Polyak. Breast cancer: origins and evolution. *The Journal of clinical investigation*, 117(11):3155–3163, 2007.

[317] Mark Shackleton, Elsa Quintana, Eric R Fearon, and Sean J Morrison. Heterogeneity in cancer: cancer stem cells versus clonal evolution. *Cell*, 138(5):822–829, 2009.

[318] Dominique Bonnet and John E Dick. Human acute myeloid leukemia is organized as a hierarchy that originates from a primitive hematopoietic cell. *Nature medicine*, 3(7):730, 1997.

[319] Tsvee Lapidot, Christian Sirard, Josef Vormoor, Barbara Murdoch, Trang Hoang, Julio Caceres-Cortes, Mark Minden, Bruce Paterson, Michael A Caligiuri, and John E Dick. A cell initiating human acute myeloid leukaemia after transplantation into scid mice. *Nature*, 367(6464):645, 1994.

[320] James M Greene, Doron Levy, King Leung Fung, Paloma S Souza, Michael M Gottesman, and Orit Lavi. Modeling intrinsic heterogeneity and growth of cancer cells. *Journal of theoretical biology*, 367:262–277, 2015.

[321] Alexander RA Anderson and Vito Quaranta. Integrative mathematical oncology. *Nature Reviews Cancer*, 8(3):227, 2008.

[322] Angela Oliveira Pisco, Amy Brock, Joseph Zhou, Andreas Moor, Mitra Mojtahedi, Dean Jackson, and Sui Huang. Non-darwinian dynamics in therapy-induced cancer drug resistance. *Nature communications*, 4:2467, 2013.

[323] Ping Wang, Lydia Robert, James Pelletier, Wei Lien Dang, Francois Taddei, Andrew Wright, and Suckjoon Jun. Robust growth of escherichia coli. *Current biology*, 20(12):1099–1103, 2010.

[324] Amit Tzur, Ran Kafri, Valerie S LeBleu, Galit Lahav, and Marc W Kirschner. Cell growth and size homeostasis in proliferating animal cells. *Science*, 325(5937):167–171, 2009.

[325] Conrad A Messam and Randall N Pittman. Asynchrony and commitment to die during apoptosis. *Experimental cell research*, 238(2):389–398, 1998.

[326] Sabrina L Spencer, Suzanne Gaudet, John G Albeck, John M Burke, and Peter K Sorger. Non-genetic origins of cell-to-cell variability in trail-induced apoptosis. *Nature*, 459(7245):428, 2009.

[327] Patrick D Bhola and Sanford M Simon. Determinism and divergence of apoptosis susceptibility in mammalian cells. *Journal of cell science*, 122(23):4296–4302, 2009.

[328] Markus Rehm, Heinrich J Huber, Christian T Hellwig, Sergio Anguissola, Heiko Dussmann, and Jochen HM Prehn. Dynamics of outer mitochondrial membrane permeabilization during apoptosis. *Cell death and differentiation*, 16(4):613, 2009.

[329] Sabrina L Spencer and Peter K Sorger. Measuring and modeling apoptosis in single cells. *Cell*, 144(6):926–939, 2011.

[330] X Xia, MS Owen, REC Lee, and S Gaudet. Cell-to-cell variability in cell death: can systems biology help us make sense of it all? *Cell death & disease*, 5(5):e1261, 2014.

[331] Nicolas Chenouard, Ihor Smal, Fabrice De Chaumont, Martin Maška, Ivo F Sbalzarini, Yuanhao Gong, Janick Cardinale, Craig Carthel, Stefano Coraluppi, Mark Winter, et al. Objective comparison of particle tracking methods. *Nature methods*, 11(3):281, 2014.

[332] Adam Filipczyk, Carsten Marr, Simon Hastreiter, Justin Feigelman, Michael Schwarzfischer, Philipp S Hoppe, Dirk Loeffler, Konstantinos D Kokkaliaris, Max Endele, Bernhard Schauberger, et al. Network plasticity of pluripotency transcription factors in embryonic stem cells. *Nature cell biology*, 17(10):1235, 2015.

[333] Ariel Amir. Cell size regulation in bacteria. *Physical Review Letters*, 112(20):208102, 2014.

[334] Manuel Campos, Ivan V Surovtsev, Setsu Kato, Ahmad Paintdakhi, Bruno Beltran, Sarah E Ebmeier, and Christine Jacobs-Wagner. A constant size extension drives bacterial cell size homeostasis. *Cell*, 159(6):1433–1446, 2014.

[335] Clotilde Cadart, Sylvain Monnier, Jacopo Grilli, Rafaele Attia, Emmanuel Terriac, Buzz Baum, Marco Cosentino-Lagomarsino, and Matthieu Piel. Size control in mammalian cells involves modulation of both growth rate and cell cycle duration. *bioRxiv*, page 152728, 2017.

[336] Judit Zámborszky, Christian I Hong, and Attila Csikász Nagy. Computational analysis of mammalian cell division gated by a circadian clock: quantized cell cycles and cell size control. *Journal of biological rhythms*, 22(6):542–553, 2007.

[337] Sungmin Son, Amit Tzur, Yaochung Weng, Paul Jorgensen, Jisoo Kim, Marc W Kirschner, and Scott R Manalis. Direct observation of mammalian cell growth and size regulation. *Nature methods*, 9(9):910, 2012.

[338] Oded Sandler, Sivan Pearl Mizrahi, Noga Weiss, Oded Agam, Itamar Simon, and Nathalie Q Balaban. Lineage correlations of single cell division time as a probe of cell-cycle dynamics. *Nature*, 519(7544):468, 2015.

[339] Kazufumi Hosoda, Tomoaki Matsuura, Hiroaki Suzuki, and Tetsuya Yomo. Origin of lognormal-like distributions with a common width in a growth and division process. *Physical Review E*, 83(3):031118, 2011.

[340] Jean-Michel Paulus. Platelet size in man. *Blood*, 46(3):321–336, 1975.

[341] AL Koch. Distribution of cell size in growing cultures of bacteria and the applicability of the collins-richmond principle. *Microbiology*, 45(3):409–417, 1966.

[342] Z Cheng and S Redner. Kinetics of fragmentation. *Journal of Physics A: Mathematical and General*, 23(7):1233, 1990.

[343] D Imrichova, L Messingerova, M Seres, H Kavcova, L Pavlikova, M Coculova, A Breier, and Z Sulova. Selection of resistant acute myeloid leukemia skm-1 and molm-13 cells by vincristine-, mitoxantrone-and lenalidomide-induced upregulation of p-glycoprotein activity and downregulation of cd33 cell surface exposure. *European Journal of Pharmaceutical Sciences*, 77:29–39, 2015.

[344] Jing Yang, Takayuki Ikezoe, Chie Nishioka, Taizo Tasaka, Ayuko Taniguchi, Yoshio Kuwayama, Naoki Komatsu, Kentaro Bandobashi, Kazuto Togitani, H Phillip Koeffler, et al. Azd1152, a novel and selective aurora b kinase inhibitor, induces growth arrest, apoptosis, and sensitization for tubulin depolymerizing agent or topoisomerase ii inhibitor in human acute leukemia cells in vitro and in vivo. *Blood*, 110(6):2034–2040, 2007.

[345] Darcy JP Bates, Bethany L Salerni, Christopher H Lowrey, and Alan Eastman. Vinblastine sensitizes leukemia cells to cyclin-dependent kinase inhibitors, inducing acute cell cycle phase-independent apoptosis. *Cancer biology & therapy*, 12(4):314–325, 2011.

[346] Bethany L Salerni, Darcy J Bates, Tina C Albershardt, Christopher H Lowrey, and Alan Eastman. Vinblastine induces acute, cell cycle phase–independent apoptosis in some leukemias and lymphomas and can induce acute apoptosis in others when mcl-1 is suppressed. *Molecular cancer therapeutics*, 9(4):791–802, 2010.

[347] Anisha Kothari, Walter N Hittelman, and Timothy C Chambers. Cell cycle–dependent mechanisms underlie vincristine-induced death of primary acute lymphoblastic leukemia cells. *Cancer research*, 76(12):3553–3561, 2016.

[348] Tom Serge Weber, Irene Jaehnert, Christian Schichor, Michal Or-Guil, and Jorge Carneiro. Quantifying the length and variance of the eukaryotic cell cycle phases by a stochastic model and dual nucleoside pulse labelling. *PLoS computational biology*, 10(7):e1003616, 2014.

[349] Joany Jackman and Patrick M O'Connor. Methods for synchronizing cells at specific stages of the cell cycle. *Current protocols in cell biology*, pages 8–3, 2001.

[350] Lawrence D Brown, T Tony Cai, and Anirban DasGupta. Interval estimation for a binomial proportion. *Statistical science*, pages 101–117, 2001.

[351] Shinji Miwa, Shuya Yano, Hiroaki Kimura, Mako Yamamoto, Makoto Toneri, Yasunori Matsumoto, Fuminari Uehara, Yukihiko Hiroshima, Takashi Murakami, Katsuhiro Hayashi, et al. Cell-cycle fate-monitoring distinguishes individual chemosensitive and chemoresistant cancer cells in drug-treated heterogeneous populations demonstrated by real-time fucci imaging. *Cell Cycle*, 14(4):621–629, 2015.

[352] Enoch Kim, Younan Xia, and George M Whitesides. Polymer microstructures formed by moulding in capillaries. *Nature*, 376(6541):581, 1995.

Acknowledgements

The completion of this thesis would not have been possible without the contribution of the following professors, colleagues and friends.

First of all, I would like to express my deepest appreciation to my supervisor Prof. Joachim Rädler. Thank you for giving me the opportunity to work on these exciting projects, for your guidance, ideas and continuous support.

Many special thanks to Prof. Georg Fey. Your avid interest and enthusiasm for cancer immunotherapy have always inspired me.

I would like to thank Prof. Karl-Peter Hopfner and Prof. Thomas Brocker for being members of my QBM TAC meeting and also Dr. Carsten Marr for our fruitful collaboration.

I am grateful to Alexandra Murschhauser for her useful feedback in our shared projects, for her support in many other matters and her kind words. Many thanks to Matthias Zorn and Christoph Schreiber for patiently answering all my microscopy-related questions. Thank you to Janina Lange as well for her valuable help during the interpretation of my experimental results. I would also like to thank Farzad Sekhavati for our effective collaboration from the very beginning until the very end. Many thanks to Philip Böhm for his support and help during the submission of this thesis. And of course all the current and previous members of the Rädler chair for creating a nice atmosphere.

I would also like to thank Claudia Roskopf from the Prof. Oduncu chair for her direct help during our collaboration, the fruitful scientific discussions we had and for always welcoming me in the lab. Many thanks to Todd Braciak too for his constructive feedback and help during our collaboration.

Many thanks to Charlott Leu for the useful feedback she always provided me, both regarding micro-structuring but also immunological issues. I am also grateful to Gerlinde Schwake for her constructive advise regarding numerous wet lab matters, her help and for warmly welcoming me in the lab. I would also like to thank Susi Kempter for her help regarding any issue in the biochemistry lab.

I am also grateful to Mara Kieke from the QBM office, from day one until the very end she was always there to help for literally any issue. I also wish to thank Margarete Meixner and Andrea Cooke for their support and help throughout all these years.

I kindly acknowledge the generous financial support from the Deutsche Forschungsgemeinschaft in the context of funding for the Excellence Graduate School in Quantitative Biosciences (QBM).

Last but not least, I am thankful to everyone else that contributed in any way to the completion of this thesis and I did not mention explicitly, and of course to my family and friends for their unconditional and ceaseless support.